# DISLOCATION MICROSTRUCTURE AND SURFACE ROUGHNESS EVOLUTION IN SINGLE AND MULTI-PHASE MICROCRYSTALS

by
Ahmed M. Hussein

A dissertation submitted to Johns Hopkins University in conformity with the requirements for the degree of Doctor of Philosophy

Baltimore, MD
August 2015

# Abstract

A better understanding of the plastic deformation of metallic materials and their failure can greatly accelerate future material development. However, attaining such an understanding is difficult through only experimental investigations and/or simple analytical models. Recent advances in coarse grained simulations using large scale discrete dislocation dynamics (DDD) simulations provide detailed spatio-temporal descriptions of the evolution of complex dislocation networks in crystals having arbitrary microstructures and initial defect distributions, and under different loading conditions. In this thesis, a DDD framework has been developed and utilized to investigate the evolution of dislocation microstructures and surface roughness in single and multi-phase metal microcrystals.

First, three atomistically identified cross-slip mechanisms, namely, bulk, intersection and surface cross-slip, have been implemented in the DDD framework and utilized to study monotonic axial deformation in single crystal Nickel microcrystals of different sizes and initial dislocation densities. It is concluded that cross-slip leads to significant dislocation density multiplication, strain hardening, the formation of dislocation cell-like structures in larger crystals and the formation and thickening of slip bands on the crystal surface. Surface cross-slip was found to be the most frequent, followed by intersection and then bulk cross-slip. These simulations are also shown to be in agreement with recent microcompression experimental observations in both Nickel and Aluminium microcrystals.

Second, the evolution of dislocation microstructure and surface roughness during cyclic mechanical loading was investigated. The cyclic response was divided into two separate stages: the early stage response starting from a random dislocation microstructure, and the response of crystals having well-developed Persistent Slip Band (PSB). In random dislocation microstructure simulations, crystals having sizes larger that 5 μm showed cyclic hardening, significant dislocation density multiplication and the formation of dislocation cell-like structures. The evolution of surface roughness due to dislocations escape has been quantified. The atomic concentration of point defects generated from dislocation annihilation in PSB walls was quantified and was found to agree with experimental estimates.

Finally, the DDD framework was extended to model the interaction of dislocations with an arbitrary distribution of precipitates that have an $L1_2$ crystal structure by explicitly tracking the creation and destruction of Anti-Phase Boundary (APB) regions. This framework was then utilized to perform the first DDD simulations of single crystal superalloy micropillars with different precipitate microstructures. The micropillar strength was found to vary linearly, follow a square-root relationship and an inverse square-root relationship with the precipitate volume fraction, APB energy and size respectively while the crystal size has no effect on its strength. The width of the inter-precipitate channels was found to be the main strength determining factor. The results were validated with detailed comparisons with recent microcompression experiments on single crystal Nickel-based superalloys.

Thesis Readers: Prof. Jaafar A. El-Awady (advisor), Prof. Kevin J. Hemker and Dr. Christopher F. Woodward

بِسْمِ ٱللَّهِ ٱلرَّحْمَٰنِ ٱلرَّحِيمِ

ٱقْرَأْ بِٱسْمِ رَبِّكَ ٱلَّذِي خَلَقَ ﴿١﴾ خَلَقَ ٱلْإِنسَانَ مِنْ عَلَقٍ ﴿٢﴾

ٱقْرَأْ وَرَبُّكَ ٱلْأَكْرَمُ ﴿٣﴾ ٱلَّذِي عَلَّمَ بِٱلْقَلَمِ ﴿٤﴾

عَلَّمَ ٱلْإِنسَانَ مَا لَمْ يَعْلَمْ ﴿٥﴾

القرآن الكريم [سورة العلق : ١-٥]

In the name of Allah, The Most Gracious, The Most Merciful
"Read! In the name of thy Lord Who createth, Createth man from a clot.
Read! And thy Lord is the Most Bounteous, Who teacheth by the pen,
Teacheth man that which he knew not."

The Holy Qur'an [96:1-5]

# Acknowledgements

I would like to acknowledge the help and support I received from several people, without which this dissertation would not have been possible.

First, I would like to express my sincere gratitude to my advisor, Professor Jaafar El-Awady for offering the guidance I needed to pursue my work, helping to shape my research skills, teaching me how to ask the right questions before attempting to answer any, offering the honest advice I needed during the times of confusion and being a senior friend rather than a boss. I would also like to thank Professor Kevin Hemker and Dr. Christopher Woodard for reading my thesis and serving on my thesis committee.

A big part of this work was done in conjunction with scientists from UES Inc. and the Air Force Research Lab. Through the long discussions I had with them, they taught me a lot, gave me a deeper appreciation of the value of my work and brought to me attention a vast number of research work that helped me validating my results and interpreting them. I would like to acknowledge the help from Dr. Satish Rao, Dr. Michael Uchic, Dr. Dennis Dimiduk and Dr. Triplicane Parthasarathy.

The Johns Hopkins community has provided a stimulating environment for learning and growing. I learned a lot through the interactions with the faculty members, postdoctoral fellows and graduate students. The long, thought provoking scientific and philosophical discussions I was lucky to get engaged in showed me how little I know and sparked further curiosity and the need to refine my ideas. I would also like

to thank all the Mechanical Engineering Department administrative staff members for their prompt and professional assistance whenever I needed any.

I would like to thank all my lab mates, especially Amin Aramoon and Dr. Kinshuk Srivastava for the stimulating discussions, necessary distractions and the Monday coffee-hour company. During my stay in Baltimore, I was lucky to get to know a number of friends who made my life richer and much more enjoyable. I am grateful for all the great times spent with Ahmed Fareed, Ismail Hameddudin, Nasir Ismail, Kendal Ackermann, Eman Sbaity, Neha Dixit, Abdulla Nabeel and Osman Yogurtcu. Special thanks go to my dearest friends overseas who tolerated my long physical absence, maintained our strong friendship, and made sure that I am not missing out on the great times, Amr ElHennawy and Dina ElMaamoun.

I cannot overemphasize the endless support of my family and how it brought me to where I am now. Dad, thanks for being a source of inspiration for all the past years, you are the biggest influence in my life and I am very lucky to be still learning from you even though we are thousands of miles apart. Mom, thanks for your love, care and tolerating my long leave. I could not have done anything or gone anywhere without the sincerity of your prayers. Mohamed and Mahmoud, thanks for being the best companions in life, for understanding when I am not there for you and for taking care of my parents, physically and emotionally, during my absence.

Few years back, I was blessed with the greatest gift in my life, Galia. I am deeply indebted to you for your endless love, care, support, sacrifice, understanding, and being a great friend before being a wife. I could not have made it without your encouragement and belief in me. I find my biggest motivation in you and our lovely son, Murad. May God assist me to be a good husband and a good father.

# Contents

# List of Tables

# List of Figures

# Chapter 1

# Introduction

## 1.1 The Development of Metallic Materials

Besides the discovery of fire, the knowledge of how to extract, process and use metals probably had the most profound effect on mankind. Technological strides, qualitative transformations in the social order, the emergence of new economic patterns and the rise and fall of empires, all stemmed from the power acquired by societies and peoples upon learning how to form metals into tools, arms, armor, structures and machinery. It is of no surprise that archaeologists and physical anthropologists named two out of the three ages of human prehistory and early history, the stone age, the bronze age, and the iron age [1], after the most common metals used in making tools during each age. In the modern age, the use of metals defines heavy industry, of which the progress demarcates the developed from the developing nations. In areas critical for sustaining and advancing the quality of life and social prosperity, such as energy and national security, there is an undeniable profuse usage of metallic alloys. Thus, the development of new metallic systems and processing methods is an essential effort that has to be undertaken by the research community.

Like in most development efforts, economics plays a major role in providing the

need to pursue further research in metallic materials in three different ways. First, failure of metallic systems has significant direct and indirect costs which can be reduced or avoided with more advanced alloys or processing methods. The direct costs include the costs of replacing the failed components and the associated production downtime. This is most pronounced in heavy industries such as the military, petrochemicals and oil and gas industries. The indirect costs are usually more severe and include the loss of lives, injuries or extreme environmental damage. Second, the operational costs of vehicles and machinery are continuously increasing due to the increase in energy costs. Since metallic systems dominate the construction of vehicles and industrial machinery, the development of lighter alloys with similar or better strength, thermal and corrosion properties would cut the operational costs appreciably at a time when energy sources are becoming increasingly scarce. Third, the cost of lost business resulting from the product development delays or failures due to the lack of appropriate alloys is increasing due to the intense business challenges in a world of knowledge democratization. This last one is difficult to quantify but the opposite case, that is, the profits resulting from developing a product that relies on a novel alloy, can provide some measures.

The open challenges in the development of metallic materials include, but not limited to, preventing or delaying failure under certain operational conditions, increasing ductility, stiffness and strength at room or higher temperatures or enhancing the metal's corrosion resistance and phase stability. This boils down to characterizing how materials respond, at the atomic level, to the various loading and environmental conditions. A perfect characterization of a material system would be the identification of the position of each atom in the system at any time. However, this is not feasible with current technologies and the amount of data one would get from such a characterization, if it exists, is even more difficult to analyze and to extract useful material evolution and deformation pathways from. Fortunately, metallic systems are crys-

talline and a great deal of abstraction can be achieved by only characterizing their crystal structure and the dynamics of their localized deviations from crystallinity, known as material defects. It turns out that many of the diverse and interesting material behavior relies mainly on how the defects evolve in time under the applied loads, as Sir Charles Frank once said, "Crystals are like people: it is the defects in them that make them interesting."

This thesis presents an attempt to characterize the defect mechanisms and their evolution in structural materials through computational simulations. The focus will be on modeling the behavior of metallic systems subject to monotonic and cyclic mechanical loads under various operational temperatures. A perfect example for such loading conditions is what happens inside gas turbines used for power generation or inside jet engines. The use of gas turbines started in the mid 1930s for small power stations and military aircraft. Over the years, significant improvements in the system design and engine materials were introduced to increase its operational limits and efficiency. A major factor in the efficiency of any gas turbine is the turbine entry temperature (TET). The higher the TET is, the more efficient the turbine becomes. At the same time, the turbine blades are subject to high cyclic inertial loads due to their rotation speeds that can reach $100,000$ rpm [2]. The materials from which turbine blades and disks are constructed should both be strong enough to sustain this cyclic load and maintain their strength as the temperature increases. Computational simulations are chosen because they can provide the full spatio-temporal evolution of the physical quantities of interest. This can greatly facilitate explaining the main deformation and failure mechanisms that take place in the components under consideration. In addition, computational simulations can be used to artificially activate or shut-off certain physical mechanisms in order to study the effect of other mechanisms in isolation. Besides, simulating the material's behavior at loading or thermal regimes that are experimentally challenging, expensive, unsafe to run or inaccurate to measure

can assist in exploring the full spectrum of materials behavior and direct experimental efforts to the potentially most useful research directions. With this knowledge in hand, the materials development process can be accelerated and its costs cut down.

## 1.2 Computational Simulations of Deformation and Failure

For any system of moderate to high complexity subject to thermomechanical loads, the finite element method (FEM) [3, 4] became a standard approach to simulating its behavior. At the heart of any FEM simulation lies a mathematical model that mimics the material's behavior, the constitutive model. It is the degree of accuracy and robustness of this model that mainly dictates the quality of FEM results. For brittle metallic materials and ceramics, damage models [5, 6] are used to model the progressive loss of strength leading to complete failure. On the other hand, metals that show some ductility prior to failure are modeled using plasticity models [7, 8] that account for metal flow and different types of hardening. Most typical plasticity models however are phenomenological in nature, that is, they are based on empirical fits that model how the material of interest behaves under laboratory tests. While this approach in constitutive model development is suitable for simulating large scale heterogeneous systems with multiple interacting components, it does not say anything about the physics of deformation or failure. These models can be used to simulate the dynamics of complex engineering systems but they cannot be used to develop an understanding of how materials behave.

Plasticity models based on the actual material structure and physics are called crystal plasticity (CP) models [9]. Since metal's plasticity is mainly controlled by dislocation motion and interactions, CP models are dislocation density based. That is, they have the dislocation density as a state variable that controls the yield strength

and hardening rates at each point in the simulation. They are based on parametrized functional forms for the dislocation density evolution. CP models can operate, in theory, on the same length and time scales of the phenomenological models. Hence, they are qualitatively different from phenomenological models in that they reflect actual material physics. However, the material deformation process occurs at various length and time scales and CP is designed to capture the defect microstructure evolution at the length scale of dislocation ensembles (tens to hundreds of micrometers) and the time scale appropriate for significant defect density variations (a few milliseconds). A deeper understanding requires resolving the deformation mechanisms at length and time scales lower than those accessible by CP. Plus, the model parameters of CP can only be obtained from simulations and experiments at lower scales.

An appropriate lower scale is that of dislocation dynamics. This ranges from about 100 nm to 50 μm in length and up to 1 ms in time. This is the range suitable for resolving the motion and interactions of individual dislocations. Two types of computational simulations are typically used at this scale, Continuum Dislocation Dynamics (CDD) [10] and Discrete Dislocation Dynamics (DDD) [11–16]. Similar to CP, the main variable in CDD is the dislocation density but no density evolution laws are assumed or fitted. The change in the dislocation density in a CDD control volume is due to the density flux into that volume or the generation (or annihilation) of dislocations in it. The long range dislocations interactions are usually neglected in CDD and the short range ones are statistically approximated [10]. Also the dislocation velocities in CDD are often assumed to be independent of the local stress[10, 17]. DDD captures the density evolution with fewer assumptions compared to CDD, hence, it can be used to fit the parameters of CP models. Also certain dislocation patterns, such as dislocation cell structure formation, have been successfully captured by CDD [17, 18]. The main assumption in CDD simulations is the dislocation velocity which can only be captured using a lower length scale method.

On the other hand, DDD discretely resolves the individual dislocations and all the short and long range dislocations interactions are accounted for. The long range interactions are modeled using the exact solution from the theory of elasticity [14, 16], which does not break down for long range interactions. Short range interactions, such as dislocation collisions, annihilation and dislocation core changes leading to cross-slip, are explicitly modeled so that they fit the results of lower length scale methods or experimental findings. DDD is also explicit in terms of modeling the effects of two and three dimensional defects, such as grain boundaries [19, 20], twin boundaries [21] and precipitates [22, 23] on the movement of dislocations. Explicit dislocation network formation and density and plastic strain evolution can be directly obtained from DDD simulations under general spatially and temporally varying stress fields and arbitrary crystal geometries. Thermally activated mechanisms can be individually modeled in DDD to faithfully reflect their occurrence in the real metal. Unlike CP and CDD, DDD is truly discrete and it does not rely on any kind of mesh or grid to run its calculations on. The only assumption used in DDD is the mobility law, which is a constitutive model that links the velocity of a dislocation point to its local stress. Like CDD, this is typically obtained from a lower scale simulation method such as molecular dynamics simulations, or by fitting experimental results.

Molecular Dynamics (MD) simulations [24] can model systems ranging in size from few nanometers to hundreds of nanometers over time intervals up to a few microseconds. MD simulations are sophisticated n-body simulations that can trace the motion of every single molecule or atom in the simulation and extract useful system information such as temperature, pressure and energy based on this data. The scale of MD simulations separates the scales where classical mechanics are valid from those which cannot be treated without resorting to quantum mechanics. In MD simulations, crystal structures emerge naturally as the minimum energy configurations for the atomic locations. Similarly, any crystal defects they contain, such as dislocations,

are introduced, or they arise, as spatially extended perturbations of the minimum energy configuration. Dislocations can be introduced into MD simulations and their mobility under various stress and temperature levels can be calculated [25]. MD simulations are also used to study individual defect mechanisms such as dislocation cross-slip [26–30], climb [31], grain boundary migration [32], and twin formation [33]. However, they suffer from severe length and time scale limitations due to their high computational costs. The only assumption made in MD simulations is in the force of interactions between different atoms. Parametrized interatomic potentials, or force fields, are required in order to properly capture the atomic interactions and the system's energy. These interatomic potentials are usually developed and fit using lower scales simulation method such as the density Functional Theory.

At the very bottom of the length and time scales lies the most basic, first principles, simulation method, the Density Functional Theory (DFT) [34]. DFT calculation are direct solutions to Schrodinger's equation that yield the electronic structure of matter. The Born-Oppenheimer [34] approximation is used to separate the slow motion of the heavier atomic nuclei from the faster, almost instantaneous, motion of the lighter electrons. Then, the Hohenberg-Kohn theory [35] provides the justification for approximating the electronic configuration by a spatially varying electron density. The main outcome of DFT calculations is the system's ground state and energy. DFT calculations are used to develop interatomic potentials suitable for different kinds of metals to be used in MD simulations [36]. The length scale of DFT calculations is typically that of a few atoms (a few Angstroms).

The methods discussed above span all the relevant length and time scales. Figure 1.1 summarizes the various length and time scales discussed above along with the appropriate simulation methods for each scale. These scales are usually connected together in a hierarchical manner where the lower length scales feed the higher length scales with the parameters they need. An alternative approach, which is beyond the

scope of this thesis, is the concurrent simulations [37] where different spatial regions are modeled using different methods at the same time with a way to bridge the state variables from one region to the other. This is typically used when certain regions of the simulation need to be resolved at a finer level such as modeling the region surrounding a crack tip using MD and the rest of the system using FEM to capture the crack propagation more accurately [38]. In the following chapters, DDD simulations will be utilized to quantify the mechanical behavior and the deformation mechanisms in both pure and multiphase metallic systems. DDD was chosen because it covers a larger gap in both length and time scales and it is an appropriate method that can connect the physical mechanisms active at the atomic scales to the engineering applications of interest.

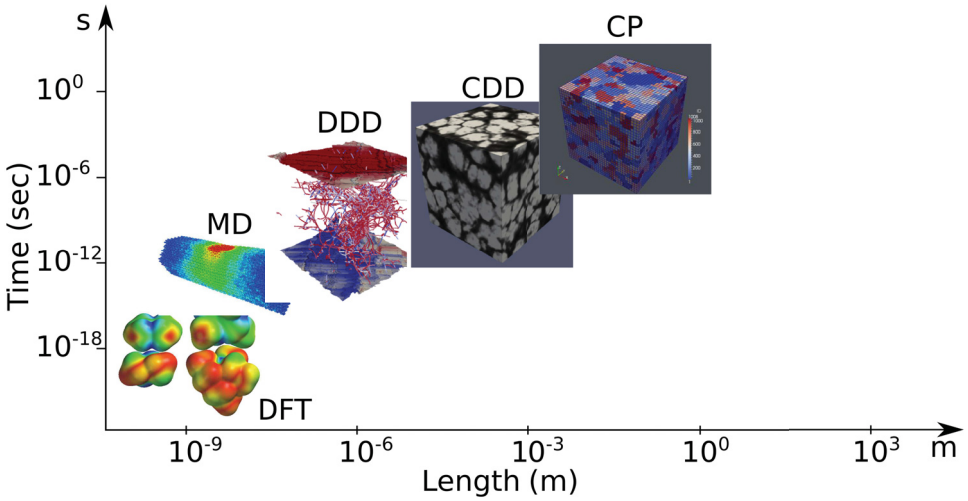


Figure 1.1: Different computational methods and their appropriate length and time scales for modeling the behavior of metallic systems. The CDD image is from Xia et. al. (DOI:10.1088/0965-0393/23/5/055009) "©IOP Publishing. Reproduced with permission. All rights reserved".

## 1.3 The Gas Turbine : A Case Study

A full characterization for the active deformation mechanisms in the turbine blade and disk materials during the typical operation of a gas turbine is far from complete. The effects of a number of well known deformation mechanisms on the overall response need to be identified. The complexity of the loading patterns and the material construction make this task more challenging. Turbine materials are subject to various operating temperatures, high frequency cyclic loading, and they are constructed from advanced alloys that have complicated microstructures.

Materials in high temperature environments typically experience frequent thermally activated deformation mechanisms [39] such as dislocation cross-slip and climb. Dislocation cross-slip is the process by which screw-dislocations glide conservatively from a low stress to a higher stress glide plane [40]. This mechanism is thermally activated because the dislocation core needs to change shape from a lower energy configuration into a higher energy configuration and this is usually not spontaneous especially in the absence of other defects. On the other hand, climb is the nonconservative motion of a dislocation in a direction normal to its slip plane [41]. It takes place mainly by the diffusion of point defects into or from the dislocation core. At higher temperature, the diffusion coefficient of point defects increases and consequently the dislocation climb rate. Cross-slip is more frequent than climb at moderate temperatures and it is one of the most important mechanisms responsible for dislocation cell structure formation and strain hardening [42–47]. Cross-slip has been studied extensively through experiments [48–50], MD [26–30, 51, 52] and DDD [11, 13, 53–55] simulations, however, physics based cross-slip mechanisms have not yet been fully implemented in DDD simulations to date. This has lead to far from accurate predictions of dislocation microstructure evolutions, and the lack of any significant dislocation patterning observations in DDD simulations. As will be shown in the following chapters, the correct mechanical response and microstructure evolution from DDD simu-

lations is critically correlated to physically-based cross-slip under monotonic loading in FCC metals.

It is well documented that cyclic loading is the main cause of failure in mechanical components [56, 57]. Failure is preceded by the nucleation of cracks, usually on the surface of the component [57, 58] or at internal interfaces, these cracks typically propagate until a critical crack size is reached, after which unstable crack propagation takes place. To date there are no physics-based theories capable of accounting for crack nucleation in these environments. Nevertheless, it is agreed that the interaction of plastic flow and the breaking of atomic bonds in regions of high local stresses both play a major role. Surface extrusions and intrusions forming due to the escape of dislocations gliding on a number of active slip planes increases the stress concentration around these sharp surface features and facilitates bond breaking. Dislocations arrange themselves in high and low dislocation density regions inside the material, such as dislocation cells [59–62] and persistent slip bands [63], which explains why dislocation escape can be localized. The interaction of dislocations during the loading and unloading stages of the cyclic loading results in the formation of these structures. In addition, cyclic strain hardening or softening takes place as more loading cycles are applied on the material. It is thus necessary to understand how the dislocations arrange themselves into dislocation patterns and how this alters the material properties, to be able to develop better fatigue resistant materials. From an operational point of view, a better understanding of fatigue failure mechanisms can help provide better and less conservative estimates for the life time of the components in question and reduce the amount of inspection and maintenance work needed for their safe operation.

Finally, modern gas turbine blades are typically made from nickel-base superalloys [64] because they maintain their strength at high temperatures. These alloys have a large number of alloying elements and usually have at least two distinct phases, termed

the $\gamma$ and $\gamma'$ phases respectively, with some alloys having a third $\gamma''$ phase. The $\gamma$ phase, (the matrix) is FCC nickel with of solute atoms dispersed throughout. The $\gamma'$ phase is $Ni_3Al$ or $Ni_3Ti$, which usually forms large precipitates that get dispersed in the matrix phase. The movement of dislocations in the $\gamma'$ phase is different than that in the $\gamma$ phase because the $\gamma'$ phase is an ordered phase where the glide of one dislocation disrupts the local chemistry of the precipitate structure resulting in a high energy configuration, hence, the precipitates resist the glide of dislocations through them. On the other hand, if a dislocation glides through a region of the slip plane that has already been disrupted by another dislocation, the minimum energy configuration is restored, and hence, the system attracts this second dislocation. This asymmetry in how the $\gamma'$ phase responds to the dislocations gliding through it gives rise to different dislocation patterning behavior and strength properties. If the dislocation shearing through precipitates is too difficult, dislocations can cross-slip, climb or loop around the precipitate to bypass it. To date, no full DDD simulations have been capable of capturing the interaction of general dislocation distributions with arbitrary precipitate microstructures. A simulation of that type can give deep insights into the role of precipitate volume fractions, sizes and types on the strength of the alloy at various temperatures and provide guidance to alloy developers on which alloys are promising for certain application areas.

## 1.4 Thesis Objectives and Organization

The objective of this thesis is to develop an extensible DDD framework capable of modeling the different deformation mechanisms discussed in section 1.3 and utilize it to study the mechanical response and the evolution of dislocation microstructures for different materials under different loading conditions. In particular, the following research efforts have been undertaken:

- The proper implementation of atomistically informed physics-based cross-slip mechanisms in DDD simulations.
- Quantify the effect of cross-slip on the response and the microstructure evolution of pure nickel.
- Quantify the evolution of dislocation microstructure and the hardening and softening behavior in nickel single crystals during cyclic loading.
- Quantify the surface roughness evolution due to dislocation escape from the crystal surface in nickel single crystals during cyclic loading.
- Model the dislocation microstructure evolution in persistent slip bands (PSB) and quantify the generation of point defects due to dipole annihilation.
- Extend the DDD framework to account for general precipitate microstructures and their interactions with dislocations.
- Quantify the mechanical response and the dislocation microstructure evolution in nickel-base superalloy microcrystals under monotonic loading.

These efforts aim to provide a link between what is known about the dynamics of individual dislocations and the macroscopic deformation behavior observed in experiments and application for materials used in gas turbines. The DDD method is probably the most suitable for the large scale modeling of the effect of these phenomena on the material response.

The thesis is organized as follows. In Chapter 2, the mathematics and computational details of the DDD methods are discussed in detail. In Chapter 3 the incorporation of physics-based cross-slip mechanisms for FCC metals in DDD are presented, and results from a parametric study on the effects in cross-slip on the strength and dislocation microstructure evolution of single crystal nickel micropillars

of different sizes and initial dislocation densities are discussed. Chapter 4 presents the application of the DDD method in studying the behavior of metals under cyclic loading. The evolution of the dislocation microstructure and the effect of dislocation activities on the evolution of surface roughness on the crystal surface is quantified for crystals of different sizes and initial dislocation densities. Finally, a number of DDD simulations of persistent slip bands (PSB) under cyclic loading are presented and the generation of point defects due to the annihilation of dislocation dipoles in the PSB walls and channels is quantified. In Chapter 5, the DDD framework is extended to account for dislocation interactions with general precipitate microstructures. A number of DDD simulations on single crystal nickel superalloy microcrystals of different precipitate microstructures are discussed. Finally, in Chapter 6, a summary of the work is presented and a number of suggested future research directions that build on the current work are presented. It is worth noting that some of the passages in Chapters 3, 4 and 5 have been quoted verbatim from a publication [65], a number of submitted manuscripts by the author [66–70].

# Chapter 2

# Mathematical and Computational Foundations

## 2.1 Mathematical Models for Dislocations and their Elastic Fields

A distinct feature of dislocation theory is that it was entirely conceived before any actual observation of dislocations. Dislocations were proposed to explain why metals flow at stress levels that are significantly lower than their theoretical values, which are on the order of the shear modulus. The actual flow strength for metals is in fact three orders of magnitude lower than the theoretical strength [40, 41]. The theoretical development of dislocations took place in two different directions. First, and before proposing their existence in materials, Volterra [71] in 1915 developed the mathematical theory that describes the elastic fields due to line defects in an otherwise compatible continuum. This mathematical development forms the basis for calculating the interaction stress between calculations. Second, the existence of dislocations was theoretically proposed independently by Orowan [72–74], Taylor [75, 76] and Polanyi [77] in 1934 to explain less-than-theoretical flow stress observed

crystals. A concise but excellent review of the developments in the dislocation theory is given by Hirth [78]. In this section, the basic models for dislocations will be reviewed and expressions for the dislocations' elastic fields will be derived.

### 2.1.1 The Somigliana Dislocation

Although it is not the first model to be conceived, the Somigliana dislocation model [79, 80] is the most general mathematical model for a linear material defect because it imposes the least number of specifications on that defect. The Somigliana model starts by the thought process of making a cut of general shape inside the material of an infinite continuum. The separated surfaces on both sides of the cut are then displaced relative to each other according to a non-uniform displacement field. The surfaces are then weld back together to restore the continuity of the medium. At the points on the cut surface where the displacement vector lies within the surface's tangent plane, the process can proceed conservatively, that is, without the insertion or removal of any material, while material insertion and removal is required for all other points. The resulting deformed structure of the continuum develops an elastic strain field. After welding, the displacement field is continuous everywhere except along the boundary curve of the cut surface. This boundary curve represents the dislocation, and due to the displacement discontinuity along the dislocation line, the strain and the stress fields are singular along it.

When dealing with Somigliana dislocations, it is difficult to reduce the features of the dislocation generation process described above to those of the dislocation curve because the imposed displacement field, which is the only restriction imposed, is spatially varying and unless there is a clever mathematical transformation that would uniquely map the two dimensional field to the one dimensional dislocation curve, the displacement information would be lost. This is only possible in the simple cases such as linearly varying displacement fields [81]. Following Eshelby [82], the displacement

at the medium point $r$ due to the presence of a Somigliana dislocation is given by

$$u_i(r) = \int_S b_j(r') p^i_{jk}(r, r') n_k(r') dS \tag{2.1}$$

where $u_i$ is the $i^{th}$ displacement component, $b_j(r')$ is the displacement imposed on the cut surface at point $r'$, $p^i_{jk}(r')$ is the $jk$ stress field component at the surface point $r'$ due to a unit force at point $r$ in the direction of the $x_i$ axis, $n_k(r')$ is the normal to the cut surface at point $(r')$ and $S$ is the cut surface. The vector $b_j(r')$ is defined to be the displacement of the cut surface in the direction of $n_k(r')$ minus that of the surface in the direction opposite to $n_k(r')$. The reasoning behind this equation comes primarily from the Betti's Reciprocity theorem [83]. Imagine an unstressed solid in which the dislocation is to be introduced and let $f_i$ be a unit force in the direction of the $x_i$ axis applied at the point $r$ at which the displacement $u_i(r)$ is desired. If one introduces the dislocation and then the force $f_i$, the total stored energy in the solid would be $E_D + E_F$ where $E_D$ is the energy due to the dislocation's introduction and $E_F$ is that due to the force application. Because the force deforms the medium in the same way regardless of the dislocation's presence, there is no work done by the dislocation when the force is introduced later on. However, if the force was applied and then the dislocation was introduced, the total stored energy would be $E_D + E_F + T_D + T_F$ where $T_D$ is the work done by the dislocation to displace the two surfaces of its cut against the traction caused by the force's presence and $T_F$ is the work done by the force when the dislocation displaces its point of application as it gets introduced. In linear elasticity, the order of the load application is irrelevant and the final state of the system, including its stored energy, should be the same either way. This means that $T_D = -T_F$ which is the statement of Equation 2.1. The left hand side is $T_F$ (notice that the magnitude of $f_i$ is unity) and on the other hand is $T_D$ which is equal to the integral

$$T_D = -\int_S b_j(r')t_j(r')dS \tag{2.2}$$

where $t_j(r')$ is the traction on the cut surface at point $r'$ due to the applied force. This traction can be written as

$$t_j(r') = p^i_{jk}(r, r')n_k(r') \tag{2.3}$$

Somigliana dislocations have not been studied heavily as separate theoretical entities due to their complex elastic fields. However, they found some applications in geophysics [82], the modeling two dimensional crystalline defects such as the interface of coherent prismatic precipitates, phase boundary sliding during high temperature deformation and tilt grain boundaries [81] and the shear of martensitic transformations [84] which is better dealt with using disclinations [85], which are special cases of Somigliana dislocations.

### 2.1.2 The Volterra Dislocation

The Volterra dislocation model [71] was developed before the Somigliana model and it is the most widely used dislocation model for theoretical and computational treatments [85, 86]. It is a special case of the Somigliana model in that the imposed displacement field is constant ($b_j(r') = b_j$) which simplifies the elastic fields expressions and allows the reduction of the dislocation surface to its bounding curve. Moreover, it is consistent with the physical theories of dislocations put forth by Orowan [72–74], Taylor [75, 76] and Polanyi [77] in that the slip around the dislocation loop is constant. A direct consequence of the constancy of imposed displacement is that the divergence of the Burgers vector must be zero everywhere in the medium which is an essential condition in continuum dislocation dynamics [87]. The displacement field of the Volterra dislocation can be obtained from that of the Somigliana dislocation

(Equation 2.1) by imposing a constant displacement

$$u_i(x) = b_j \int_S p^i_{jk}(x, x') n_k(x') dS \tag{2.4}$$

The function $p^i_{jk}(r, r')$ can be obtained from the displacement's Green's function $U^k_i$, which, for isotropic elasticity, is [85]

$$U^k_i(x) = \frac{1}{4\pi\mu} \left( \frac{\delta_{ik}}{r} - \frac{r_{,ik}}{4(1-\nu)} \right) \tag{2.5}$$

where $\mu$ and $\nu$ are the material's shear modulus and Poisson's ratio respectively, $\delta_{ij}$ is the Kronecker delta, the comma denotes differentiation and $r$ is the magnitude of the vector connecting the field point $x$ to the source point $x'$. This is the displacement at point $x$ in the $i^{th}$ direction due to a unit force at point $x'$ in the $k^{th}$ direction. A full derivation for Green's function is given in Appendix A. The strain field $E^k_{ij}(x)$ due to the same force is

$$E^k_{ij}(x) = \frac{1}{2} \left( U^k_{i,j} + U^k_{j,i} \right) \tag{2.6}$$

which upon substituting Equation 2.5 in 2.6 gives

$$E^k_{ij}(x) = \frac{-1}{16\pi\mu(1-\nu)r^2} \left( \frac{3r_i r_j r_k}{r^3} - \frac{\delta_{ij} r_k}{r} + \frac{1-2\nu}{r} (\delta_{ik} r_j + \delta_{jk} r_i) \right) \tag{2.7}$$

The stress field $\sigma_{ij}$ for isotropic elasticity is given by

$$\sigma_{ij} = \lambda \delta_{ij} \epsilon_{kk} + 2\mu \epsilon_{ij} \tag{2.8}$$

where $\lambda = \frac{2\mu\nu}{1-2\nu}$, by substituting Equation 2.7 in 2.8, one gets an expression for $p^k_{ij}$

$$p_{ij}^{k}(x) = \frac{-1}{8\pi\mu(1-\nu)r^2}\left(\frac{3r_i r_j r_k}{r^3} + \frac{1-2\nu}{r}(\delta_{ik}r_j + \delta_{jk}r_i - \delta_{ij}r_k)\right) \tag{2.9}$$

Substituting Equation 2.9 in 2.10 gives an expression for the Volterra dislocation's displacement field which, after rearranging, is

$$u_i(x) = \frac{1}{8\pi}\int_S b_i r_{,ppj} dS_j + \frac{1}{8\pi}\int_S (b_k r_{,ppk} dS_i - b_j r_{,ppi} dS_j) + \frac{1}{8\pi(1-\nu)}\int_S (b_j r_{,ppi} - b_k r_{,ijk}) dS_j \tag{2.10}$$

where $dS_i = n_i dS$, this expression can be rewritten in the following form

$$u_i(x) = \frac{1}{8\pi}\int_S b_i r_{,ppj} dS_j + \frac{1}{8\pi}\int_S (\delta_{jt}\delta_{iq} - \delta_{it}\delta_{jq}) b_j r_{,ppt} dS_q + \frac{1}{8\pi(1-\nu)}\int_S (\delta_{qp}\delta_{jt} - \delta_{qj}\delta_{pt}) b_t r_{,pqi} dS_j \tag{2.11}$$

Using the Levi-civita - Kronecker delta connection

$$\epsilon_{ijk}\epsilon_{ilm} = \delta_{jl}\delta_{km} - \delta_{jm}\delta_{kl} \tag{2.12}$$

one can rewrite Equation 2.11

$$u_i(x) = \frac{1}{8\pi}\int_S b_i r_{,ppj} dS_j + \frac{1}{8\pi}\int_S \epsilon_{lji}\epsilon_{ltq} b_j r_{,ppt} dS_q + \frac{1}{8\pi(1-\nu)}\int_S \epsilon_{lqj}\epsilon_{lpt} b_t r_{,pqi} dS_j \tag{2.13}$$

and from Stokes theorem

$$\int_S \epsilon_{ijk} T_{\alpha\beta.....i,j} dS_k = \int_C T_{\alpha\beta.....i} dl_i \tag{2.14}$$

for any tensor $T_{\alpha\beta.....i}$. Applying this theorem on the last two terms in Equation 2.13, one gets

$$u_i(x) = \frac{1}{8\pi}\int_S b_i r_{,ppj} dS_j + \frac{1}{8\pi}\oint_C \epsilon_{ikj} b_j r_{,pp} dl_k + \frac{1}{8\pi(1-\nu)}\oint_C \epsilon_{kpj} b_j r_{,pi} dl_k \quad (2.15)$$

where $C$ is the curve bounding the surface. The first term in expression 2.15 can be transformed from a surface integral to a line integral using the surface integral expression for solid angles. A solid angle $\Omega$ subtended by an object at a point is defined to be the area of the object's radial projection on a unit sphere centered at the point. The projection of an area element $dS$ on the surface $S$ bounded by the dislocation loop on the unit sphere is equal to

$$dS^p = \frac{r_{,i} n_i}{r^2} dS \quad (2.16)$$

where $r_{,i}$ is the unit vector starting at the angle calculation point and pointing at the area element, $n_i$ is the normal to the area element and $r$ is the distance between the calculation point and the area element. The solid angle then becomes

$$\Omega = \int_{S^p} dS^p = \int_S \frac{r_i n_i}{r_3} dS = \int_S \frac{r_j}{r_3} dS_j \quad (2.17)$$

this expression has the same form as the first integral in Equation 2.15 after multiplying it by a factor of $-2$ (because $r_{,ppj} = -2\frac{r_j}{r^3}$). This gives the final expression for the displacement field of a dislocation loop in an infinite isotropic medium

$$u_i(x) = \frac{-b_i \Omega}{4\pi} + \frac{1}{8\pi}\oint_C \epsilon_{ikj} b_j r_{,pp} dl_k + \frac{1}{8\pi(1-\nu)}\oint_C \epsilon_{kpj} b_j r_{,pi} dl_k \quad (2.18)$$

This expression depends only on the dislocation loop and not on the cut surface that formed the dislocation. The first term is the solid angle subtended by the dislocation at the point $x$ at which the displacement field is required. The strain field of a dislocation loop can be directly calculated from the stress field

$$\epsilon_{ij}(x) = \frac{-1}{8\pi}(b_i\Omega_{,j}+b_j\Omega_{,i})+\frac{1}{16\pi}\oint_C b_m(\epsilon_{ikm}r_{,ppj}+\epsilon_{jkm}r_{,ppi})dl_k+\frac{1}{8\pi(1-\nu)}\oint_C \epsilon_{kpm}b_m r_{,pij}dl_k \tag{2.19}$$

The derivative of the solid angle $\Omega_{,j}$can be obtained from its surface integral expression

$$\Omega_{,j} = \frac{\partial}{\partial x_j}\left(-\frac{1}{2}\int_S r_{,ppl}dS_l\right) = -\frac{1}{2}\int_S r_{,pplj}dS_l \tag{2.20}$$

Since $r_{,ppll} = 0$ for all cases, one can rewrite the previous expression

$$\Omega_{,j} = \frac{1}{2}\left(\int_S r_{,ppll}dS_j - \int_S r_{,pplj}dS_l\right) = \frac{1}{2}\int_S \left(\delta_{tl}\delta_{qj} - \delta_{ql}\delta_{tj}\right) r_{,pplt}dS_q \tag{2.21}$$

Using the Levi-Civita Kronecker delta connection one more time then applying Stoke's theorem

$$\Omega_{,j} = \frac{1}{2}\int_S \epsilon_{ktq}\epsilon_{klj}r_{,pplt}dS_q = \frac{1}{2}\oint_C \epsilon_{klj}r_{,ppl}dl_k \tag{2.22}$$

Substituting back into Equation 2.19

$$\epsilon_{ij}(x) = \frac{1}{16\pi}\oint_C \left(b_i\epsilon_{kjq}r_{,q} + b_j\epsilon_{kiq}r_{,q} + b_m\epsilon_{ikm}r_{,j} + b_m\epsilon_{jkm}r_{,i}\right)_{,pp} + \frac{2\epsilon_{kpm}b_m}{(1-\nu)}r_{,pij}dl_k \tag{2.23}$$

Finally, using equations 2.8 and 2.23, one can obtain the stress field of a dislocation loop after some rearrangement

$$\sigma_{ij}(x) = \frac{\mu b_m}{8\pi}\left[\oint_C r_{,pp\alpha}\left(\epsilon_{\alpha mi}dl_j + \epsilon_{\alpha mj}dl_i\right) + \frac{2}{(1-\nu)}\oint_C \epsilon_{\alpha mk}\left(r_{,ij\alpha} - \delta_{ij}r_{,pp\alpha}\right)dl_k\right] \tag{2.24}$$

This equation is valid only for infinite isotropic media. To handle anisotropic solids, a different Green's function (Equation 2.5) is required. A series solution for anisotropic elasticity Green's function that uses Fourier transforms was given by Mura [88]. For materials with cubic crystal structures, the anisotropy is minimal (equal axial, shear and shear strain-axial stress coupling stiffness moduli) and the number of stiffness constants reduce to 3. This justifies the use of isotropic media dislocation stress fields in most DDD simulations because the computational cost of using the anisotropic elasticity stress fields is huge compared to using the isotropic ones. On the other hand, the anisotropy due to dislocations' glide on energetically favorable slip planes is perfectly accounted for in DDD simulations without any approximations.

### 2.1.3 The Non-Singular Dislocation Model

A Volterra dislocation is a curve that separates the displaced region from the undisplaced region according to the Somigliana construction explained in Section 2.1.1. Since the transition between the two regions takes place abruptly, all the elastic fields derived in Section 2.1.2 are singular. This results in numerical inaccuracies when calculating the stress fields from a dislocation loop at a point which is very close to, or on, the loop. A nonsingular dislocation theory was developed by Cai et. al. [89] where the transition between the displaced and undisplaced regions takes place gradually over a width $a$ which is defined to be the dislocation's core width. The theory does not assume a certain shape for the dislocation core. In terms of Volterra dislocations, the nonsingular dislocation can be thought of as a continuous distribution of Volterra dislocations each of an infinitesimal Burgers vector. The dislocation's

core distribution is chosen so as to facilitate the calculation of the interaction force between two dislocations, which is the most expensive and error-prone step in DDD simulations. In particular, the Burgers vector of the nonsingular dislocation can be written as

$$b = \int_{\Lambda} g(x) d\Lambda \tag{2.25}$$

where $\Lambda$ is a planar region in the plane normal to the dislocation's tangent vector at the point at which the Burgers vector is required. The dislocation's core is spread out in that plane. The function $g(x)$ is the shape of the dislocation's core which is to be solved for. When calculating the force from one dislocation loop on another, the stress $\sigma_{ij}$ from the source loop $C_s$ is integrated over the target loop $C_t$ according to Peach-Koehler relationship as follows

$$f_k = \oint_{C_t} \epsilon_{ijk} \sigma_{ip} b_p dl_j = \frac{\mu}{8\pi} \oint_{C_t} \epsilon_{ijk} \oint_{C_s} b_m^s A_{ipmq} b_p^t dl_q dl_j \tag{2.26}$$

where $b_i^s$ and $b_i^t$ are the Burgers vectors of the source and target dislocations respectively and $A_{ipmq}$ is a 4th-order tensor equivalent to the integration kernel of Equation 2.24. The core distribution $g(x)$ is chosen such that its convolution $w(x) = g(x) * g(x)$ when convoluted with $r(x)$ gives $r_a(x)$ which has the form

$$r_a(x) = r(x) * w(x) = \sqrt{r_i r_i + a^2} \tag{2.27}$$

Since the expansion of $A_{ipmq}$ consists of terms of the form $r_{,ijk} * w(x)$, replacing all $r_{,ijk}$ with $r_{a,ijk}$ results in an expression which cannot be singular even for zero $r$. The function $w(x)$ was found to be

$$w(x) = \frac{15}{8\pi a^3 \left(\frac{r^2}{a^2} + 1\right)^{7/2}} \tag{2.28}$$

However, a closed form solution for $g(x)$ cannot be found and a numerically fit solution for it was given in [89]. $g(x)$ is essential for calculating the stress field from a nonsingular dislocation at a point while $w(x)$ is all that is required to calculate the force of interaction between two dislocations.

## 2.2 The Discrete Dislocation Dynamics Method

The DDD method is a computational method by which dislocation networks can be introduced into a thermomechanically loaded medium and subsequently evolved in time [11–15, 54]. The dislocations move under the effects of the applied and interaction stresses. Other factors that can affect their motion is shearing of precipitates or collisions with other dislocations. The DDD system iterates, indefinitely, over a fixed sequence of computations resulting in the proper modeling of the evolution physics and the estimation of the overall mechanical response. In the sections below, the basic DDD loop will be described along with the details of each step. The DDD simulation system used in this work is a heavily modified and extended version of ParaDis, a DDD system developed in Lawrence Livermore National Laboratory [16].

### 2.2.1 Basic DDD Loop

The main DDD loop is qualitatively similar to the main molecular dynamics (MD) loop [24]. Initially, the dislocation microstructure is represented as a network as explained in Section 2.2.2 and is input along with the crystal geometry and all the boundary conditions. Each time step begins by calculating the applied loads as described in sections 2.2.3 and 2.2.4. This is followed by calculating the forces on the different dislocation segments which is the most computationally intensive step in the entire DDD loop. Section 2.2.5 gives the details of these calculations and Section 2.3 describes some of the methods used to accelerate this part. With the

segment and nodal forces in hand, the velocities of the dislocation nodes can then be calculated using the chosen mobility functions. All the crystallographic constraints, including the proper handling of dislocation nodes moving on the crystal surfaces, are imposed in this step as detailed in Section 2.2.6. Similar to MD, time integration then follows as described in Section 2.2.7. In the case of using periodic boundary conditions (PBC), the integrator is responsible for handling where the dislocation nodes should end up in case they exit the boundary in any direction and maintaining the connectivity with other dislocation nodes. This step terminates the main part of the loop and all the mechanical properties can be calculated and output at this point as described in Section 2.2.8.

The rest of the DDD loop handles the topological changes in the dislocation network and the dynamic load balance which is necessary for efficiently simulating larger systems. First, an extensive search for all the dislocation reactions is undertaken and all the reactions are handled. Section 2.2.9 describes the 3 types of dislocation reactions and how the system modifies the dislocation network in each case. Second, the dislocation network is adaptively remeshed, which is another topological modification in the network and. The final step is presented in Section 2.2.10 and it is the dynamic balancing of the computational load over the computational resources available for the simulation. A flowchart that represents the overall DDD loop is given in Figure 2.1.

### 2.2.2 Dislocation Network Representation

There are numerous ways by which dislocation microstructures can be computationally represented for DDD simulations. Ghoniem et. al. [14] represented dislocations as parametric curves lying on planes in 3D whose shapes are controlled by their end nodes in case of linear splines, end nodes and tangent vectors in case of cubic splines and end nodes, tangents and curvatures in case of quintic splines. On the other hand,

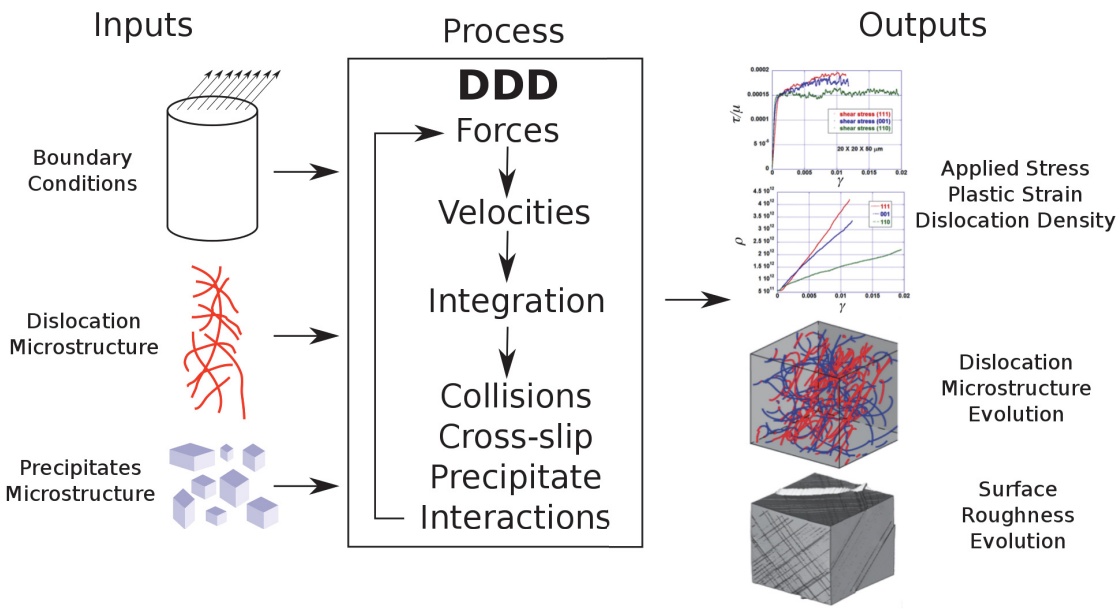


Figure 2.1: The basic input, output and DDD loop steps

Kubin et. al. [11] used a simpler representation where dislocation segments can either be edge or screw segments or make an angle of 60 degrees with the screw orientation [90]. The representation of dislocations in this work however is based on the way dislocations represented in the original ParaDis code [16]. The dislocation microstructure is represented by a set of three-dimensional nodes which are interconnected by linear dislocation segments. The segments can have any orientation and they are not constrained to lie in a particular plane. The dislocation nodes define the shape of the dislocation network while the dislocation segments that connect them carry the actual dislocation information such as its slip plane and Burgers vector. Dislocation nodes are allowed to have any number of neighbours and the overall topology of the system is time varying. This way, the dislocation microstructure is represented truly as a graph structure [91] with the vertices being the dislocation nodes and the edges being the dislocation segments. This proved to be useful in handling some necessary search and processing operations such as the efficient implementation of cross-slip event detection.

The different representations presented vary in terms of the accuracy of representing the dislocation microstructure and the computational load required for their simulation. The parametric representation has the advantage of requiring a fewer number of nodes which reduces the overall number of degrees of freedom. Besides, it guarantees a certain degree of continuity depending on the order of the employed spline. Finally, it guarantees that the dislocations will always remain planar which is preferred especially when modeling FCC crystallographic systems where dislocation off-plane motion is less likely. However, to maintain the higher order continuity, the nodes, tangents and curvatures of the splines have to be evolved in a consistent manner because they are coupled through the spline equation. This results in a system of linear equations that has to be solved during the time integration. This is a serious drawback especially for larger simulations where the number of degrees of freedom can be quite large. On the other hand, the edge-screw representation is the simplest, does not require solving linear systems for evolution as it depends only on the nodal positions, but it results in a lower representation accuracy for mixed-type dislocation unless a huge number of nodes is used. The graph representation relaxes the orientational constraints imposed in the edge-screw representation and does not require solving linear systems for integration since nodes can move independently, however, it still needs more degrees of freedom for a better microstructure representation compared to the parametric case.

A dislocation node can have one of three types, pinned, free or surface. Pinned nodes cannot move at all and they are used to model the ends of Frank-Read sources. Free nodes are free to move under constraints imposed by the slip planes of their connected segments. That is, a free node connected to two segments on the same plane can move on that plane while a free node connected to two segments on different planes can only move along the line of intersection of the two planes. Surface nodes are free nodes with an extra constraint that they have to move tangent to the crystal

surface at all times. Hence, a surface node connected to one segment moves along the curve of intersection of the crystal surface with the slip plane of that segment. Free nodes cannot be connected to only one segment because this violates the Burgers vector continuity. The sum of the Burgers vectors of the segments connected to any free node should be zero. Given the previous constraints, one can see that free nodes connected to more than 2 segments are likely to be pinned if at least 3 segments are on different slip planes. Plus, surface nodes cannot be connected to anything different than 1 segment or 2 segments on the same plane or else they cannot move at all.

### 2.2.3 Applied Load Calculations

The calculation of the applied loads is a central part of the DDD loop because it is the way by which the flow stress can be calculated. DDD systems are flexible in terms of the kind of loading scenarios that can be implemented. The applied load can be either a stress controlled or a strain controlled load. For stress controlled cases, time varying stress tensor is imposed on the crystal while for the strain controlled cases, a time varying strain tensor is imposed from which the corresponding stress tensor is calculated. The strain controlled loading cases can be further subdivided into total strain controlled and plastic strain controlled loading.

Depending on the problem geometry and the applied load, the stress field can be specified analytically or obtained numerically. For the simple geometries and loading cases where the full stress distribution can be solved analytically, it is preferred to input the stress distribution to the DDD system so as to reduce the computational load required to solve for the stress field at every time step. For more complicated boundary value problems, the Finite Element Method (FEM) can be used to solve for the stress field distribution accurately at the expense of the simulation runtime.

The simplest load case is that of the constant applied stress which is usually used to model creep deformation. The stress tensor is given as an input and it is constant

in space and time such that all dislocations move under the effect of the same applied stress. The load case used for most of the work described in this dissertation is the total strain rate controlled loading where an imposed strain rate is given and the system is loaded in a way such that this total strain rate is achieved at all times. In DDD simulations, infinitesimal strains are always assumed and hence, the additive decomposition of the total strain tensor $\epsilon$ [7] holds

$$\epsilon_{ij} = \epsilon_e^{ij} + \epsilon_{ij}^p \tag{2.29}$$

where $\epsilon_{ij}^e$ and $\epsilon_{ij}^p$ are the elastic and plastic strain tensors respectively. The stress $\sigma_{ij}$ corresponding to a given elastic strain state can be calculated given the material stiffness constants $C_{ijkl}$

$$\sigma_{ij} = C_{ijkl}\epsilon_e^{ij} = C_{ijkl}(\epsilon_{ij} - \epsilon_{ij}^p) \tag{2.30}$$

Rewriting this equation in the rate form

$$\dot{\sigma}_{ij} = C_{ijkl}(\dot{\epsilon}_{ij} - \dot{\epsilon}_{ij}^p) \tag{2.31}$$

and multiplying by the time step duration $\Delta t$

$$\dot{\sigma}_{ij}\Delta t = \Delta\sigma_{ij} = C_{ijkl}(\dot{\epsilon}_{ij}\Delta t - \dot{\epsilon}_{ij}^p\Delta t) = C_{ijkl}(\dot{\epsilon}_{ij}\Delta t - \Delta\epsilon_{ij}^p) \tag{2.32}$$

gives a general formula for updating the stress increment

$$\sigma_{ij}(t + \Delta t) = \sigma_{ij}(t) + \Delta\sigma_{ij} = \sigma_{ij}(t) + C_{ijkl}(\dot{\epsilon}_{ij}\Delta t - \Delta\epsilon_{ij}^p) \tag{2.33}$$

From the previous expression, it is obvious that the plastic strain increment during the time interval $\Delta t$ needs to be calculated. The details of this calculation will be presented in Section 2.2.8.

In order to calculate the stress tensor as described above, two assumptions need to be made. First, the stress is uniform or the stress gradients are small and negligible. This assumption is needed to justify the uniform stress field imposed throughout the sample. Second, the crystal is small enough so that the plastic strain tensor is uniform or has low gradients. Without this assumption, a plastic strain field has to be calculated, with corresponding elastic strain and stress fields. The assumption of small simulation volume amounts to modeling the representative volume element surrounding a single Gauss point in an FEM simulation.

Relaxing the first assumption, especially for the cases where high stress accuracy is required near the simulation volume boundaries where the stress gradients are high, can be achieved using an FEM solver coupled to the DDD simulation system. The plastic strain increment can be passed to the FEM solver and an accurate stress field can be solved for. Notice however that still the second assumption of uniform plastic strain field is imposed in this case. In the work presented in this dissertation, no effort was undertaken to relax the second assumption and compute localized plastic strain fields from DDD simulations and passing them to the FEM solver. It is also worth mentioning that the imposed total strain rate can be time varying so that cyclic loading problems can be modeled as well as simple axial loading cases. In the case of using FEM to solve for the stress field, a fully dynamic 3D FEM was used to account for the inertia effects of time varying loads.

### 2.2.4 Image Stresses

In deriving the dislocation stress field presented in Section 2.1.2, the crystal was assumed to be infinite in size. This assumption is valid when the problem has PBCs. However, for finite sized crystals, the stress field needs to be corrected to account for the presence of surfaces bounding the simulation volume.

Mathematically, the difference between a finite sized crystal and an infinite crys-

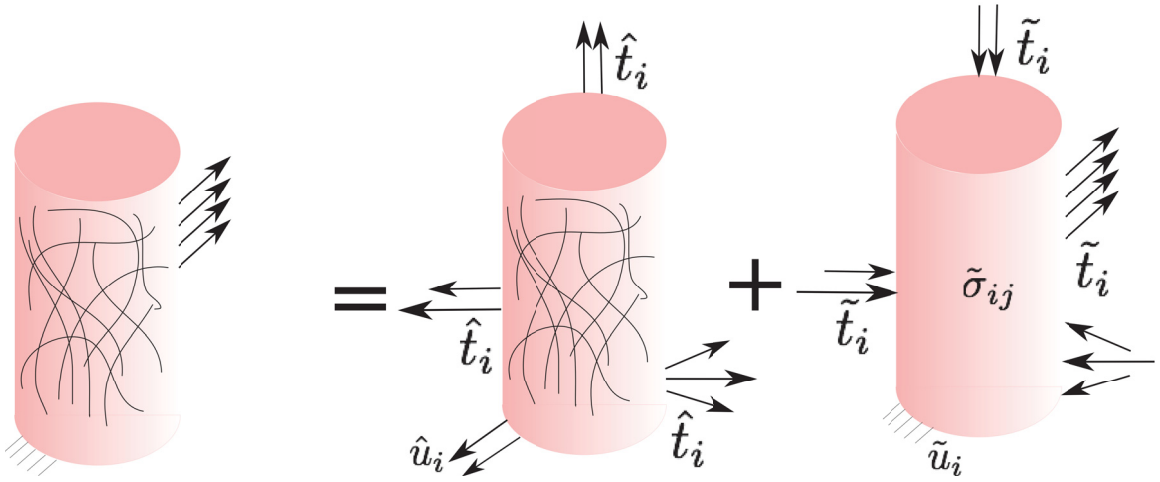


Figure 2.2: The decomposition of the finite size crystal problem into two problems. The first is for an infinite crystal with the dislocation microstructure and no boundary conditions. The tractions $\hat{t}_i$ and the displacements $\hat{u}_i$ on the surface of the crystals due to the dislocation network are calculated. The second is for a dislocation free finite sized crystal with the boundary conditions in addition to the negative of $\hat{t}_i$ and $\hat{u}_i$ applied. The solution of the second problem gives a stress field $\tilde{\sigma}_{ij}$ which is the correct stress field for the finite sized crystal with the dislocations present.

tal is that for the finite sized crystal, extra kinematic and kinetic constraints are imposed. For instance, for a finite sized crystal with free surfaces, the traction has to vanish everywhere on the surface. For a finite sized crystal with an imposed traction distribution, the traction due to the overall stress field must match the imposed traction. In general, for a finite sized crystal with any distribution of imposed boundary conditions (on the displacement or traction), the deformation fields must satisfy that distribution. This view, along with the linearity assumption, provide a method to correct for the dislocation stress fields [12, 54, 55] by breaking down the linear elasticity problem into two problems as schematically shown in Figure 2.2. The first is that of an infinite crystal with the dislocation network, the second is that of a finite dislocation free crystal. Let the imposed displacement field on the surface point $x_j$ be $u_i(x_j)$ and the imposed traction distribution be $t_i(x_j)$. Also let the dislocation displacement and stress fields from the first problem be $\hat{u}_i(x_j)$ and $\hat{\sigma}_{ij}(x_k)$. The tractions due to the dislocation stress field are given by

$$\hat{t}_i(x_j) = \hat{\sigma}_{ip}(x_j) n_p(x_j) \tag{2.34}$$

where $n_p(x_j)$ is the surface normal at $x_j$. The image displacement $\tilde{u}_i(x_j)$ and stress $\tilde{\sigma}_{ij}(x_k)$ fields are then

$$\tilde{u}_i(x_j) = u_i(x_j) - \hat{u}_i(x_j) \tag{2.35}$$

and

$$\tilde{t}_i(x_j) = t_i(x_j) - \hat{t}_i(x_j) \tag{2.36}$$

The image fields $\tilde{u}_i(x_j)$ and $\tilde{t}_i(x_j)$ have no closed form solution and hence, they are always passed to an FEM solver in order to solve for the corresponding stress field $\tilde{\sigma}_{ij}$, termed the image stress. The image stress is then added to the stress due to the applied loads calculated using the methods described in Section 2.2.3 and the total stress is used as the applied stress. Notice that the FEM solver is optionally used for the applied load stress calculation but it has to be used for the image stress calculations.

Since one needs the dislocation displacement and traction distributions on the surface of the crystal only, a triangular mesh is used to represent the surface and the tractions are directly calculated from the dislocation network at the mesh points. The surface displacements due to individual dislocations are in the order of 1 Burgers vector magnitude, which is significantly smaller than the typical simulation size ( 1000 to 10000 times the Burgers vector magnitude), the surface displacements due to dislocations $\hat{u}_i(x_j)$ were neglected which significantly reduces the computational load given that this calculation has to be performed before every FEM calculation. In order to reduce the computational load further, updating the image stress is performed only every $k$ DDD time steps where $k$ is around 1000 to 10000. Finally, for

bigger crystals, the image forces can be safely neglected since their contribution on the dislocation stress can be as low as 1% of the contribution of the interaction stress [92, 93].

### 2.2.5 Force Calculations

The force calculation is the heart of the DDD system as it is the most computationally intensive step. As far as this work is concerned, there are two main forces acting on dislocation segments; the forces due to the applied stresses and those due to interaction stresses. Sections 2.2.3 and 2.2.4 describe how the former is calculated while the calculation of the latter is the subject of this Section. The force per unit length $f_k$ acting on a dislocation can is related to the overall stress (applied and interaction) acting on it through the famous Peach-Koehler formula [41]

$$f_k = \epsilon_{ijk}\sigma_{ip}b_p t_j \tag{2.37}$$

where $\sigma_{ij}$ are the components of the total stress tensor at a dislocation segment point, $b_p$ are the components of the dislocation Burgers vector, $t_j$ are the components of the vector tangent to the dislocation at the point at which the force is required and $\epsilon_{ijk}$ is the permutation symbol.

A naive way for calculating the interaction stresses between the dislocation segments would be to iterate over all the dislocation segments and calculate the stresses they induce on a particular target segment and repeat this for all the target segments. This is an $O(N^2)$ which becomes increasingly limiting as the problem size grows larger.

Approximate methods can be used to speed up the force calculation part by dividing the dislocation segments interacting with a particular segments into groups based on the interaction strength. The dislocation stress field is inversely proportional with

the distance from the dislocation, hence, further dislocations do not have the same effect on the dislocation in question and it is more justifiable to approximate their stress fields. A generic approach to categorize dislocations is to divide the simulation volume into equally sized subvolumes, sometimes called cells, and classifying the dislocation segments according to the cell that contains them. The cells are labeled with three indices $(i, j, k)$ according to their order in each of the three directions.

For a dislocation segment in cell $(i, j, k)$, the full $N^2$ interactions are calculated with the dislocation segments that are in the same cell and those that are in a neighbouring cell, that is, all cells with labeled $(i+l, j+m, k+n)$ where $l$, $m$ and $n$ range from $-1$ to 1. The interaction with the dislocation segments external to these 27 cells can be neglected if the overall dislocation density is low or handled using one of the methods described in Section 2.3 if a more accurate calculation is required. The overall calculation complexity is still $O(N^2)$ but with $N$ being the number of the dislocation segments in the surrounding cells instead of all the dislocation segments in the system. As the number of cells is increased, the calculation speed increases at the expense of its accuracy.

### 2.2.6 Dislocation Mobility

Dislocations move under the actions of applied and interaction stresses and their velocities are in general nonuniform. The equation of motion of a dislocation point is given by [92, 94]

$$m_{eff}(\dot{x})\ddot{x} + B(\dot{x})\dot{x} = f(x) - \tau_f(x)b \tag{2.38}$$

where $m_{eff}$ and $B$ are the dislocation's effective mass and the viscous drag coefficient respectively, $f$ and $\tau_f$ are the force per unit length and the glide friction stress acting on the dislocation and $b$ is the magnitude of the dislocation's Burgers vector

[94]. The effective mass and the drag coefficient are nonlinear and they depend on the dislocation's velocity. In most cases, especially when the dislocation speeds are significantly lower than the speed of sound in the material, the effective mass is about 11 orders of magnitude less than the drag coefficient [94] and hence, the acceleration term is usually neglected and the dislocation motion is considered to be overdamped. These observations have been confirmed experimentally as well [95] by studying the dislocation displacements in response to applied stress pulses of known time durations. In the light of these observations, one can rewrite the nonlinear force-velocity relationship in the following form

$$v_i = M(f_j, \tau_f, t_k, b_l, T) \tag{2.39}$$

which will be termed the dislocation mobility relationship. In this equation, $v_i$ is the velocity vector at a dislocation point and $f_j$,$t_k$ and $b_l$ are the total force acting at this point per unit length, the tangent to the dislocation curve and the dislocation's Burgers vector respectively and $T$ is the system's temperature. The dislocation mobility is the relationship between the stress experienced by a dislocation segment and its glide velocity and it is one of the few steps where material specific properties are required in DDD simulations. The mechanisms by which dislocations move have been the subject of several investigations [92, 94, 96] and a full review of them is beyond the scope of this dissertation. These mobility functions serve as the "constitutive laws" for DDD simulations.

Because dislocations are line defects, the motion of a dislocation point in the direction of the dislocation curve tangent at this point is meaningless, hence, dislocation points move in a plane normal to their tangents and the velocities defined by the mobility functions are two-dimensional in nature. The crystallographic systems studied in this dissertation are mainly FCC systems and their derivatives, such as the $L1_2$ system. The dislocations in these systems dissociate into two Shockley partials on the

same glide plane as the perfect dislocation [40]. The planar dislocation core restricts its motion on the glide plane which means that the velocity vector cannot have an off-plane component. This reduces the mobility function from a three-dimensional vector function to a scalar function with the scalar velocity component $v^n$ being the velocity in the glide plane normal to the dislocation curve tangent. In addition to the dislocation core being planar in FCC materials, the glide resistance stress for close-packed metals is on the order of $10^{-4}\mu$ where $\mu$ is the elastic shear modulus of the material and this number increases to about $10^{-2}\mu$ for diamond cubic semiconductors [92] which makes the resistance stress less than 10 MPa for metals which is significantly less than the typical flow stresses of the materials of interest. For this reason, the resistance stress dependence will be dropped in the mobility functions used in the studies discussed in this dissertation. The mobility function then becomes

$$v^n = M(f_j, t_k, b_l, T) \tag{2.40}$$

A further restriction that can help simplifying the functional form is the glide plane isotropy. The mobility of a certain dislocation segment does not depend on the absolute orientation of that segment in the glide plane, it depends only on the segment's orientation relative to the dislocation's Burgers vector. Thus, the two vectors $t_k$ and $b_l$ can be replaced by the angle $\theta$ between them, which carries the dislocation character information. A final assumption is the linearity of the velocity-force relationship [13, 95, 96] which holds true when the dislocation speed is less than the speed of sound [94]. In the simulations to be discussed later in this dissertation, the mean dislocation speed is on the order of tens of meters per second while the speed of sound in the metals of interest are on the order of thousands of meters per second. Also the linearity in the relationship holds at room and lower temperatures [94]. This gives the form of the mobility function used in this work

$$v^n = M_d(\theta, T) f^n \tag{2.41}$$

where $f^n$ is the force component in the direction of $v^n$ and $M_d(\theta, T)$ is the viscous drag term, the dependence of which on the dislocation character $\theta$ is given by [97]

$$M_d(\theta, T) = M_e(T) cos^2(\theta) + M_s(T) cos^2(\theta) \tag{2.42}$$

where $M_e(T)$ and $M_s(T)$ are the mobilities of the edge and screw dislocations respectively. These mobilities can be calculated from molecular dynamics simulations by applying a constant stress field on a crystal containing a single edge or screw dislocation at a fixed temperature and measuring the time taken by the dislocation to travel a certain distance. A detailed example of such studies can be found in [98].

### 2.2.7 Time Integration

The evolution of the dislocation microstructure takes place during the time integration step. Each dislocation node advances in space according to its velocity, calculated as described in Section 2.2.6 and the time step duration. There are several integrators available for DDD simulations but in this work, simple Forward Euler integration was used where the nodal position $x_i^{n+1}$ at the time step $n+1$ is obtained from the previous nodal position at time $n$ according to

$$x_i^{n+1} = x_i^n + v_i \Delta t^n \tag{2.43}$$

where $v_i^n$ is the nodal velocity at time step $n$ and $\Delta t^n$ is the duration of the $n^{th}$ time step. Because the Forward Euler integrator is conditionally stable [99], an adaptive time stepping technique is employed to make sure that the time step is small enough in order to capture the correct evolution dynamics. The time step is computed such that the fastest moving dislocation node cannot move a distance bigger than $r_{max}$ at

any time step.

$$\Delta t^n = \frac{r_{max}}{max(||v_i||)} \tag{2.44}$$

where the maximization takes place over all the nodes in the system. The maximum distance $r_{max}$ is always chosen to be less than 5% of the average dislocation segment length so that the segment shape does not change significantly during time stepping. The rate controlling nodes are usually the ones in high density regions. Thus, limiting how far they can travel in one step helps making the simulation more accurate because the interaction forces get repeatedly updated as they move and interact with the nearby dislocation segments.

A particular problem which causes the time step to drop significantly and eventually slows down the simulations is the dislocation node oscillations. In high density regions, nodes connected to shorter dislocation segments tend to oscillate over their equilibrium position at a high frequency which makes these nodes the fastest moving nodes and the system gets locked in this oscillatory mode where most of the dislocation microstructure is at rest and the few oscillating nodes are the only active ones. A damping algorithm was developed in order to solve this problem. At time step $n+1$, and before updating the nodal velocity, the old nodal velocity $v_i^n$ and the new one $v_i^{n+1}$ are compared to see whether the node is oscillating. A node is considered oscillatory if the velocity vector fully reverses its direction over one time step such that the quantity

$$\frac{v_i^{n+1} v_i^n}{||v_i^{n+1}||||v_i^n||} < -s \tag{2.45}$$

where $s$ is taken to be $0.7 \approx 0.9$. If the condition is satisfied, the node is switched to the damping mode and it is given an integer $k$ which is taken to be 5 in all the simulations. The velocity of the node is then damped according to

$$v_i^{n+1} \leftarrow 10^{-(k-(m-n-1)} v_i^{n+1} \tag{2.46}$$

where $m$ is the current time step and $n+1$ is the step at which the damping began. Once the factor $(k-(m-n+1)$ reaches zero, the node is taken out of the damping mode and its time integration proceeds normally. Thus, the node damping does not continue for more than $k$ time steps in all cases and the damping degree decreases as time proceeds until it vanishes completely. It was found that this method helps several simulations from being stuck in an everlasting oscillatory mode which is problematic especially for controlled total strain rate simulations such as the ones described in Section 2.2.3.

### 2.2.8 Mechanical Properties Calculation

The mechanical response is the primary output of DDD systems. Several load and deformation variables can be obtained from the dislocation configuration and history including the plastic strain and its rate, the dislocation velocity distribution and the dislocation density. The last two can be directly calculated knowing the nodal velocities and the segments' lengths. The former however requires a more involved calculation.

With no loss of generality, consider a planar Volterra dislocation loop as shown in Figure 2.3. The displacement at any point due to the dislocation introduction only is given by the curve in the Figure where $y = (x_i - p_i)n_i$ is the normal distance between the point in question $x_i$ and any point on the dislocation's plane $p_i$ and $n_i$ is the normal to the slip plane. The green rectangle in the Figure represents the region in which the displacement due to the dislocation varies and it has a thickness $h$ which can be arbitrarily chosen but it is typically on the order of 1 to 2 atomic spacings. The variation is drawn to be linear but it can follow any other nonlinear form. The

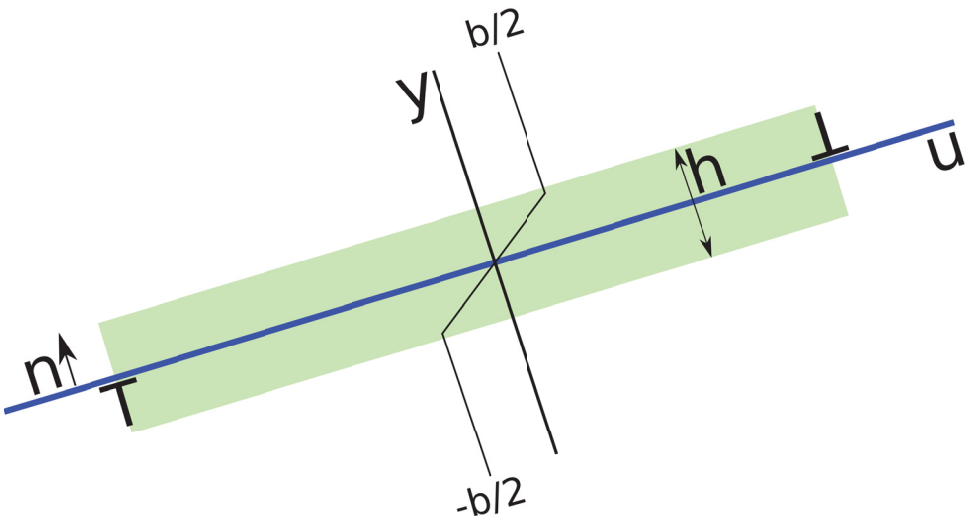


Figure 2.3: A schematic showing the displacement field variation due to a dislocation loop. The blue line is an edge-on view for the slip plane, the height of the green rectangle $h$ is equal to the dislocation core with. The displacement variation is given on the $u$ axis as a function of the distance from the dislocation cut surface on the $y$ axis. $n$ is the vector normal to the slip plane

displacement vector $u_i^p$ at any point can be written as

$$u_i^p = \begin{cases} -b_i/2 & \text{if } y < h/2 \\ yb_i/h & \text{if } |y| \leq h/2 \\ b_i/2 & \text{if } y > h/2 \end{cases} \tag{2.47}$$

where $b_i$ is the Burgers vector of the dislocation loop. Notice that the cut surface does not have to be planar and the equation applies as long as the local cut surface normal is taken instead of the slip plane normal in this case. The displacement gradient in this case becomes

$$u_{i,j}^p = \begin{cases} 0 & \text{if } |y| > h/2 \\ n_j b_i/h & \text{if } |y| \leq h/2 \end{cases} \tag{2.48}$$

from which the plastic strain can be obtained

$$\epsilon_{ij}^{p} = \frac{1}{2}(u_{i,j}^{p} + u_{j,i}^{p}) \begin{cases} 0 & \text{if } |y| > h/2 \\ (n_j b_i + n_j b_i)/2h & \text{if } |y| \leq h/2 \end{cases} \tag{2.49}$$

This is the case for a single dislocation. All the points that are outside the influence region are unstrained. As the dislocation loop moves (expands or shrinks), points move in or out of the influence region, hence, they become strained (unstrained). The average plastic strain in the sample can then be calculated from

$$\langle \epsilon_{ij}^{p} \rangle = \frac{1}{V} \int_{V} \epsilon_{ij}^{p} \mathcal{I}(x) dV = \frac{1}{V} \int_{A} (n_j b_i + n_j b_i)/2h h dA = \frac{1}{2V} \int_{A} (n_j b_i + n_j b_i) dA \tag{2.50}$$

where $V$ is the simulation volume, $\mathcal{I}(x)$ is an indicator function which is equal to 1 when the point $x$ lies inside a dislocation's influence region and zero otherwise, $A$ is the area of the dislocation loop on its slip plane.

The change in the average plastic strain in the system at a given time step is then equal to the change in the area swept by the dislocation at this time step

$$\Delta \langle \epsilon_{ij}^{p} \rangle = \frac{1}{2V} (n_j b_i + n_j b_i) \Delta \int_{A} dA = \frac{\Delta A}{2V} (n_j b_i + n_j b_i) \tag{2.51}$$

In the case of multiple dislocations acting at the same time, the change in the average plastic strain $\Delta E^{p}$ is the sum of the changes resulting from each one independently.

$$\Delta E_{ij}^{p} = \frac{1}{2V} \Sigma_k \Delta A^k (n_j^k b_i^k + n_j^k b_i^k) \tag{2.52}$$

where $k$ denotes the $k^{th}$ dislocation.

### 2.2.9 Dislocation Reactions, Mesh Coarsening and Refinement

Dislocation reactions are the events that take place when two dislocations get very close to each other so that their cores, which are finite sized, start overlapping. Depending on the dislocations nature (edge, screw or mixed), their relative orientations and slip planes, different processes can take place. Handling dislocation core reactions is important for two reasons, to capture the correct physics and to reduce the computational load. For instance, when the configuration of the dislocation network is such that two dislocations can and should annihilate, not annihilating them results in a number of problems. First, the accuracy of the interaction stress calculations between them decrease because they are stuck in a configuration where each dislocation is bordering the region in which the linear theory breaks down for the other. The stress field expression derived in Section 2.1.2 cannot be applied when they are that close incorrect forces get applied on the two dislocations. Second, annihilating the two dislocations effectively removes their nodes and segments from the system which reduces the computational load. A third, but latent, effect for not annihilating them is the reduction in the simulation time step is described in Section 2.2.7. This section describes the basic dislocation reactions and how they are handled in DDD simulations.

Before any dislocation reaction events are detected, the entire dislocation network is spatially categorized into virtual cells that decompose the space into equal regions. These cells have no computational use and they do not affect the dynamic in any way, unlike the force calculation cells described in Section 2.2.5. The reactions are then handled on a per-cell basis such that dislocation segments react with other segments in the same and surrounding cells only. This guarantees that every potential dislocation reaction gets handled properly. One restriction on dislocation reactions is that dislocations cannot undergo two different reactions in the same time step.

That is, a dislocation cannot annihilate and then collide with another dislocation. The first allowable detected reaction takes place regardless of all other potential reactions. Because the simulation system is distributed, the dislocation segments are distributed over different processors such that each segment gets handled exclusively by one processor. A sophisticated event data communication process takes place after the reactions handling so as to inform the rest of the dislocation network with the reactions that took place to maintain the accuracy of future dislocation network evolution.

The first and simplest dislocation reaction is that of dislocation annihilation. Annihilation takes place when two dislocations of the same Burgers vector but opposite line directions come close to each other within a few atomic spacings. An essential requirement for annihilation is that the two dislocations must be gliding on either the same slip plane or on two parallel slip planes. In the used DDD system, if they glide on parallel slip planes, an annihilation event takes place while if they are gliding on the same slip plane, the more general dislocation collision event, which is described below, takes place. They both lead to the same configuration but the collision event can handle more general cases. When two dislocation segments annihilate, their end points are converted from free nodes, that can move freely on the glide plane, to pinned nodes, that cannot move at all, and the segments themselves are removed. Usually, annihilation takes place over dislocation chains of more than one segment but the process remains the same. The resulting structure is that of completely removed chains with pinned points at their two ends. All the pinned points that were generated intermediately get removed once the two segments on their sides are removed. For two segments to annihilate, in addition to the previous requirements, their lengths have to be in the same range and they should be either perfectly parallel or make an angle of less than $15^o$ with each other. If they satisfy all the requirements except for the length similarity, the longer dislocation gets split into a number of

segments with the one of them matching the length of the shorter segment and then it annihilates with the shorter dislocation segment.

A more general reaction takes place when two dislocations, moving on the same plane or non-parallel planes, collide. For the case of dislocation segments moving on non-parallel planes, which is the most common case, when two of them get sufficiently close to each other within a distance of no more than $5b$ where $b$ is the Burgers vector magnitude, an out-of-plane collision event takes place. In this case, each segment is split at the point closest to the other segments at the two splitting nodes get merged at a common collision point. This results in a 4-node connected to 2 pairs of arms with each pair lying on one slip plane. The collision node location is chosen to be on the common line of intersection of the two non-parallel planes and it minimizes the sum of the squared distance between the two splitting nodes. This guarantees that the dislocation segments remain on their correct slip planes. The new node can then only move on the line of intersection of the two planes to maintain the segments planarity. In the case of dislocation segments on the same exact plane, the same conditions apply but the segments get split at their midpoints instead and the newly created node is placed at the midpoint of the line connecting the two splitting nodes. This node moves on the common slip plane and no planarity violation is possible in this case. An essential condition for both types of dislocation collisions is that the two segments have to be attracting each other for the collision to take place. This helps avoiding unnecessary locking of naturally repelling dislocations. Hence, a force and velocity calculations take place before handling any collision events to determine the interaction type. An important feature of collision events in general is that they do not add or remove any dislocation segments from the system.

A special case of the collision reaction happens when the two colliding segments share a common node. This is called the zipping reaction and depending on the Burgers vectors of the colliding segments, the zipping reaction can result in dislocation

merging or annihilation. The latter is the main mechanism by which dislocation defeat of forest dislocations is modeled. The same conditions of collision reactions apply for zipping reactions, however, splitting takes place only for the longer segment. Because the two segments are not necessarily moving on the same plane, the common collision point is the point on the line parallel to the common intersection line of the two planes and passing by the common node of the dislocation segments that minimizes the distance between the two dislocation nodes. If the lengths of the two colliding segments are nearly the same (within 10% difference), no splitting takes place and the end nodes get merged at the collision point. Right after collision, the two colliding segments are replaced by one segment whose Burgers vector is the sum of the two Burgers vector of the colliding segments. If the resultant Burgers vector is zero, that means that the collision reaction is in fact an annihilation reaction and the segment is removed completely from the system. Otherwise, it is a merging reaction and a new slip plane, needs to be assigned for the new dislocation segment. The normal vector $n$ of the new slip plane is calculated from $n = b \times t$ where $t$ is the segment's line direction and $b$ is its new Burgers vector. If the segment is a screw dislocation (such that $b \times t = 0$), a random $\{111\}$ slip plane gets assigned for FCC simulations. Besides being the basis of most energy minimization reactions in DDD simulations, the zipping reaction also prevents the dislocation's curvature to increase to unrealistic values by zipping the segments neighbouring the high curvature nodes.

A final core reaction is that of triangular loop elimination. This takes place when exactly 3 non-planar dislocation segments form a loop. The 3 nodes of this loop become highly immobile because each node would move along a straight line that cannot accommodate the motion of the other two nodes which results in an increase in the dislocations lengths, something that linearly raises the system's energy and hence, is highly unlikely to happen. The triangular loop represents a dead computational load so once they are detected, they are removed immediately.

Dislocation segment remeshing is necessary to maintain the accuracy of the dislocation network representation and evolution. A very coarse mesh can lead to skipping otherwise occurring dislocation motions such as squeezing between obstacles. A very fine mesh greatly increases the computational load. In the current simulations, remeshing is adaptive, that is, in every time step, all the segments get checked for remeshing and those who need refinement or coarsening are handled accordingly. A segment gets refined by splitting it at its midpoint if it is longer than the maximum segment length allowed in the simulation and two neighbouring segments get merged if they are too short such that the distance between their opposite ends is less than the maximum segment length. Merging segments have to lie on the same slip plane and have the same Burgers vector which means that the common node cannot be anything other than a 2-node.

All the dislocation reactions and remeshing operations are algorithmically performed using 2 operations, namely, SplitNode and MergeNode, which have been extensively described in [16].

### 2.2.10 Dynamic Load Balancing

The final step in the DDD loop is the dynamic load balancing where the problem space gets decomposed into regions, called domains, each of which is assigned to a certain processor. After decomposition, the dislocation nodes are migrated from one processor to another as necessary so that they end up in the memory of the processor handling the domain to which they belong. The decomposition can be a node count based or force calculation based. In the former, the problem space is decomposed so that each domain has nearly an equal number of nodes while in the latter, each domain has nearly an equal number of force calculation operations. The difference between the two is because some nodes, such as pinned nodes, do not need any force calculations. In either case, the domain decomposition is three dimensional and

hierarchical where the domain gets decomposed along the $X$ direction first, then each subdomain gets decomposed along the $Y$ direction and finally each sub-subdomain gets decomposed along the $Z$ direction.

Following the decomposition process, all the nodes get scanned and new domains get assigned to them. Then, an extensive communications operation takes place where all the data for the nodes is moved around the distributed system to end up in their proper locations and the nodes get renamed based on their new domains. This is followed by a connectivity check where all the connections between the nodes (through segments) are updated to reflect the new node locations and names and all necessary remote data gets communicated. Necessary remote data is the data of the nodes in a certain domain that is required by a different domain to perform the force calculations. A typical example is when a domain node is connected to an out-of-domain node.

## 2.3 Accelerating Dislocation Force Calculations

The force calculation is the most time consuming step in the DDD loop. In this section, two methods that help accelerate this step are described briefly.

### 2.3.1 The Cell Charge Method

A first order approximation for the stress field due to a number of dislocations at a point far away from them can be obtained by the cell charge method. In this method, the simulation volume is uniformly divided into a number of cells and the dislocations segments are distributed over the cells. A superdislocation is created in each cell which accounts for all the segments in this cell by forming the $3 \times 3$ cell charge tensor $C_{ij}$ such that

$$C_{ij} = \Sigma_{k=0}^{N} b_i^k t_j^k \tag{2.53}$$

where $b_i^k$ and $t_i^k$ are the $i^{th}$ components of the $k^{th}$ segment Burgers and line vectors respectively and $N$ is the number of dislocation segments in the cell. For field points far away from a certain cell, the stress field due to dislocation segments inside that cell can be approximated by the sum of the stress fields due to 9 dislocations each with a Burgers vector and line direction corresponding to 1 element in the $C_{ij}$ tensor passing by the center of the cell. This approximates the stress field when the distance between the field point and the cell center is much larger than the cell size because as the field point moves away, the spatial differences between different dislocations become insignificant.

### 2.3.2 The Fast Multipole Method

The Fast Multipole Method (FMM), introduced by Greengard et. al. [100], is a general method for summing the contribution of a number of spatially distributed sources at a number of locations, usually coinciding with the source locations. It reduces the computational cost from $O(n^2)$ to $O(n)$ by evaluating an approximation for the field in question to an arbitrary level of accuracy rather than the exact field. In DDD simulations, the stress field from the dislocations reasonably far away from a point in question is approximated using the FMM method to reduce the overall computational cost. In the DDD framework used in this dissertation, the FMM reduces the simulation runtime further by allowing the stress field due to dislocations stored on memories of different processors be accounted for locally without transferring all the dislocation segment data between processors, a process which can at times be a performance bottleneck. Instead, the FMM expansion coefficients, which form a significantly smaller data set, are moved from one memory space to another. In this

section, a description for the FMM used in these simulations will be briefly presented.

Let $x$ be the point at which the stress field from all the dislocations in the simulation is required. The direct evaluation of the stress field by summing up expressions of the form given in Equation 2.24 is an $O(N)$ operation where $N$ is the number of dislocation segments in the system. In reality, the stress field needs to be calculated on each dislocation segment, which makes the overall cost of stress (force) evaluations an $O(N^2)$ operation. The main idea behind the FMM is to derive a static expression for the stress field at $x$ due to a subset of the dislocation segments in the problem subvolume $\Omega_q$ which is well separated from $x$. By a static expression, it is meant that the expression parameters are independent of $x$, thus, they can be evaluated once and the stress field at all $x$ far away from $\Omega_q$ can be evaluated using the same expression by passing $x$ to it. This reduces the computational cost to the sum of the expression parameters determination plus $M < N$ expression evaluation operations. In order to derive the stress field approximation, two analytical results are required. Starting from Equation 2.24, one can rewrite this integral as the sum of integrals acting on the dislocation segments used to discretize the dislocation loops as discussed in Section 2.2.2.

$$\sigma_{ij}(x) = \frac{\mu}{8\pi}\Sigma_{n=1}^{N} b_m^n \left[ \int_n r_{,pp\alpha} \left( \epsilon_{\alpha mi} dl_j^n + \epsilon_{\alpha mj} dl_i^n \right) + \frac{2}{(1-\nu)} \int_n \epsilon_{\alpha mk} \left( r_{,ij\alpha} - \delta_{ij} r_{,pp\alpha} \right) dl_k^n \right] \tag{2.54}$$

where $n$ denotes the $n^{th}$ dislocation segment in the system. One can then notice that the expression boils down to the evaluation of the integral

$$I_{ijkm}(x) = \Sigma_{n=1}^{N} \int_n r_{,ijk} dl_m^n \tag{2.55}$$

Following Wang et. al. [101], $r_{,ijk}$ can be expanded in Taylor series about the point $O$ to be

$$r_{,ijk} = R^O_{,ijk} + R^O_{,ijkp} r_p + \frac{1}{2!} R^O_{,ijkpq} r_p r_q + \frac{1}{3!} R^O_{,ijkpqs} r_p r_q r_s + ... \tag{2.56}$$

where $R^O_{,ijkpqs...}$ is a higher order derivative of $r_i = x_i - O_i$. $O_i$ is the center point of a volume $\Omega_O$ containing the $N_O$ dislocations for which the stress contributions are required. By substituting in Equation 2.55, one gets

$$I_{ijkm}(x) = \Sigma_{n=1}^{N_O} \int_n \left( R^O_{,ijk} + R^O_{,ijkp} r_p + \frac{1}{2!} R^O_{,ijkpq} r_p r_q + \frac{1}{3!} R^O_{,ijkpqs} r_p r_q r_s + ... \right) dl^n_m \tag{2.57}$$

Noticing that $R^O_{,ijkpqs...}$ is a constant under the integration sign (it only depends on $x$ and $O$ but not on the dislocation segment point), the expression can be recast in the following form

$$I_{ijkm}(x) = R^O_{,ijk} \alpha_m + R^O_{,ijkp} \beta_{mp} + \frac{1}{2!} R^O_{,ijkpq} \gamma_{mpq} + \frac{1}{3!} R^O_{,ijkpqs} \eta_{mpqs} + ... \tag{2.58}$$

where

$$\begin{aligned} \alpha_m &= \Sigma_{n=1}^{N_O} t^n_m \int_n dl \\ \beta_{mp} &= \Sigma_{n=1}^{N_O} t^n_m \int_n r_p dl \\ \gamma_{mpq} &= \Sigma_{n=1}^{N_O} t^n_m \int_n r_p r_q dl \\ \eta_{mpqs} &= \Sigma_{n=1}^{N_O} t^n_m \int_n r_p r_q r_s dl \end{aligned} \tag{2.59}$$

and $t^n_m$ is the $m^{th}$ component of the tangent vector for the $n^{th}$ dislocation segment. Expression 2.58 is all what is required to evaluate the stress field at $x$ due to all the dislocations in $\Omega_O$. In order to exploit the full power of the FMM however, another expression is required. That is, the expansion coefficients $(\alpha^P_m, \beta^P_{mp}, \gamma^P_{mpq}, \eta^P_{mpqs}, ...)$ at

point $P$ from those at point $O$ $(\alpha_m^O, \beta_{mp}^O, \gamma_{mpq}^O, \eta_{mpqs}^O, ...)$. Consider the vector $d_i = O_i - P_i$, the coefficients at $P$ are

$$\begin{aligned}
\alpha_m^P &= \Sigma_{n=1}^{N_O} t_m^n \int_n dl = \alpha_m^O \\
\beta_{mp}^P &= \Sigma_{n=1}^{N_O} t_m^n \int_n r_p^P dl = \Sigma_{n=1}^{N_O} t_m^n \int_n (d_p + r_p) dl = d_p \alpha_m^O + \beta_{mp}^O \\
\gamma_{mpq}^P &= \Sigma_{n=1}^{N_O} t_m^n \int_n (d_p + r_p)(d_q + r_q) dl = d_p d_q \alpha_m^O + d_p \beta_{mq}^O + d_q \beta_{mp}^O + \gamma_{mpq}^O \\
\eta_{mpqs} &= d_p d_q q_s \alpha_m^O + d_p d_q \beta_{ms}^O + d_q d_s \beta_{mp}^O + d_p d_s \beta_{mq}^O + d_p \gamma_{mqs}^O + d_q \gamma_{mps}^O + d_s \gamma_{mpq}^O + \eta_{mpqs}^O
\end{aligned} \tag{2.60}$$

Expressions 2.59 and 2.59 converge only when the evaluation (field) point is far away from the source dislocation. A careful subdivision of space is required to guarantee that these expressions will be used only if they will converge. $L$ subdivision levels are required for the FMM algorithm. In each level $l = 0...L-1$, the problem space is subdivided into $8^l$ FMM cells as follows. In the first level $l = 0$, the problem space is not divided at all and only one cell is present. For $l = 1$, the unique cell at $l = 0$ is uniformly divided into 8 subcells by bisecting the parent cell along the $X$, $Y$ and $Z$ directions. For each subsequent level $l = 2...L-1$, each cell in level $l-1$ is uniformly divided into 8 cells int the same way. This results in a tree structure where each cell at level $l$ has exactly 8 children cells at level $l+1$. The two-dimensional version of the subdivision is given in Figure 2.4. The cells form relationships between each other according to the following definitions. For cell $i$, a **neighbour** cell is a cell $j$ that is on the same level as $i$ and shares at least one point with it. This means that $i$ is neighbour to itself. A **well separated** cell is a cell $j$ that is on the same level as $i$ but they are not neighbours. An **interacting** cell is a well separated cell $j$ that is a child of $i^{th}$ parent neighbours. The three cell relationship types are shown in Figure 2.4. Notice that all the neighbourhood, separation and interaction relations are symmetric, that is, if $i$ interacts with $j$ then $j$ interacts with $i$. In three-dimensions,

each cell has at most 27 neighbours and 189 interacting cells. If cells $i$ and $j$ interact, then the expression 2.59 due to all the dislocations in the volume of cell $j$ converges for all points inside cell $i$ and vice versa. The sets of interaction cells of a cell and its parent are disjoint.

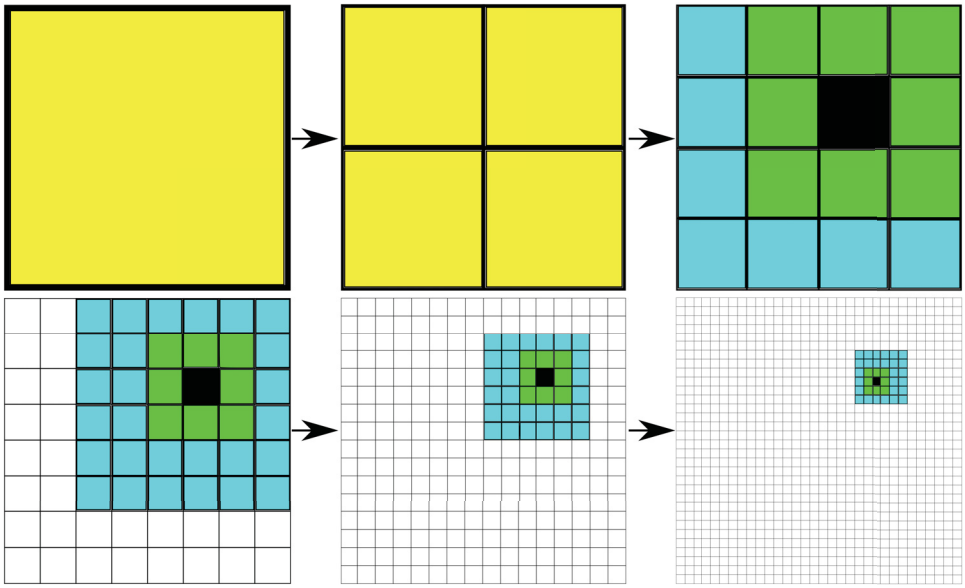

Figure 2.4: The recursive division of the problem space into FMM cells of different sizes. The first 6 levels (0 through 5) are shown here. The well neighbours of the black cell in each level are shown in green, the interacting cells in blue and the well separated cells in white. Notice that the cells of the first two levels have no well separated or interacting cells.

The FMM method proceeds in the four steps, initialization, upward pass, localization and downward pass. In the initialization step, the space is divided in the manner described above and the dislocations are assigned to the cells of the finest level $l = L - 1$. For each cell in level $L - 1$, the multipole expansion coefficients are calculated for the dislocations inside the volume of that cell according to the expression 2.59. For the upward pass, the multipole expansion at the parent cells at level $L - 2$ is obtained from the expansions at the $L - 1$ cells by summing up the translation expression 2.60 from all the children cells. This process is recursively repeated all the way up to level 2. At this point, the multipole expansion at each cell in each

level has been obtained and stored. In the localization step, expression 2.60 is used to translate the multipole expansion of cell $i$ to all cells $j$ that interact with $i$ for all cells $i$ in level $l$ for all levels $l = 2...L-1$. When a multipole expansion is translated from an interacting cell to this cell, its coefficients are added to the coefficients from all the other interacting cells. This process is local to the subdivision level and no parent-child translations take place. At the end of this stage, each cell will have 1 local multipole expansion that can be used to evaluate the stress at any point inside that cell due to the sources in the cell's interaction list. In the final downward pass step, starting from the coarsest level $l = 2$, the obtained local multipole expansions in the localization step are translated to the center of each child cell and passed to it. The child cell adds the expansion coefficients to the coefficients of its local expansion. This way, the local expansion in the child cell accounts for all the sources in the child's interaction list as well as its parent. This process proceeds recursively down the tree hierarchy until the finest level is reached. When done, the finest level cells will have a local multipole expansion that accounts for the dislocations everywhere in the system except for its neighbour cells. A cell's local multipole expansion converges for all $x$ in it.

Finally, when the stress field at point $x$ is desired, the finest level cell $i$ containing $x$ is determined and the local multipole expansion at $i$ is evaluated at $x$. Then, the resulting stress field is added to the stress field calculated from the dislocation segments in the neighbours of $i$. The last operation is still $O(N^2)$ but with $N$ significantly lower than the number of the dislocation segments in the system. The FMM method was successfully implemented in DDD simulation systems and its accuracy and performance have been reported in [101] and [16].

# Chapter 3

# The Effect of Cross-Slip on the Deformation Response of FCC Microcrystals

Cross-slip is a thermally activated deformation mechanism by which screw dislocations can conservatively change their glide plane from one plane to another that contains their Burgers vector [40]. Cross-slip is thought to influence the multiplication of dislocations [102, 103], work-hardening [43–47], the onset of stage III in the work hardening of single crystal FCC materials [104–106], and the formation of dislocation patterns [42]. Moreover, dislocations can avoid unshearable obstacles, such as precipitates, by cross-slip [107, 108]. Unlike dislocation interactions with solute atoms or stacking fault tetrahedra where the interactions are localized in space, cross-slip is an extended mechanism which affects the glide of longer segments of dislocations [41]. Thus, it has a significant effect on how the dislocation microstructure evolves. As Puschl [109] puts it, "It [cross-Slip] is the most important single process underlying complex spatio-temporal developments in microstructure leading to hardening, pattern formation, and dynamic recovery". An understanding of how cross-slip takes

place and how it affects the mechanical behavior of metals is an essential step in demystifying the complexity of material defects interactions. This chapter presents some of the efforts undertaken to computationally model the phenomena of cross-slip in FCC metals along with some relevant findings and physical insights.

In FCC, dislocations glide on on the {111} planes and have Burgers vectors of the $\frac{1}{2}\langle 110\rangle$ type. Any screw dislocation can be contained in exactly 2 crystallographic slip planes. In BCC metals however, the dislocations have Burgers vectors of the type $\frac{1}{2}\langle 111\rangle$ direction but they do not have very well defined slip planes [110, 111]. There are 12 slip planes, three {110}, three {112} and six {123}, that contain the Burgers direction and screw dislocations can belong to any of them. Thus, screw dislocations can switch from one slip plane to the other frequently, which results in wavy slip as reported experimentally [112]. In this chapter, only FCC cross-slip will be considered because the theories and experiments describing the involved mechanisms are more mature and amenable to numerical implementation [109, 113, 114].

## 3.1 Preliminaries: Cross-Slip in FCC Metals

In close-packed crystal structures, the tangent vector for a dislocation and its Burgers vector of a dislocation define a slip plane, whose normal is the cross-product, on which the dislocation glides conservatively. Screw dislocations, by definition, have their Burgers vectors in the same direction of their tangents, which means that a unique slip plane cannot be determined and the dislocation can theoretically glide on any plane. In real crystal structures, it is energetically more favorable for dislocations to glide on close-packed planes, which limits the number of planes on which screw dislocations can glide to a small and finite set of planes. Cross-slipping from one of these slip planes to another is relatively easy and takes place under various combinations of stresses and temperatures [109].

An important feature of the discreteness of crystal lattices is that the system attains an overall lower strain energy when dislocations dissociate into Shockley partials with a stacking fault in between which results in a more complex dislocation core structure [40]. The partials spacing is inversely proportional to the stacking fault energy. A typical in dislocation dissociation reaction in FCC metals is given by

$$\frac{1}{2}[\bar{1}10](111) \rightarrow \frac{1}{6}[\bar{2}11](111) + \frac{1}{6}[\bar{1}2\bar{1}](111) \tag{3.1}$$

For a dislocation to cross-slip, the stacking fault ribbon has to be compressed along the length of the cross-slipping part of the dislocation to form a perfect dislocation, momentarily, and then to expand again but on the cross-slip plane. This mechanism can be broken down to four main steps. First, a constriction forms on the stacking fault ribbon which brings the two Shockley partials together at a point. Second, the two partials start zipping, starting from the constriction point, in one or two directions. Third, The, now perfect, dislocation dissociates on the cross-slip plane. Finally, the dislocation bows out on the cross-slip plane. These steps are schematically given in Figure 3.1.

Following Puschl [109], a simple calculation for the energy required for cross-slip is given in Equation 3.2. Neglecting the energy associated with the dislocation's dissociation on the cross-slip plane, the overall energy $\Delta G$ required for a cross-slip even to take place can be written as

$$\Delta G = E_c + \Delta E L + T\Delta s - \tau b \Delta A \tag{3.2}$$

where $E_c$ is the energy required to form the initial constriction, $\Delta E$ is the energy per unit length required to zip the two partials, $L$ is the zipped length, $T$ is the line tension that resists the increase in the dislocation's length, $\Delta s$ is the increase in the dislocation's length on the cross-slip plane due to bowing, $\tau$ is the local resolved shear

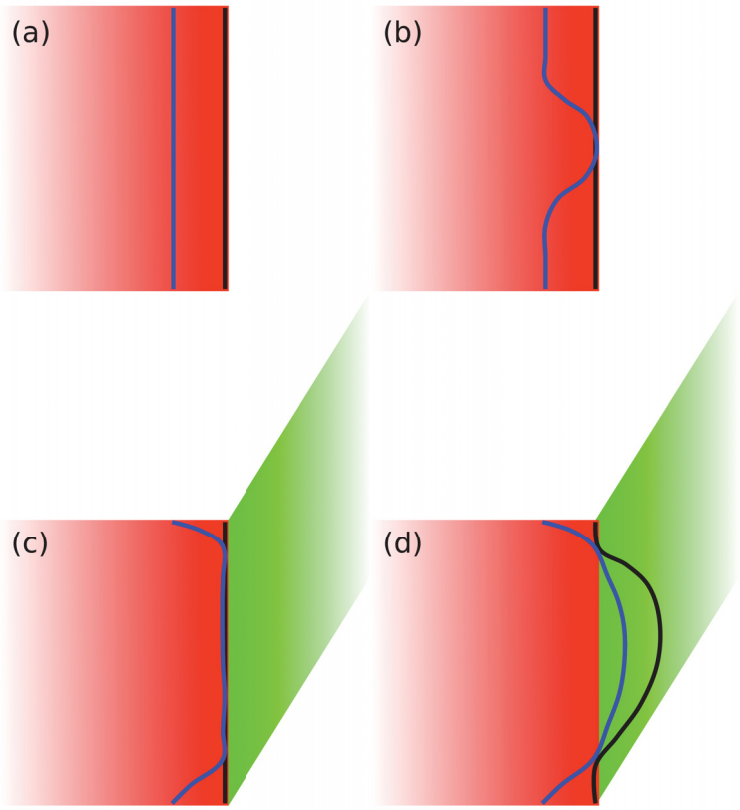


Figure 3.1: The steps leading to a cross-slip event. The red plane is the glide plane and the green plane is the cross-slip plane. The two partials (black and blue) start in configuration (a) parallel to each other and bounding a stacking fault in between. In configuration (b), the two partials form a constriction. In (c), they zip together and finally, in (d), they dissociate and bow out on the cross-slip plane.

stress on the glide plane, $b$ is the magnitude of the dislocation's Burgers vector and $\Delta A$ is the stacking fault ribbon area. The first two terms can be together termed the recombination energy, the fourth term is negative because the stress assists in the recombination process.

In an analogy with chemical reactions, the cross-slip reaction will absorb, or release, an amount of energy $\Delta G$, which is the Gibbs free energy. This analogy becomes exact for the cases when the crystal is kept at a constant temperature and pressure (a constant applied stress), such as in creep loading conditions. The transition state theory [115] can then be used to predict the rate of cross-slip events $f$ according to

the exponential expression given in Equation 3.3.

$$f = f_o \exp\left(-\frac{\Delta G}{k_B T}\right) \tag{3.3}$$

where $f_o$ is a pre-exponential factor to be determined from the specifics of the cross-slip model, $k_B$ is Boltzmann constant and $T$ is the temperature of the system. Because the local stresses on the glide and cross-slip planes play an important role in the process, it is usually preferred to explicitly model their effect in the cross-slip rate Equation so that it becomes

$$f = f_o \exp\left(-\frac{E_a - \tau V}{k_B T}\right) \tag{3.4}$$

where $E_a$ is the energy required for cross-slip to take place at zero local stresses, and it is called the activation energy, $\tau$ is a resolved shear stress component where the resolution plane depends on the cross-slip model used, and $V$ is the rate of change of the cross-slip energy with stress (also known as the activation volume since it has the dimensions of volume). A final point to make from this analysis is that cross-slip is easier for materials with higher stacking fault energies such as nickel [116] because less energy is required for the recombination of their partials.

## 3.2 The Friedel-Escaig Cross-Slip Model

A number of theoretical models for cross-slip can be found in the literature. The first theoretical work on cross-slip was undertaken by Schoeck and Seeger [117] and Wolf [118], where they assumed that the screw dislocation partials recombine over an extended portion on the glide plane before bowing out, without dissociation, on the cross-slip plane. The activation energy obtained from their calculations is too high which explains why this model did not become popular for FCC metals [114]. A model

by Friedel [119] came out next where the constriction and recombination took place over a shorter length of the dislocation on the glide plane and then the dislocation was allowed to dissociate on the cross-slip plane. The activation energy was found to be significantly lower such that purely thermally activated cross-slip can take place without any stress assistance. On the other hand, Fleischer [120] hypothesized that cross-slip can take place without the formation of any constrictions or recombination. In this model, the stacking fault ribbon folds over from the glide to the cross-slip plane and forms a leading Shockley partial on the cross-slip plane, stair-rod dislocation at the intersection of the glide and cross-slip planes and a trailing Shockley partial on the glide plane. This process requires a higher activation energy because there is no energy recovery associated with the recombination compared to the case where recombination occurs, however, atomistic simulations confirmed that this mechanism takes place at high stresses and low temperatures [121, 122]. Washburn [123] was the first to suggest that cross-slip can happen due to interactions with forest dislocations threading the glide plane. Similar to the Friedel model, the Friedel-Escaig model [107] uses the line tension model to estimate the activation energy of cross-slip events. The model has been experimentally confirmed for higher temperature and low stress loading conditions [48, 49]. The implementation of the various cross-slip mechanisms to be described in this chapter are all based on the Friedel-Escaig model.

The Friedel-Escaig model follows the basic cross-slip event sequence described in Section 3.1. Escaig [107] developed a mathematical theory to estimate the recombination energy based on the constriction energy formation calculations by Stroh [124]. An essential feature for the model is that dislocation cross-slip is stress assisted. The resolved shear stress on the glide plane can be decomposed into two components, one in the direction of the dislocation line (and hence, the Burgers vector), termed the Schmidt stress, and the other in a direction normal to it, termed the Escaig stress. The same decomposition applies for the resolved shear stress on the cross-slip plane.

The two partials of a screw dislocations have opposite edge components, hence, the Escaig stress, which is the resolved shear stress for the edge components of the two partials, works on bringing the partials together, thus, reducing the overall energy required for the cross-slip event activation, or separate them further, thus, increasing the cross-slip event activation energy. The Escaig stress has the same effect on the screw components of the partials (moving them in the same direction). On the cross-slip plane, the Escaig stress plays the same role. The difference between the Escaig stress on the glide plane and that on the cross-slip plane is taken in this work to be the stress assisting cross-slip. When this difference is positive, the energy required for cross-slip drops, because the partials are now closer to each other and when the difference is negative, the energy required increases because cross-slipping from the cross-slip plane to the glide plane (the reverse process) is now easier. Equation 3.4 can now be written as

$$f = f_o \exp\left(-\frac{E_a - \Delta\tau_E V}{k_B T}\right) \tag{3.5}$$

where $\Delta\tau_E = \tau_E^G - \tau_E^{CS}$ is the Escaig stress difference. It is to be noted that the Escaig model only gives an estimate for the energy required for cross-slip but it does not describe the conditions that trigger cross-slip events. From a thermodynamic point of view, cross-slip can take place spontaneously and it is more likely at higher temperatures. However, the cross-slip rate calculated from Equation 3.5 is too low in the absence of stress for cross-slip to be of any significance. Usually, a high stress field local to the dislocation due to a forest dislocation, a precipitate or any other source can help initiate the cross-slip sequence, hence, increasing the cross-slip rate. The dislocation would only cross-slip if the cross-slip plane has a higher resolved shear stress. This is an important distinction to make, a positive Escaig stress difference, meaning that the glide plane has a higher Escaig stress than the cross-slip plane, helps with cross-slip because it lowers the chances of the reverse cross-slip process

from taking place. However, it is energetically more favorable for the dislocation to glide on the higher shear stress plane. This fact forms the basis of the experimental technique by which the Escaig mechanism was confirmed [48] and it has to be properly implemented in all DDD codes incorporating cross-slip.

## 3.3 Characterization of Cross-Slip Mechanisms

Experiments and Molecular Dynamics (MD) simulations can be used to determine the conditions that trigger a cross-slip event, the exact path taken by a dislocation during cross-slip and the cross-slip process parameters such as the activation energy and volume. MD simulations allow the exploration of the various deformation mechanisms and the relevant parameters. Although experiments are generally limited in terms of what can be measured or observed, some experimental studies have been successful in estimating the cross-slip activation parameters. Bonneville and Escaig [48, 49] designed an experimental technique by which a number of cross-slip events can be induced at the yield point so that the deformation of the crystal gets dominated by the cross-slip effects and the activation volume and energies were estimated. Couteau et. al [50] repeated the same experiment and obtained significantly lower activation volumes and energies suggesting some inaccuracies in the experimental technique mainly related to controlling the active deformation mechanism. For this and similar reasons, the majority of cross-slip studies have been computational in nature. Compared to theoretical models, computational studies help avoid the simplified assumptions employed by theoretical models such as the zero width constriction and the infinitely long, parallel and straight dislocation partials [124]. A summary of previous studies, especially utilizing MD simulations, is presented in the following paragraphs to shed light on the cross-slip mechanisms and their characteristics.

MD simulations of the screw dislocation core structure and the activation energy

for cross-slip in pure copper showed that the equilibrium stacking fault width at zero stress is about $d_o = 1.5 \pm 0.2$ nm and the core width of the two partials is about 0.9 nm [51, 52]. An important finding in these simulations is that cross-slip takes place according to the Friedel-Escaig mechanism, however, after the initial constriction is formed and the dislocation dissociates on the cross-slip plane, two twisted constrictions (shown as points $A$ and $B$ in Figure 3.2) are formed at both ends of the cross-slipped segment of the dislocation, which move in opposite directions leading to an increase in the length of the cross-slipped dislocation segment, as shown in Figure 3.2. The constriction at $A$ has an "edge-like" character while that at $B$ has a "screw-like" character. The actual constriction points are always pure screw dislocations but the distribution of the dislocation partials' Burgers vectors around them gives rise to the difference in their characters. The energy of a constriction is defined to be the difference between the energy of the system with the constricted partials and the energy of that with straight partials. It was found that the edge-like constriction has a positive energy while the screw-like constriction has a negative energy, which does not necessarily mean that the system spontaneously forms screw-like constrictions, however, it is energetically more favorable compared to the edge-like one because there is an energy barrier that needs to be overcome before forming screw-like constrictions. Another important finding in the same study is that the partials of a screw dislocation terminating on a free surface will tend to recombine with a low or no energy barrier if their Burgers vectors were pointing away from each other, and they would subsequently dissociate forming a screw-like constriction on the cross-slip plane. For a screw dislocation intersecting two free surfaces on both of its ends, the dislocation partials recombine on one surface and split further apart on the other, depending on the orientation of the surface with respect to their Burgers vectors. These findings show that cross-slip of surface dislocations (termed hereafter surface cross-slip) could be easier than that of in-crystal dislocations (termed hereafter bulk

cross-slip).

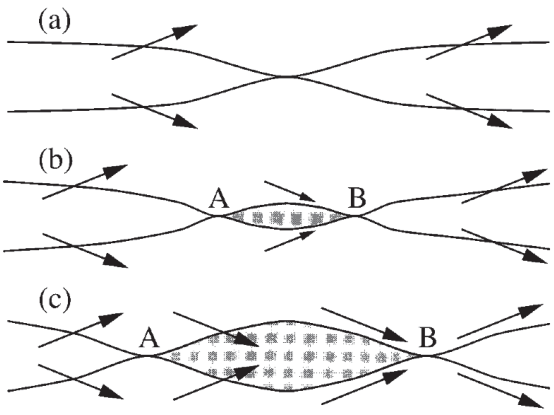


Figure 3.2: The dissociation of the constriction on the cross-slip plane according to the Friedel-Escaig model (a) The formation of the initial constriction on the glide plane, (b) The dissociation of the constriction on the cross-slip plane, two twisted constrictions $A$ and $B$ are formed at the ends of the dissociated length, (c) the separation of the two constrictions. The arrows represent the Burgers vectors of the dislocation partials. From the distribution of the Burgers vectors around the two constrictions $A$ and $B$, it is apparent that they are of different types. Schematic is taken from Rasmussen et. al. (http://dx.doi.org/10.1103/PhysRevLett.79.3676) with permission from APS.

Vegge et. al. [125] conducted some MD simulations of bulk cross-slip to determine the effect of the presence of jogs and kinks on the cross-slip activation energy. They reported an activation energy of $E_a = 3.4$ eV for jog free dislocations and $E_a = 0.8 \approx 1.0$ eV for dislocations with jogs or kinks. They concluded that jogs act as pre-existing constrictions at which the partials can dissociate and unzip in the cross-slip plane, hence, reducing the energy required for the constriction formation.

Building on the work of Rasmussen [52], Rao et. al. [30] further explored the phenomenon of surface cross-slip through MD simulations. For surface-surface dislocations making a right angle with a (111) surface, dislocations were found to reside either fully on the glide plane or partially on the glide plane and partially on the cross-slip plane with a screw-like constriction in between. If the surface is a cube (001) plane, dislocations were found to reside either fully on the glide plane, fully

on the cross-slip plane or partially on both with the same type of constriction. For dislocations that are inclined to (001) surfaces, dislocations were only found on the glide plane or partially cross-slipped and the entire dislocation rotates to minimize the total energy of the system. The dislocation line direction controls whether the dislocation will reside on the glide plane or if it will partially cross-slip. These results confirm that cross-slip can easily nucleate on the surface. An estimate for the activation energy for surface cross-slip was calculated to be around $E_a = 0.05$ eV for nickel and $E_a = 0.09$ eV for copper.

In a different work, Rao et. al. [26] investigated the possibility of cross-slip nucleation at the sites of the intersection of a screw dislocation with a forest dislocation, termed intersection cross-slip. Depending on the Burgers vectors of the intersecting dislocations, different core structures were observed in the simulations. Dislocations can either fully reside on the glide plane, the cross-slip plane or in a partially cross-slipped state. In some cases, the partially cross-slipped state has a lower energy compared to the other configurations. The activation energies for intersection cross-slip were calculated from MD simulations and they were found to be between $E_a = 0.65$ eV and $E_a = 1.13$ eV for copper [27]. In a different MD study [29], athermal cross-slip scenarios where the dislocations cross-slip without the need of any activation energy were characterized. This takes place when the intersecting dislocation repels the screw dislocation, hence, its name, repulsive intersection cross-slip. The name attractive intersection cross-slip is reserved for the thermally activated intersection cross-slip cases with nonzero activation energies. Unlike bulk and surface cross-slip, intersection cross-slip can explain a great deal of the flow phenomena in FCC metals because its rate scales up with the dislocation density [26].

From the previous discussion, it is apparent how the theoretical models based on elasticity are limited in their detail level and accuracy. The fact that different configurations result in different core structures and activation energies can be very

challenging to capture using analytical models. The same applies for experiments where the core structure is difficult to observe let alone an isolated cross-slip event. It was shown that there are numerous pathways for cross-slip in FCC metals, such as surface and intersection cross-slip, that have lower activation energies compared to the more understood bulk cross-slip. This means that they are likely to dominate the cross-slip activity in any loading scenario. Most previous DDD implementations of cross-slip incorporated bulk cross-slip only [11, 13, 53–55]. For this work, the three discussed types of cross-slip were implemented in a DDD framework according to the observations and parameters obtained from MD simulations.

## 3.4 Computational Method

The incorporation of cross-slip mechanisms in DDD simulation codes requires a number of carefully designed extensions to the existing framework. The open source dislocation dynamics simulation code, ParaDis [16], was the starting point upon which all the modifications and extensions were built. Since cross-slip involves the change of the slip plane of gliding dislocations, a fundamental requirement for any DDD code is the definition of a slip plane for each dislocation segment to begin with. ParaDis was modified in house to guarantee that all of the dislocation segments lie and move on their correct slip planes at all times for FCC simulations. Also the movement of dislocations terminating on the surface of the crystal was implemented so that surface dislocation nodes are guaranteed to move on the surface and the slip plane at the same time for arbitrarily complex surface geometries. A third situation where dislocation nodes can go off-plane is the collision of non-coplanar dislocations where the dynamically created dislocation nodes can be slightly off-plane. Any deviation from planarity means that all the intersection cross-slip calculations will be flawed in some way.

As it will be shown next, the cross-slip calculations are computationally expensive. Since cross-slip events will be checked for in every DDD simulation time step, an efficient algorithm is required to guarantee that the minimum number of cross-slip checks will be performed every time step, and at the same time, that no potential cross-slip event goes undetected. In order to make the discussion easier to follow, the following terminology will be used. A p-node is a dislocation node that is connected to $p$ segments. A dislocation segment is a straight line connecting exactly two dislocation nodes. A dislocation chain is a connected sequence of dislocation segments that is topologically equivalent to $\mathbb{R}$, the one dimensional Euclidean space, that is, with the exception of the end nodes of the chain, all the other nodes are 2-nodes. The end nodes can be connected to any number of segments. A dislocation chain can be entirely or partially screw in character. The entire dislocation microstructure can be cast in the form of an undirected graph structure [91] where the graph nodes are the dislocation nodes and the graph edges are the dislocation segments. A dislocation chain is a path on the graph between two nodes that has the property that every node along the path is visible to any node not on the path only through the path end nodes. Two types of nodes can be identified in this graph structure, physical nodes, which are p-nodes where $p \neq 2$, and computational nodes, which are 2-nodes. Physical nodes define the topology of the dislocation microstructure and computational nodes refine the shape of the dislocation chains.

The main task of this algorithm is to detect all the screw character dislocation chains in the simulation and discard any other non-screw chains. In order to be computationally efficient, the longest screw type chain should be detected rather than dealing with small connected screw chains. Moreover, the probability of cross-slipping increase linearly with the dislocation length, hence, handling smaller screw chains could result in reducing the probability of cross-slip. The starting point of the algorithm is to break down the dislocation graph structure into a number of

dislocation chains. A sophisticated procedure that uses graph algorithms operating on two levels is described in details in Appendix B. Next the generated chains are split based on their slip planes and node types. Any abrupt change in the slip plane of the chain indicates that this chain lies on two or more slip planes. This can be due to the topology of the initial microstructure or a past cross-slip event. Cross-slip rules for chains depend on their slip planes so the chain needs to be broken down into a number of subchains such that each chain lies entirely on one slip plane. A similar chain refinement takes place based on the node type such that pinned dislocation nodes can only exist and the ends of the chain. The reason for that latter condition is because the cross-slip process moves the dislocation nodes slightly before cross-slip in order to maintain their slip planes and a pinned dislocation node is not allowed to move.

The refined list of dislocation chains gets distributed next over two sublists, one is for screw type chains and the other is for everything else. It is important to keep a list of non-screw chains because they will be used later to provide information necessary for intersection cross-slip event prediction. Because it is practically unrealistic to expect to find a dislocation chain that is perfectly aligned in the screw direction, a more relaxed procedure is used to decide whether a chain is a screw chain. The procedure runs over the chain segments and it keeps two states, one of them is whether the chain was initially screw, meaning, the first segment is in the screw direction, and the second is whether the chain is currently screw, meaning that the line connecting the current chain node to the initial chain node is in the screw direction. To determine whether this connecting line is in the screw direction, the line is tested to see if it lies within the virtual cone whose apex angle is 15 degrees, and whose vertex is the initial chain node. The choice of 15 degrees allows the segments which are not perfectly in the screw direction to be considered for cross-slip. For each node on the chain, the procedure checks to see if the chain is currently in the screw direction. Four cases can

result from this check at each node. First, if the chain is both initially and currently screw, the procedure moves on to the next node in the chain. Second, if the chain is initially not a screw and currently became a screw the chain gets split into two chains at this node. Third, if the chain was initially in the screw direction but broke out of this orientation at this node, the procedure looks ahead for up to 3 nodes, if the deviation from the screw orientation continues, the chain gets split, otherwise, the chain is considered to be a screw chain even though portions of it (of length of less than 3 nodes) are not in the screw direction. Practically, there cannot be many of these non-screw portions within the same chain because this will gradually cause the chain to deviate from the screw orientation and get split. Fourth, if the chain was not in the screw direction initially and continues to be out of the screw direction at this node, the procedure moves on to the next node and keeps looping until it reaches the second case described earlier or the end of the chain.

As a result of the observation of constriction formation from MD simulations in the intersection and surface cross-slip scenarios as presented in Section 3.3, a final chain refinement step is required. Any screw chain spanning the crystal from one surface to another (a surface to surface chain) forms a constriction somewhere along its length and it partially cross-slips. Hence, the entire chain cannot cross-slip in the same time step. A surface to surface chain gets split into two surface chains and a condition is implemented such that at most one of them cross-slips in a given time step. Currently, a simplifying assumption is made such that the chain gets split right at its midpoint. The same refinement applies to chains that connect two p-nodes where $p > 2$ so as to prevent a chain intersecting two forest dislocations from cross-slipping entirely in one time step for the same reason.

Now with all the screw chains identified, the type of the potential cross-slip event can be assigned for each chain according to the following rules. First, no two cross-slip types can take place for the same chain in the same time step. Surface cross-slip,

since it has the lowest activation energy, has the highest priority. Thus, a chain terminating on the surface from one end and intersecting a forest dislocation from the other end will be treated as a candidate for surface cross-slip only. If the chain is entirely contained within the crystal and it intersects a dislocation which is not on its glide or cross-slip plane, the chain becomes a candidate for intersection cross-slip. If none of the two conditions is satisfied then the chain is considered to be a candidate for bulk cross-slip. The case where jogs and kinks form to facilitate bulk cross-slip is not explicitly handled in this implementation. However, it can be modeled by modifying the pre-exponential factors and/or the activation energy in the cross-slip rate Equation 3.5.

Intersection cross-slip has several different configurations that depend on the Burgers vectors of the intersecting dislocations and they are all tabulated in [26]. To determine which intersection cross-slip event can happen, the Burgers vectors of the screw dislocation chain and the intersecting dislocation chain are summed. If the sum is a vector of the $\langle 112 \rangle$ type, a repulsive intersection cross-slip can take place. If the sum is of the $\langle 100 \rangle$ type, the intersection forms a Hirth-lock and the required activation energy will be that of Hirth-lock intersection cross-slip. If the sum is of the $\langle 110 \rangle$ type and the intersecting dislocations lie on either the $\{110\}$ or $\{100\}$ planes, then the possible cross-slip type is that of the attractive intersection Lomer-Cottrel (LC) type. If the sum is of the $\langle 110 \rangle$ type and both dislocations lie on $\{111\}$ type planes, the cross-slip is a attractive intersection glide-lock cross-slip. The previous rules are all encoded in a flowchart given in Figure 3.3.

The detection of the appropriate cross-slip types helps identifying the correct cross-slip activation parameters for the event prediction. However, there are two more checks that need to be made before a cross-slip event is triggered. First, as noted in Section 3.2, dislocations cross-slip only if the resolved shear stress on the cross-slip plane is higher than that on the glide plane. This condition should be

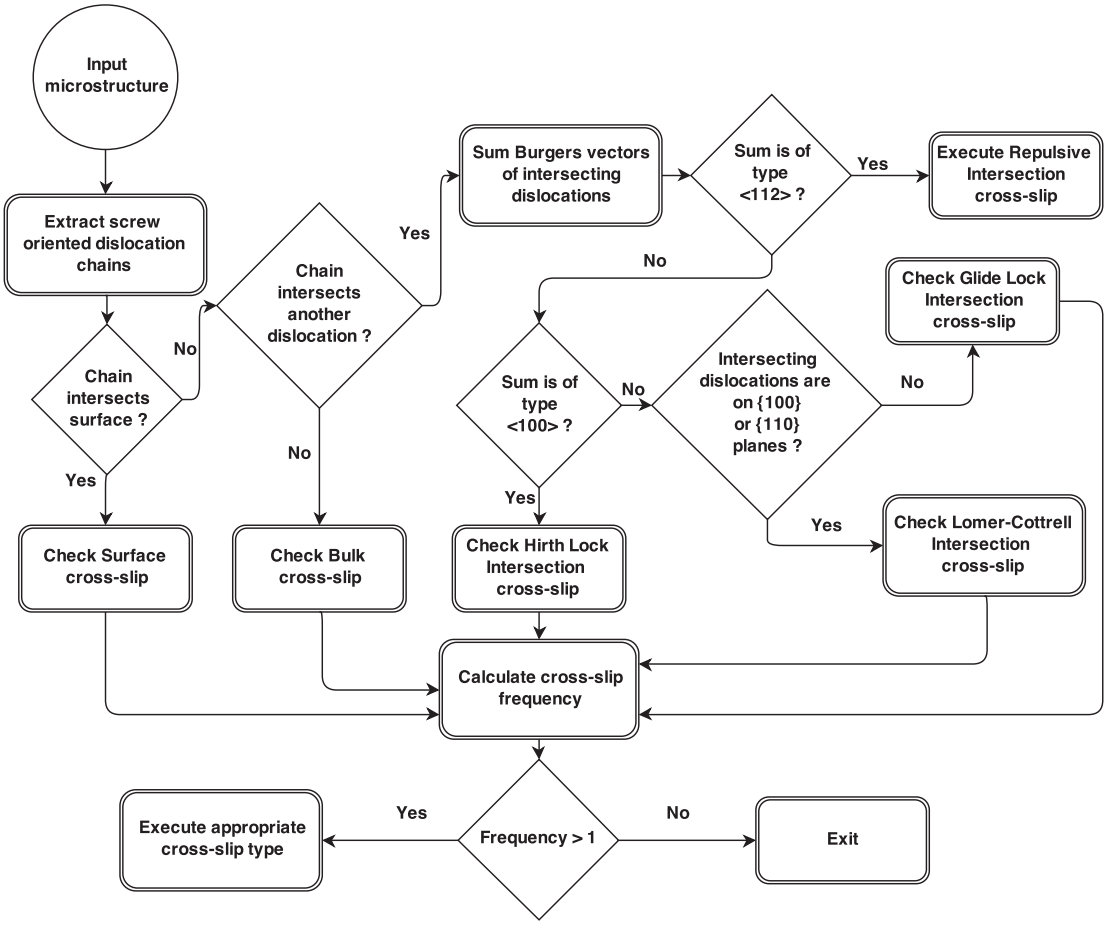


Figure 3.3: Flowchart of the proposed rules for cross-slip mechanisms as incorporated into the DDD framework

satisfied regardless of the potential cross-slip event type. Second, the resolved shear stress on the cross-slip plane should be at least at least $\frac{\mu b}{10L}$ where $\mu$ is the material shear modulus, $b$ is the dislocation's Burgers vector magnitude, and $L$ is the length of the screw chain. This ensures that the dislocation will glide away from the cross-slip event location after cross-slip. This prevents any repeated cross-slip events from one plane to the other at the same location multiple times, which is not physical and increases the computational load.

With the exception of repulsive intersection cross-slip, a final check needs to be made in order to guarantee that the cross-slip rate is physical and consistent with

the theory, experiments and MD simulations. The candidate chain cannot undergo cross-slip unless the frequency of cross-slip multiplied by the time interval of the DDD time step is greater than 1. The cross-slip rate given in Equation 3.4 can be rewritten as [11]

$$f = \omega_a \frac{L}{L_o} exp\left(-\frac{(E_a - V\Delta\tau_E)}{k_B T}\right) \tag{3.6}$$

where $\omega_a = \eta\omega_D$ is the attempt frequency, that is, the number of times a dislocation of length $L_o$ would attempt to form a constriction somewhere along its length second and $\omega_D$ is the material's Debye frequency. The scaling factor $\eta$ is the ratio of the applied strain in the simulations to that of the experiment, and it is used to match the number of constriction formation attempts in both simulations and experiments over the same time interval. The Debye frequency is estimated from experiments performed at low strain rate or quasistatic loading conditions (such as creep loading). The reference length $L_o$ is the dislocation chain length at which bulk cross-slip events occur with a frequency of 1 event per second at room temperature given identical Escaig stresses on the glide and cross-slip planes ($\Delta\tau_E = 0$) and an attempt frequency equal to the Debye frequency (a low strain rate simulation). The number of constrictions formed scales linearly with the length of the dislocation because constriction formation events are considered to be independent, thus, the expression is scaled by the ratio $\frac{L}{L_o}$ where $L$ is the actual constriction forming length of the dislocation chain.

The Escaig stress on a plane (either the glide or the cross-slip plane) can be obtained by constructing a local 3D coordinate system whose Z-axis is the slip plane normal vector and X-axis is the Burgers vector direction. The origin of the coordinate system is irrelevant. A 3D transformation for the stress tensor from the global coordinate system to the local coordinate system gives the Escaig stress as the $\tau_{yz}$ component of the stress tensor. In this local view, the $\tau_{yz}$ stress acts on the edge components of the partial dislocation and brings them together for a positive $\tau_{yz}$ stress,

or a pushes them apart for a negative $\tau_{yz}$ stress. This is what is defined to be the Escaig stress and hence, this choice of a stress resolution is justified. A final note on Equation 3.6 is that the cross-slip activation energy is the term $E_a - V_a \Delta\tau_E$ while the constriction formation energy is $E_a$. Cross-slip takes place if the frequency calculated from Equation 3.6 is greater than unity. Otherwise, a random number in the interval $[0, 1]$ is uniformly generated and cross-slip only occurs if this number is less than the calculated frequency. This guarantees that cross-slip will take place at the same rate dictated by the thermal activation condition.

For bulk cross-slip, the constriction forming length of the dislocation is taken to be the actual length of the dislocation chain. On the other hand, for intersection and surface cross-slip, the constriction forms near the intersection point or the surface. In the simulations presented here, the intersection and surface cross-slip lengths are taken to be 2.5 and 1.25 nm respectively. These lengths were chosen such that the cross-slip rate matches the experimentally and computationally estimated rates.

The activation energies and volumes used in the current simulations depend on the cross-slip type in question and they were obtained from MD simulations of nickel [26–30], and are summarized in Table 3.1. The scaling factor $\eta$ for the attempt frequency is 50000 since the experimental strain rate is on the order of $10^{-3}$ $s^{-1}$ while the simulation strain rate is on the order of 50 $s^{-1}$. In order to further reduce numerical oscillations, cross-slip of chains of less than four segments was not accounted for to prevent the cross-slip of small chains. If all the above conditions are satisfied, the cross-slip event proceeds by picking a dislocation node on the chain to be the pivot node, constructing a straight line that passes by the pivot node and in the direction of the dislocation's Burgers vector, and moving all the chains nodes so as to fall on that line. This guarantees that all of the chain nodes lie on the line of intersection of the glide and cross-slip planes. The glide plane of the cross-slipped chain segments are then switched to the cross-slip plane, thus, these segments would subsequently

glide on the cross-slip plane.

| Cross-Slip Type | Activation Energy, $E_a$ (eV) | Activation Volume, $V_a$ |
|---|---|---|
| Bulk | 0.8 | $20b^3$ |
| Surface | 0.2 | $20b^3$ |
| Hirth-lock | 0.2 | $20b^3$ |
| LC-Lock | 0.6 | $20b^3$ |
| Glide Lock | 0.5 | $20b^3$ |

Table 3.1: Nickel Cross-slip parameters as obtained from atomistic simulations (Rao et. al. 2009, 2010, 2011, 2012, 2013)

## 3.5 Numerical Simulations

In all the current simulations the simulation cell is of a right parallelepiped with square cross sections of side length $D$ that varies between 0.5 and 10 μm. Smaller simulation volumes with $D \leq 5$ μm have a height-to-edge ratio of 3 to avoid any buckling effects. Larger crystals are cuboidal in shape (height-to-edge ratio of 1) to reduce the computational load. A tension load with a constant strain rate of 50 $\text{sec}^{-1}$ and the stress field was assumed to be uniform. The load was oriented in the multislip [001] direction which activates 8 FCC slip systems simultaneously. The material properties used were those of nickel single crystals. The initial dislocation densities were varied between $5 \times 10^{10}$ $\text{m}^{-2}$ to $10^{13}$ $\text{m}^{-2}$.

Frank-Read sources of normally distributed mean lengths that scales with the crystal size and a standard deviation of 10% of the mean length were uniformly randomly generated on all of the {111} family of planes. Their line directions make arbitrary angles with their Burgers vectors to obtain a distribution of dislocation sources of all types. No error is introduced by generating artificial pinning points in the simulation (due to the pinning at the ends of the Frank-Read sources) since they

give the same quantitative response in terms of size-scale effects as the same relaxed dislocation density simulations that do not have any pinning points initially [126].

## 3.6 Results

The effect of cross-slip on the engineering stress-strain response and the evolution of the dislocation density are shown in Figure 3.4 for four representative crystal sizes of $D = 0.5, 1.0, 5.0$, and $10.0$ μm, respectively. For each size, the results from simulations accounting for all cross-slip types as well as simulations without cross-slip are shown. For crystal sizes $D = 0.5$ and $1.0$ μm, no clear effect of cross-slip on the flow stress is observed as can be seen in Figure 3.4-(a). Both simulations with and without cross-slip show no strain hardening up to 0.8% strain. In addition, the average dislocation density is weakly affected by cross-slip and remains relatively constant throughout the simulations, as shown in Figure 3.4-(b). Nevertheless, it is clear that more significant dislocation bursts are observed in simulations with cross-slip as evident by the larger stress drops and accompanying dislocation density spikes.

On the other hand, significant early stage strain hardening can be observed for the $D = 5.0$ μm case and a lower hardening rate can be observed for the $D = 10.0$ μm case as shown in Figure 3.4-(c). In addition, as shown in Figure 3.4-(d) the dislocation density increases rapidly for both crystal sizes in the presence of cross-slip. At 0.5% strain, the dislocation density in both crystal sizes is observed to increase by an order of magnitude from the initial dislocation density, while simulations without cross-slip show a steady state dislocation density throughout the simulation.

Figure 3.5 shows the number of junctions as a function of engineering strain from the simulations of the four crystal sizes reported in Figure 3.4. Both simulations with all types of cross-slip and without any cross-slip are shown. Two observations can be made here. First, the number of junctions increases more significantly in the presence

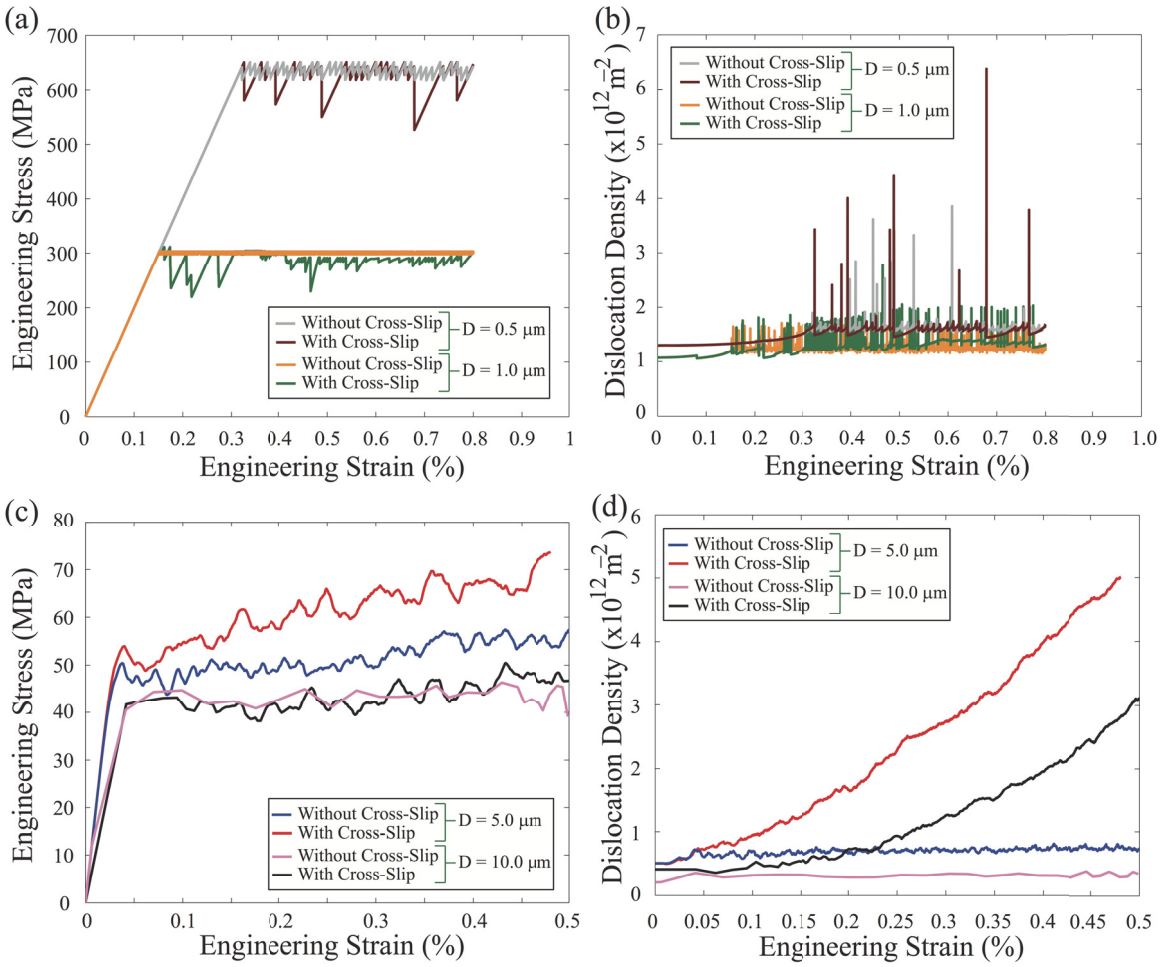


Figure 3.4: (a) and (b) engineering stress and dislocation density versus engineering strain, respectively, for $D = 0.5$ and 1.0 μm simulation cells. (c) and (d) engineering stress and dislocation density versus engineering strain, respectively for $D = 5.0$ and 10.0 μm. simulation cells

of cross-slip as compared to simulations without cross-slip. Second, the number of junctions increases more rapidly for the $D = 5.0$ and 10.0 μm crystals as compared to the two smaller crystals.

Figure 3.6 shows the initial and final dislocation microstrucutres from simulations with and without cross-slip for the cases reported in Figure 3.4. It is clear that while the initial dislocation density in the smaller two samples is double that in the larger samples, no clear dislocation density build up is observed in the smaller crystals either with or without cross-slip. Similarly, for the two larger simulations without

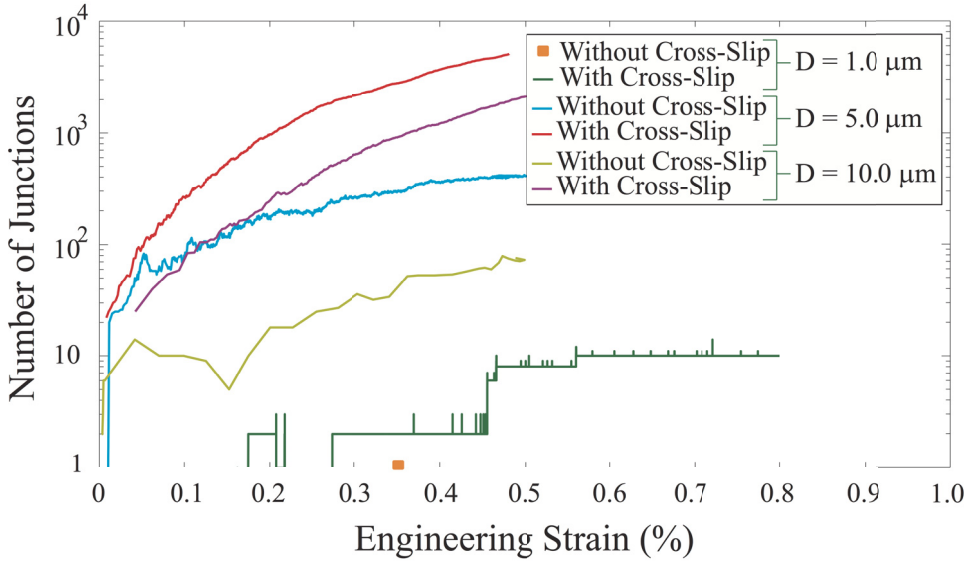


Figure 3.5: Number of junctions versus engineering strain for the $D = 1.0, 5.0$ and 10.0 μm microcrystals discussed in Figure 3.4 with and without cross-slip. No junctions were found in the $D = 0.5$ μm microcrystal in simulations with or without cross-slip.

cross-slip, no clear dislocation build-up is observed although multiple sources have been activated throughout the simulations. On the other hand, in the same two larger samples when all cross-slip types are accounted for a dislocation build-up is clearly observed showing an early stage self-organization in high dislocation density walls and lower dislocation density channels. The dislocation walls form mainly at the center of the crystal creating partial dislocation-cell structures that intersect the crystal surfaces. Animations of the 3D microstructres showing the dislocation pattern formation in the $D = 5.0$ and 10.0 μm crystals are shown in the supplementary movie1.avi, and movie2.avi, respectively.

In order to investigate the effect of the different cross-slip types on the evolution of the dislocation microstructure, the simulations have been repeated with the same initial dislocation network but with only one cross-slip mechanism enabled at a time. The initial dislocation density in these simulations was $5 \times 10^{11}$ m$^{-2}$ and the crystal size was $D = 5.0$ μm. Figure 3.7 shows the predicted microstructures from these simulations at 0.25% strain. Figure 3.7-(a) shows the predicted dislocation mi-

crostructure from simulations taking into account only bulk cross-slip, while all other cross-slip types being disabled. Similarly, the dislocation microstructure from simulations accounting only for intersection cross-slip, and surface cross-slip are shown in Figure 3.7-(b), and (c), respectively. It is clear from these results than no distinct dislocation pattern emerges from any of these simulation cases up to 0.25% strain. On the other hand, when all cross-slip types are accounted for in the simulations, the microstructure shows a clear pattern formation starting even at such a relatively low strain level, as shown in 3.7-(d). It should be noted it might be possible to develop dislocation patterns in simulations accounting only for one cross-slip type at much higher strains. However, with all cross-slip types accounted for it is clear that the dislocation pattern is predicted to emerge at much lower strain levels. Recent experimental observations on FCC metals [60–62] have confirmed the emergence of dislocation patterns at strain levels close to the ones predicted by these simulations.

Cross-slip was also found to influence the formation of surface slip traces on the crystal surface. Figure 3.8 shows the dislocation microstructure and the corresponding surface slip traces at different strain magnitudes from DDD simulations of a $D = 20.0$ μm simulation cell initialized with a single Frank-Read source of length 8.0 μm, which corresponds to an initial dislocation density of $10^9$ m$^{-2}$. A strong shear localization is first observed on the slip plane of the original Frank-Read source. However, as plasticity evolves, multiple secondary localized slip bands are observed on two specific slip systems, one parallel to the original Frank-Read source plane, and the other parallel to its cross-slip slip plane. The density of these slip bands and their heights increase with increasing strain. It is clear that the slip band thickening is accommodated by an increase in dislocation density in the crystal on multiple slip systems. It should be noted that the slip activity is not simultaneous, but rather intermittent with slip occurring on different planes for a limited time, then suppressed while slip commences on other planes. Slip band patterns similar to the one presented

here have been experimentally observed in FCC single crystals [127, 128]. Figure 3.8 shows slip band patterns from a Ni microcrystal having a 20.0 μm diameter after 12.7% strain [127] qualitatively showing similar patterns to the current simulations.

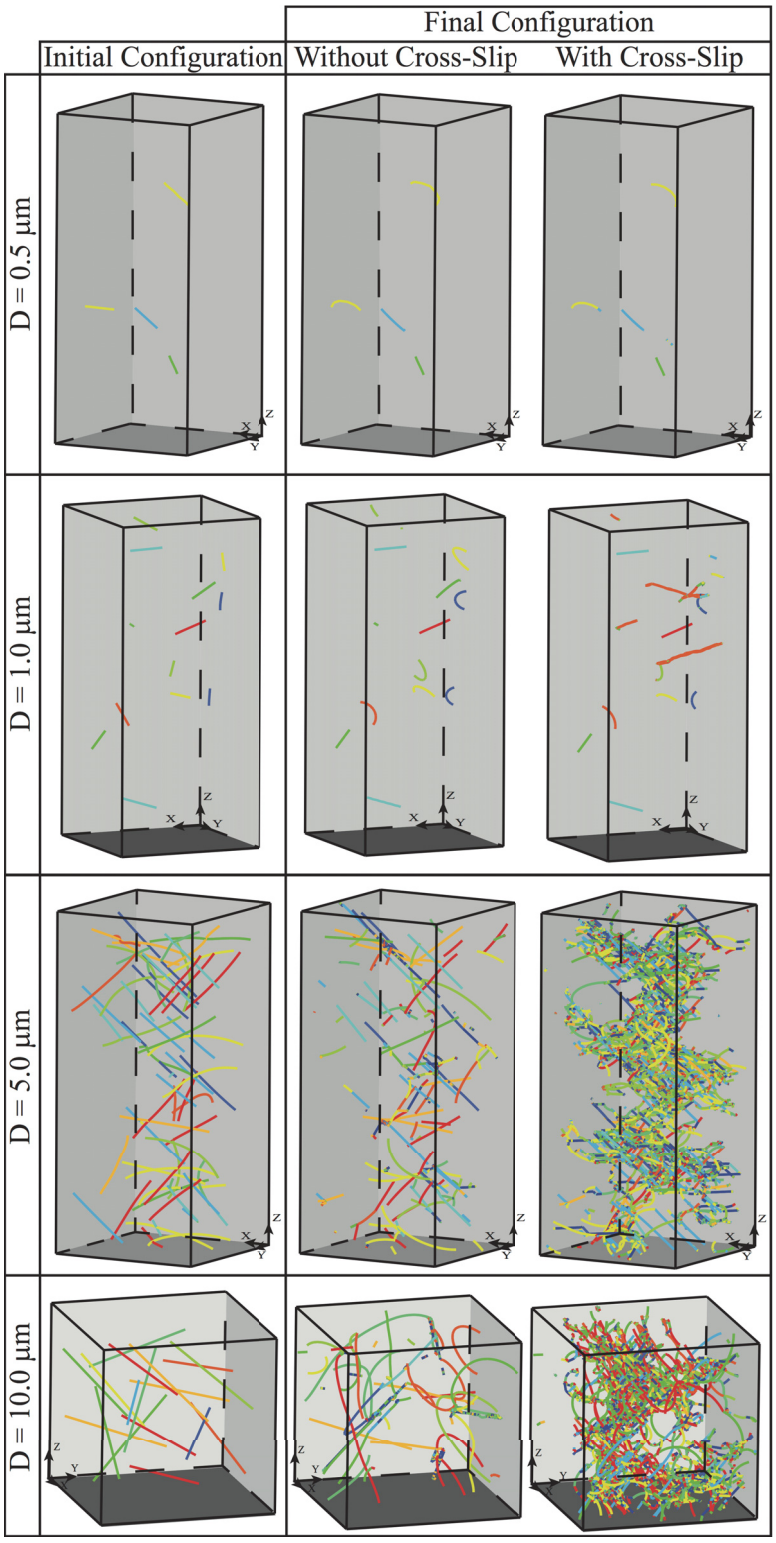


Figure 3.6: The initial and final dislocation configurations in the four microcrystals discussed in Figure 3.4 with and without cross-slip. The final configurations are reported at 1.0% strain for the $D = 0.5$ μm and $D = 1.0$ μm crystals and at 0.5% strain for $D = 5.0$ μm and $D = 10.0$ μm crystals

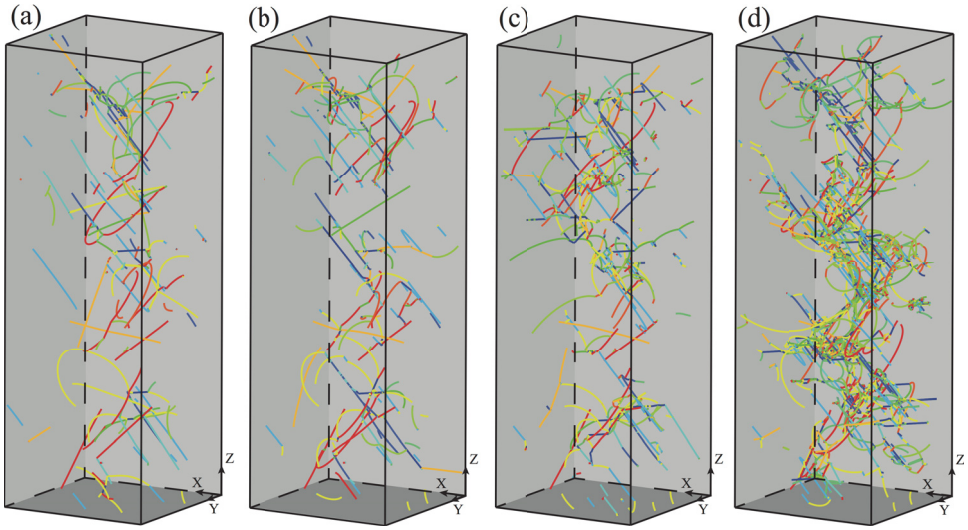


Figure 3.7: Dislocation microstructure at 0.25 % strain for simulations starting with the same initial dislocation network while accounting for (a) only bulk cross-slip; (b) only intersection cross-slip; (c) only surface cross-slip; and (d) all cross-slip types. The simulation cell had size $D = 5.0$ μm and the initial dislocation density was $5 \times 10^{11}$ $\mathrm{m}^{-2}$. Dislocations are colored based on slip system.

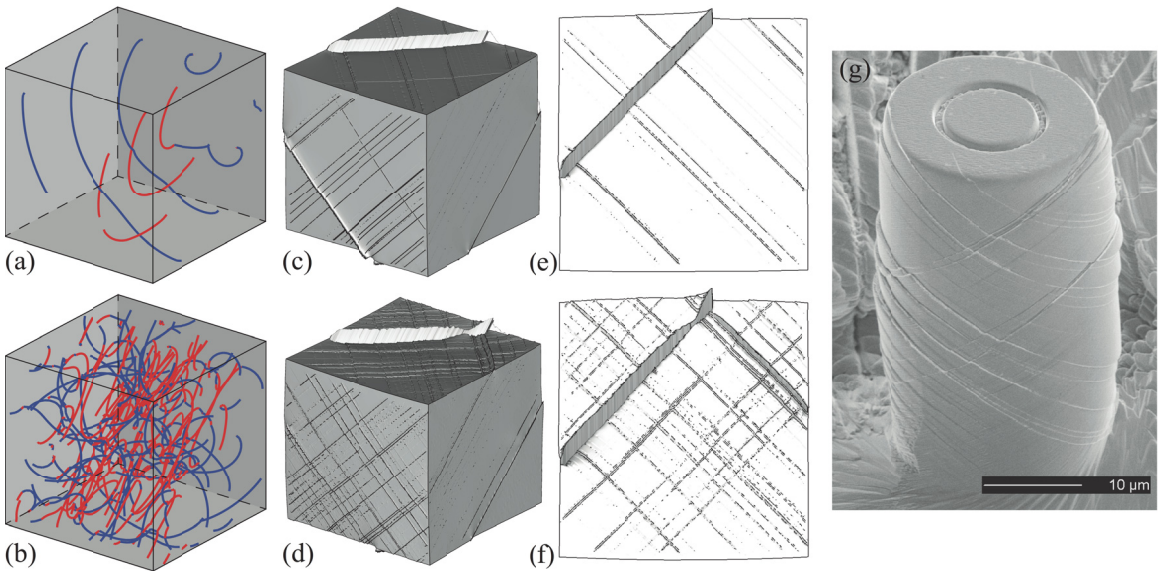


Figure 3.8: Dislocation microstructure at (a) 0.15%; and (b) 0.3% strain. The corresponding 3D surface slip traces are shown in (c), and (d), while a top view is shown in (e), and (f), respectively. The simulation cell is $D = 20.0$ μm and a single Frank-Read source of length 8.0 μm was introduced in the cell, which corresponds to an initial dislocation density of $10^9$ m$^{-2}$. Dislocations are colored based on slip system and the initial dislocation corresponds to the blue slip system. (g) Slip band patterns from a 20.0 μ diameter Ni microcrystal after 12.7% strain qualitatively showing similar patterns to the current simulations from El-Awady et. al. 2013

## 3.7 Discussion

### 3.7.1 Cross-slip Effects on Dislocation Microstructure Pattern Formation

Dislocation pattern formation is a self organizing phenomenon occurring at the grain length scale, which is typically in the micron and sub-micron ranges. The formation and evolution of dislocation patterns during the deformation of FCC single crystals has been well characterized experimentally in large crystals. Dislocation-cell structures have been routinely observed in all stages of deformation, with the dislocation-cell size decreasing with increasing strain [129]. Furthermore, *in situ* transmission electron microscopy (TEM) tensile tests of pre-strained single crystals Al thin films also show the accumulation of dislocations within a cell boundary at stage-III of strain hardening in double slip conditions [130]. More recently, *in situ* scanning electron microscope (SEM) compression experiments of aluminum (Al) microcrystals oriented for multislip have shown that the formation of dislocation cells is observed when the crystal size is $D > 2.5$ μm, however no dislocation cells were observed in smaller crystals [59]. In the current DDD simulations, when accounting for all cross-slip types, dislocation microstructure pattern formation is clearly observed during the deformation of microcrystals having sizes $D = 5.0$ and 10.0 μm, as observed in Figure 3.6. On the other hand, for microcrystals having sizes $D = 0.5$ and 1.0 μm no dislocation patterns were evident. These results qualitatively agree with the experimental observations, and suggest that dislocation cell structures are suppressed due to the geometric limitations of the crystal when the crystal size is $D \leq 5.0$ μm with initial dislocation densities in the range of $5 \times 10^{11}$ to $5 \times 10^{12}$. It should be noted that this critical size could be strongly dependent on the initial dislocation density since bulk-like response can be expected for any crystal size if the dislocation density is above a critical value [131, 132].

As it was shown in Section 4.6, there is an increase in the number of junctions formed when cross-slip was active, and that the number of junctions increases more rapidly for the larger $D = 5.0$ μm and $D = 10.0$ μm crystals. This is mainly due to the much shorter distance a dislocation can travel in the smaller crystals before exiting the crystal, and thus reducing the probability of intersecting other dislocations, even with cross-slip fully accounted for. The dislocation pattern formation is observed to be associated with an enhanced dislocation junction formation. A junction in the current simulations is identified as any dislocation node where three or more dislocation segments, usually belonging to different slip systems, intersect. Junctions are typically difficult to move since they must satisfy glide restrictions of all intersecting dislocations slip systems simultaneously. If the intersecting dislocation segments lie on three or more different slip planes, then the junction will remain immobile. In our current simulations, once the junction forms, in most cases, it is difficult to break. Thus, junctions typically serve as sites at which high dislocation densities build-up are observed, which subsequently promotes dislocation patterning.

Cross-slip, in general, helps redirect dislocations around obstacles that block their glide. These obstacles are forest dislocations in the current study. It can also aid in propagating dislocations to glide on a different slip planes where the resolved shear stress is higher. As dislocations cross-slip, the probability of them interacting with other dislocations on other slip systems increases and subsequently the number of junctions increases. Thus, cross-slip acts as a mechanism by which the substructure evolves throughout the crystal. This is in contrast with the no cross-slip case where the dislocations remain on their original planes without the potential of multiplying on other slip planes and thus limiting the number of junction sites. On the other hand, the crystal size plays an important role in the formation of dislocation patterns as well. If the crystal size is small, dislocations have a higher probability of escaping the crystal before interacting with other dislocations and forming strong junctions.

This is evident in the $D = 0.5$ and 1.0 μm microcrystals showing only a modest increase of junctions in the presence of cross-slip. As previously stated, an increasing dislocation density would lead to increasing the number of strong junctions in smaller crystals which could subsequently lead to pattern formation in these crystals. However, the dislocation densities modeled here in the two smaller crystals are 1-2 orders of magnitude smaller than the typical dislocation density at which bulk response is expected to be recovered [131].

Previously published DDD simulations accounting for only bulk cross-slip, as implemented using equation (3.4), have also suggested the formation of dislocation "cell-like" structures in large simulation cells ($\approx 10.0$ μm$^3$) with periodic boundary conditions imposed [42]. However, in the presence of free surfaces similar structures were only reported in much larger simulation cells (15.0 μm$^3$) [133]. From the individual cross-slip type simulations, it is clear that the local dislocation density buildup in the crystal is not strong enough to form a well defined pattern at the strain levels reached here. On the other hand, when all cross-slip mechanisms are accounted for, a much clearer dislocation structure is observed. Further anaylsis on the rate of new dislocation source generation from these individual cross-slip type simulations are discussed in Section 3.7.3.

### 3.7.2 Surface Slip Band Thickening

Formation of surface slip traces and steps is a natural consequence of dislocation interactions with crystal surfaces. It is generally common to observe these slip traces distributed randomly on the crystal surface in bulk [134, 135] and microcrystals [136, 137], with the slip trace density and step height depending on strain. Slip typically concentrates on few planes with rather strong shear in addition to the formation of localized slip bands along the length of the deforming crystal length. The formation of localized slip bands might be surprising especially for microcrystals containing few

initial dislocation sources (equivalently at dislocation densities on the order of $10^{12}$ $m^{-2}$).

In the absence of cross-slip, DDD simulations typically show localized strong shear on a limited number of slip planes with no clear slip band formation [55]. However, in our current simulations with cross-slip, localized slip bands are commonly observed in all simulated crystal sizes. In the following we examine surface cross-slip as a potential mechanism that can be responsible for the formation of localized slip bands in microcrystals. Upon taking a closer look at the microstructure evolution, a specific repeating mechanism was observed to take place. When a bulk dislocation intersects a free surface, the dislocation splits into a surface step of height $\mathbf{b}$, and two single-ended dislocation segments that continue to glide away, extending the surface step. If either the two single-ended dislocations reaches a screw orientation as they continue to glide, and given the low surface cross-slip activation energy, they can subsequently cross-slip on the surface and glide on a new glide plane. Similarly, after the dislocation cross-slips it can further double cross-slip on the surface and start glide on a third plane, which is parallel to its original plane. Because surface cross-slip activation energy is relatively low, these dislocations can keep cross-slipping in this manner till an array of dislocations, all gliding on parallel planes, are created. All these dislocations have originated from the same initial source and subsequently their interaction with the free surface will result in a localized slip band. Figure 3.9 shows schematically the 4 steps of this process.

At the beginning of the slip band formation, the dislocation traverse distance is almost purely stochastic and the second cross-slip event can occur anywhere. However, as the dislocation array gets denser, the stresses from the dislocations gliding on parallel planes can reduce the surface cross-slip activation energy further. Thus, the local stress field can become the influencing factor in cross-slip probability, and dislocations would preferentially cross-slip on unoccupied parallel planes where the

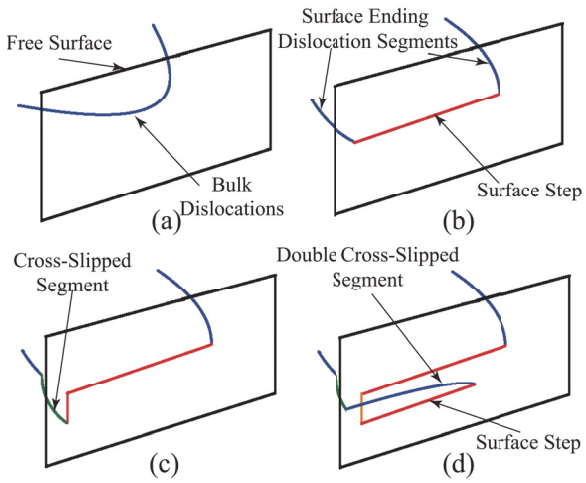


Figure 3.9: A schematic showing the surface slip localization mechanism. The blue and green dislocations lie inside the crystal on slip planes P1, and P2, respectively, while the red surface segments represent dislocation segments that exited the crystal. In (a) a dislocation approaches the surface on P1. In (b) the dislocation intersects the surface forming a surface step represented by the red line. In (c) one of the surface intersecting dislocation segments cross-slips and glides onto P2 as shown by the green segment. This results in a new surface step on P2. In (d) the newly formed segment on P2 cross-slips back to a plane parallel to P1 and subsequently forming another surface step on that plane parallel to the first surface step on P1. The two blue dislocations in (d) glide on two parallel planes.

back stresses are relatively lower, rather than a plane occupied by other dislocations on which the back stresses are relatively higher.

### 3.7.3 Cross-Slip Statistics

It is of interest to quantify the influence of each cross-slip type on the evolution of dislocations in the crystal. It is particularly important to identify the effect of each cross-slip type on the rate of generation of new dislocation sources in an effort towards developing dislocation density evolution continuum models [138]. Towards that goal, Figure 3.10 shows the number of new sources formed, after 0.5 % strain, due to each cross-slip type as a function of initial dislocation density and crystal size from all the simulations. The crystal sizes were varied between $D = 0.5, 1.0, 5.0$, and 10.0 μm and

the initial dislocation density was varied between $5 \times 10^{10}$ to $10^{13}$ $m^{-2}$.

As seen in Figure 3.10, there is a positive correlation between the source generation and the crystal size. While bulk cross-slip source generation is not that sensitive to crystal size, surface and intersection cross-slip source generation show a significant sensitivity. Smaller crystals, especially at low dislocation densities, do not show significant source generation by cross-slip compared to larger crystals in general. Furthermore, for a given initial dislocation density, the larger the crystal size the more dislocation sources it will contain, and consequently, the higher the number of sources being generated. A possible explanation is that for larger crystals the probability of dislocation collisions and subsequent junction formation is higher than that for dislocations to escape from the free surface, which enhances the chances of intersection cross-slip.

Initially, as bulk dislocations evolve and intersect the surface, surface dislocations are created, which alters the actual number of sources of each type responsible for cross-slip. Based on the physics of each cross-slip type, as a first order approximation it can be expected that the number of sources generated due to bulk or surface cross-slip must be proportional to the number of dislocation sources in the microcrystal. On the other hand, since the frequency of junction formation can be expected to be proportional to the square of the number of the available sources, the number of newly generated sources due to intersection cross-slip should also be expected to scale with the square of the number of dislocation sources in the microcrystal. By examining Figure 3.10, and noting that the initial dislocation density is a measure of the number of sources in the system, it is observed that the slope of the curves is roughly equal to 1.0 for surface cross-slip, and 2.0 for intersection cross-slip. This is consistent with the aforementioned phenomenological discussion. However, the slope of the curves for the bulk cross-slip cases are significantly smaller ($\approx 0.1 - 0.3$), which deviates considerably from the expected linear dependence as discussed above. This

can be explained by taking into account that the activation energy of bulk cross-slip is much higher than surface or intersection cross-slip. Furthermore, given the short mean free path for bulk dislocations in microcrystals, most bulk segments, especially at low densities, will intersect the surface before they get a chance to cross-slip in the bulk, thus, further reducing the rate at which bulk cross-slip generates new sources.

Finally, from the simulations performed with a single cross-slip type enabled at a time (see Figure 3.7) it is possible to determine the synergistic effects of the different cross-slip types. In the simulation with only bulk cross-slip, 19 new sources have been created at 0.25% strain. In the simulation with intersection cross-slip only, the number of new sources was 308 at this strain level. Finally, in the simulation with only surface cross-slip accounted for, the number of new sources was 1128. However, when all cross-slip types were accounted for the number of events from each cross-slip type has almost doubled with 38, 708, and 1830 bulk, intersection, and surface cross-slip events recorded after 0.25% strain. This is due to the synergistic effects resulting from the activity of all cross-slip types simultaneously. For instance, as surface cross-slip is induced, the probability of junction formation increases, which subsequently increases the probability of intersection cross-slip. Furthermore, a higher density of screw dislocations are expected to traverse the crystal, which subsequently increases the probability of bulk cross-slip, and vice versa. This is consistent with the idea of source generation rate dependence on the existing number of sources. As more cross-slip types are activated, more sources are generated, which further induces source generation.

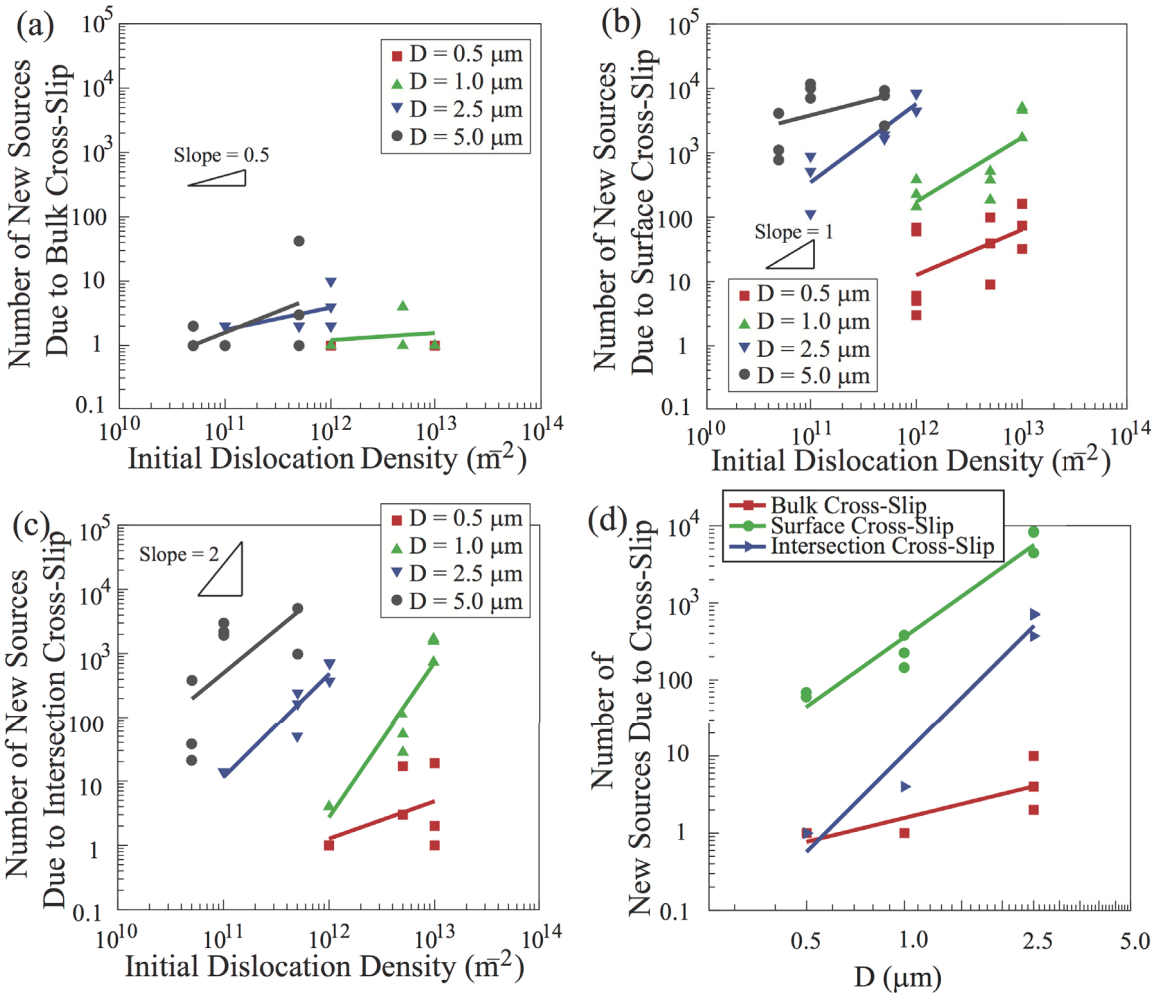


Figure 3.10: Number of new dislocation sources as a function of initial dislocation density and crystal sizes due to: (a) bulk cross-slip; (b) surface cross-slip; c) intersection cross-slip and d) number of new dislocation sources as a function of the crystal size for a given initial dislocation density of $10^{12}$ m$^{-2}$ due to bulk cross-slip, surface cross-slip and intersection cross-slip.

## 3.8 Summary and Conclusions

In this chapter, three new mechanisms of cross-slip in FCC crystals that were recently identified from MD simulations were implemented into discrete dislocation dynamics simulations to study the evolution of dislocation microstructures of various crystal sizes and dislocation densities. A summary of the findings are listed below.

- Early stages of strain hardening was observed in larger crystals ($D \geq 5$ μm) which was correlated with significant cross-slip activities. On the other hand, no significant strain hardening was observed in smaller crystals.
- The dislocation density was observed to increase significantly in larger crystals, which was facilitated by cross-slip.
- The number of fixed points generated in a crystal increases significantly when cross-slip is accounted for.
- Clear dislocation cell structures were observed in larger crystals ($D \geq 5$ μm) starting at strain levels as low as 0.5% only when all cross-slip types are accounted for in the simulations. When only individual types of cross-slip are accounted for, these dislocation cell structures are absent or significantly delayed.
- The formation of surface slip bands were observed to be correlated with the activation of surface cross-slip.
- Bulk cross-slip events are the least frequent, followed by intersection cross-slip and then surface cross-slip.

The results are in good agreement with experimental observations of uniaxial compression experiments on Ni and Al microcrystals. Overall, the observations suggest

that surface and intersection cross-slip are more influential in microstructure evolution and early strain hardening and emphasis should be placed on further exploration of those mechanisms. It should be noted that the pre-exponential factor in the cross-slip rate equation should be adjusted through further simulations and experiments so as to match the strain-hardening rates with the ones observed experimentally.

# Chapter 4

# Microstructure and Surface Roughness Evolution during Mechanical Cyclic loading in Nickel Micro-Crystals

This chapter presents DDD simulation results and physical insights of the mechanical cyclic deformation mechanisms of FCC microcrystals as investigated through DDD simulations.

## 4.1 Introduction

Failure under cyclic loading is one of the most common ways by which mechanical and structural components fail [56, 57]. According to one estimate, the annual cost of mechanical components failure due to fatigue is about 4% of the U.S. gross national product [56]. Historically, fatigue failure was one of the earliest failure mechanisms to be studied [58, 139]. However, after about 150 years of research, a complete un-

derstanding of the mechanisms that lead to fatigue failure is still elusive [139]. On one hand, the fatigue failure process is sensitive to the component geometry, loading type, pre-straining, inclusions, previously existing cracks, material heterogeneity, and environmental conditions among other factors [140]. On the other hand, the mechanisms responsible for fatigue crack initiation and propagation take place over multiple length and time scales [141]. These two reasons explain the complexity of the fatigue failure process.

The fatigue failure process is usually divided into two stages, fatigue crack initiation (nucleation) and fatigue crack propagation [58, 140]. There is no clear boundary between the two stages. For designers and practitioners, fatigue crack initiation ends when the crack first reaches a length that is detectable by a non-destructive testing method [142], hence, it is a definition that is largely based on the current crack detection technologies. From a more physical point of view, fatigue crack initiation can be defined as the stage during which an initially uncracked component develops a crack of the same length as the microstructural features of the material such as grains and inclusions [142]. The total number of loading cycles to failure can be broken down into [143]

$$N_T = N_{int} + N_{msc} + N_{psc} + N_{lc} \tag{4.1}$$

where $N_{int}$ is the number of cycles for crack initiation, and $N_{msc}$ is the number of cycles, beyond crack initiation, required to form a microstructurally small crack, which is a newly nucleated crack that has propagated through the first few barriers to its motion such as inclusions and grain boundaries. $N_{psc}$ is the number of cycles, beyond microstructurally small crack nucleation, required to nucleate a physically small crack, which is a crack that is long enough to propagate through the microstructural features but still short for a linear elastic fracture mechanics treatment due to the surrounding plastic zone. This is typically a crack of about several hundred microns

in length [144]. Finally, $N_{lc}$ is the number of cycles, beyond physically small crack nucleation, taken by a long crack to propagate through the component until it fails. This last part can be safely studied using linear elastic fracture mechanics. The point at which to draw the line between crack nucleation and its propagation is unclear, however, one possible demarcation would be that the nucleation number of cycles is $N_{nuc} = N_{int} + N_{msc}$ and the propagation number of cycles is $N_{prp} = N_{psc} + N_{lc}$. The crack nucleation stage is the least understood of the two. At the same time, understanding crack nucleation is the first step to extend the lifespan of components through an appropriate design of microstructure. According to Suresh [58], "developing a quantitative understanding of crack initiation processes must be regarded as one of the most important tasks".

Current fatigue failure prediction theories employed in design methodologies, such as stress-life, strain life and damage tolerant approaches [58], are mostly based on experimental observations and continuum mechanics, which breaks down near the crack front. Thus, a number of statistically justified safety factors need to be employed, which renders the designs overly conservative. The need of lighter and stronger components, especially for the aerospace industry, calls for a physics based understanding of how cracks nucleate and how to stop or slow down their propagation so as to extend their lifespan. To this end, the aim here is to provide a physical understanding for the micromechanical processes that take place during of cyclic loading, prior to any failure. These processes are heavily controlled by dislocation activity [58]. While several models of dislocation interactions with grain boundaries and twin boundaries have been recently implemented in DDD [21, 145], the current simulations are limited to FCC free standing single crystal simulations to reduce the complexities introduced by dislocation grain/twin boundary interactions. Grain boundaries were found to either slow down or completely stop the propagation of cracks under cyclic loading depending on the grain boundary type and the crack front geometry [146]. FCC metals were

chosen because of their heavy use in mission critical components subject to extreme environmental conditions such as gas turbine engine blades where they get cyclically thermomechanically loaded [147]. The mechanisms identified can supplement the theories based on experimental observations by providing more spatio-temporal details about the plastic flow and they can be later incorporated into computational methods that are typically used for higher length and time scale analyses, such as crystal plasticity [144], so as to connect them to the macroscopic failure process.

## 4.2 Background: Fatigue Crack Nucleation

Fatigue cracks have been observed to nucleate at interfaces such as grain boundaries [148], near or at the surface of an inclusion [149], or from the crystal surface [140, 141, 150]. Grain boundary fatigue crack nucleation typically takes place at higher temperatures and strain amplitudes [150]. This makes the free surfaces of crystals the most common sites for fatigue crack nucleation, and for pure single crystals, the only interface at which cracks nucleate. One of the first experimental observations of what was understood later as a sign of fatigue crack nucleation was made by Ewing et. al. [151] where they observed sharp slip lines on the surface of polycrystalline iron specimens, called slip bands. These slip bands are higher, or lower, than the original specimen surface and their heights (depths) increase with the number of cycles. Eventually, some of these bands will turn into cracks. The presence of bands is a sign of something more fundamental, that is, strain localization where the dislocation activity gets concentrated in a small region in the crystal. As the crystal is stressed in each loading cycle, dislocations move back and forth and interact in the process. Because the motion is not fully reversible, the dislocation density builds up over time. This has been experimentally verified through electrical resistivity measurements [152]. The increase in dislocation density in turn increases the strain energy of the crystal,

which drives dislocations to form structures like dislocation dipoles or persistent slip bands (PSB) so as to minimize the overall strain energy of the crystal [63].

Mughrabi et. al. studied the evolution of dislocation patterns, in fatigued single crystal FCC copper oriented for single slip at room temperature under total plastic strain control [153]. When the crystal is loaded in fully reversed cyclic loading at a constant plastic strain amplitude, the peak shear stress was found to increase with the cumulative plastic strain $\gamma_{pl}^{T}$ up to a certain point where the shear stress saturates over a long range of $\gamma_{pl}^{T}$, then it finally increases again until the sample fails. These three regions are shown in Figure 4.1 and are termed regions $A$, $B$ and $C$. The cumulative plastic strain $\gamma_{pl}^{T}$ is defined to be the total imposed shear strain throughout the cycling process [58]

$$\gamma_{pl}^{T} = 4\Sigma_{i=0}^{i=N}\gamma_{pl}^{i} \tag{4.2}$$

where $\gamma_{pl}^{i}$ is the plastic shear strain imposed in one loading or unloading motion in the $i^{th}$ cycle. If the stress required to maintain the imposed plastic strain amplitude is below the saturation stress, the system will never reach region $B$ and it would be possible to load it indefinitely without failure. This corresponds to cycling below the failure limit in a typical S-N curve.

In region $A$, called the pre-saturation stage, fine straight slip traces start forming on the surface [154]. These slip traces are not persistent and they disappear upon polishing the surface. Further cycling causes more of them to appear and they are almost spatially uniformly distributed. Inside the crystals, dislocations arrange themselves in cell-like structures very early [154] with dense dislocation walls surrounding nearly perfect material. These cells are mostly on the primary glide plane with a vein like structure developing on the cross glide plane that contains the shared Burgers vector with the primary plane. The size of the cells decreases with increasing the cumulative plastic strain. This microstructure is similar to that found in stage-I deformation in

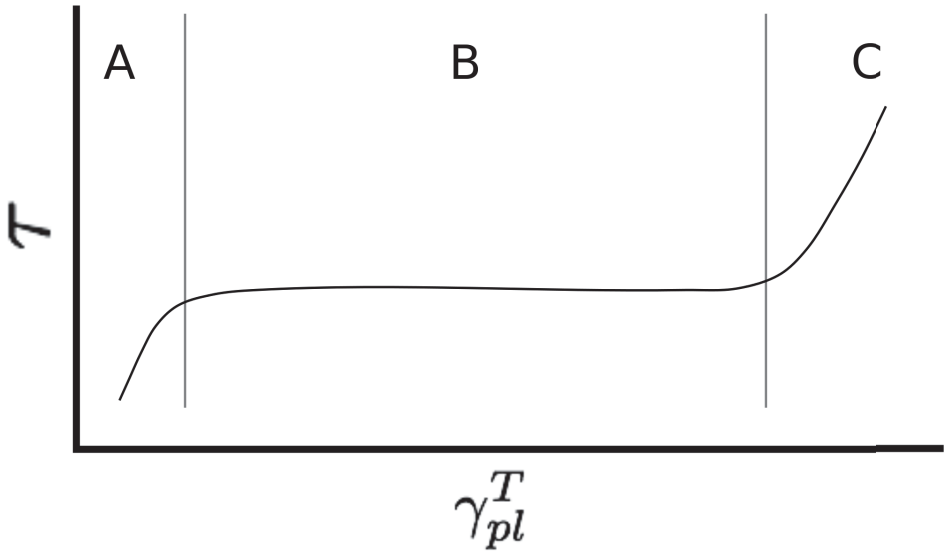


Figure 4.1: A schematic for a typical cyclic stress strain curve. $\gamma_{pl}^T$ is the accumulative plastic strain and $\tau$ is the stress required to maintain the imposed plastic strain. $\tau$ varies as the accumulative plastic strain $\gamma_{pl}^T$ increases as shown.

tension [154].

As $\gamma_{pl}^T$ approaches a certain threshold value (about $8 \times 10^{-5}$ for copper [153]), transitioning to region $B$, or the saturation stage, takes place. On the crystal surface, similar slip traces, like those observed in the pre-saturation stage, appear, however, upon polishing, these slip traces do not go away and that is why they are termed persistent slip bands (PSB) [63] and shown in Figure 4.2. The persistence of PSBs indicates that they are features rooted in the bulk of the crystal not just on the surface. Inside the crystal, PSBs have a ladder like structure of high dislocation density walls spaced out by low density channels. The walls are formed mainly of edge dipoles with a density of $\rho_w = 5 \times 10^{15}$ m$^{-2}$ [155], and their planes are normal to the Burgers vector of the dipoles with a wall spacing of about 1.4 μm at room temperature. The channels contain mainly screw dislocations with a lower density of about $\rho_w = 1.5 \times 10^{13}$ m$^{-2}$. PSBs span entire grains and end on either crystal surfaces or the grain boundaries [58]. They are the main carriers of plasticity in the saturation region and as the

number of cycles increases, more PSBs form, preferentially near other existing PSBs [156]. The volume fraction of PSBs keeps increasing until it reaches 100% by the end of the saturation stage. A similar behavior was found in nickel and silver single crystals [157].

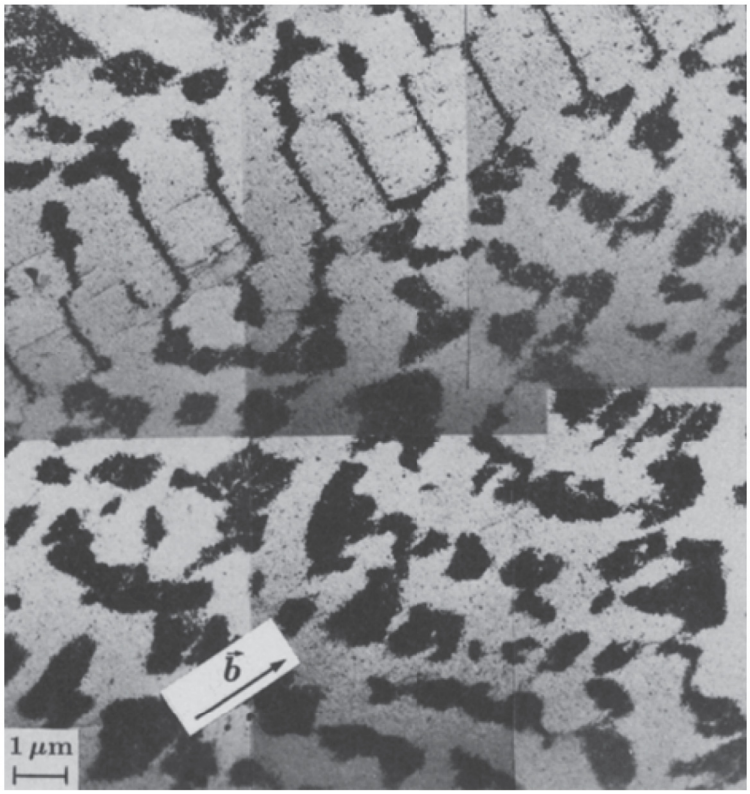


Figure 4.2: A micrograph showing a PSB embedded in a matrix structure after a cumulative plastic strain of $2.2 \times 10^{-3}$ taken from Holzwarth et. al. (DOI:10.1007/BF00331434) with kind permission from Springer Science and Business Media.

Since the PSBs are dislocation dense, they are generally softer than the surrounding matrix. The intersection of the soft-hard interface with the crystal surface is the first location at which cracks can nucleate [63]. The Essmann, Gosele and Mughrabi (EGM) developed a model to explain how dislocations inside PSBs interact, annihilate and deposit dislocations along that interface, a process during which the PSB dislocations escape from the surface gives rise to surface roughness while the generation of

point defects alters the volume of the PSB [158]. This increase in volume manifests itself on the surface in the form of an extrusion. A schematic for the configuration of the PSBs and surface extrusions is shown in Figure 4.3 after [158].

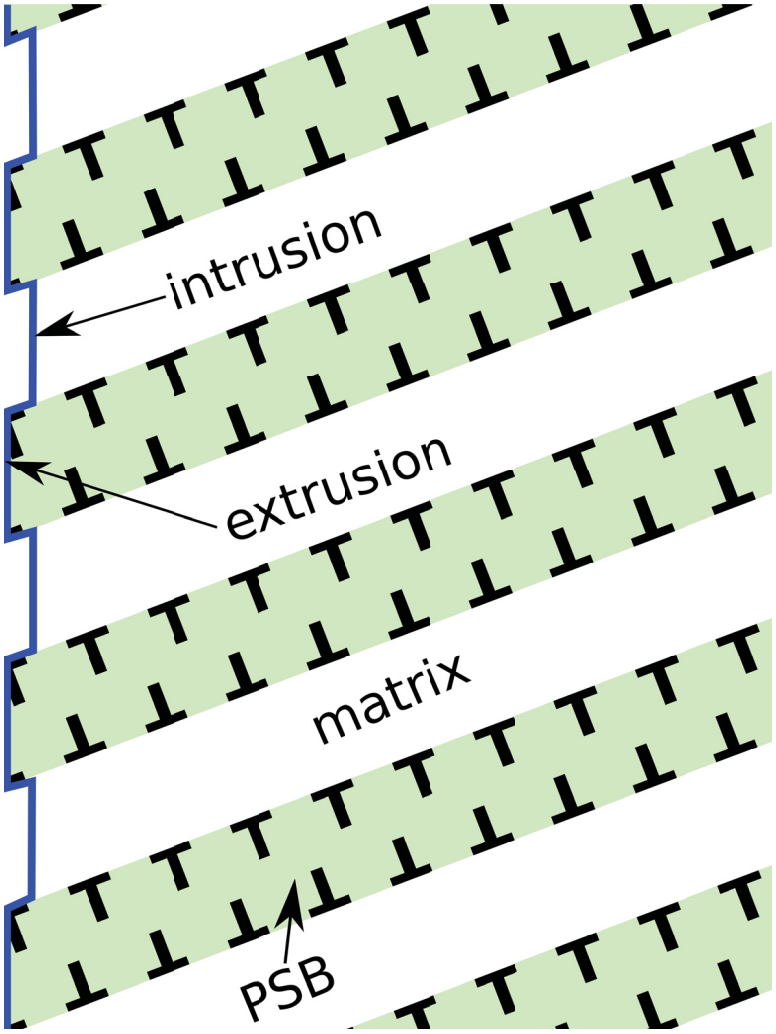


Figure 4.3: A schematic of the distribution of PSBs (green) in a matrix (white). The resulting surface extrusions and intrusions are shown.

The corners of the extrusions act as stress concentrators and when the local stress is high enough, local atomic bonds can break, an event which constitutes the formation of a small crack. The stress at the crack tip, due to its sharpness, is higher than the far field stress, which leads to more bond breaking, resulting in the propagation of the crack into the material. A micrograph of cracks nucleating near such extrusions

are shown in Figure 4.4.

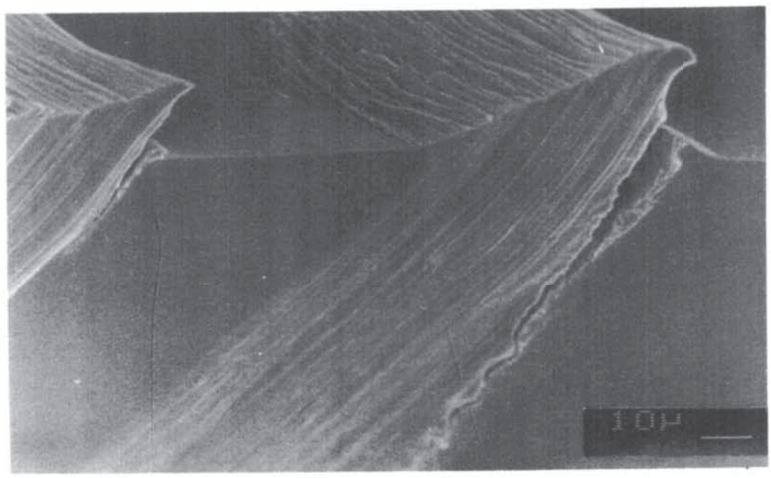


Figure 4.4: A micrograph of two PSBs intersecting the specimen surface. The surface steps due to dislocations escape are clear. Cracks nucleating at the PSB-matrix interface can also been seen. Reprinted from Publication by Basinski and Basinski (DOI:10.1016/0079-6425(92)90006-S) with permission from Elsevier

From the previous discussion, it can concluded that dislocation activity leads to surface roughness evolution, which is subsequently responsible for surface crack nucleation. A number of theoretical and computational studies attempted to explain the formation of the observed dislocation structures and surface topographies. Starting from a simple force balance calculations on two dimensional distributions of edge dislocations, Neumann showed that several stable structures can form under various levels of applied stress such as a diamond and ladder geometries (similar to PSBs) [159]. One drawback of this work is that it lacks any sort of short range dislocation interactions such as annihilation and that it is restricted in terms of the dislocation type. A series of studies by Walgraef, Aifantis and co-workers [160–164] used the nonlinear reaction-diffusion equation to model the evolution of dislocation densities in space and showed that for a certain choice of model parameters, periodic sharp rises in the density, similar to PSB walls, naturally evolve. Their approach is based on continuous dislocation density fields rather than discrete dislocations and

the connection between the model parameters and the physical mechanisms active during cyclic loading are difficult to establish. Repetto and Ortiz [165] developed a crystal plasticity model that takes into account dislocation activity, annihilation and vacancy generation in particular, within PSBs and the resulting surface motion that amounts to a small groove after a number of loading cycles. The model does not explicitly predict the generation of PSBs. In their model, the surface deformation depends mainly on the outward flux of vacancies. The model however suffers, like most crystal plasticity models, from the problem of parameter estimation. On the surface roughness side, the EGM model [158] is based on the production of vacancies due to the annihilation of PSB dislocations and their subsequent migration to the surface of the crystal or to the matrix. Polak et. al. [166] extended the EGM model and calculated the profiles of extrusions and intrusions.

Besides theoretical and crystal plasticity models, discrete dislocation dynamics (DDD) simulations are capable of providing more details on the distribution of dislocations, how it evolves in time, accurate vacancy production distributions and surface roughness development based on the interaction of dislocations with the surface, all while accounting for the complex three dimensional dislocation far-field and short range interactions. Deshpande et. al. [167–170] used 2D DDD simulations to model the interaction of dislocations with an already existing crack under mode-I monotonic and cyclic loading and the resulting crack growth. Excessive dislocation slip activity takes place around the crack tip due to the locally higher stress field. The cracks were found to suddenly burst at the beginning of the cyclic loading and then, depending on the stress intensity factor, they grow smoothly. Brinckmann et. al. [171] studied the accumulation of dislocation density and stresses in a surface grain cyclically loaded. They also modeled the generation of dislocation dipoles from Frank-Read sources when the local stress exceeds a predefined source strength. This is particularly important for problems containing either predefined or nucleated cracks since

the stress around the crack tip should be high enough for dislocations generation. Unfortunately, dislocation generation is challenging and very restrictive for 3D DDD simulations. After a few number of loading cycles, stress concentrations were visible along high dislocation density bands running parallel to the primary slip plane. A huge increase in the dislocation density on the same slip planes was also reported in this work. However, the concentrated stresses were still well below the limit for fatigue failure because they only simulated a few number of loading cycles. While these DDD simulations remove many of the assumptions usually used in theoretical models, they are limited to only edge dislocations moving in two dimensions. Both the geometric features (such as cell structures and PSBs) and the kinetic ones (such as the stress distribution) found in fatigued crystals are three-dimensional in nature which calls for a more accurate description of the defect dynamics.

Depres et. al. presented an extensive 3D DDD study on the evolution of microstructure and surface roughness in early cycle fatigue [172]. Starting with a single Frank-Read source inside a surface grains of different sizes where all the grain boundaries are impenetrable by dislocations except for one, the system was cycled at a constant plastic strain amplitude with bulk cross-slip enabled (see Section 3.3). Their simulations showed the formation of a cell-like structures after a very few number of cycles ($N \leq 20$), especially for crystals loaded in multislip orientation. They proposed a mechanism for the formation of the cell structures that is based on double cross-slip and the interactions between dislocations on parallel planes. One interesting finding from that study was that the thickness of the cell walls is proportional to the square of the grain diameter while the spacing between the walls is proportional to the grain diameter which shows that there is a size effect on the characteristics of the cell structure. In a later work [93], the same authors analyzed the surface slip markings associated with the dislocation activity and they found that the height of the surface steps increases with the number of cycles and the imposed plastic strain

amplitude. They also quantified the stored strain energy due to dislocation structures and they concluded that the regions within the dislocation channels store the highest elastic strain energy and consequently, cracks are more likely to nucleate there. Two major drawbacks of this work is that they used the simplified edge-screw dislocation model that does not allow dislocations of mixed types to exist and they started their simulations with only a single Frank-Read source, which gives an unrealistically low initial dislocation densities for the volumes they simulated ($D$ = 10 to 22 μm). In a different study [173] by the same group, the crack propagation was studied in 3D DDD by explicitly introducing a crack surface and allowing the dislocations to escape from the two faces of the crack. Dislocation nucleation ahead of the crack tip was modeled by distributing dislocations sources on all of the possible slip systems near the crack tip. This is one example of successful dislocation nucleation in 3D DDD simulations. El-Awady et. al. utilized 3D DDD simulations to study the effect of the long range stresses resulting from the dipolar dislocation walls on the dynamics of screw dislocations in PSB channels as well as the interactions of screw dislocations on parallel slip planes and how they affect the PSB flow strength [174].

The effect of stress field heterogeneity was addressed by Kiener et. al. [175] through both experiments and 3D DDD simulations of single crystal copper microbeams subject to a fully reversed bending load. They reported that dislocations accumulate near the neutral plane, however, their simulations did not show any signs of cyclic hardening or irreversible dislocation microstructure buildup since they only were able to simulate one loading cycle and the dimensions of the microbeams were smaller than the characteristic dimensions of dislocation cell structures. Likewise, Senger et. al. [176] performed 3D DDD simulations on monotonically and cyclically loaded pillars in torsion and found that dislocations accumulate near the axis of the pillar and that stable irreversible structures develop after a few number of cycles ($N \approx 4$) with cross-slip playing a major role in their formation.

Fatigue in complex material systems had their share of DDD studies as well. Shin et. al. [177] studied the interaction of dislocations with shearable precipitates of different sizes in nickel-base superalloys under cyclic loading. They concluded that with larger precipitates, surface slip markings similar to those developing on the surfaces of pure crystals are found. With smaller precipitate sizes, PSB like structures develop inside the crystal and a pronounced cyclic softening follows. Huang et. al. [178] modeled the dislocation interaction with a transgranular crack in a cyclically loaded polycrystalline nickel-base superalloy using 2D DDD. Their model accounts for both dislocation climb and dislocation-grain boundary (GB) penetration. High rate dislocation density multiplication and activation of multiple slip systems were observed in grains surrounding the crack tip as opposed to single slip activity in farther grains. Also dislocation climb was found to contribute more than GB penetration at elevated temperatures.

While these previous studies of the early fatigue behavior using DDD simulations show the capabilities of the method and the level of detail it can provide, there are many open questions that need to be addressed. Here, realistic large scale 3D DDD simulations of pure nickel single crystals having various sizes are performed to gain a better understanding of the active deformation mechanisms and their contributions to the overall microstructure evolution, surface roughness and mechanical response. By realistic, it is meant that minimal non-physics based restrictions are imposed on the initial dislocation microstructures and the governing dynamics. For instance, dislocations can be of any type, the initial microstructure is not limited to a single Frank-Read source, cross-slip, is accurately modeled according to an atomistically informed implementation in a DDD framework as discussed in Chapter 2 [65], and proper analyses are performed in order to validate the obtained results with experiments and enrich the future development of fatigue crack initiation models.

## 4.3 Computational Method

The DDD simulation framework used for the current simulations is the same as the one described in Section 3.4. Cross-slip is active for all the simulations using the parameters given in Table 3.1. While the accurate handling of the motion of surface dislocation nodes was important for surface cross-slip calculations, in the current simulations, it is more important because the surface displacements, from which surface roughness will be calculated, depend entirely on how the dislocations move and escape the surface. Moreover, because the current simulations are large, an efficient way to calculate surface displacement is not a matter of luxury. The number of expensive computations required to reconstruct the deformed surfaces grows rapidly with the number of cycles and the crystal size, and it may become prohibitively difficult to handle in certain cases. To that end, the following procedure is used in order to minimize the number of surface roughness calculations. It is worth noting that the surface displacements are calculated only from dislocations that escape the crystal and not from the entire dislocation microstructure. This is an approximation that significantly reduces the computational load and has an insignificant effect on the predicted surface roughness since bulk dislocations induce a smoothly varying displacement fields on the surface of the crystal while the surface dislocations produce sharp steps which are more significant from the surface roughness' point of view.

For every interaction between a dislocation segment and the crystal surface, a surface event (SE) is created. A SE is a record for the dislocation-surface interaction (DSI) that stores the location of the interaction, its time, the Burgers vector, and the slip plane normal of the dislocation intersecting the surface. These SEs are then post-processed to reconstruct the DSI distribution and history. A DSI can take two forms. First, when a dislocation node that lies initially inside the simulation volume moves outside it in the next simulation time step, thus, the dislocation segments connected to it get split at the points of their intersection with the surface and a number of

SEs are created to record the lengths of the initial segments lost by splitting the segments. The lost segments are physically removed from the simulation to reduce the computational load, since no further interactions between them and the rest of the system. Second, when a surface node (representing the node at which a dislocation intersects the surface) moves on the surface, an SE is created to record the end points of the node's motion.

At the end of any one simulation, an enormous number of SEs get accumulated and a clever way of processing this amount of data is required. The first processing step is to filter out the SEs irrelevant to the time step at which the surface roughness is desired. Because the surface roughness is cumulative in nature, if the surface roughness is required at the time $t_o$, all the SEs that were created after $t_o$ are discarded and the processing works only for those with time stamps $t$ such that $t \leq t_o$. Because the evolution of surface reconstructions is required as well, a divide-and-conquer approach is followed where the SEs are grouped into time slices where all the SEs with $t_{i-1} < t \leq t_{i+1}$ are grouped into the $i^{th}$ SE time slice. This way the surface reconstruction at $t_o$ can be directly calculated as the sum of all the surface displacement fields at time slices before $t_o$. Another advantage of this approach is that the $O(n^2)$ reduction process, described next, operates on a smaller number of SEs which lowers the overall processing time.

In the reduction step, a certain time slice SEs are processed to reduce them to the minimum number of SEs that contain exactly the same amount of data. A common situation where reduction is possible is when there are two SEs that resulted from two successive displacements of a surface node, the first from point $A$ to $B$ and the second from point $B$ to $C$. Since the two SEs have the same Burgers vector and slip plane normal, a new SE describing the motion between points $A$ and $C$ can replace the two original SEs. The only piece of information that is lost is the time step of the SE which becomes the time step of the latter event. However, since the SEs are

reduced within the same time slice, no harm is done because the displacement field resulting from a time slice is approximately the one that is present at the end of the time slice. An even better situation exists when the two SEs move from $A$ to $B$ and from $B$ to $A$ respectively where the two SEs annihilate. Given the number of simulation steps and the oscillatory behavior of many of the surface nodes, the reduction process results in an average of 85% compression ratio for the SE data. Reduction however does work when SEs have different slip plane normals, Burgers vectors or are non-touching. Naively, the reduction is an $O(n^2)$ process where $n$ is the number of SEs in a time slice because every SE has to be checked against every other SE. However, an algorithm was developed that automatically breaks down the time slice SEs into smaller spatially localized SEs where reduction can operate on a smaller input size and then the algorithm recursively merges the subgroups and reduces them so that any further reductions are properly handled. Reduction stops when there is absolutely no further possible SE merging in the entire time slice SE group. It turns out that the reduction is not only important to reduce the computational load, it is also necessary for numerical accuracy so that the numerical error due to summing multiple displacement fields from tiny nodal vibrations does not build up as it has been shown to happen [179–181]. The SEs resulting from the reduction step are used in the surface displacement field calculations.

Besides the surface roughness calculations, some post-processing methods were employed in this work to quantify the degree to which the microstructure is patterned, quantify the dislocation microstructure cell sizes and quantify the surface roughness. In the following sections, these analysis methods will be presented.

### 4.3.1 Displacement Field Calculation

In the mathematical formulation of dislocations, a dislocation is defined as a curve bounding an open surface embedded in a crystal where the two sides of the surface

are relatively displaced by one Burgers vector [86]. This description has the advantage of defining exactly where the strain incompatibility due to a dislocation is. This definition however can be replaced by the simpler concept of a dislocation loop, which is the boundary of that surface. However, with this simpler representation, the information about the strain incompatibility is lost, because the surface bounded by the dislocation loop is not unique. While this does not affect the interactions between the dislocations and their evolution, it does affect the calculation of the displacement field of a dislocation loop. From isotropic elasticity, a closed form solution for the displacement field of a dislocation loop can be written in the form of a line integral over the dislocation loop [86]:

$$u_i = -\frac{b_i \Omega}{4\pi} + \frac{1}{8\pi} \oint_C \epsilon_{ikl} b_l r_{,pp} + \frac{1}{1-\nu} \epsilon_{kmn} b_n r_{,mi} dl_k \tag{4.3}$$

where $u_i$ is the $i^{th}$ displacement component, $\Omega$ is the solid angle subtended by the dislocation loop at the field point at which the displacement is to be calculated, $b$ is the dislocation's Burgers vector, $C$ is the dislocation loop curve, $\epsilon_{ijk}$ is the permutation symbol, $\nu$ is the material's Poisson's ratio and $r$ is the distance between a point on the dislocation curve and the field point of interest.

In most DDD simulation systems, especially in ParaDiS, the loops to which the dislocation segments belong are not explicitly stored. Moreover, an approximation that is common in the DDD community [20, 182, 183] is to model the dislocation networks as Frank-Read sources, especially when modeling high aspect ratio dislocation dipoles or dislocations that frequently undergo cross-slip. The end result is that the dislocation segments deposited on the surface are seldom part of a well defined dislocation loop in the simulation.

In order to compute the displacement fields for these dislocations, a virtual dislocation loop is created for each segment in question. As shown in Figure 4.5, for each surface dislocation segment ($AB$), an equivalent 5-segment loop ($OACDB$) is

generated. The generation begins by choosing an anchor point inside the simulation volume, which has to have a surface that is geometrically convex for this method to robustly work. This anchor point ($O$) can be chosen arbitrarily but in the current simulations, it is chosen to be the point of intersection of the segment's slip plane with the z-axis. The first segment in the five-segment loop is the segment ($OA$) connecting the anchor point to the starting point of the dislocation segment, and the last segment ($BO$) in the equivalent loop connects the end point of the dislocation segment back to the anchor point. A copy ($CD$) of the dislocation segment ($AB$) is created parallel to it on the same slip plane at a distance $d$ such that both vectors ($AC$) and ($BD$) are normal to the crystal surface and lie on the same slip plane. The remaining segments ($AC$), ($CD$) and ($DB$) are created accordingly. The distance $d$ determines the accuracy of the displacement calculation; the larger it is the more accurate the calculation will be as shown in [54].

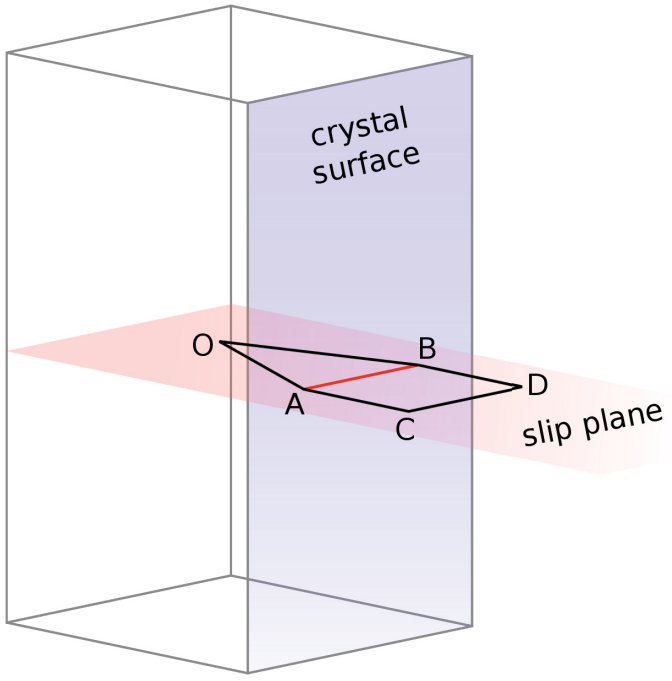


Figure 4.5: A sketch showing the original surface dislocation ($AB$) in red and the equivalent dislocation loop anchored at point O in black

The equivalent loop has an important property; it is planar and it lies on the slip plane of the dislocation segment. Consequently, when generating the equivalent loops for all the surface dislocation segments, the displacement fields from the segments $(OA)$ of one loop and $(BO)$ of the adjacent loop cancel out. A similar situation happens for the segments $(AC)$ and $(DB)$. Hence, the end result of the displacement calculation is the displacement due to the actual surface dislocations without any contribution from the added equivalent dislocation loop segments. This makes the process of calculating the displacement fields of planar and non-planar loops straightforward and no further special handling is required, unlike what has been previously proposed [184].

Another difficulty that arises in these calculations is computing the solid angle term. The solid angle term can be written as an equivalent closed loop integration [185]. This formulation uses an arbitrary vector which results in non-unique displacements in certain cases. The solid angle of a geometric object subtended at a point $P$ is defined as the area of the projection of the object on a unit sphere centered at $P$. This gives rise to an alternative approach in which the now planar dislocation loops are easily triangulated and the individual triangles are then projected on a unit sphere centered at the field point. The area of the projected triangles can be calculated and summed giving the exact value for the solid angle.

### 4.3.2 Dislocation Microstructure Metric

A simple and familiar metric for the evolution of the dislocation microstructure with time is the information theoretic entropy [186], also known as the Shannon entropy, of the dislocation density distribution. For a discrete non-negative distribution, $f_i$, that sums to unity, Shannon entropy is a positive real number defined as

$$S = -\Sigma_i^N f_i ln(f_i) \tag{4.4}$$

where $f_i$ is the value of the distribution at the $i^{th}$ point, and $N$ is the total number of points. Here, the simulation cell is uniformly meshed into $l \times m \times n$ elements and the total dislocation length inside each element is computed from the dislocation microstructure in that element. The distribution $f_i$ is then defined at the center of each element, and the entropy can be calculated using Equation (4.4). Before calculating the entropy, the values of the distribution $f_i$ are normalized by the total dislocation length so that $\Sigma_i^N f_i = 1$.

From Equation (4.4), it can be shown that the entropy of a uniform distribution is maximum, while that of a singleton is zero. In terms of dislocation distributions, a crystal with all dislocations concentrated at a single point will have a zero entropy, while that where the dislocations are uniformly distributed will have a maximum entropy, which in this case will equal $S_{max} = \ln(l \times m \times n)$. The simulations start with a number of Frank-Read sources, which mimic the case of a singleton, although not perfectly, and it evolves over time into bigger regions that have a uniform dislocation density. By calculating the relative entropy, defined to be the ratio of the dislocation density distribution entropy to the maximum possible entropy, it is possible to measure how far the system has evolved in terms of forming dislocation structures. Simulations which show no relative entropy change maintain their initial configuration of random dislocation distributions, while those that show an increase in their relative entropy develop dislocation structures.

### 4.3.3 Quantifying the Dislocation Microstructure Size

As will be discussed in Section 4.6, in the current simulations dislocation cell-like structures evolve and it is important to quantify their average size. Since these cells are not geometrically ideal, a simple method, such as fitting ellipsoids to the low dislocation density cell interior, will be sensitive to the irregularities of the dislocation structure and is not expected to give good accuracy.

Alternatively, the method used here builds on the work of Zaiser et. al. [187], which was based on image analysis of 2D transmission electron microscopy (TEM) micrographs of dislocation cell structures to estimate a number of fractal dimensions, and subsequently quantify dislocation cell sizes. In the 3D setting of DDD, at any particular time the simulation cell is meshed into elements and the dislocation density is calculated in each element. All elements with a dislocation density less than a threshold value of $\rho_{th} = 10^{14}$ m$^{-2}$ are neglected. Subsequently, the remaining elements, that correspond to the interior of a dislocation wall are represented as a number of points, $p_i$, and their distribution gives the general shape of the dislocation walls. A box-counting procedure is performed over the points $p_i$. The simulation cell is then divided one more time into cubes $c_i$ of edge length $\epsilon$. The total number of points, $p_i$, that are contained within each cube are added and then the number of cubes, $n$, that have at least one point is recorded. The process is repeated for cubes of different edge lengths, $\epsilon$, to get the final distribution $n(\epsilon)$. A 2D schematic representation of the cube counting process is shown in Figure 4.6(a).

The distribution, $n(\epsilon)$, is then used to estimate the dislocation cell size, $\epsilon_c$, and dislocation wall thickness, $\epsilon_w$ [187]. By plotting $n(\epsilon)$ versus $\epsilon$, the distribution is usually constant at low and high $\epsilon$ values and decreases for intermediate values of $\epsilon$, as shown in Figure 4.6(b). For small values of $\epsilon$, increasing $\epsilon$ does not result in a significant change in $n(\epsilon)$ because the cube edge length is not yet equal to the dislocation wall thickness. When $\epsilon$ is equal to the dislocation wall thickness, $\epsilon_w$, there is one cube that spans the entire wall thickness. Any further increase in the cube's edge length will cause the cubes at the cell corners to cover more dislocation wall regions, which consequently reduces the number of the cubes needed to cover the entire dislocation wall (i.e. $\epsilon > \epsilon_w$, $n(\epsilon)$ decreases). As $\epsilon$ is increased further, each cube covers increasingly growing regions of the dislocation wall structure and fewer cubes are needed, which maintains the decreasing monotonicity of $n(\epsilon)$. When $\epsilon$

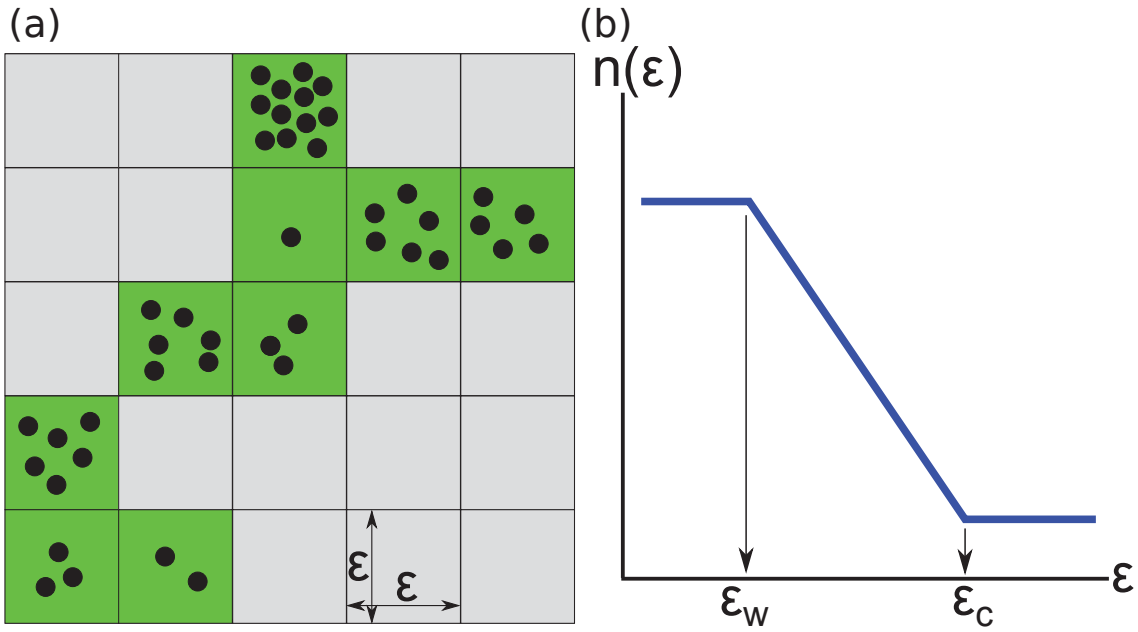


Figure 4.6: (a) A 2D schematic of the box-counting process. The black circles are the centers of the cells having a dislocation density higher than the threshold dislocation density. The squares (cubes in 3D) are equal in size with a side length $\epsilon$. The green squares contain at least one high dislocation density point. In this example $n(\epsilon) = 9$. (b) A typical plot of $n(\epsilon)$ versus $\epsilon$ showing the transitions at which the wall thickness, $\epsilon_w$, and the cell size, $\epsilon_c$, can be quantified.

becomes large enough that one cube spans an entire dislocation cell, (i.e. $\epsilon = \epsilon_c$), any further increase in $\epsilon$ will not result in any change in $n(\epsilon)$, since each cube now covers about one dislocation cell and its surrounding dislocation walls. The dislocation wall thickness and dislocation cell size determined by this method are approximate values and they are sensitive to several factors such as the threshold dislocation density and how uniform the dislocation structure is. Nevertheless, this gives a first order approximation for the characteristic length scales of the dislocation microstructure.

### 4.3.4 Surface Roughness Quantification

The surface roughness is typically quantified using displacement amplitude features such as the maximum peak height, the minimum peak depth and the first few statistical moments of the amplitude distributions [188]. These parameters are suitable for

correlating surface roughness to crack nucleation and failure events [140]. However, in order to correlate the surface roughness to the dislocation microstructure activity and be able to compare the roughness on different surfaces, a roughness measure that takes into account the displacement amplitudes as well as their spatial distribution is required since the dislocation distribution inside the crystal is usually heterogeneous which makes the distribution of the dislocation surface escape events spatially non-uniform.

One of these measures is the Hausdorff dimension [189, 190] which ranges between 2 for perfectly smooth surfaces and 3 for infinitely rough surfaces. To calculate the Hausdorff dimension, the undeformed surface is uniformly discretized into square cells of size length $\epsilon$ and the surface displacement field is interpolated at the corners of these cells to get the deformed cell geometry. The areas of the deformed cells are then summed up to get an approximation for total surface area of the deformed surface $A$. This approximation becomes more accurate as $\epsilon$ decreases. Several values of $\epsilon$ are used and the approximate area is obtained for each value and then the $\epsilon - A$ pairs are fit into a power law of the form

$$A(\epsilon) = A_o \epsilon^{2-D} \tag{4.5}$$

where $A_o$ is the area of the undeformed surface and $D$ is the Hausdorff dimension.

Hausdorff dimension can be directly related to slope of the power spectral density (PSD) distribution curve [191, 192] which can also be used as a roughness measure itself. The PSD distribution gives the power in the normal displacement signal as a function of the normal displacement wavelength (or frequency). The surface roughness increases when higher powers are associated with higher frequencies and vice versa. The advantage of using the Hausdorff dimension over the PSD is that the Hausdorff dimension is a single scalar that quantifies the roughness distribution over the surface while the PSD is a one dimensional distribution.

## 4.4 Numerical Simulations

In the current simulations, the cyclic loading response of pure single crystal nickel (Young's modulus $E = 210$ GPa and Poisson's ratio $\nu = 0.31$) during the early stages of loading as well as after developing PSBs are investigated. In all simulations, fully reversed loading at a constant strain rate of 200 $\text{sec}^{-1}$ and a total strain amplitude of 0.4% is imposed. All cross-slip types are allowed in all of the simulations.

In the early fatigue simulations, the simulations cells are cubic crystals having side length ranging from 0.5 μm to 7.5 μm, and the initial dislocation density is varied in the range of $10^{11}$ $\text{m}^{-2}$ to $10^{14}$ $\text{m}^{-2}$. The load is applied in the multislip crystallographic [001] direction. The dislocations are allowed to escape from all six surfaces of the simulation cell mimicking the experimental case of a single crystal axially loaded with soft grips at both ends to avoid any external influences on dislocation activities. The initial dislocation microstructure consists of Frank-Read sources randomly distributed over the twelve FCC slip systems with uniform probability. The lengths of the sources are normally distributed with a mean that is 60% of the simulation cell side length and a standard deviation of 20% of the mean for all crystal sizes and initial dislocation densities. The system is loaded for a number of cycles that depends on the computational load with the less computationally expensive simulations (smaller crystals and low initial dislocation densities) loaded up to eighty cycles, while the more computationally expensive ones loaded up to two cycles. The effect of the image forces in these simulations is neglected since they do not have a significant effect on the results as was reported previously [93].

In the simulations having well developed PSBs, the simulation cell size is 2 μm $\times$2.2 μm $\times$3 μm with periodic boundary conditions imposed in all three-directions. The PSB is introduced in the middle of the simulation cell, thus these simulations mimic the case of an array of parallel PSBs. The purpose of these simulations is to investigate how the dislocations move and interact within PSBs and to study the

generation of vacancies due to dislocation annihilation. The PSB is composed of parallel edge dislocation dipolar walls, with the wall normal in the burgers vector direction. The height of the walls is 1 μm, the wall thickness is 0.1 μm, and the channel spacing is 1 μm. Due to the imposed PBCs, the spacing between parallel PSBs is 1 μm from each other. The PSB walls consist of edge dipoles with a dislocation density of $1.5 \times 10^{15}$ m$^{-2}$ and Burgers vector $[10\bar{1}]$ while the channels consist mainly of screw dislocations spanning the channel between the walls with a dislocation density of $3 \times 10^{13}$ m$^{-2}$. The plane of the walls is normal to the $[1\bar{2}1]$ direction and all the dislocations glide on the $\{111\}$ plane. A typical initial PSB microstructure is shown in Figure 4.7. The simulations are for one full loading cycle, which mimics experiments of a one half cycle or one full cycle of a crystal containing well developed PSBs [157]. Although dislocation climb is not explicitly allowed in these simulations, dislocation annihilation through climb is modeled in these simulations such that any two dislocations gliding on parallel slip planes, aligned in the same direction, with a tolerance angle of $15^o$ and having opposite Burgers vectors can annihilate if the spacing between the glide planes is less than 6 A, which lies in the range of annihilation distances predicted from experiments [193] and atomistic simulations [194].

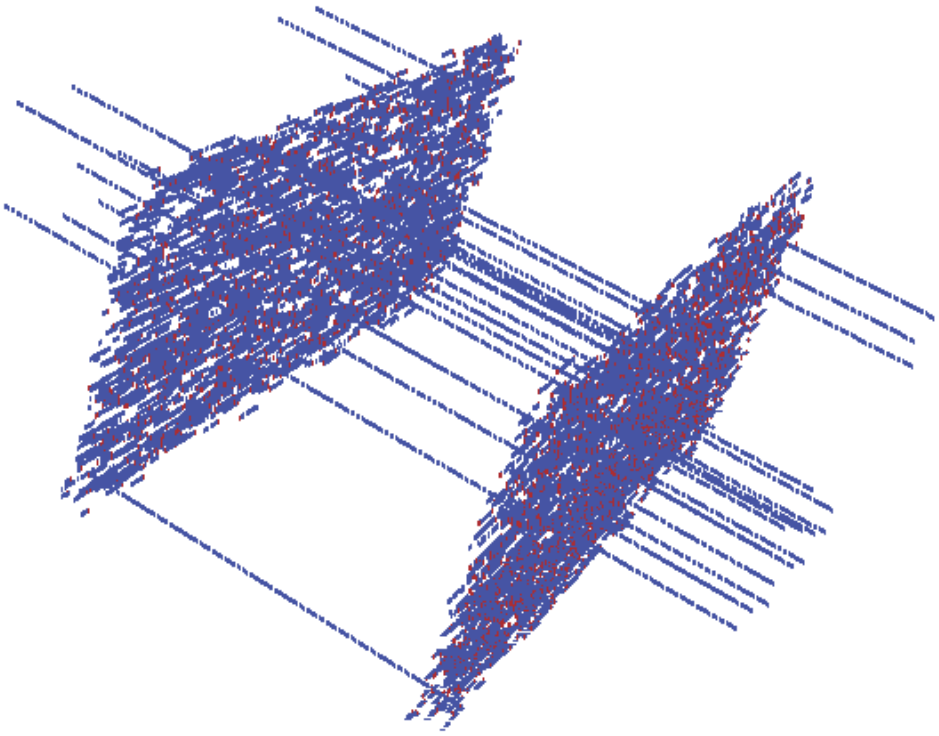

Figure 4.7: A typical initial PSB structure. Two PSB walls can be seen with screw dislocations running between them in the channels. The input is periodic in all three directions which simulates the case of a infinite number of parallel spaced out PSBs of an infinite width and number of walls.

## 4.5 Mechanical Behavior and Microstructure Evolution During the Early Stages of Cyclic Loading

## 4.6 Results

The engineering stress versus engineering strain curves under cyclic loading are shown in Figure 4.8 from representative simulations having different crystal sizes and initial dislocation densities. For smaller crystal sizes, the overall strength is higher and it decreases as the crystal size increases. The successive drops in the stress after yield correspond to plastic strain bursts, which are less pronounced at higher dislocation

densities or larger crystal sizes. At lower dislocation densities and smaller crystal sizes, a larger scatter in the flow stress is observed from one loading cycle to another, and this scatter decreases with increasing dislocation density. Furthermore, for the smallest crystals having size $D = 0.5$ μm and initial dislocation density of $\rho_o = 10^{14}$ $m^{-2}$ display no sharp yield points, and the stress-strain curve transitions smoothly in a nonlinear manner from elastic loading to plastic flow. This is due to plastic activity initiating early, leading to continuous softening. This is also observed for the $D = 2.0$ μm crystals having an initial dislocation density of $\rho_o = 10^{13}$ $m^{-2}$.

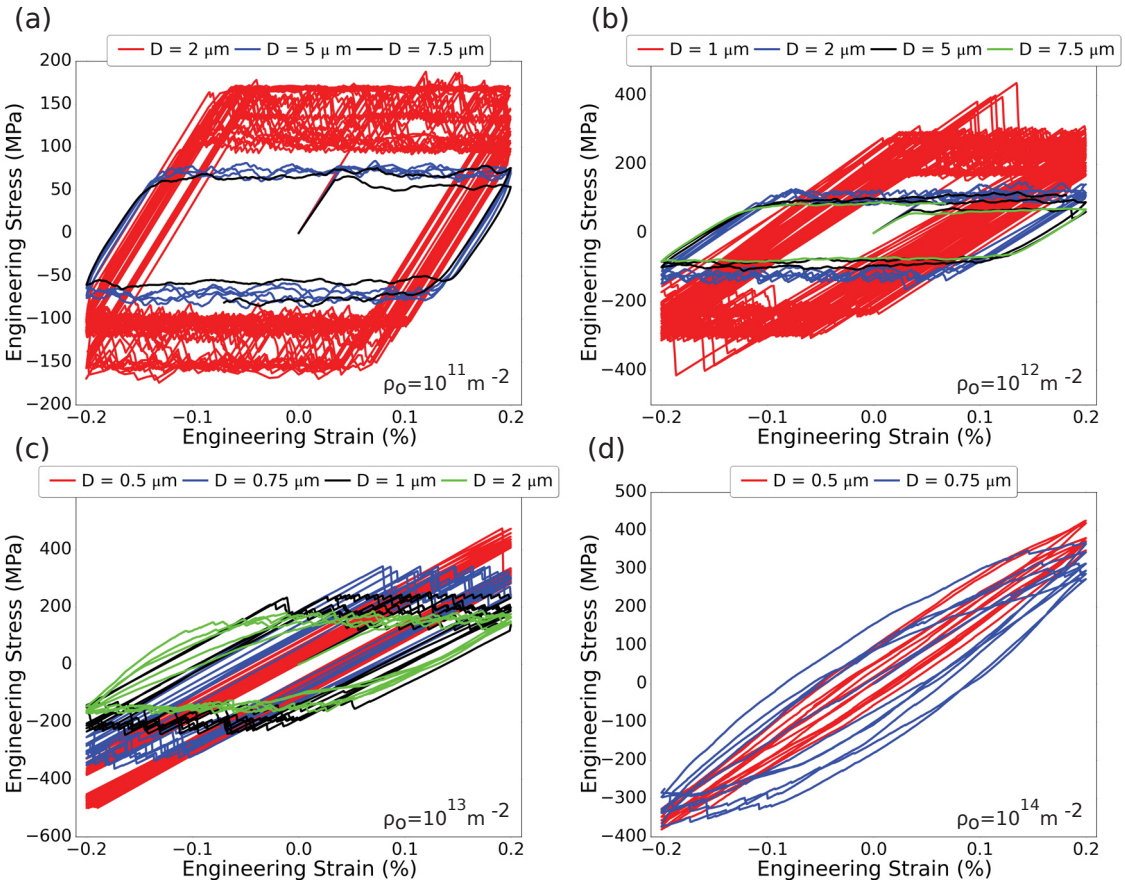


Figure 4.8: The engineering stress-strain curves from representative simulations having different crystal sizes and grouped by the initial dislocation density: (a) $\rho_o = 10^{11}$ $m^{-2}$; (b) $\rho_o = 10^{12}$ $m^{-2}$; (c) $\rho_o = 10^{13}$ $m^{-2}$; and (d) $\rho_o = 10^{14}$ $m^{-2}$.

Figure 4.9 shows the crystal strength and dislocation density versus simulation time from representative simulations of each crystal size, all having an initial dislo-

cation density of $\rho_0 = 1 \times 10^{12}$ m$^{-2}$. Three observations can be made here. First, the strength decreases with increasing crystal size. Second, for the number of cycles simulated, the dislocation density in the crystals having sizes $D \leq 1.0$ μm remains constant even with increasing number of cycles. The almost regular spikes in the dislocation density evolution, which coincide with the stress drops, correspond to the activation of one, or at most a few, dislocation sources and their subsequent escape from the crystal surface. On the other hand, the density multiplies significantly faster in crystals having sizes $D \geq 2.0$ μm, even after just a few cycles. These results indicate that the dislocation density multiplication factor is size dependent, with the dislocation density multiplication increasing with increasing crystal size. Finally, strong cyclic hardening is also observed in crystals having sizes $D \geq 5.0$ μm, and almost none are observed for smaller crystals for the number of cycles simulated.

In addition to the effect of the crystal size, the initial dislocation density plays an important role in controlling both the overall response as well as the evolution of the dislocation microstructure. Figure 4.10 shows representative engineering stress and dislocation density curves as a function of the simulation time for two different crystal sizes starting with three initial dislocation densities each. In both crystal sizes, the overall strength decreases with increasing initial dislocation density, which agrees with the predictions of the generalized size-dependent Taylor-strengthening law [131]. It is also observed that for $D = 0.75$ μm, the dislocation density does not change much, for the number of cycles simulated, irrespective of the initial dislocation density. This indicates that the dislocation multiplication and escape rates are equal in smaller crystals. For the $D = 2.0$ μm, the dislocation density is observed to significantly increase for simulations with higher initial dislocation densities, while it remains mostly constant for simulations with lower initial dislocation densities.

The initial and final dislocation microstructures for crystals of different sizes and an initial dislocation density of $\rho_o = 10^{12}$ m$^{-2}$ are shown in Figure 4.11. Further-

more, the evolution of the dislocation microstructure in a $D = 2.0$ μm having an initial dislocation density of $\rho_o = 10^{13}$ m$^{-2}$, is shown in supplementary movie I, while the 3D view of the dislocation microstructure in a $D = 5.0$ μm crystal having an initial dislocation density of $\rho_o = 10^{12}$ m$^{-2}$ is shown in supplementary movie II. Smaller crystals having $D < 2.0$ μm do not exhibit any microstructure buildup, even after 80 cycles, and the final microstructure has the same random distribution features as the initial microstructure. Larger crystals having $D \geq 5.0$ μm, however, show the formation of regions of high dislocation densities surrounding regions of low dislocation densities, starting after only two cycles. These emerging dislocation microstructures resemble the experimentally observed dislocation cells with dislocation dense walls and less dislocation dense interiors [195, 196]. The high dislocation density regions are dominated by immobile dislocations, which act as forest dislocations that pin mobile dislocations. It is also observed that many dislocations in the wall regions originate from the multiplication of a few sources from the initial dislocation network due to successive intersection cross-slip events. The high local stresses resulting from the high dislocation densities around the walls reduces the activation barrier for cross-slip further, which subsequently leads to increasing the dislocation wall's local dislocation density.

Figure 4.12 shows the initial and final microstructure for $D = 2$ μm crystals having different initial dislocation densities. For low initial dislocation densities ($\rho_o \leq 10^{11}$ m$^{-2}$), no dislocation buildup is observed. As the initial dislocation density increases, dislocations start to form dislocation rich regions through dislocation pinning and multiplication. These dislocation rich regions, however, do not have the same geometric features as dislocation cell structures.

It is clear from Figures 4.11 and 4.12 that both the crystal size and the initial dislocation density play an important role in the subsequent evolution of the dislocation microstructure. For the same initial dislocation density, simulations of smaller

crystals show no dislocation cell structure formation, while clear dislocation cell structures are observed for simulations of larger crystals. On the other hand, for the same crystal size, simulations with low initial dislocation densities show negligible dislocation cell structure formation even after 80 loading cycles, while simulations with higher initial dislocation densities show the formation of dislocation cell structures even after a few cycles. Nevertheless, it could be expected that a similar dislocation buildup would take place for smaller crystals with higher initial dislocation density, or larger crystals with lower initial dislocation densities, after a considerably larger number of cycles. This is however not attainable in the current simulations since the number of degrees of freedom involved makes simulations of higher number of cycles unachievable with the currently available computational power.

The dislocation density relative entropy (DDRE) versus time for crystals of different sizes an initial dislocation densities is shown in Figure 4.13. Larger crystals having $D \geq 5$ μm and a low initial dislocation density of $\rho_o = 10^{11}$ m$^{-2}$ show a continuous increase in DDRE, indicating the formation of a dislocation cell structure. This is opposed to smaller crystals having sizes $D \leq 2.0$ μm and the same initial dislocation density, even though they are simulated for a higher number of cycles. For simulations with a higher initial dislocation density of $\rho_o = 10^{12}$ m$^{-2}$, the larger crystals, having sizes $D \geq 5.0$ μm show an earlier increase in DDRE, which indicates that dislocation cell structure formation starts even sooner. In addition, crystals having sizes $D = 2.0$ μm and the same initial dislocation density show an increase in DDRE and dislocation cell structure buildup only after a larger number of cycles. However, smaller crystals having sizes $D < 2.0$ μm and this same initial dislocation density do not show any dislocation cell structure formation and the DDRE oscillates around a low value even for a higher number of cycles. For simulations with an initial dislocation density of $\rho_o = 10^{13}$ m$^{-2}$, crystals having sizes as small as $D = 1.0$ μm show some slow DDRE increase, which indicates that a more pronounceable dislo-

cation cell structure formation might develop if the simulations are continued for a higher number of cycles. In addition, crystals having size $D = 2$ μm now show a significant DDRE increase and a corresponding dislocation cell structure formation much earlier in the simulations. Finally, for simulations with an initial dislocation density of $\rho_o = 10^{14}$ m$^{-2}$, no dislocation cell structure formation or increase in DDRE are observed for simulated crystals having $D < 1.0$ μm up to the number of simulated cycles. However, at this high density, the DDRE oscillates in a manner similar to the oscillations observed for larger crystals at lower densities before they showed any dislocation cell structure formation (e.g. $D \leq 2.0$ μm and $\rho_o < 10^{12}$ m$^{-2}$), which suggests that dislocation cell structure formation could take place if these crystals were simulated for a higher number of cycles or if the initial dislocation density was higher. These observations suggest the existence of a size-dependent critical dislocation density beyond which dislocation cell structure formation takes place. It also should be noted that the monotonic increase in the DDRE observed for simulations of larger crystals indicates that the load reversal does not break the dislocation cell structures that have formed.

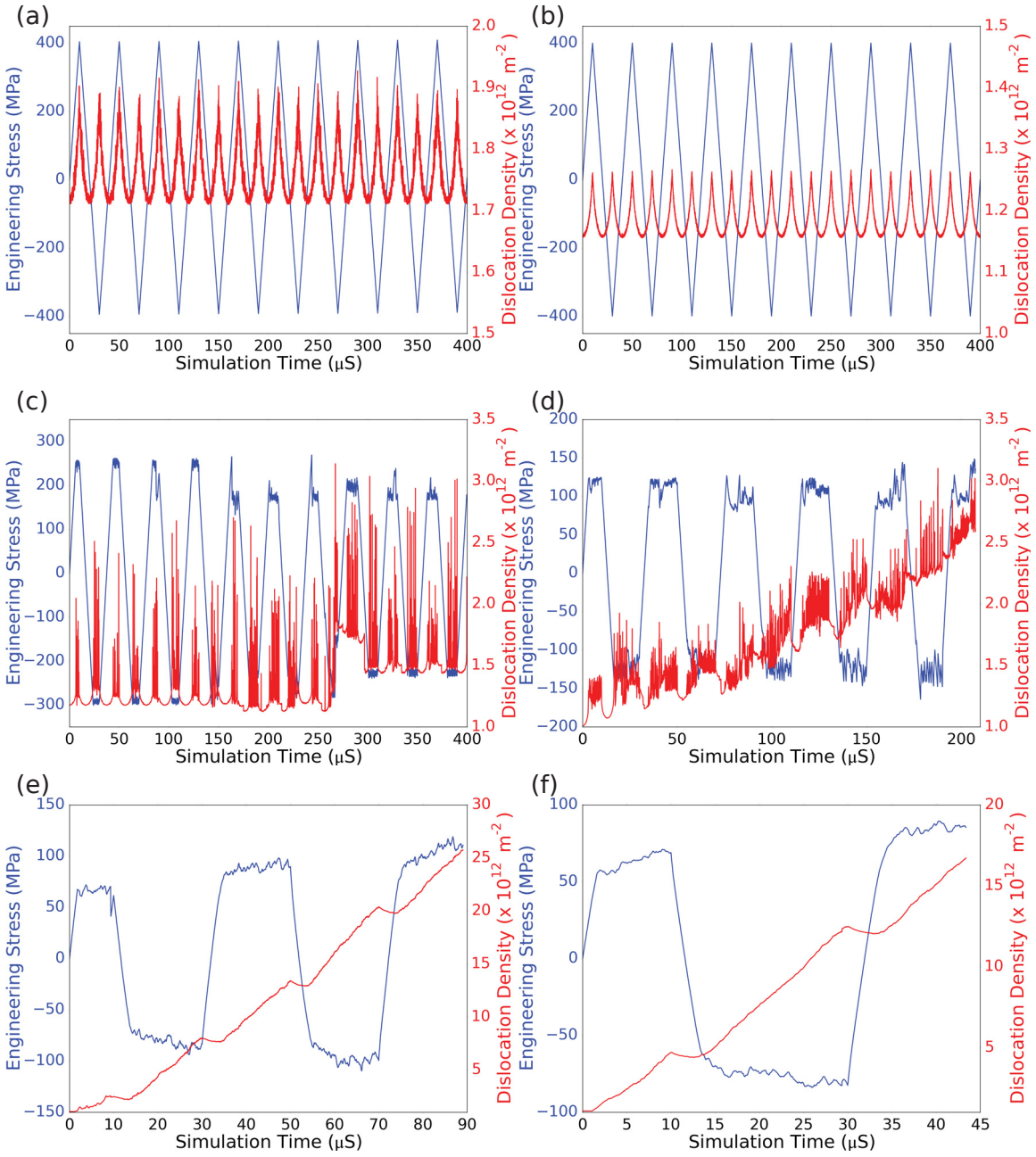


Figure 4.9: The engineering stress and dislocation density as a function of simulation time for simulations with an initial dislocation density of $\rho_o = 10^{12}$ m$^{-2}$ and crystal sizes: (a) 0.5 μm; (b) 0.75 μm; (c) 1.0 μm; (d) 2.0 μm; (e) 5.0 μm; and (f) 7.5 μm.

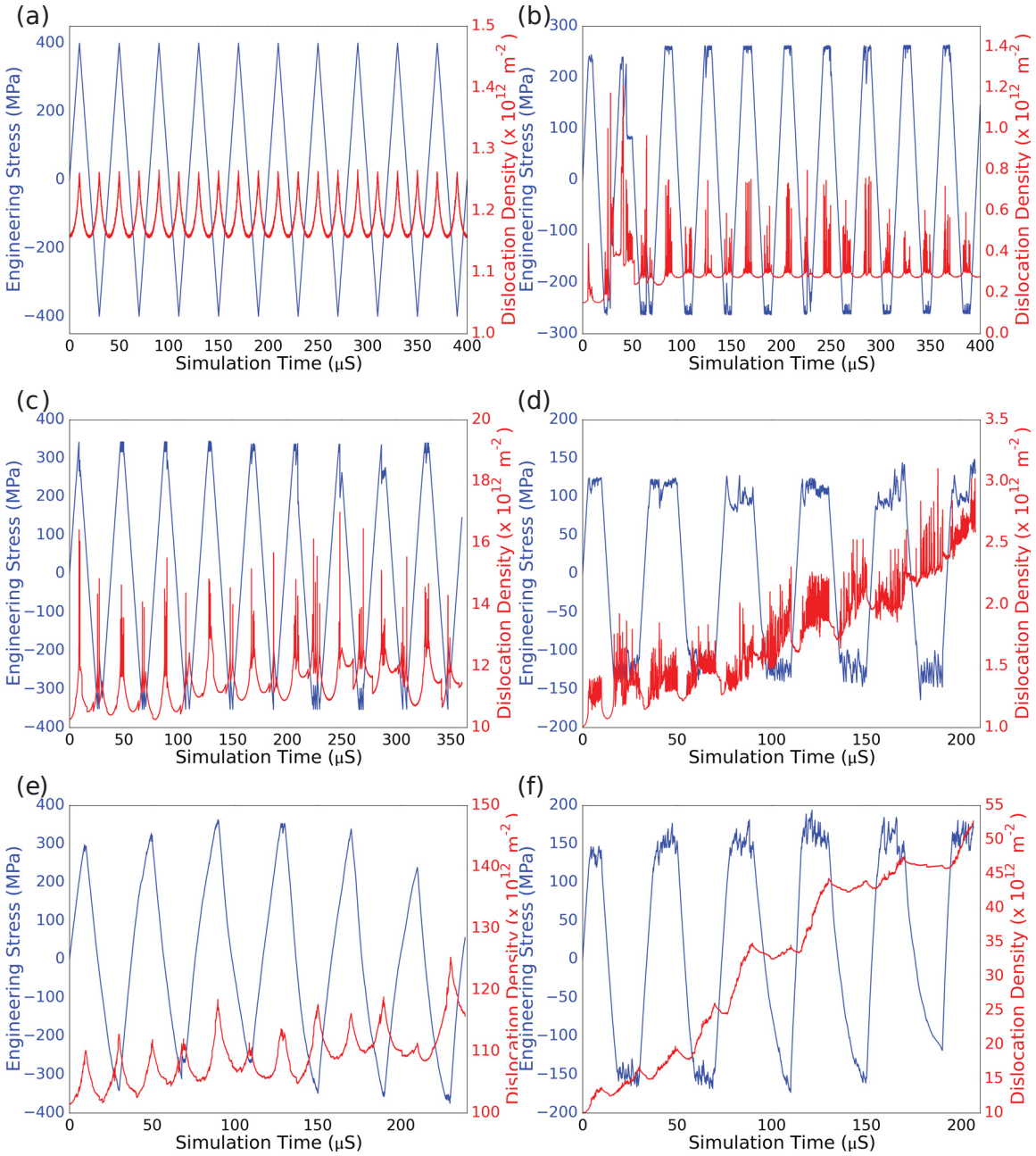


Figure 4.10: The engineering stress and dislocation density as a function of simulation time for crystals having size $D = 07.5$ μm and: (a) $\rho_o = 10^{12}$ m$^{-2}$, (b) $\rho_o = 10^{13}$ m$^{-2}$, (c) $\rho_o = 10^{14}$ m$^{-2}$; and crystals having size $D = 2$ μm and: (d) $\rho_o = 10^{11}$ m$^{-2}$, (e) $\rho_o = 10^{12}$ m$^{-2}$ and (f) $\rho_o = 10^{13}$ m$^{-2}$.

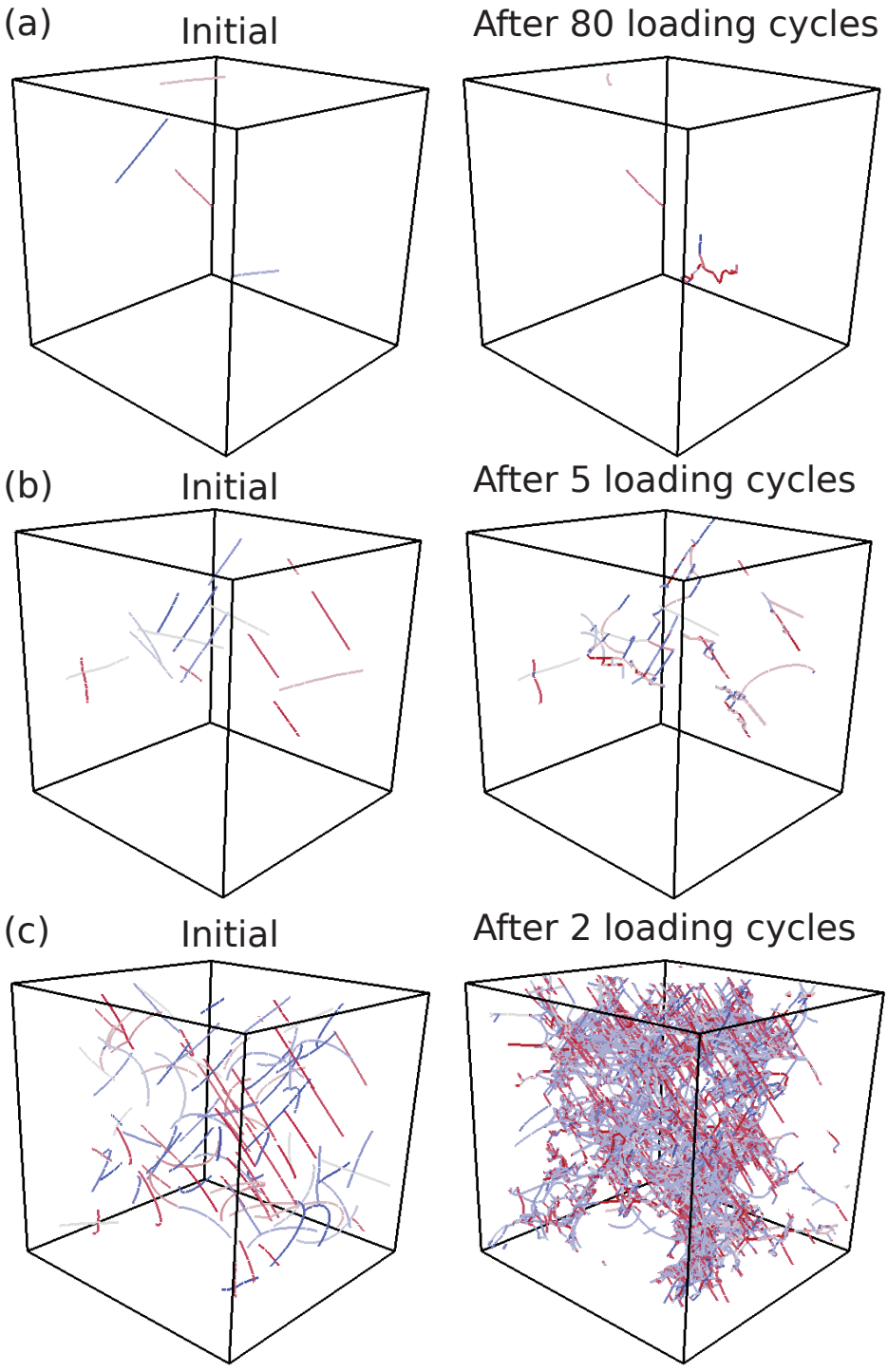


Figure 4.11: The initial and final dislocation microstructures for simulations having an initial dislocation density of $\rho_o = 10^{12}$ m$^{-2}$ and sizes: (a) $D = 1.0$ μm; (b) $D = 2.0$ μm; and (c) $D = 5.0$ μm.

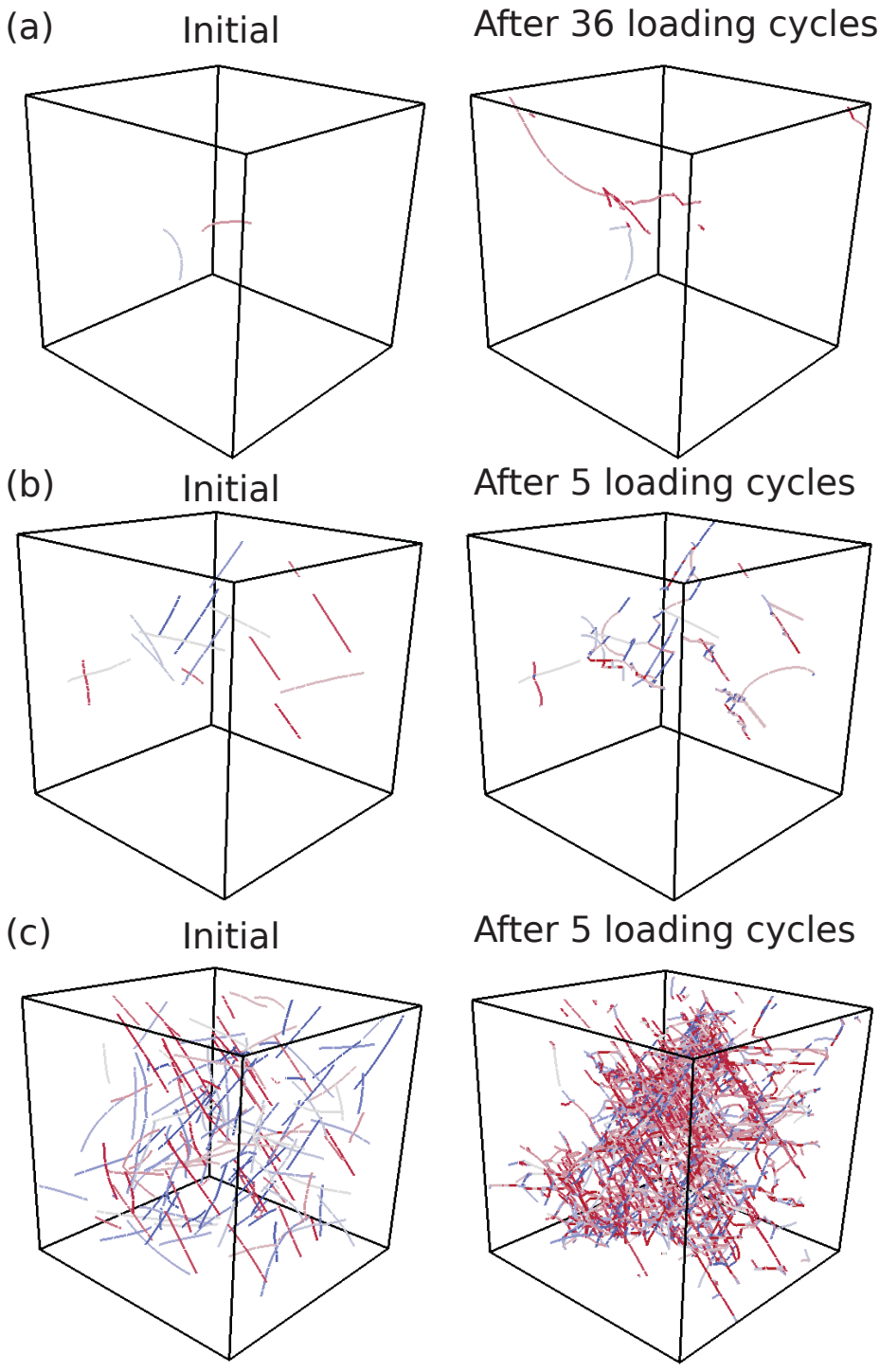


Figure 4.12: The initial and final dislocation microstructures for simulations of crystals having sizes $D = 2.0$ μm and: (a) $\rho_o = 10^{11}$ m$^{-2}$; (b) $\rho_o = 10^{12}$ m$^{-2}$; and (c) $\rho_o = 10^{13}$ m$^{-2}$.

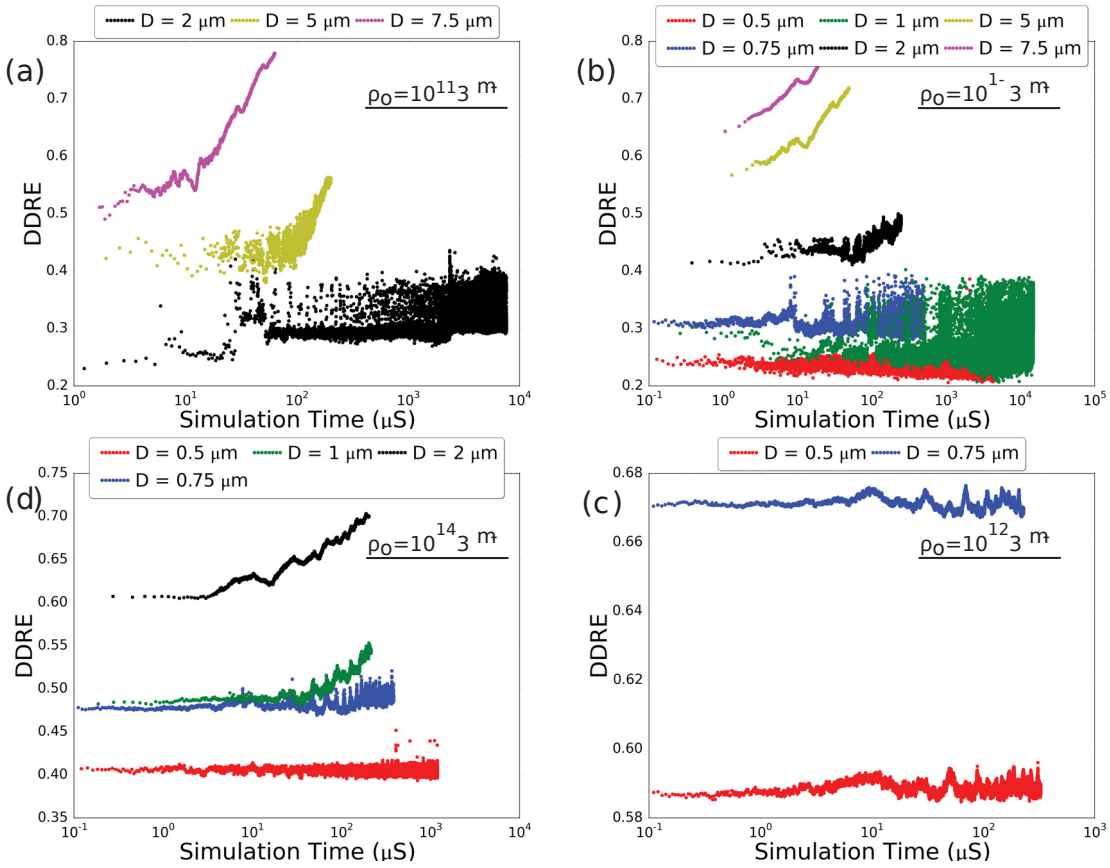


Figure 4.13: The dislocation density relative entropy (DDRE) versus simulation time for different crystal sizes and: (a) $\rho_o = 10^{11}$ m$^{-2}$; (b) $\rho_o = 10^{12}$ m$^{-2}$; (c) $\rho_o = 10^{13}$ m$^{-2}$; and (d) $\rho_o = 10^{14}$ m$^{-2}$.

## 4.7 Discussion

### 4.7.1 Dislocation Density Evolution

Figure 4.14(a) shows the ratio of the dislocation density at the end of each cycle to the initial dislocation density versus the number of loading cycles for different crystal sizes and initial dislocation densities. Each data point is an average of three different simulations with varying initial random dislocation distributions. It is observed that larger crystals show a high rate of dislocation density multiplication, which is a direct result of significant dislocation cross-slip events, and in particular intersection cross-slip at the collision points of dislocations on non-parallel planes, as shown in Figure 4.14(b). Dislocations glide, collide, then cross-slip in a repeated manner, which leads to storing more dislocations within the crystal rather than their escape. The dislocation density multiplication can reach up to 75 times after only two loading cycles for the larger crystals. This is the main reason these simulations are computationally challenging to run for a larger number of loading cycles. The increase in the number of degrees of freedom over time makes the simulation computationally demanding and it becomes impractical to continue the simulations further.

A similar mechanism was suggested by Déprés et. al. [172] to explain the formation of dislocation microstructures, however, they had only accounted for the traditional bulk cross-slip mechanism. In an earlier study, the current authors showed that the number of new dislocation sources generated during monotonic loading due to intersection cross-slip increases considerably with increasing crystal size [65]. On the other hand, when bulk cross-slip is only accounted for the dislocation multiplication is significantly slower and no considerable dislocation buildup is expected during early stages of the deformation. This latter case is in contradiction with experimental observations showing dislocation cell structure formation starting even at low strain levels [60–62].

The dislocation density evolution per slip system versus time is shown in Figure 4.15 for some representative simulations. As shown in Figure 4.15(a), in smaller crystals having $D \leq 2.0$ μm, the dislocation density remains relatively constant, with some fluctuations on all slip systems. This is typical for all crystals in Figure 4.14(a) that show little or no density multiplication. When significant dislocation density multiplication is observed (i.e. for larger crystals or higher initial dislocation densities), two dislocation density evolution trends can be identified. In particular, one pair (Figure 4.15(c)), or multiple pairs (Figure 4.15(b) and (d)) of slip systems show a significant density increase, while other slip systems show negligible dislocation density buildup. The slip systems of each pair share a common Burgers vector, which indicate that the increase in dislocation density on these slip systems is due to continuous cross-slip of dislocations back and forth from one slip plane to the other. The number of slip system pairs that are active depends on the number of sources that have the potential to multiply and cross-slip. This number increases with increasing crystal size and/or the initial dislocation density. Hence, for larger crystals (Figure 4.15(d)) or crystals with a higher initial dislocation density (Figure 4.15(b)), multiple pairs activate, in contrast with lower initial dislocation density crystals (Figure 4.15(c)) where only one pair is active. Smaller crystals (Figure 4.15(a)) do not show such a behavior because dislocations can escape from the crystal surface shortly after becoming active and before getting a chance to be engaged in any intersection cross-slip activity.

### 4.7.2 Flow Strength and Cyclic Hardening

Early cyclic strain hardening has been experimentally studied in pure copper and nickel [153, 197, 198]. Morrison et. al. [198] observed that cyclic hardening rates are higher for crystals oriented for multislip due to the interactions of dislocations on different slip systems. They also showed that the buildup of dislocation microstructures,

particularly dislocation cell structures, goes hand in hand with cyclic hardening. In the current DDD simulations, larger crystals showed early cyclic hardening, which is attributed to the buildup of large immobile dislocation assemblies as discussed in Section 4.7.3. These dislocation walls reduce the mean free path of mobile dislocations in the crystal. The relative strength at the end of different loading cycles to the strength at the end of the first quarter cycle for all the simulated cases is shown in Figure 4.14(c). Each data point is the average of three simulations with the same configuration but different random initial dislocation distributions. Smaller crystals that do not form any dislocation cell structures do not show any cyclic hardening even up to 80 cycles. On the other hand, larger crystals that show the development of dislocation cell structures show up to 40% increase in the yield strength after only two loading cycles. Experimental observations of copper single crystals fatigued in a multislip orientation suggest that cross-slip may play an important role in early cyclic hardening [199]. Those experimental suggestions along with the results in Figure 4.14(b), which indicate that cross-slip is frequent in larger crystals that show cyclic hardening, show the agreement between the current DDD simulations and the experimental observations when it comes to predicting cyclic hardening response.

On the other hand, recent DDD simulations of size effects during monotonic loading of microcrystals [131] have lead to the development of a generalized Taylor-law, which takes into account the effects of crystal size and initial dislocation density on its strength, such that

$$\frac{\tau}{\mu} = \frac{\beta}{D\sqrt{\rho}} + \alpha b\sqrt{\rho} \tag{4.6}$$

where $\tau$ is the crystal strength, $b$ is the Burgers vector magnitude, and $\alpha = 0.57$ and $\beta = 1.76 \times 10^{-3}$ are two dimensionless constants [131]. Figure 4.16 shows $\frac{\tau}{\mu}\sqrt{D}$ versus $D\rho$ from all the simulations at the end of each quarter cycle, as well as the predictions from Equation (4.6) for comparison. While, as expected, there is a high scatter in the

simulation results, the simulations agree on average with the predictions of Equation (4.6). The predictions from Equation (4.6) are slightly lower than the simulation data, which is mainly because the constants $\alpha$ and $\beta$ in [131] were computed based on the initial dislocation density, while the simulation results in Figure 4.16 are the instantaneous strength and dislocation density at the end of each quarter cycle. For larger crystal sizes or higher initial dislocation densities, the slope of the simulation data in Figure 4.16 agrees well with the slope predicted from Equation (4.6) for the same range of $\rho D$. For smaller crystals or at low initial dislocation densities, the simulation data mostly oscillates around a constant value since no dislocation multiplication or cyclic hardening is observed. These results show the correlation between the flow strength, cyclic hardening, and the dislocation density evolution.

### 4.7.3 Microstructure Evolution

As discussed earlier, an interesting observation from the current simulations is the formation of dislocation cell structures in larger crystals. These dislocation cell structures have been previously observed experimentally in larger crystals [59] and at low strains [60–62]. Furthermore, recent continuum dislocation dynamics studies have also shown the emergence of self organized cell like dislocation structures [17]. The current simulations show that the dislocation density buildup is irreversible. This is also clear from the relative entropy plots shown in Figure 4.13, where the relative entropy is monotonically increasing. One measure for the strength of a dislocation network is the number of pinning points present in the system at any instance of time. Here, a pinning point is a dislocation node that is connected to at least three dislocation segments that lie on three different slip planes. This point is effectively incapable of moving due to the glide constraints associated with its dislocation arms. Figure 4.14(d) shows the number of pinning points versus the number of cycles for the first few cycles of different crystal sizes and initial dislocation densities. It can

be observed that larger crystals develop a significant number of pinning points even after a few cycles, while smaller crystals, especially at lower densities, do not, even after 80 cycles.

The mechanisms discussed in Section 4.7.1, by which the dislocation density increases in larger crystals, partially explain the significant increase in the number of pinning points in larger crystals. As dislocations collide, they form pinning points, become less mobile and act as barriers for subsequent dislocation activity. In addition, intersection cross-slip, which takes place when a screw dislocation collides with a forest dislocation, becomes more frequent [26, 27, 65]. Intersection cross-slip requires less activation energy and it is more likely to take place than bulk cross-slip, which requires a high activation energy [65]. Cross-slip changes the glide plane of dislocations making them subject to further collisions with less mobile dislocations threading different glide planes, which subsequently results in further cross-slip and pinning point creation. Cross-slip, which is a thermally activated and a stress assisted process, is further promoted by the high local stresses in high dislocation density regions. By comparing Figures 4.14(b) and 4.14(d), there is an obvious one-to-one correlation between the number of pinning points and the number of cross-slip events.

Finally, the cell size quantification method discussed in Section 4.3.3 is utilized to analyze the dislocation cell structures emerging in the current DDD simulations. Figure 4.17 shows the box-count plots for crystals of different sizes, initial dislocation densities and number of cycles from a representative number of simulations that showed dislocation cell structure formation. The dislocation cell wall thicknesses are 0.03 μm, 0.1 μm, and 0.15 μm, while the dislocation cell sizes are 0.6 μm, 1.6 μm, and 2.5 μm, for the 2.0 μm, 5.0 μm, and 7.5 μm crystals, respectively. Both the dislocation wall thickness and the dislocation cell size do not change with increasing number of cycles for the number of cycles simulated, which suggests that they could be intrinsic length scales that depend on the crystal size, and possibly the initial

dislocation density.

The box-count of small and medium sized boxes increases with increasing the number of cycles while that of bigger boxes remains the same. This indicates that the number of dislocation walls increases, but their thickness and the dislocation cell size remain constant. For this to happen, the previously formed dislocation cells are not refined by developing new dislocation walls that run across them. Alternatively, new dislocation walls develop external to the fully developed cells. Indeed, an inspection of the dislocation microstructure reveals that the complexity of the dislocation structure grows over time as can be seen in the supplementary movie II. Experiments on prestrained copper single crystals cyclically loaded in multislip orientation showed the formation of dislocation cell structures after about 50 loading cycles with dislocation cell sizes in the range of 0.7 μm after prestraining up to $\epsilon_{prestrain} = 0.4$ for larger crystals [200] . In addition, the cell size decreases with increasing prestraining level and the mean dislocation wall thickness is in the range of 0.05 to 0.1 μm. These observations agree with the current simulation results. The discrepancy in the dislocation cell size could be due to prestraining effects, which are absent in the current simulations, or due to the mismatch between the crystal sizes in the simulations and experiments.

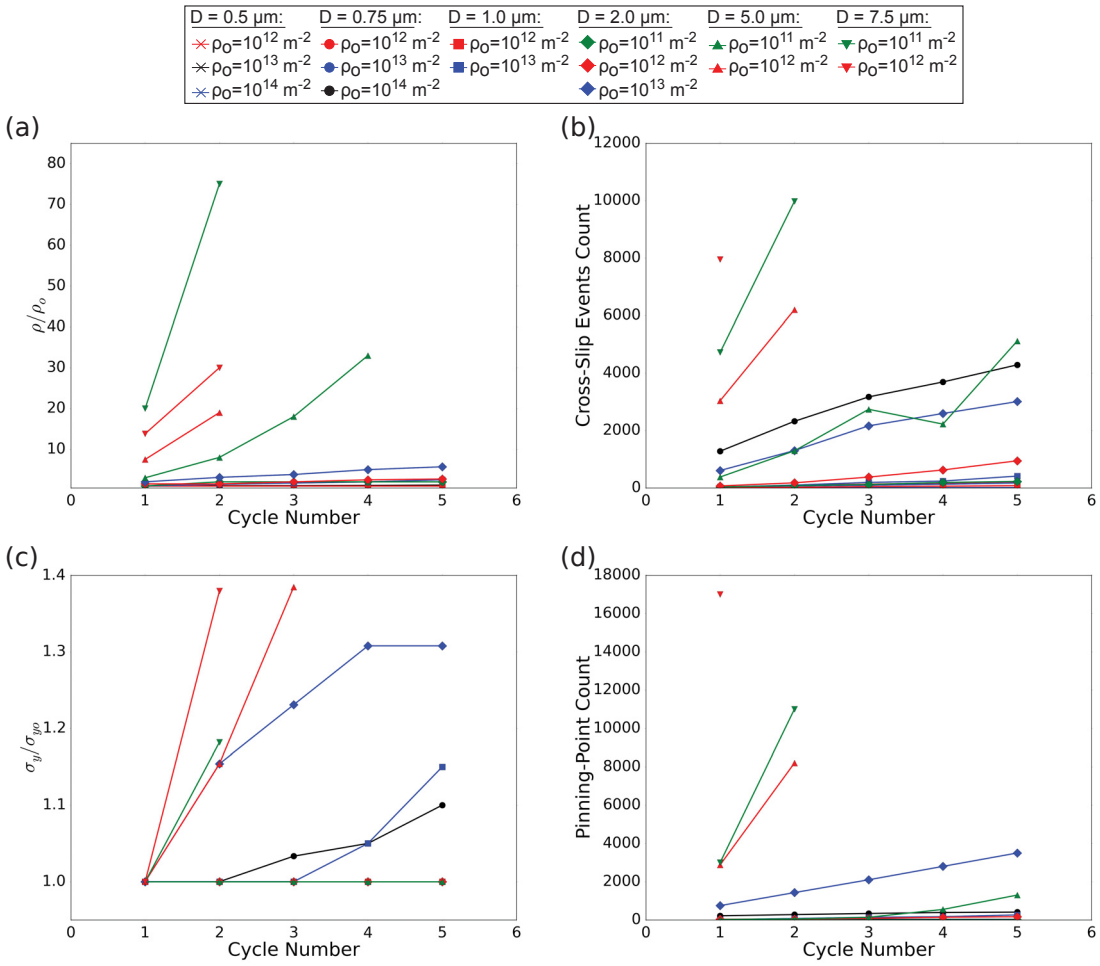


Figure 4.14: (a) Dislocation density multiplication factor; (b) number of cross-slip events; (c) relative flow strength; and (d) number of dislocation pinning points, as a function of the number of loading cycle for different simulation conditions. Each data point is an average of three different simulations with varying initial random dislocation distributions.

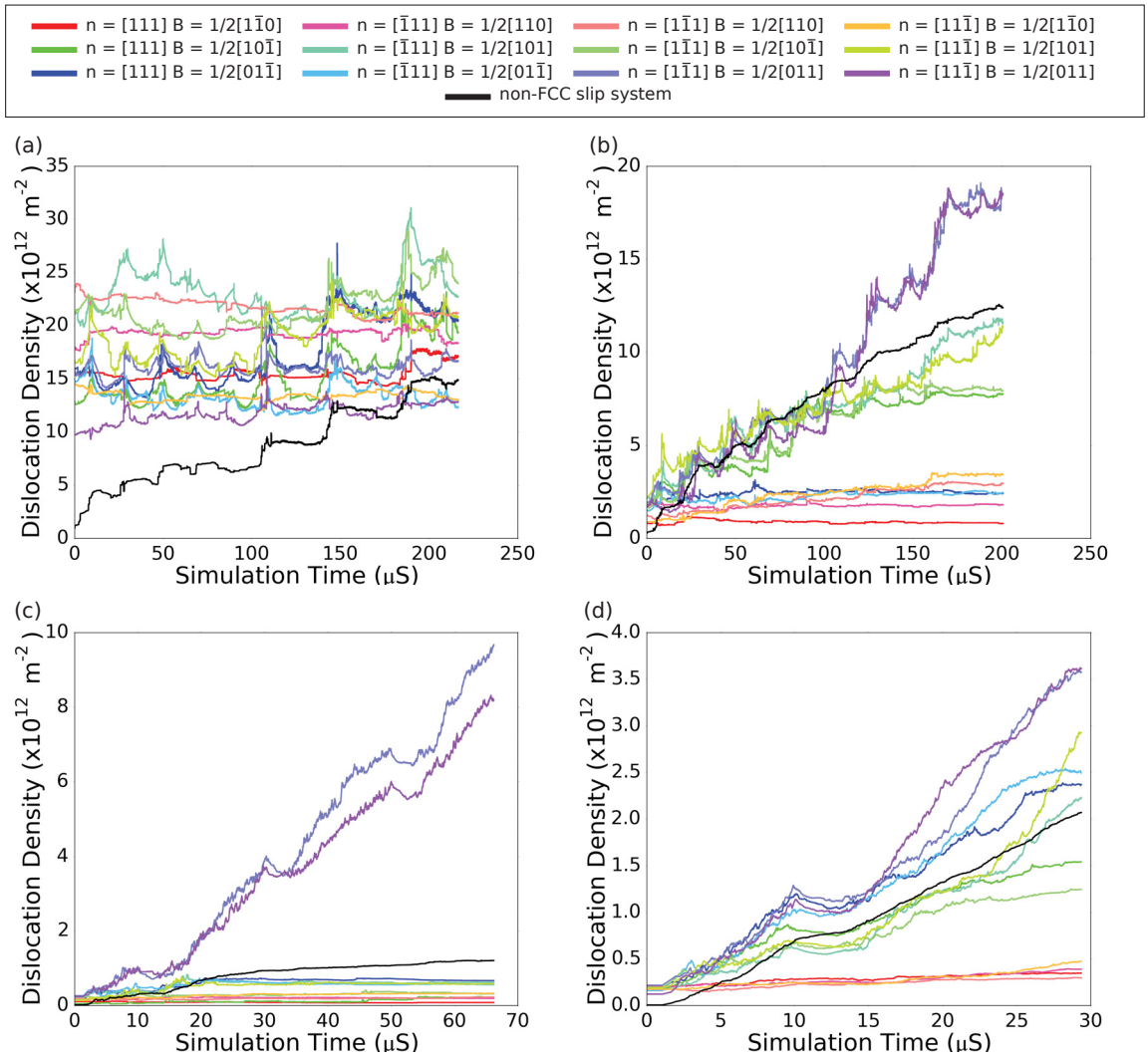


Figure 4.15: The evolution of dislocation density per slip system as a function of simulation time for different crystal sizes and initial dislocation densities: (a) $D = 0.75$ μm and $\rho_o = 10^{14}$ m$^{-2}$; (b) $D = 2.0$ μm and $\rho_o = 10^{13}$ m$^{-2}$; (c) $D = 5.0$ μm and $\rho_o = 10^{12}$ m$^{-2}$; and (d) $D = 7.5$ μm and $\rho_o = 10^{12}$ m$^{-2}$.

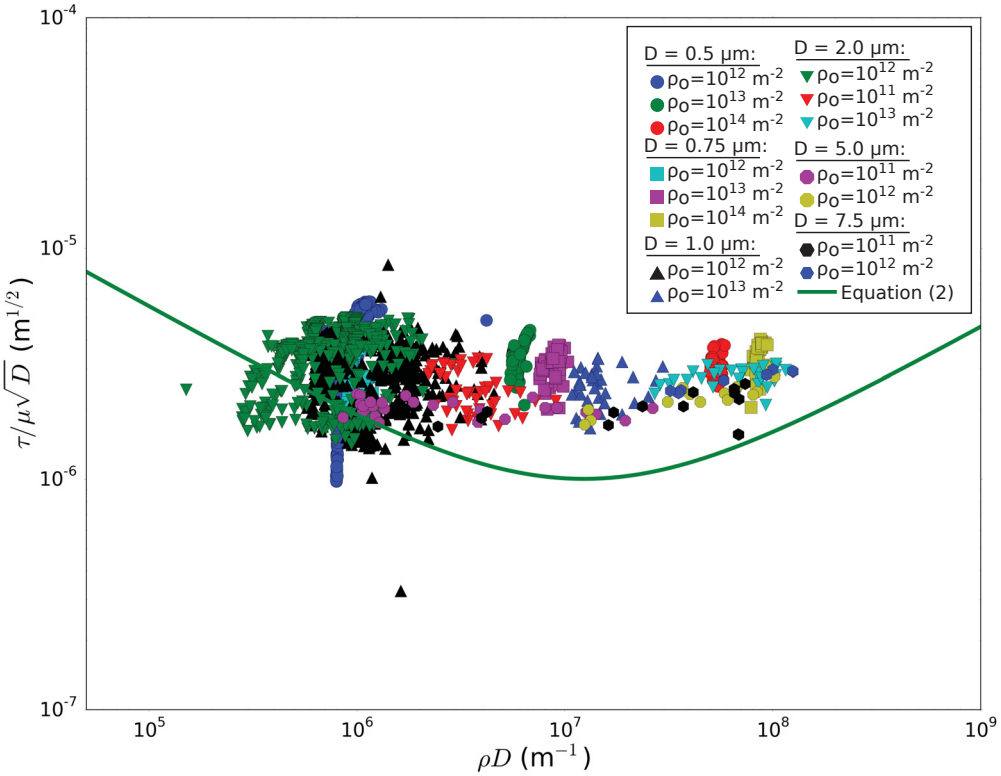


Figure 4.16: The flow strength normalized by the shear modulus and multiplied by the square root of the crystal size versus the dislocation density multiplied by the crystal size at the end of each quarter loading cycle from all the simulations.

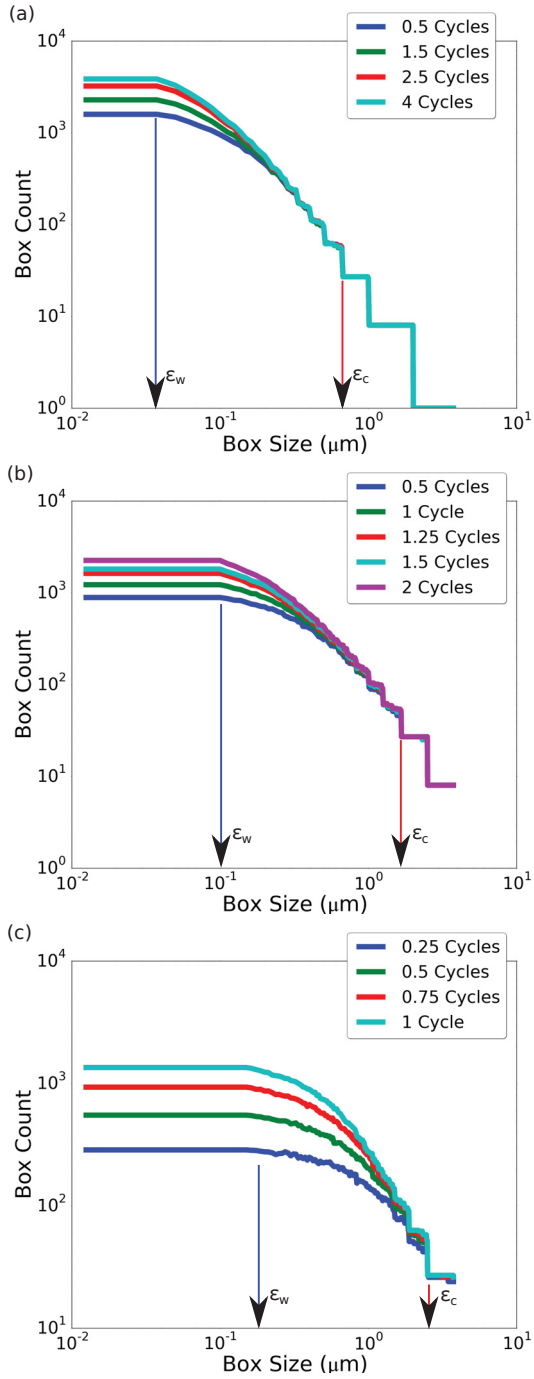


Figure 4.17: The box-counting method applied to representative dislocation microstructures from the current DDD simulations: (a) $D = 2.0$ μm and $\rho_o = 10^{13}$ m$^{-2}$; (b) $D = 5.0$ μm and $\rho_o = 10^{12}$ m$^{-2}$; and (a) $D = 7.5$ μm and $\rho_o = 10^{12}$ m$^{-2}$. The blue arrows indicate the wall thickness and the red ones indicate the cell size.

## 4.8 Surface Roughness Evolution During the Early Stages of Cyclic Loading

Active dislocations near the free surface of the crystal can escape leaving behind surface steps in the direction of the dislocation's Burgers vector having heights equal to the Burgers vector magnitude. As deformation progresses, the surface steps increase and the surface topography continuously evolves from a flat planar initial surface to a rough one with features similar to valleys and ridges. In Figure 4.18, representative deformed surfaces from four crystals having different edge lengths and initial dislocation densities are shown after a varying number of loading cycles. Two main modes of roughness evolution can be generally observed. First, the case when most of the roughness is localized to a few deformation bands (Figure 4.18(a)). In this case, surface steps are formed and they evolve contiguously within these bands with the rest of the surface being mostly smooth. The crystals showing this behavior are generally smaller in size and/or have a low initial dislocation density. Second, the case when the roughness is distributed uniformly over the entire surface of the crystal (Figure 4.18(d)). This usually takes place in larger crystals with higher density where more dislocations become active and the surface escape activity gets spread out. In addition, distinct steps that are higher than their surroundings are also observed. It can also be argued that the uniform roughness distribution takes place at the very early cycles while localization in slip bands takes place later. This has been observed by Dépres et. al. [93]. The major discontinuities on the surface correspond to slip planes where the dislocation activity is the highest. The minor steps parallel to the major ones form as a result of double cross-slip events that introduce dislocations on parallel slip planes. On some surfaces, especially for smaller crystals when few dislocations are active, major surface steps make an angle of $\frac{\pi}{4}$ with each other. This is a sign of a single cross-slip event introducing dislocations on the cross-slip planes of the

planes containing the initial Frank-Read sources since FCC slip planes intersect the surface {001} planes at lines making an angle of $\frac{\pi}{4}$ with the principal axes. In some cases (such as in Figure 4.18(c)), severe surface deformation and large slip bands exist right next to almost flat surfaces. This happens when there is a family of dislocations originating from the same source due to cross-slip and interacting with the surface forming surface steps that grow into deep and wide surface slip bands. On surfaces whose planes contain the Burgers vector of this family of dislocation, no observable surface roughening takes place although the surface atoms are still displaced within their plane. In other cases (such as in Figure 4.18(a)), it can be seen that the major roughening is due to one family of dislocations that grows in one direction, possibly due to the non-uniform stress field resulting from the complex dislocation network. This is why the surface shows varying degrees of roughness on one side of the most active slip plane and it sharply transitions to a rather smooth surface on the other side.

In an attempt to explain the deformed surface topography in terms of the evolving dislocation microstructure described in Section 4.5, Figure 4.19 shows both the surface roughness as well as the subsurface dislocation microstructure after different loading cycles. Near the center of the simulation cell a higher dislocation density is observed while the regions closer to the surfaces have significantly lower dislocation densities since the dislocation density flux is unidirectional on the surface in the current simulations, that is, dislocations can escape from the surface but they cannot nucleate and glide back into the crystal. In all of the simulations, surface step reversal is rare. A formed step usually persists even with the load reversal. For a step to be erased, a dislocation with a Burgers vector opposite to that of the step has to be deposited in the exact location of the original step. The load reversal guarantees that these dislocations exist even in the cases of very low densities (in fact, a single Frank-Read source loaded cyclically would deposit both positive and negative steps

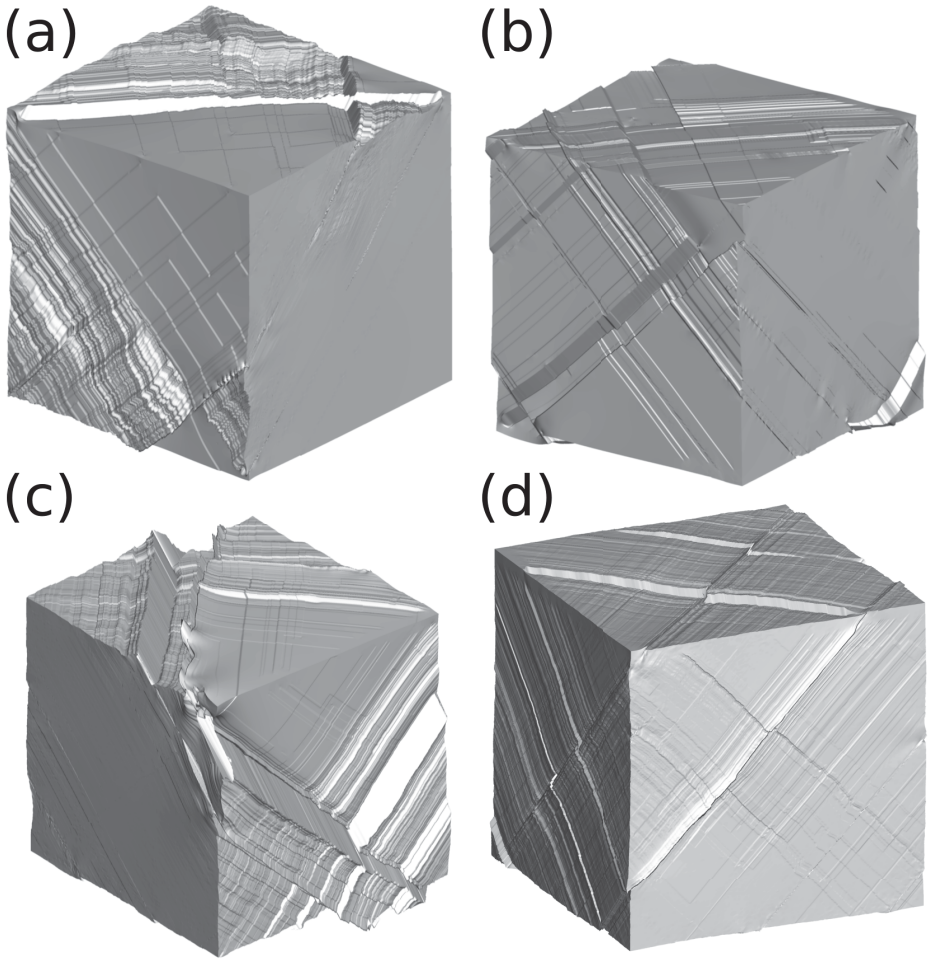


Figure 4.18: Reconstructions for the crystal surfaces after being deformed due to dislocation activity. The surface displacement is magnified 10 times (a) $D = 0.75$ μm, $\rho_o = 10^{14}$ m$^{-2}$ after 5 cycles, (b) $D = 1.0$ μm, $\rho_o = 10^{12}$ m$^{-2}$ after 50 cycles, (c) $D = 2.0$ μm, $\rho_o = 10^{13}$ m$^{-2}$ after 5 cycles and (d) $D = 5.0$ μm, $\rho_o = 10^{11}$ m$^{-2}$ after 2 cycles

on the surface), however, cross-slip usually takes the erasing dislocations to parallel planes before they get a chance to be deposited over the already formed steps because the time-scale at which cross-slip operates is much smaller than that of one half of a loading period. This explains the emergence of high displacement frequency regions on the surface formed of positive and negative steps right next to each other but on parallel planes.

The first few statistical moments of the surface height distribution can be used to

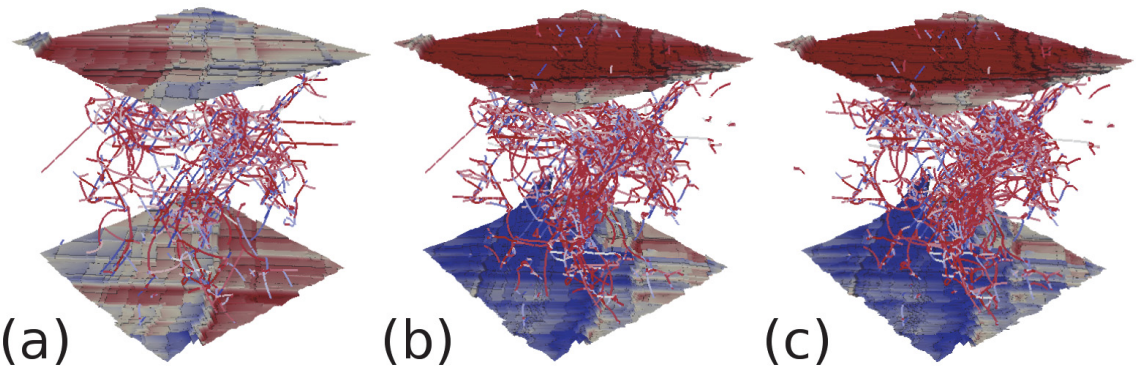


Figure 4.19: The dislocation microstructure and surface roughness evolution in a $D = 2.0$ μm crystal having an initial dislocation density of $\rho_o = 10^{13}$ m$^{-2}$ after (a) 2, (b) 3 and (c) 5 loading cycles. The surfaces are color coded according to the normal displacement field and the dislocations according to their slip system.

describe the deformed surface topography and its evolution over time. Surface height maps were calculated from the normal surface displacement over a grid covering the undeformed surface from which the first two statistical moments, the mean and the standard deviation, of the height maps were calculated. The mean height is proportional to the number of surface steps and their lengths, while the height standard deviation can be used as a basic measure of surface roughness with lower standard deviation values corresponding to rougher surfaces. Figures 4.20 and 4.21 show the variation of the first two moments with the number of cycles for a number of crystals having different sizes and initial dislocation densities.

In all simulated cases, there is a persistent surface step growth as previously predicted from the deformed surface visualizations. Although step reversal that can be observed as drops in the mean height curves, the overall trend of all curves is of a continuous increase. No clear correlation between the initial dislocation density and the mean height growth rate can be deduced from the current results. Nevertheless, the mean height growth rate is higher in larger crystals compared to the smaller ones. The step reversal is more pronounced in bigger crystals as well. The height growth follows a staircase pattern in some cases (Figure 4.20(c)), where there is a burst in

step formation followed by a longer time interval with no new steps forming. The bursts take place slightly after the beginning of the cycle which corresponds to the end of the elastic loading. This is the time when the applied stress reaches its peak value right before yielding. This shows that the applied stress is the main driver for surface features development rather than the interaction stresses which is consistent with the observation of surface roughening far from the regions of dislocation structure formation. Given the low number of cycles reached in these simulations, the growth rate is higher at the first few loading cycles and decreases for most cases at later loading cycles. The average height growth rate ranges between 0.01 nm/cycle and 0.45 nm/cycle. These numbers match the experimental values reported by Man. et. al. [201] who also report a continuous surface topography growth in the first few cycles and a lower growth rate at higher cycles as predicted by the current simulations. Similar to the mean height, the height standard deviation (HSDEV) grows continuously but with fewer and weaker fluctuations. Larger crystals have a higher HSDEV, which suggests that the surface steps are more uniformly distributed over their surfaces compared to smaller crystals.

The first statistical moments are reasonable choices for describing the general features of the deformed surface. In fatigue life studies, the maximum surface height is typically used [140] because it can be correlated to the stress concentrations developing near the surface steps. As it was discussed in Section 4.3.4, the maximum height correlates well with the Hausdorff dimension (HSD), however, the latter has the advantage of taking into account not only the maximum height amplitudes, but also their location over the surface. The Hausdorff dimensions for the cases discussed earlier are shown in Figure 4.22 against the number of cycles. Certain features are similar to those observed from the statistical moments evolution curves such as the continuous increase and the direct relationship between the roughening rate and the crystal size. This relationship however does not hold for HSD as strictly as it holds

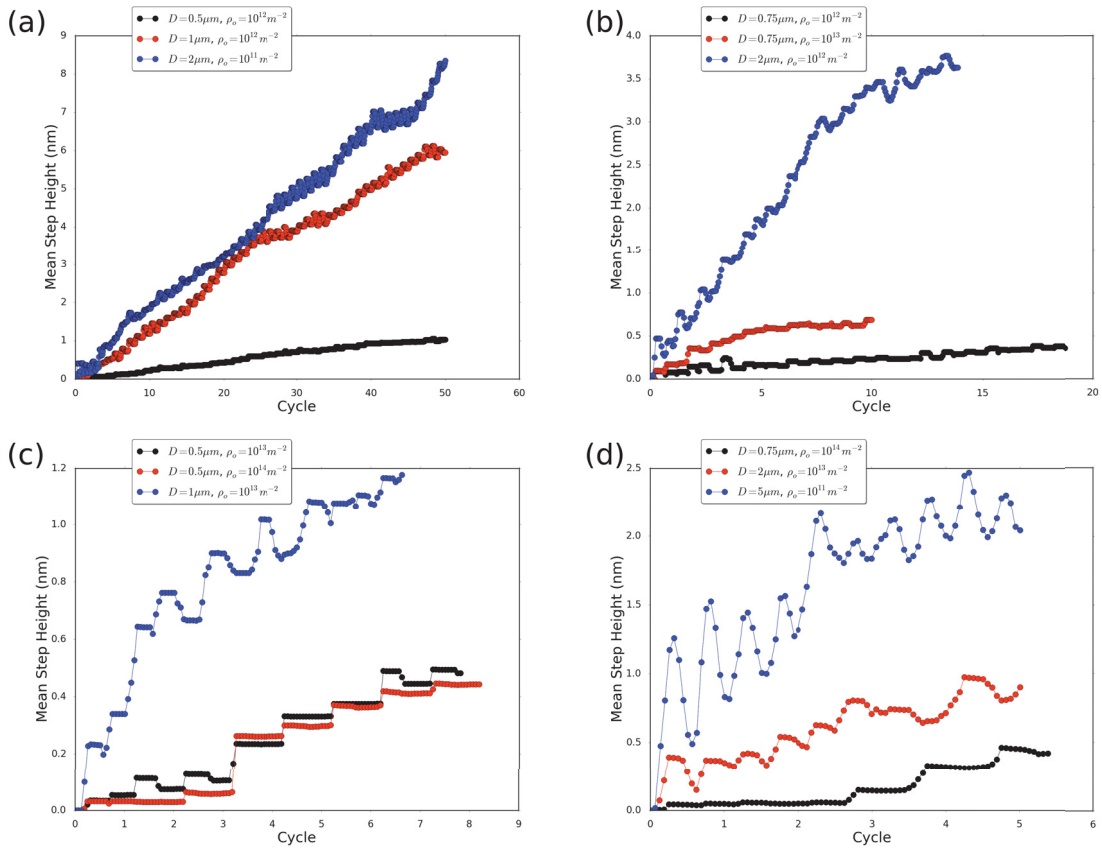


Figure 4.20: The mean surface height vs the cycle number for a number of simulated cases. For visual clarity, the curves are grouped based on the maximum number of cycles reached in the simulation.

for the mean height and its standard deviation because in some cases smaller crystals at higher initial dislocation densities show a faster HSD increase in the first few cycles. In addition, the drops in the HSD curves are almost non existent in the HSD curves. This is because the partial removal of a surface step by a dislocation of the opposite sign, an event that would reduce the mean surface height, does not affect the surface roughness. The only way by which the surface roughness, and hence, the HSD, decrease is by the complete removal of a surface step such that the surface can return locally to its undeformed configuration. Practically, this should be an extremely rare event because it requires the exact number of oppositely signed dislocations depositing right on the surface step causing it to recede (or advance for

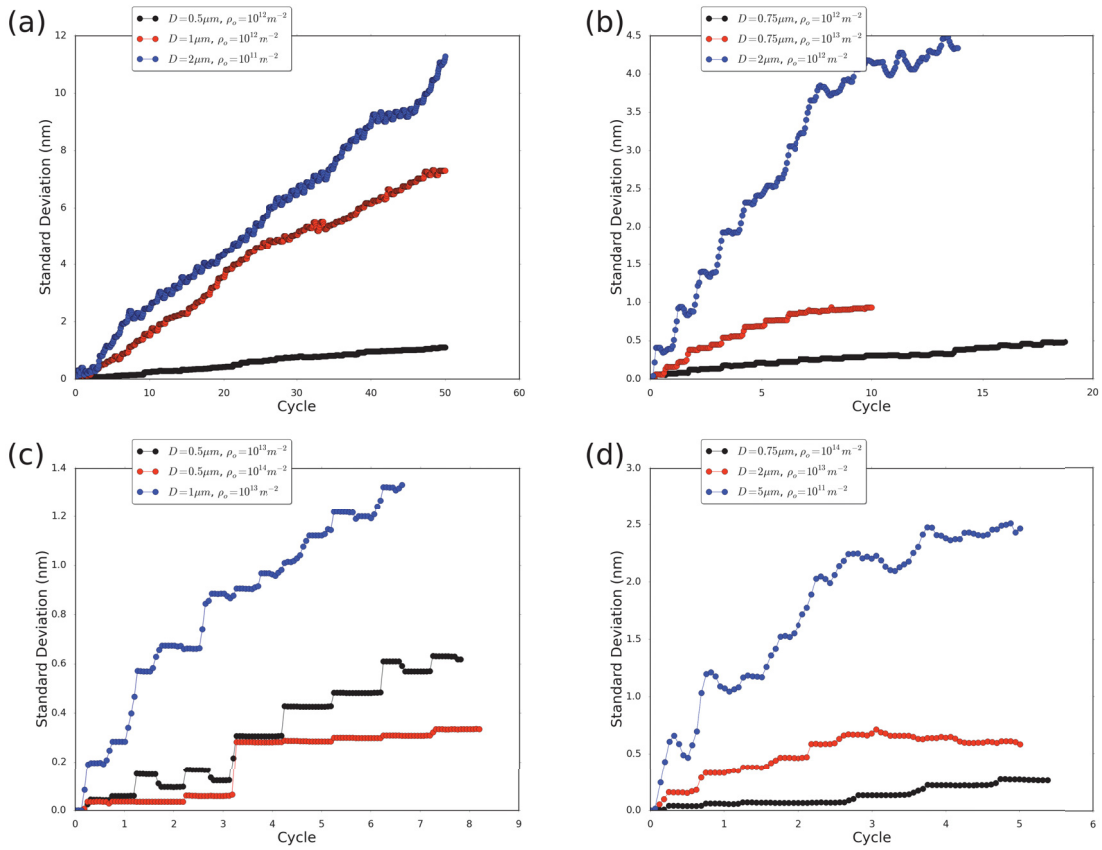


Figure 4.21: The surface height standard deviation vs the cycle number for a number of simulated cases. For visual clarity, the curves are grouped based on the maximum number of cycles reached in the simulation.

intrusions) and vanish.

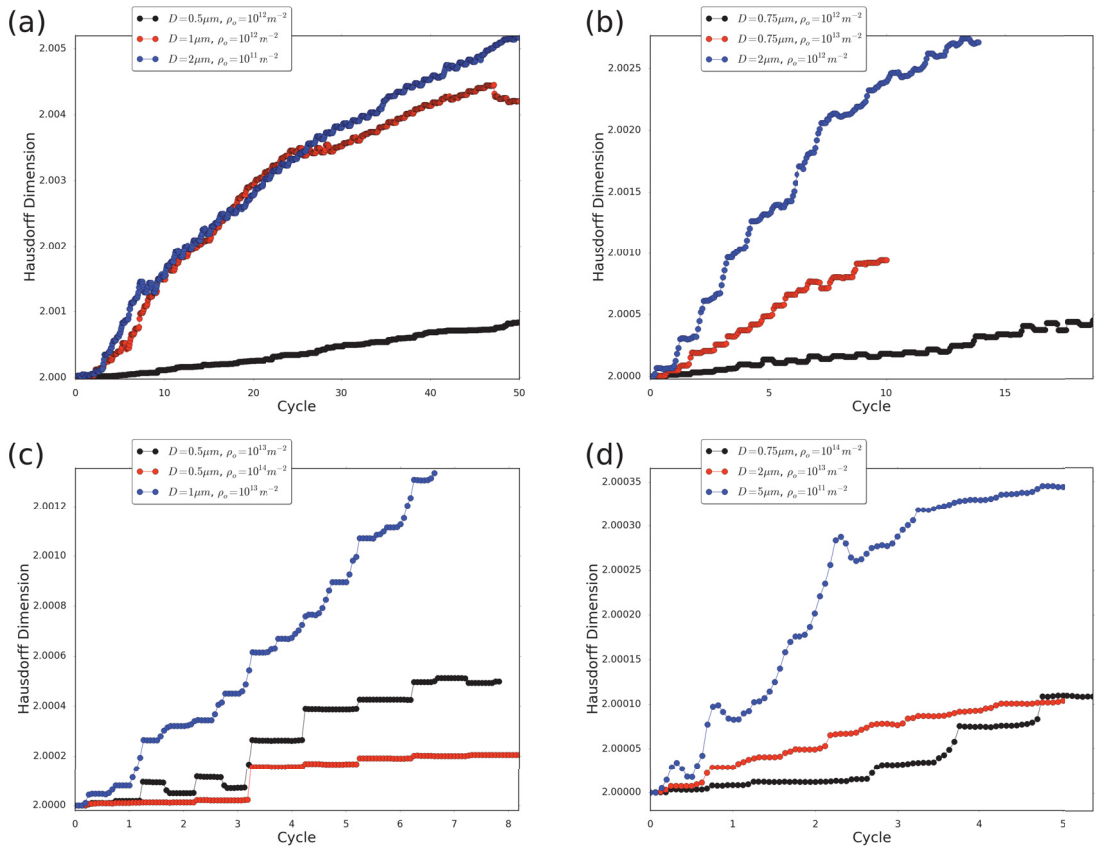


Figure 4.22: The variation of the Hausdorff dimension with the number of cycles for a number of simulated cases. For visual clarity, the curves are grouped based on the maximum number of cycles reached in the simulation.

## 4.9 Deformation Evolution in Persistent Slip Bands

Figure 4.23 shows a close-up of the dislocation microstructure near one of the PSB walls after one quarter of a loading cycle from a representative PSB simulation. Few edge dipoles move into the channels while the majority remain inside the PSB wall. The motion of the edge dipoles appears to be sensitive to the local stress, rather than the applied stress. This is because the applied stress works to expand the two edge dislocations of the dipolar loops in opposite directions resulting in zero net motion while the local stress acting on the two segments is different, which results in the observed loop drift. The shorter edge dipoles move rigidly without any expansion

while the longer ones expand slightly because the shear stress required for the dislocation expansion decreases with increasing its length. On the other hand, the screw dislocations in the channels move laterally much faster than the edge dipoles and they carry almost all of the plastic strain. It is also commonly observed that larger dislocation dipoles in the walls can expand in the channels leading to the formation of new screw dislocations.

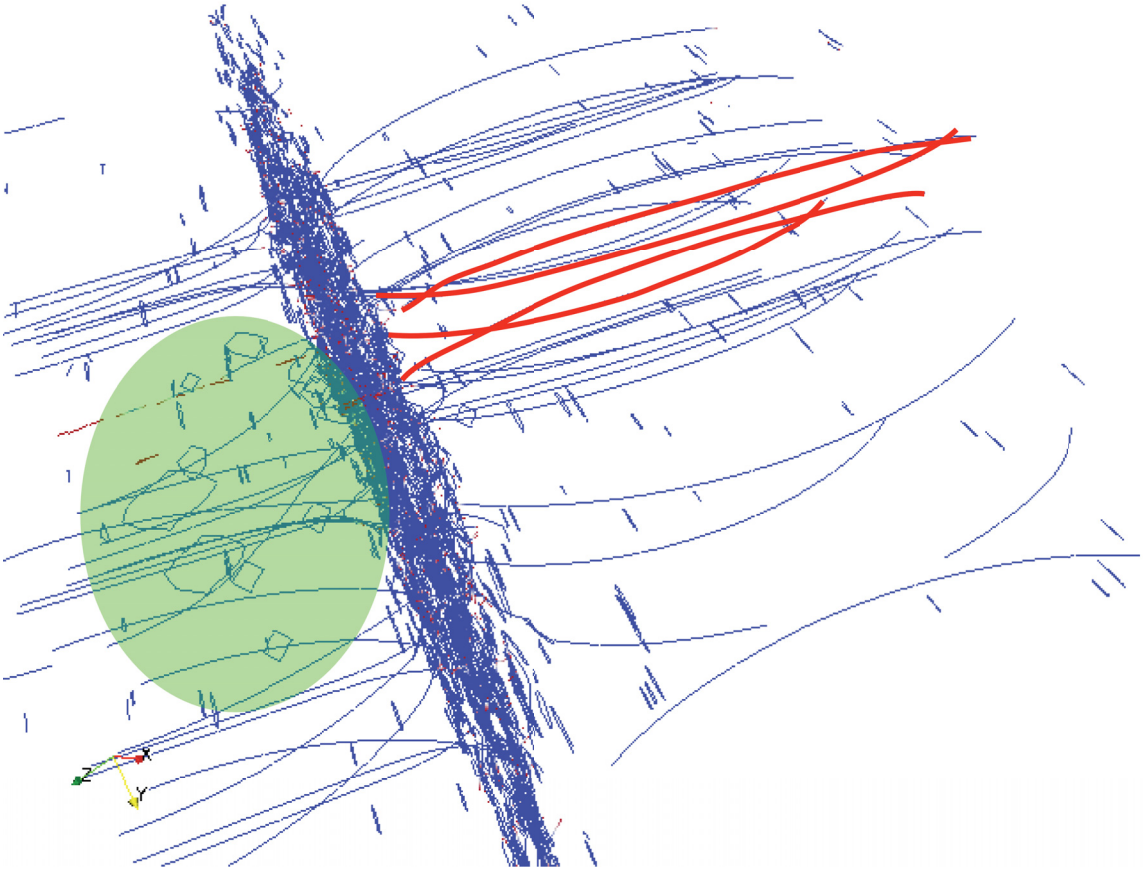


Figure 4.23: A close-up near one PSB wall during deformation after one quarter of a loading cycle. A number of edge dipoles that have expanded and moved out of the PSB wall can be observed in the green shaded region. The screw dislocations in the channel form screw dipoles as they move. Two screw dipoles are highlighted in red.

Snapshots from the dislocation microstructure evolution are given in Figure 4.25 for one of the PSB simulations. Initially, all the screw dislocations in the channels are straight. As the stress is applied, they start bowing out and their curvatures increase

with increasing the applied stress. Most of the screw dislocations show the same degree of curvature simultaneously, as shown in Figure 4.26, which means that the applied stress is the stress that controls their shapes not the interaction stress with the PSB walls or other screw dislocations. The stress from the PSB walls has a minimal effect because the walls are made of small dipolar dislocation loops whose stress fields vanish as one moves further away from the dipole center. An exact analysis for the stress field of the PSB wall in the channel builds upon Equation 2.24 for the stress field of a dislocation loop. From Equation 2.24, one can see that the integration kernel depends mainly on the third derivative of the position vector $r_{,ijk}$. For the case of two parallel dislocations of finite length $l$, placed at a distance $h$ apart and having opposite Burgers vectors, the entire integration in Equation 2.24 boils down to evaluating the integral $I_{ijk}$ given by

$$I_{ijkl}(x) = \int r^1_{,ijk} - r^2_{,ijk} dl_l \tag{4.7}$$

where $r^1$ and $r^2$ are the distances between the point $x$ and a general point on the two dislocation segments of the dipole as shown in figure 4.24. The difference is taken rather than the sum because the two dislocations are identical in everything except for their Burgers vector which are exactly opposite to each other. The vectors $r_i$, $r^1_i$ and $r^2_i$ can be written as

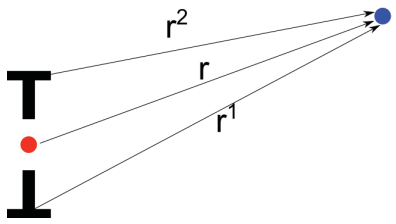


Figure 4.24: A schematic showing the distances $r$, $r^2$ and $r^1$ between the dislocations forming the dipole and a general point $x$. The point $x$ is in blue while the center of the dipole is in red.

$$\begin{aligned} r_i &= x_i - t_i \eta l \\ r_i^1 &= x_i - t_i \eta l - \tfrac{h}{2} m_i \\ r_i^2 &= x_i - t_i \eta l + \tfrac{h}{2} m_i \end{aligned} \tag{4.8}$$

where $\eta \in [\frac{-1}{2}, \frac{1}{2}]$, $t_i$ is a unit vector in the dislocation's line direction and $m_i$ is a unit vector connecting the dipole's center with the midpoint of one of the dipole's dislocations. The ratios of the magnitudes of $r^1$ and $r^2$ to $r$ are

$$\begin{aligned} \frac{||r^1||^2}{||r||^2} &= 1 + \frac{h^2}{4||r||^2} + \frac{h m_i}{||r||^2}(t_i \eta l - x_i) \\ \frac{||r^2||^2}{||r||^2} &= 1 + \frac{h^2}{4||r||^2} - \frac{h m_i}{||r||^2}(t_i \eta l - x_i) \end{aligned} \tag{4.9}$$

In the current PSB simulations, the PSB wall thickness is 0.1 μm and the dipole height $h$ is about 4.5 nm which gives an average spacing between the dipole center and any point in the PSB channel of about 0.5 μm. The ratio $\frac{h}{||r||}$ in this case becomes $\frac{h}{||r||} \approx \frac{1}{100}$. Hence, the second and third terms in equations 4.9 can be safely neglected as they are on the order of $10^{-4}$ and $10^{-2}$ respectively, resulting in $||r|| \approx ||r^1|| \approx ||r^2||$. The expression for $r_{,ijk}$ is given by

$$r_{,ijk} = \frac{-1}{r^3}(\delta_{ij} r_k + \delta_{ik} r_j + \delta_{jk} r_i) + \frac{3 r_i r_j r_k}{r^5} \tag{4.10}$$

Substituting back in Equation 4.11 knowing that $||r|| \approx ||r^1|| \approx ||r^2||$ and $r_i^1 - r_i^2 = -h m_i$

$$I_{ijkl}(x) = \int \frac{h}{r^3}(\delta_{ij} m_k + \delta_{ik} m_j + \delta_{jk} m_i) - \frac{3 h^3 m_i m_j m_k}{r^5} dl_l \tag{4.11}$$

where the first term is also on the order of $10^{-2}$ and the second term on the order of $10^{-4}$. This analysis explains why the deformation of the screw dislocations in the channels does not depend on the dislocation density in the PSB walls except in the regions very close to the walls whose thickness is on the order of the wall's thickness.

Because the channels are 10 times thicker than the wall, the dynamics of the screw dislocations in the channels are not affected by the presence of the PSB walls for all practical purposes which is in agreement with both the experimental results and analytical models presented by Mughrabi [202]. The analysis also suggests a method by which PSB simulations can be sped up. Because the wall dipoles do not carry any of the plastic strain and their stress fields rapidly die off, one can precompute and store the stress field due to the PSB wall dipoles in the walls and the channel layers in contact with the PSB wall and use it instead of performing the expensive $O(N^2)$ stress field calculation every time step over the wall dislocation segments, especially that their count is huge. At the same time, the PSB dipoles can still be explicitly modeled within the walls and their dynamics tracked to study the point defect generation process. In this case, the dipoles will move under the influence of the precomputed stress but their stress field will not be calculated. A similar approach was used in [174, 203] where the PSB walls were replaced with a fixed rigid infinite edge dipoles placed on the wall surface.

As the applied stress increases further, the curved screw dislocations in the channels lose their stability and start gliding laterally across the PSB channel once their curvatures reach a certain threshold that depends on the channel width. During their glide, the move in an intermittent fashion where they glide and then get locked in a screw dipole configuration, shown in Figure 4.23, when passing over another screw dislocation on a different slip plane. This lock remains as long as the local stress is below the passing stress. As the local stress increases, they unlock and glide again until another similar lock gets formed. When the glide planes of the two locked screw dislocations are closely spaced, the screw dislocations cross-slip and annihilate, reducing the dislocation density in the channel. As the screw dislocations glide along the channel, they deposit edge dislocations on the PSB walls. The formation of screw dipoles in the PSB channels has been shown to be the controlling factor for the flow

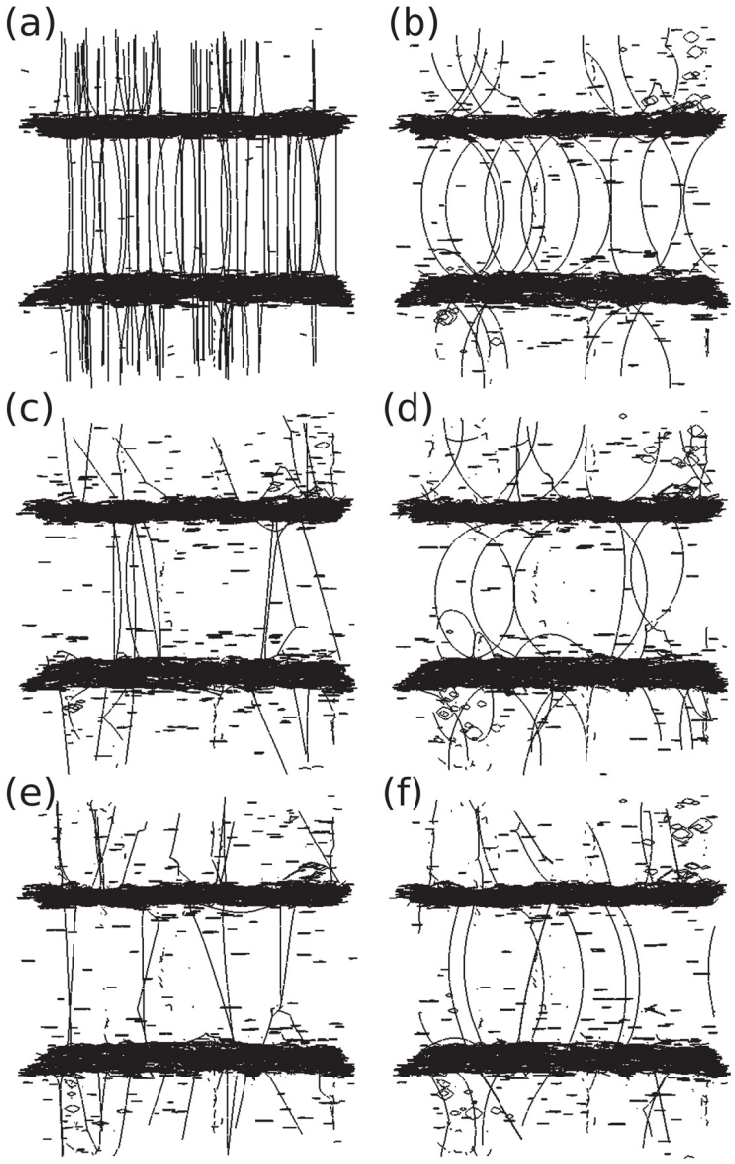


Figure 4.25: A top view of the evolution of the dislocation microstructure in the first loading cycle: (a) the initial microstructure; (b) after the tensile loading at the end of the first quarter-cycle; (c) after unloading, at the end of the first half cycle; (d) after the compressive loading at the end of the third quarter-cycle; (e) after unloading, at the end of the first cycle and (f) at the end of the first quarter cycle of the second loading cycle.

stress of the PSB [203–205]. The flow stress $\tau_f$ for a PSB can be shown to be given by [205]

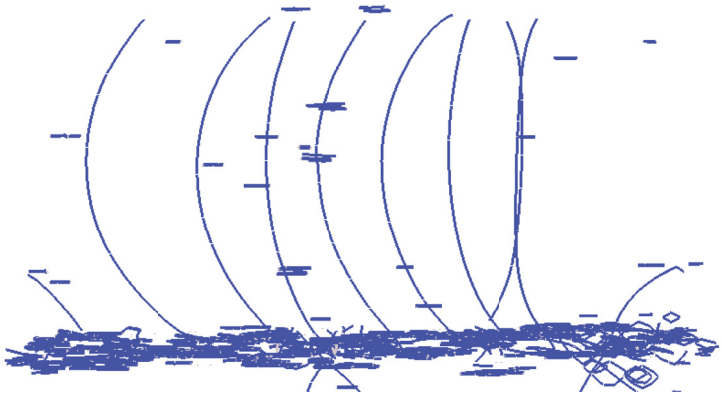

Figure 4.26: The expansion of screw dislocations in the PSB channel.

$$\tau_f = \frac{\mu b}{2\pi}\left(\frac{1}{(1-\nu)d} ln\left(\frac{d}{a_o}\right) + \frac{1}{2y}\right) \tag{4.12}$$

where $d$ is the channel spacing, $a_o$ is the dislocation core radius and $y$ is the distance between two locked screw dislocation. This model assumes that flow takes place when the screw dislocations are mobilized, which in turn requires: (1) the screw dislocations to start bowing out; and (2) they pass each other when they get into a lock configuration. The stresses required for (1) and (2) are expressed by the first and second terms of Equation 4.12, respectively. Plugging in the values for the parameters used in the current simulations and taking $a_o = b$

$$\tau_f \approx 38.3 + \frac{1.6 \times 10^{-6}}{y} MPa \tag{4.13}$$

The average spacing between the dislocations can be assumed to equal the mean free spacing, $\lambda$, between the dislocations, which can be obtained from the dislocation density in the channel $\rho_c$ according to

$$y \approx \lambda = \frac{1}{\sqrt{\rho_c}} \tag{4.14}$$

Plugging back into Equation 4.13 gives

$$\tau_f \approx 38.3 + 1.6 \times 10^{-6}\sqrt{\rho_c} = 38.3 + 1.6 \times 10^{-6}\sqrt{10^{13}} = 43.36MPa \tag{4.15}$$

Figure 4.27 shows the variation of the applied stress and dislocation density with simulation time for two different PSB simulations. The engineering stress in these results ranges between 80 and 100 MPa. Since the loading orientation is the $[\bar{1}23]$ direction, the screw dislocations slip plane is the $\{111\}$ plane and their Burgers vector is in the $[10\bar{1}]$ direction, the Schmidt factor in this case is $m = 0.467$. Hence, the shear stress on the screw dislocation that corresponds to the applied engineering stress is in the range of 37.33 MPa $\leq \tau_f \leq$ 46.66 MPa which agrees with the estimate given by Equation 4.15. The discrepancy can be due to the approximation employed in [205] and the fact that the actual flow stress that would be reported in the DDD simulations is the strength of the weakest screw dislocation lock, the one with highest plane spacing, $y$, not the average lock spacing that is used in this calculation. A close value, $\tau_f = 50MPa$, was found by Tippelt et. al. [206] in their experiments on PSBs in nickel at room temperature.

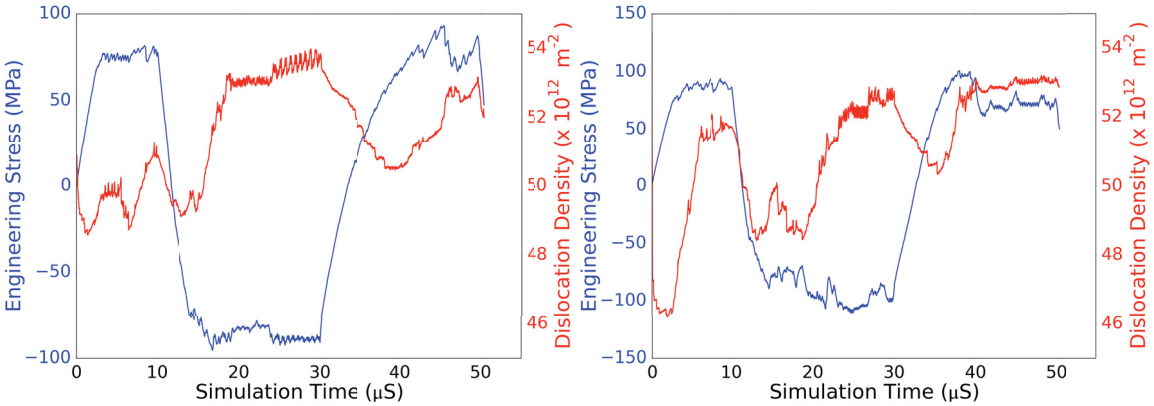


Figure 4.27: The engineering stress and dislocation density versus time for two different PSB simulations.

The increase in the dislocation density, as observed in Figure 4.27, corresponds to

the bowing out of the screw dislocations in the channels before their glide. On the other hand, the decrease in the dislocation density is associated with the annihilation of dislocation segments through collisions, cross-slip or climb because periodic boundary conditions are employed in the current simulations. After one loading cycle, an average of 45 bulk cross-slip and 75 intersection cross-slip events were detected. Annihilation by cross-slip does not leave behind any point defects. Annihilation by climb however results in the generation of point defects when the annihilating dislocations have a non-zero edge component. Point defects, once generated, they diffuse through the crystal and might end up around the PSB-matrix interface or on the crystal surface. The accumulation of vacancy-type point defects results in the formation of voids, which, depending on their location, can cause a change in the volume of the PSB or the nucleation of cracks if they are close to the intersection of the PSB-matrix interface with the crystal surface [158]. Here, the atomic point defect concentrations were calculated from the DDD simulations and the increase in the atomic concentration of vacancy-type and interstitial-type point defects with simulation time is given in Figure 4.28. The atomic point defect concentrations after 1 loading cycle are $2.2 \times 10^{-4}$ and $1.76 \times 10^{-4}$ for the two simulations, respectively. This also agrees well with the predictions of the analytical model presented in [207] where it was predicted that the generated atomic point defect concentration per loading cycle is about $2 \times 10^{-4}$. It should be noted that point defect diffusion was not accounted for these calculations.

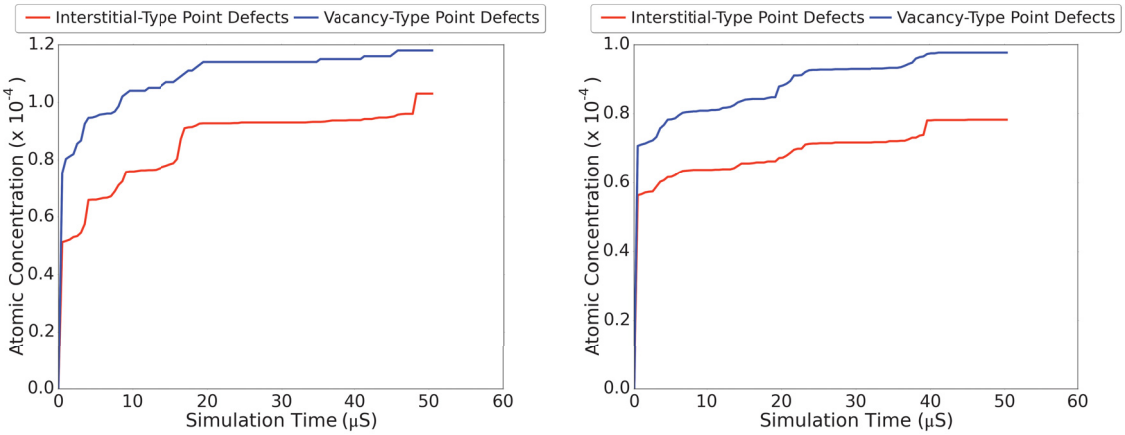


Figure 4.28: The evolution of point defect atomic concentration with simulation time for the two PSB simulations.

## 4.10 Summary and Conclusions

In this chapter, DDD simulations of nickel single crystals subject to cyclic loading were presented and discussed. The initial dislocation microstructure in these simulations was either a random distribution of FR sources or a well developed PSB microstructure. The mechanical response, dislocation microstructure evolution, surface roughness evolution, and the concentration of point defect generation were studied and compared with experimental results and analytical models. A metric to measure the extent to which a dislocation microstructure is patterned has been proposed and used to study the formation of cell-like dislocation structures in crystals of different sizes and initial dislocation densities during the early stages of cyclic loading. Dislocation cell sizes have been quantified using a box-counting method. A number of surface roughness measures were also used to study the evolution of the surface roughness as a function of number of loading cycles. The change in the atomic concentration of the generated point defects with time in the PSB simulations was also predicted. The following observations were made and explained in terms of the active dislocation mechanisms.

- Larger crystals exhibit cyclic hardening, rapid dislocation density multiplication and the evolution of dislocation cell-like structures.
- Dislocation cell-like structure formation relies on the formation of pinning points, which in turn depends on the frequency of cross-slip.
- Larger crystals show dislocation patterning earlier than smaller crystals and at lower initial dislocation densities. It has been hypothesized that there is a size dependent critical initial dislocation density after which dislocation cell structures form under fatigue loading.
- The dislocation cell size and the thicknesses of their walls change with crystal size but not with the number of loading cycles. Over time, the system develops more cells external to the already formed ones. Cell refinement has not been observed up to the number of loading cycles simulated.
- The surface roughness in smaller crystals is localized to narrow bands of severe surface deformation while in larger crystals they are more uniformly distributed over the surface of the crystal.
- The growth of surface steps is persistent, that is, it is rare for a surface step to be removed by the deposition of an oppositely signed dislocation on the surface during the load reversal.
- The screw dislocations in the PSB channels carry most of the plastic strain while the edge dipolar loops in the PSB walls show minimal to no movement.
- Larger edge dipoles can expand in the channels leading to the formation of new screw dislocations in the channels.
- The strength of the PSB depends on the stress required to activate the screw dislocations in the channels which in turn depends on the channel width and

the average spacing between the screw dislocations.

- The annihilation of edge dipoles leads to the development of point defects with an atomic concentration of about $2 \times 10^{-4}$ per cycle.
- The results are in good agreement with experimental observations and analytical model predictions.

# Chapter 5

# The Deformation Response of Nickel-Base Superalloy Microcrystals under Monotonic Loading

## 5.1 Introduction

Structural materials need to display a relatively high yield and ultimate strength, ductility and fracture toughness. More stringent requirements are placed on the structural materials used in higher temperature applications, such as jet engines and gas generation power turbines. Materials for high temperature applications should be capable of withstanding the applied stresses, have a relatively low creep strain rate, and resist mechanical degradation and life reduction due to oxidation effects and chemical attacks usually associated with high temperature environments. Over the past few decades, material scientists have produced Ni-base alloys that provide this combination of characteristics and thus, they were called Ni-base superalloys [64].

Ni-base superalloys are the state of the art materials used in jet engines and power turbines [64]. Thanks to their unique balance of structural, thermodynamic and kinetic properties, they are heavily used in the most demanding temperature and stress sections of turbine engines. These alloys contain secondary phases, and unlike most other materials that show a reduction in the yield stress with the temperature increase, they exhibit an anomalous dependence of their yield strength on the temperature where the yield strength increases with temperature up to a temperature of about 750°C to 850°C [208–210]. The extended exposure to applied stresses in a high temperature environment triggers a number of thermally activated mechanisms [39] that need to be characterized in order to fully understand their deformation behavior. Nickel superalloys show a number of unique deformation mechanisms including Kear-Wilsdorf lock formation [211, 212], solid solution strengthening [64], precipitate shearing, as well as creep mechanisms such as climb bypass [213] and microtwin formation [214], have not been introduced in large scale computational simulations.

Superalloy development started in the 1940s with the development of the Nimonic and Waspaloy series [64, 215]. These alloys could withstand 1000 hours of creep life under an applied stress of about 140 MPa and a temperature ranging from 750°C to 950°C. The turbine blades were typically manufactured in wrought form but when vacuum induction casting was developed in the mid 1950s, the blades manufacturing switched to casting and new superalloys such as the Inconel series and Rene 80, which can operate at temperatures around 1000°C, were developed [215]. A significant improvement in superalloys properties took place when directional solidification was invented. This allowed the alloy developers to remove the transverse grain boundaries completely. The creep temperature under the same stress increased to 1100°C. In the early 1980s, single crystal superalloys, such as Rene N5 and N6 were introduced and grain boundary strengthening elements, such as Boron and Carbon, were completely removed. These alloys pushed the creep temperature limit to about 1050°C to 1100°C

[64, 215], or a homologous temperature of about 0.8.

The future of superalloy development can greatly benefit from a sound understanding of the collective dynamics of dislocations inside the crystal and how it is affected by the superalloy microstructural features, alloying elements and composition. The rapid elimination of suboptimal combinations of alloying elements from the search space through large scale computer simulations of dislocation motion and interactions in superalloys can reduce the cost, time, and effort required to bring a new alloy to the market by directing the research and experiments to the most promising candidates for the next generation alloys. This chapter describes a study undertaken to extend the DDD simulations framework to simulate the dislocation motion inside a superalloy and the results of simulating the monotonic loading of a number of superalloy microstructures. The developed framework, can be extended to incorporate more physics relevant to the deformation mechanisms active in superalloys in the future.

## 5.2 The Structure of Nickel-Base Superalloys

About fourteen elements typically enter the composition of superalloys including chromium, cobalt, molybdenum, tungsten, aluminum and titanium. The early single crystal superalloys (e.g. PWA1480 and Rene N4) contained higher amounts of Al, Ti and Ta, while increasing amounts of Re ($3 \approx 6$ % wt.) appeared in alloys that were introduced later (e.g. PWA1484, CMSX-4, CMSX-10, Rene N5 and Rene N6). Ruthenium, which was not a typical alloying element, entered in the composition of the more modern alloys (e.g. MC-NG and TMS-162). Since they have excellent creep resistance properties, the base materials for all superalloys are either nickel or cobalt, although they do not have the highest melting temperatures among metals, with Ni being more common [64].

The alloying elements that enter the mix of superalloys end up residing in different phases. Ni reacts with Al, Ti and Ta to form the intermetallic $Ni_3$(Al,Ti,Ta) which has the $L1_2$ crystal structure shown in Figure 5.1 forming a distinct phase called the $\gamma'$ phase. This phase takes the form of precipitates dispersed in the alloy matrix [213]. The matrix is a continuous phase, called the $\gamma$ phase which consists mainly of FCC Ni with small concentrations of solute atoms of Co, Cr, Mo, Ru and Re. When Fe and Nb are present, other phases can form such as the $\gamma''$ phase which has the $D0_{22}$ crystal structure [216]. The interaction of dislocation with $\gamma''$ phases is beyond the scope of this work. There are no phase boundaries between the $\gamma$ and $\gamma'$ phases because they have the same orientations when the $\gamma$-$\gamma'$ misfit is small. The misfit is measured by the misfit parameter $\delta$ defined as

$$\delta = 2\frac{a_{\gamma'} - a_{\gamma}}{a_{\gamma'} + a_{\gamma}} \tag{5.1}$$

where $a_{\gamma'}$ and $a_{\gamma}$ are the lattice constants for the $\gamma'$ and $\gamma$ phases, respectively. The shape of the $\gamma'$ precipitates depends on the heat treatment process used and it was found that the precipitates coarsen and change morphology as they age. At low aging times, the $\gamma'$ precipitates take the form of spheres, as the aging continues, they transform into cuboids, then arrange themselves in cuboidal arrays, then finally they start forming a dendritic structure [217]. The misfit parameter was found to control the size at which the transition from spherical to cuboidal precipitates takes place. The $\gamma$-$\gamma'$ misfit also introduces a stress field in both phases which affects the dislocations motion near their common interface. Figure 5.2 is a micrograph showing the aged microstructure of CMSX-3 where cuboidal precipitates can be observed. The $\gamma'$ precipitates have been found to remain stable up to a temperature of 1375°C [218], which is very close to the melting point of Ni ($1455^{o}$C).

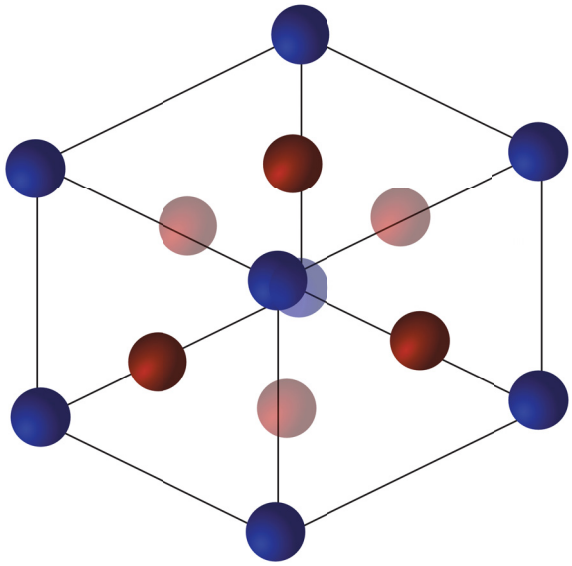

Figure 5.1: The $L1_2$ crystal structure. The (Al,Ti) atoms are in blue while the Ni atoms are in red.

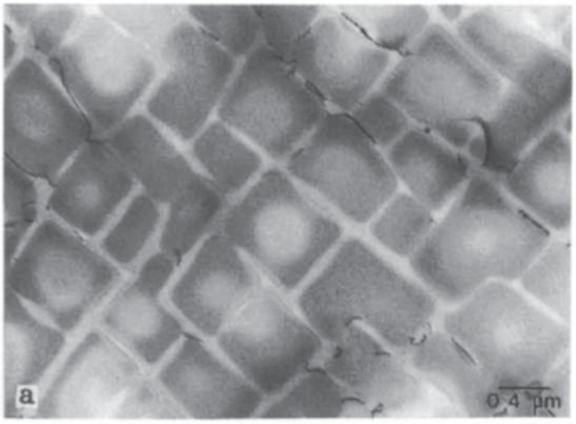


Figure 5.2: The microstructure of aged CMSX-3 superalloy. The cuboidal precipitates can be seen along with some interfacial dislocations. Figure taken from Pollock et. al. (DOI:10.1016/0956-7151(92)90195-K) with permission from Elsevier.

## 5.3 Dislocations in Nickel-Base Superalloys

Figure 5.3 shows the unit cell and the distribution of atoms on the highest packed plane (the {111} plane) for both pure FCC crystals (e.g. Ni) and $L1_2$ intermetallics (e.g. $Ni_3Al$) along with two out of the three glissile Burgers vectors on this plane. Because the two phases have the same orientations, dislocations can glide from one phase

to another with no interface resistance. When a typical FCC dislocation ($\frac{1}{2}\langle 110\rangle$) glides over such a plane, all the atoms swept by the dislocation are shifted in the direction of the Burgers vector. For Ni, this takes a Ni atom and places it in a location that was occupied by another Ni atom which does not change the overall energy of the system. On the other hand, for $Ni_3Al$, a similar dislocation glide would place a Ni atom in a location that was occupied by an Al atom. This disturbs the local chemistry of the system and puts it in a higher energy state. The region of distorted local atomic arrangements on the slip plane is called an Anti-Phase Boundary (APB) region, the creation of which is resisted by the crystal structure so as to maintain the minimum energy state. The force per unit length exerted on a dislocation line resisting its creation of an APB is equal to the energy per unit APB area, called the APB energy $\Gamma_{APB}$. When a dislocation glides over an APB region, which was created by another dislocation of the same or opposite Burgers vector, the atoms get shifted again so as to end up in locations that were occupied by similar type atoms, leading to the reduction of the energy of the crystal and the destroying the existing APB region. The destruction of the APB regions is energetically preferred, hence, the dislocations that would destroy an APB are attracted towards the APB region by a force per unit length equal to $\Gamma_{APB}$ [219]. $\Gamma_{APB}$ is a material property and it typically lies in the range of 0.12 to 0.4 $J/m^2$ [220, 221].

A dislocation with twice the typical FCC Burgers vector (i.e. $\langle 110\rangle$) would penetrate the precipitate and glide smoothly without creating or destroying any APB regions, since it does not disturb the local crystal structure. Such a dislocation is called a superdislocation and it is energetically more favorable for it to dissociate into two similar identical superpartials of $\frac{1}{2}\langle 110\rangle$ Burgers vector bounding an APB region in between. Because $\frac{1}{2}\langle 110\rangle$ dislocations naturally dissociate into two Shockley partials bounding a complex stacking fault (SF) in between, the dislocation core in intermetallics is more complicated than in FCC. Pollock et. al. [213] argued that

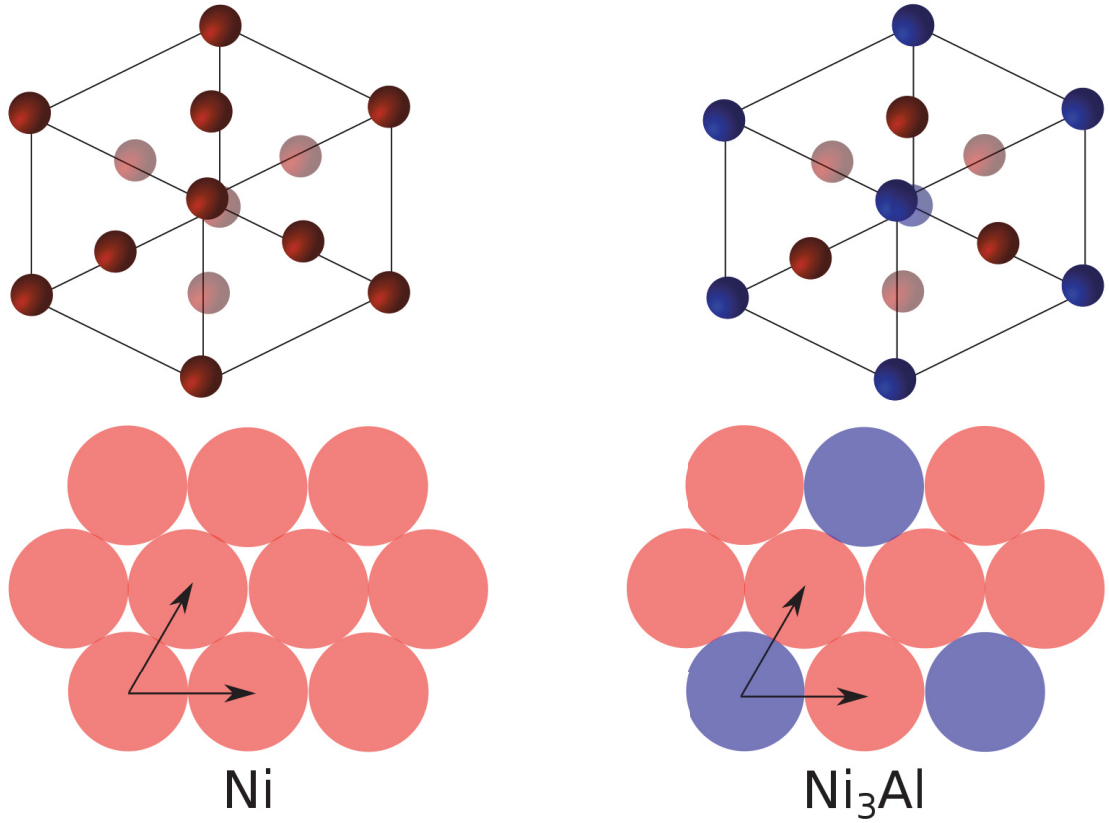


Figure 5.3: The unit cell of Ni and $Ni_3Al$ (top) and the arrangement of atoms on the highest packing plane {111} in both cases (bottom). The Ni atoms are in red while the Al atoms are in blue. The black arrows indicate the directions of 2 out of the 3 glissile Burgers vectors on that plane.

precipitate penetration by superdislocations requires that the precipitate blocks the motion of the leading dislocation pressing on it until the formation of a two-dislocation pile-up, which requires a local stress close to 950 MPa, which is higher than the stress required for a single superpartial to defeat the precipitate when $\Gamma_{APB} \leq 0.23$ J/m$^2$. When $\Gamma_{APB}$ is too high and the formation of superdislocations is difficult, dislocations can glide in the narrower $\gamma$ channels, given sufficient stress, and form loops around the precipitate. Alternatively, at higher temperatures, dislocation cross-slip and climb [222] take place to avoid the obstacle introduced by the precipitate.

Screw-oriented superdislocations gliding inside an intermetallic can form locks

when the leading superpartial cross-slips from an octahedral {111} plane to a cubic {100} plane. Because dislocations cannot easily dissociate on the low atomic density {100} plane, the superpartial immediately dissociates on one of the two {111} planes containing its Burgers vector after cross-slip [212, 223], which prevents it from gliding on the {100} plane. Both the leading and the trailing superpartials cannot glide further because their glide would create an extended APB region with no other dislocation to destroy it. The height of the APB region on the {100} plane due to cross-slip is about one atomic spacing. This locked configuration is called a Kear-Wilsdorf (KW) lock [211, 212] and it occurs more frequently at higher temperatures, which can help explaining the anomalous increase in the strength of $Ni_3Al$ with temperature. When a portion of the superdislocation forms a KW lock, the rest of the superdislocation glides until another portion locks and a superkink is formed in between [210, 224]. The lateral motion of superkinks, their multiplication, and annihilation are believed to affect the crystal strength by immobilizing the remobilizing screw oriented superdislocations [225]. Dislocation glide on the cube plane takes place at higher temperatures as it has been confirmed by the surface slip-trace analysis for $Ni_3$(Al,Nb) single crystals loaded at temperatures ranging from 77 to 910 K, where it was found that below the peak stress temperature (850°C) the primary slip plane is the octahedral plane, while at higher temperatures it switches to the cube plane [226]. Other sources reported wavy slip traces at temperatures ($T > 850^o$C) suggesting that the dislocations alternate, through successive cross-slip events, between gliding on the cube and octahedral planes such that the resultant glide is along the maximum shear plane [227].

Besides their stress anomaly, $Ni_3Al$ shows both tension/compression asymmetry and load orientation dependence of the flow stress [223, 228]. The core dissociation of the $\{111\}\frac{1}{2}\langle 110\rangle$ superpartials into two Shockley partials was proposed by Lall et. al. to be the source of this asymmetry [229]. According to the Escaig cross-slip

model [107], the local stress alters the dissociation width of the screw dislocation core, which in turn alters the activation energy required for cross-slip. If tensile stresses result in an increase in the core width, making it harder for cross-slip to take place, compressive stresses will result in the opposite situation. The increase/decrease in cross-slip rate controls the frequency of KW lock formation and consequently controls the flow stress. Takeuchi et. al. [227] used cross-slip as well to explain the flow stress orientation dependence by suggesting that the different components of the local stress tensor modify the core width in different ways giving rise to variations in the cross-slip rates between the different slip planes. The pinning of the two superpartials after cross-slip was found to be stronger when the crystal's anisotropy was taken into account [230] since the anisotropy results in the creation of a torque between the two superpartials, in addition to the interaction force between them that makes their further glide more difficult.

From the previous discussion, it is obvious that there is a large number of interacting mechanisms that result in a number of interesting flow phenomena in Ni based superalloys. The complexity of the deformation behavior calls for the use of computational simulations to identify and characterize the active mechanisms and the parameters that influence them the most. In the following sections the past efforts undertaken to simulate the behavior of Ni based superalloys, the newly developed DDD simulation method, and the results of the current simulations are discussed in more details.

## 5.4 Previous DDD Simulations of Nickel-Base Superalloys

Foreman et. al. [231] conducted the first simulation on the strength of precipitate hardened materials where they treated the precipitates as point obstacles facing a

single gliding dislocation. Because no precipitate shearing can take place in this case, the strength of different precipitates was modeled using the breakaway angle at which the dislocation can bypass the point obstacle. This was not a DDD simulation in the typical sense because the dislocations experienced sudden circular expansions to either the equilibrium radius under the applied stress or to the next nearest obstacle. The first true DDD simulations of Ni based superalloys strength was performed by Devincre et. al. [232] who studied the glide of a superdislocation in $L1_2$ on an octahedral plane and the formation and destruction of KW locks. Their simulations confirmed the important role of superkinks in carrying the plastic strain at lower temperatures, where KW locks are difficult to unlock. The dynamics of multiple interacting dislocations in $L1_2$ was investigated later using a 2D end-on simulation [233] and both the stress anomaly and high strain hardening rates were reproduced by these simulations. The strength of precipitate hardened materials was investigated by Mohels et. al. [234, 235] for a single dislocation interacting with an array of randomly dispersed coherent spherical particles of different aging conditions at low volume fractions. The effect of incoherent particles, which are unshearable, on the strength was studied later for a range of particle sizes and volume fractions [236, 237]. The interaction of up to four dislocations and superdislocations with arrays of precipitates of varying coherency, size, and $\Gamma_{APB}$ was discussed in [238]. High volume fraction precipitate hardening was studied in superalloys [221], and inverse superalloys [239] (superalloys with $\gamma$ precipitates dispersed in a $\gamma'$ matrix) for a superdislocation shearing through precipitates of different shapes, sizes, and APB energies. The strength was found to vary linearly with the APB energy for small precipitate sizes, while it follows a square-root relationship for larger precipitates. A more realistic dislocation microstructure was modeled in [240] where a number of FR superdislocation sources glide, bow and shear through the precipitate array.

One of the first 3D DDD simulations of superalloys was presented by Shin et. al.

[241] where a dislocation loop was placed surrounding a precipitate under no applied loads. The loop moved under the effect of line tension but did not shrink all the way to the precipitate. It was suggested that the image stress resulting from the mismatch in the elastic properties between the $\gamma$ and $\gamma'$ phases blocked the loop's motion and this could be one of the precipitate hardening mechanisms in superalloys. The effects of precipitate size and spacing on the superalloy strength were studied by Shin et. al. [242], where they simulated a screw dislocation moving with two impenetrable spherical precipitates in its way. Yashiro et. al. [243] simulated the nucleation and motion of superdislocations due to a single FR source inside a single cubic precipitate and the superdislocation's interaction with a network of interfacial dislocations. The gradual loss of precipitate penetration strength in cyclically loaded crystals was modeled by assuming an initial strength that decreases linearly with every dislocation shear [177, 244]. Vattré et. al. studied the effects of precipitate volume fractions, APB energy and channel width on superalloy strength by simulating the interaction of a pair of identical dislocations with a periodic array of cubic precipitates [245]. They also studied the effect of load orientation on crystal strength for superalloys with impenetrable precipitates [22]. It was found that significant hardening takes place when the load is oriented in the multislip direction. The effect of precipitate shape was considered by Huang et. al. through simulating the interaction of superdislocations with shearable precipitates [246]. Yang et. al. studied the effect of the transition from superdislocations bounding APBs to those bounding superlattice intrinsic stacking faults (SISF) that takes place at low temperatures on the superdislocation shearing of precipitates, and they concluded that lower stresses are obtained when the transition takes place [247]. The effect of dislocation climb on the superalloy strength was also investigated through simulating the motion of superpartial dislocations around an unshearable precipitate [248]. Yang. et. al. made an extensive study that takes into account the effects of KW locking and unlocking on superalloy strength and they

were able to match the tension/compression asymmetry found in experiments [23]. The motion of networks of interfacial dislocation in the channels between unshearable precipitates was studied by Liu et. al. where they were able to characterize the effects of the applied, misfit, and interaction stresses on the dislocation activity, especially the formation of Lomer and Hirth junctions [249]. Finally, the effect of the misfit strain on the glide of superdislocations in the channels of an infinite periodic array of crystals was carefully considered by Gao et. al. [183].

Most of the DDD studies described above have used simplified precipitate geometries (cubic or spherical), arrangements (a single precipitate or a regular array of precipitates), and simple precipitate shearing rules where the precipitate can either be unshearable or shearable only by superdislocations. However, a realistic superalloy simulation requires the capability of handling precipitates of geometries and distributions similar to those found in experiments. In addition, the formation of superdislocations in the simulation should take place only if the local stresses and precipitate resistance allow it to happen. This has been challenging for the DDD community in the past due to the geometric complexity of the problem. The target of the study described in this chapter is to extend the DDD framework to take in an experimentally captured precipitate microstructure and simulate the motion of random 3D dislocation distributions of arbitrary Burgers vectors in microcrystals. Dislocations are allowed to shear through the precipitate, loop around them, or cross-slip to avoid them. Superdislocation formation is naturally accounted for when two dislocations with the same Burgers vector pile up on the surface of the precipitate on the same slip plane. The DDD framework has been extended to handle the more complex flow dynamics in superalloys. The necessary extensions to the DDD framework described in Chapter 2 are discussed in the next section.

## 5.5 Computational Method

The main difficulty that arises when modeling general microstructure superalloys (GMS) (a superalloy crystal that has arbitrarily distributed precipitates of arbitrary geometries with a general dislocation microstructure spanning the matrix phase, the precipitates or both) that is not found in pure single phase (PSP) metals is that the forces acting on the dislocations depend on the history of the dislocation activity in the region local to the dislocation segment. In PSP metals, the forces acting on a dislocation segment are those due to the applied stress, interaction stress, and the lattice resistance stress (Peierls stress). These stresses do not depend on the history of the dislocation activity in the region where the dislocation of interest is or anywhere else in the crystal. In GMSs, a fourth force needs to be considered, that is, the APB force. This can be zero, if the dislocation is gliding in the matrix, $\frac{-\Gamma_{APB}}{b}$ if the dislocation is gliding on an undistorted plane in the $\gamma'$ phase, or $\frac{\Gamma_{APB}}{b}$ if it is gliding on a distorted plane in the $\gamma$ phase. Moreover, the mere act of dislocation glide inside the $\gamma'$ phase changes the distortion state of the planar region swept by the dislocation during its motion. In the case of unshearable precipitate this scenario is avoided by blocking the dislocations off any precipitates, and in the case of superdislocations the extra APB force does not act on the dislocation. Either of these two assumptions can greatly simplify the simulation. In more advanced simulations [245], the superdislocation is forced to nucleate by starting with one or two sources and preventing the leading dislocation from penetrating the precipitate until the trailing dislocation gets sufficiently close. Once they penetrate, they move as a pair of dislocations with the appropriate APB force applied on each since their ordering (leading or trailing) is known in advance. After the pair exits the precipitate, no net distortion effect remains so the future glide activity is independent of the pair glide. The handling of the most general case requires explicitly storing and updating the distortion state of every point in the simulation volume. This process amounts to

tracking the APB regions as they get created or destroyed. The APB representation and updating will be discussed next, however, an important prerequisite for APB tacking is a flexible precipitate geometry representation.

### 5.5.1 Precipitate Geometry Representation

Because APB regions exist only inside precipitates, a proper representation of the precipitate geometry is the starting step for any APB tracking implementation. The target representation needs to be flexible so that it can represent all the geometries of interest, be robust in determining whether a point is inside or outside the precipitate, have a low memory footprint so that crystals with hundreds to thousands of precipitates can be efficiently simulated, and have a fast point containment check routine because containment checks will run for all the dislocation nodes in every DDD time step to capture all dislocation penetration and exiting events and handle them properly.

A good candidate representation is the convex hull of a number of 3D points. The convex hull of a set of points is defined to be the smallest convex geometry that contains all the points in the set. A convex geometry is a region $H$ in $\mathbb{R}^n$ such that for all $x, y \in H$, the set $x+(y-x)\eta \in H$ for $0 \leq \eta \leq 1$. That is, any two points inside a convex geometry can be connected by a line segment that lies entirely inside the convex geometry. Any convex geometry is also the intersection of a number of infinite half spaces in $\mathbb{R}^n$. This latter property guarantees the representation robustness because the point containment check reduces to checking the signs of a number of vector dot products. An infinite half space $L^j$ is the set of all $\mathbb{R}^n$ points $x$ such that

$$L^j = x : (x_i - p_i^j)n_i^j \leq 0 \tag{5.2}$$

where $p^j$ is any point on the boundary of the half space and $n^j$ is the vector normal

to the half space boundary in the outward direction. A convex geometry $H$ is then the set defined by

$$H = \cap_{j=1}^{N} L^j = \cap_{j=1}^{N} (x_i - p_i^j) n_i^j \leq 0 \tag{5.3}$$

where $N$ is the number of intersecting half spaces that make up the convex geometry. The point $x$ is outside $H$ unless it is contained in every single half space $L^j$ forming $H$. This also satisfies the last two requirements of the representation. The representation's memory footprint is low as only $6N$ floating point numbers are required to represent the entire precipitate (3 numbers for each $p_i$ and another 3 for each $n_i$). The point containment check is fast because it is linear in the number of half spaces and the complexity of the half space containment check is constant and low.

In terms of the flexibility, the convex hull can represent any convex geometry exactly. For concave geometries, the accuracy of the representation depends on the degree of concavity. Extremely concave and self intersecting geometries are the least accurately represented geometries using convex hulls. According to [213, 217], the precipitates in superalloys usually have spherical or cuboidal geometries, which are both convex. In the current simulations, a concave precipitate will be replaced with its closest convex geometry.

It is of interest to model precipitate geometries obtained from TEM micrographs of superalloy crystals. Through basic thresholding techniques, the precipitate microstructure in a TEM micrograph can be represented as a set of binary pixels as shown in Figure 5.4. Serial sectioning can then be used to represent the entire precipitate microstructure in the form of a number of pixelated layers. The convex hull of the precipitate can be calculated based on the layer pixels if the number of layers is at least two. Points are placed at the pixel locations and used to generate a triangular mesh that represents the convex hull face. Each triangle in the mesh lies on the boundary of one of the half spaces defining the convex geometry. The incremental

convex hull generation algorithm, discussed in [250], is used to generate the convex hull from the pixel locations.

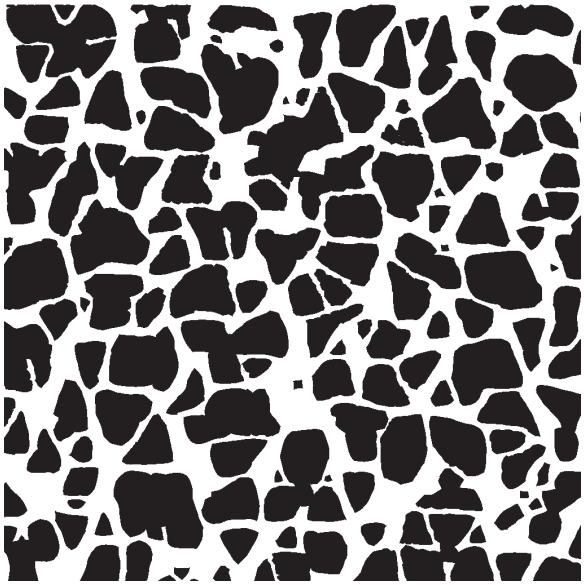

Figure 5.4: A precipitate microstructure after thresholding. The black regions are precipitates while the continuous white region is the matrix

### 5.5.2 APB Tracking

An APB can be represented by its geometry on the slip plane and its shearing Burgers vector. The boundary of an APB region is either a $\frac{1}{2}\langle 110\rangle$ dislocation that separates the sheared from the unsheared regions, the intersection curve of the precipitate that contains the APB region with the slip plane that the APB region is on, or a mixture of both. The most accurate and memory efficient representation for APBs is the one that uses its bounding curves. However, because the bounding dislocations move and interact, tracking how the APB changes shape over time becomes challenging.

An alternative static representation can be realized by using a planar grid of cells on the "APB plane" that coincides with the slip plane of the shearing dislocation and spans the entire crystal, as shown in Figure 5.5(a). Each cell on this grid is either unshearable or shearable depending on whether it lies outside or inside any precipi-

tates. Initially, the system is free of any APB planes, however once a dislocation tries to shear into a precipitate, an APB plane coinciding with the dislocation slip plane is created, and its cells initialized to shearable or unshearable. The APB plane resides in memory for as long as the simulation is running so that if the same dislocation whose motion necessitated its creation, or any other dislocation gliding on the same slip plane, shears all the way through a precipitate, exits, and shears through another, no need for a new APB plane to be added to the system. Each cell stores a shearing vector, $v_i$, which is initially zero. For simulations running on multiple processors, the creation of an APB plane is an event that gets communicated to all the other processors so as to avoid multiplicity (different processors creating the same plane). An increase in the resolution of the APB cells allows for a more precise representation of the APB geometry at the expense of the memory required. Although it is possible to create all the APB planes and distribute them initially based on the slip planes of the initial dislocation microstructure, the dynamic creation and distribution described earlier is necessary to handle more complex mechanisms such a cross-slip where the location of the cross-slip event is not known in advance.

As the dislocations shear through the precipitate, each dislocation segment is tested at every time step to see whether it has swept the midpoint of an APB cell. If no sweeping takes place or if the cell is unshearable the APB state remains the same. If, however, the dislocation swept the midpoint of a shearable cell, the Burgers vector of the dislocation is added to the shearing vector $v_i$ stored for the cell. A cell is considered unsheared if there is an integer $k$ that satisfies the equation

$$v_i - k\langle 110\rangle = \begin{cases} \langle 000\rangle \\ \langle 100\rangle \end{cases} \tag{5.4}$$

which states that with successive dislocation shears, $v_i$, sum up to an even integer multiple of a $\frac{1}{2}\langle 110\rangle$ shifted by at most one $\langle 100\rangle$ vector, the cell is unsheared. This

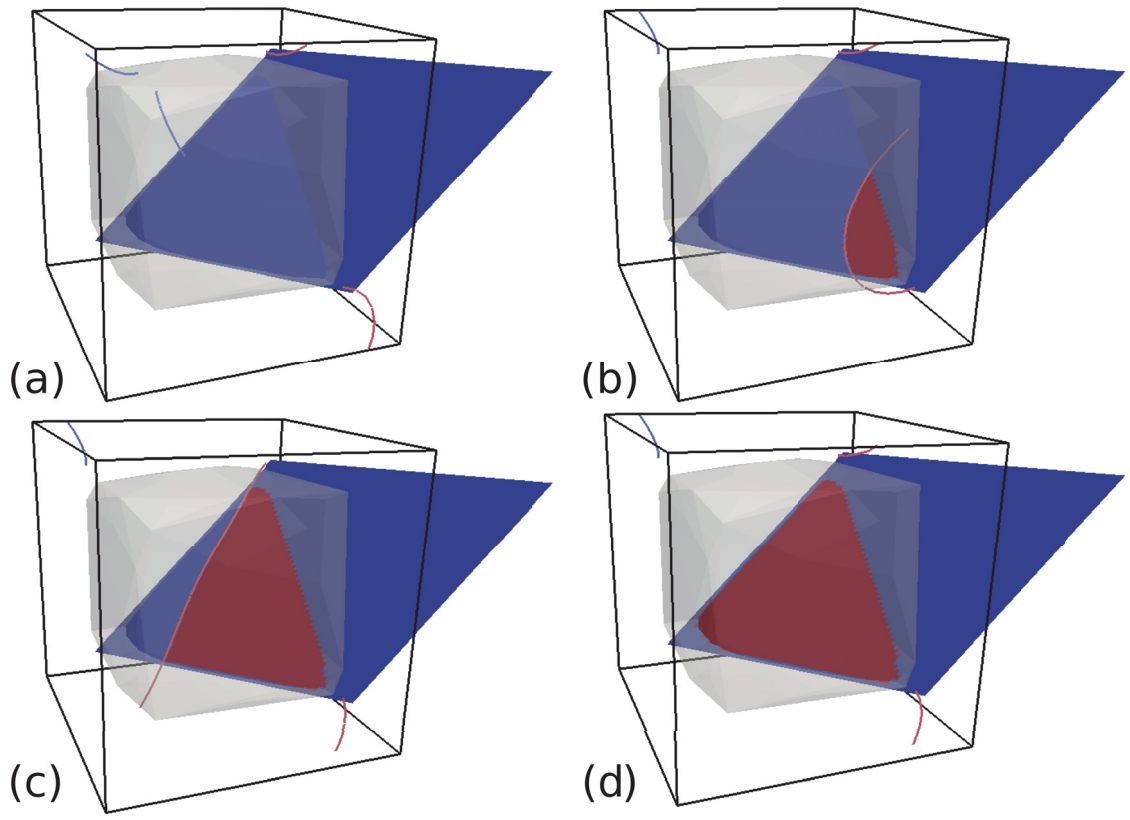


Figure 5.5: A sequence showing A dislocation (red) penetrating a precipitate (grey) and the resulting APB creation process: (a) the APB plane (blue) is initially unsheared; (b) the dislocation penetrates the precipitate and an APB region (red) is created behind it; (c) the dislocation shears a larger area creating a larger APB region behind it and (d) the dislocation exits the precipitate and the entire sheared area in the precipitate is now an APB region.

corresponds to the case of two identical $\frac{1}{2}\langle 110\rangle$ or three mutually different $\frac{1}{2}\langle 110\rangle$ dislocations gliding in succession. If an integer $k$ is found, the cell's shearing vector $v_i$ is reset to zero.

The detection of segment-cell midpoint sweep requires a great deal of precision because any sweeping events that pass undetected would render the APB cell state wrong. For this reason, the 3D configuration is projected onto a 2D configuration where the sweeping detection depends on the sign of a dot product. Figure 5.5 shows the sequence of events associated with the creation of the APB region during the shearing of a precipitate with a gliding dislocation.

### 5.5.3 APB Force Calculation

In order to apply the correct APB forces on dislocations, each dislocation node is tested at every time step whether it is inside a precipitate or not. This justifies the requirement for a fast point containment check discussed in Section 5.5.1. If the initial position of the node is inside a precipitate, a hash search [251] for the APB plane is performed and the dislocation node coordinates are used to determine the APB cell in which this node lies. Because the system would try to minimize the APB sheared area, if the APB cell containing the node is sheared, a force per unit length of magnitude $\frac{\Gamma_{APB}}{b}$ and directed towards the APB cell midpoint (the APB region is attracting the dislocation) is added to the node while the force is directed away from the midpoint (the APB region is repelling the dislocation) when the cell is unsheared. This process is shown schematically in Figure 5.6.

### 5.5.4 Method Validation

The implementation of the APB tracking algorithm described above been validated through a number of planar simulations where a pair of identical $\frac{1}{2}\langle 110\rangle$ dislocations are placed outside a single cubic precipitate and a constant stress is applied as shown in Figure 5.7. The same configuration is loaded at different stress levels and the yield stress is considered the lowest stress that would cause the dislocation pair to move. Periodic boundary conditions are used to eliminate any strength effects associated with the dislocation length.

In this configuration, the leading dislocation needs a shear stress of $\frac{\Gamma_{APB}}{b}$ to penetrate the precipitate. This stress comes from two sources, the applied shear stress $\tau_a$ and the interaction shear stress $\tau_i$ with the trailing dislocation (which is repulsive). The latter is given by [41]

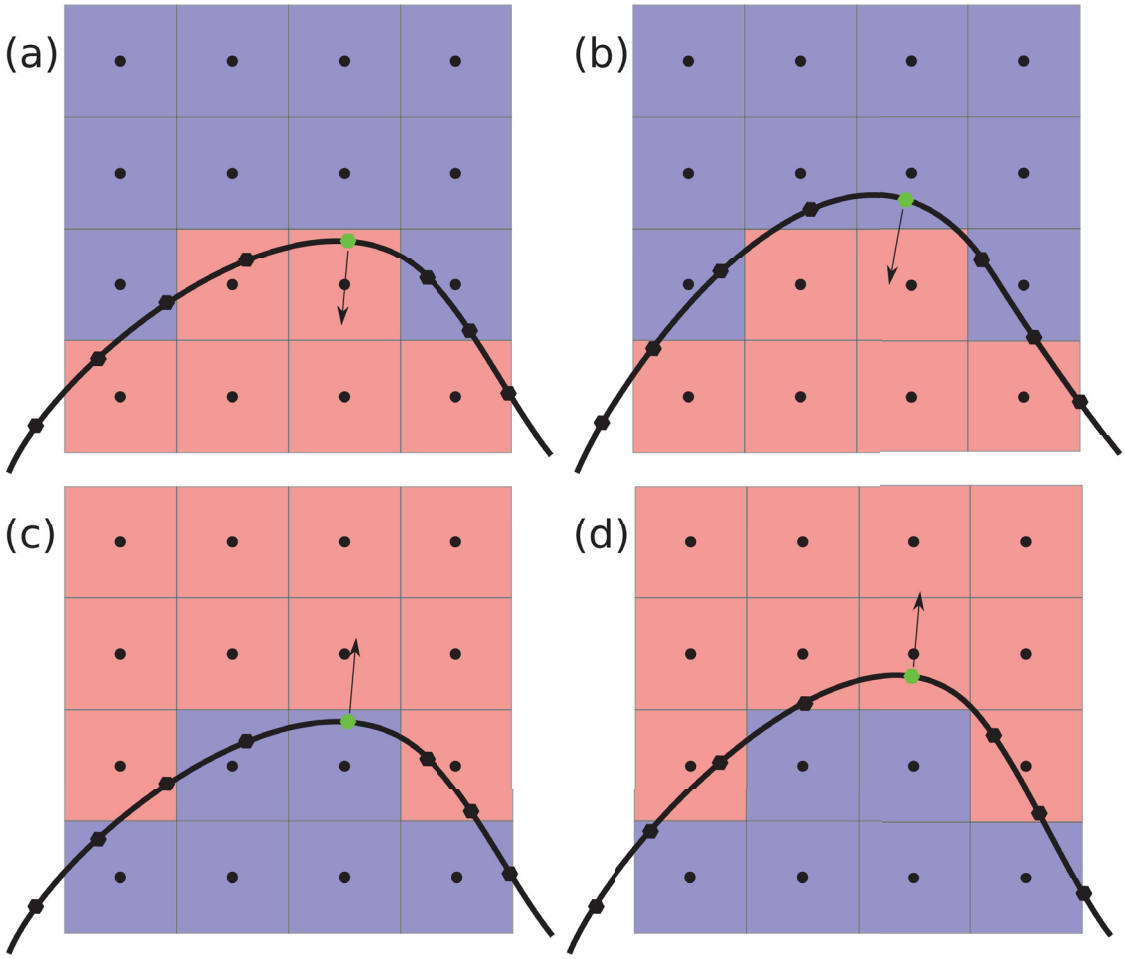


Figure 5.6: A schematic showing the calculation of the APB force direction for a dislocation that is moving upwards. The red APB cells are sheared and the blue ones are unsheared. The black arrow in each case shows the force direction. The APB force direction on the green dislocation node depends on the APB cell it resides in, such that the force is towards the cell's midpoint if the cell is sheared and away from it if it is unsheared because the system tries to minimize the APB region. Hence, in cases (a) and (b) where the APB region is growing, the APB force is resisting the dislocation's motion while in cases (c) and (d) where the dislocation's motion would reduce the APB region, the dislocation is attracted.

$$\tau_i = \frac{\mu b}{d} \tag{5.5}$$

where $\alpha$ is a factor that depends on the dislocations orientation and $d$ is the distance between the two dislocations. At the same time, the distance $d$ depends on the

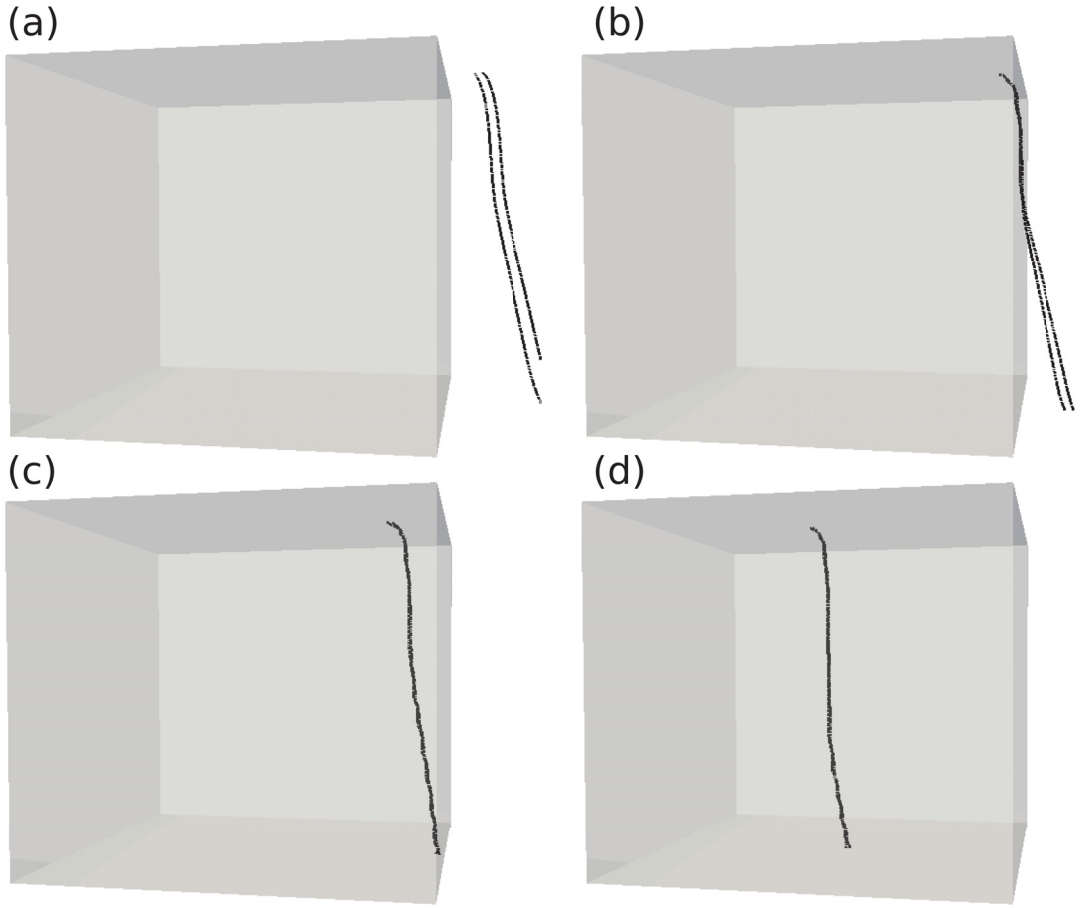


Figure 5.7: A pair of dislocations (black) shearing through a cubic precipitate (grey): (a) the pair is outside the precipitate; (b) the dislocations automatically squeeze into a superdislocation configuration because the leading dislocation is blocked at the surface of the precipitate; (c) the formed superdislocation breaks into the precipitate and (d) glides through it such that the pair are bounding an APB region

applied shear stress $\tau_a$. At zero applied stress, the leading dislocation is blocked by the precipitate surface, as the applied stress increases the trailing dislocation is brought closer to the leading dislocation. Under any applied stress, the trailing dislocation is under static equilibrium between the repulsion from the leading dislocation and the forcing of the applied stress, thus, the equilibrium distance $d_{eq}$ is given by

$$d_{eq} = \frac{\alpha \mu b}{\tau_a} \tag{5.6}$$

where $\alpha$ is a geometric factor. At the applied stress when the leading dislocation penetrates the precipitate, the force equilibrium on the leading dislocation is the balance of the APB resistance on one hand and the applied and interaction stresses on the other

$$\frac{\Gamma_{APB}}{b} = \tau_i + \tau_a = \frac{\alpha\mu b}{d_{eq}} + \tau_a = \frac{\alpha\mu b}{\frac{\alpha\mu b}{\tau_a}} + \tau_a = 2\tau_a \tag{5.7}$$

Hence, the condition for yield is $\tau_a = \frac{\Gamma_{APB}}{2b}$. Figure 5.8 shows the variation of the yield strength with the APB energy for all the simulated cases. A linear variation can be observed as predicted from Equation 5.7. Extrapolating this curve to zero APB energy gives a zero applied stress for yield which is true and has been simulated. A negligible shear stress, on the order of 0.3 MPa was found to be required for yield.

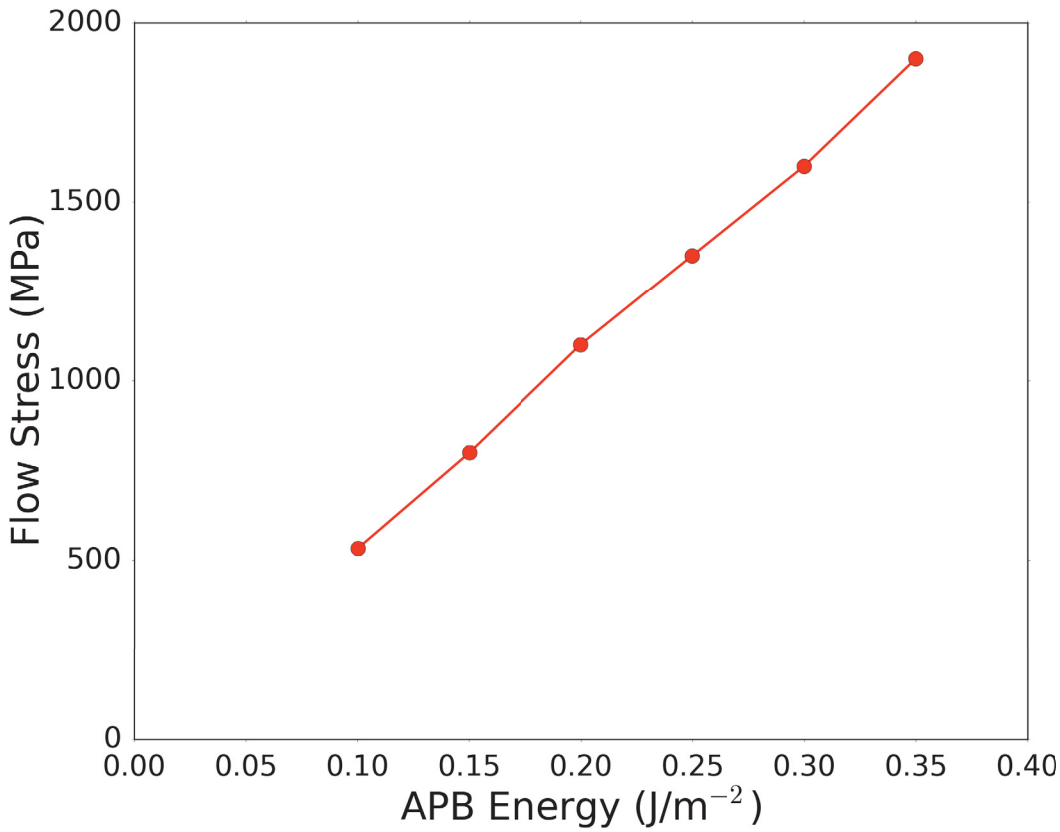


Figure 5.8: The flow stress for the case of a superdislocation shearing through a single precipitate spanning the entire crystal volume versus the precipitate's APB energy.

## 5.6 Numerical Simulations

In this work, Ni based superalloy micropillars with square cross-sections are populated with precipitates of varying sizes, APB energies at different volume fractions and loaded with a constant total strain rate of 500 sec$^{-1}$ in the [001] multislip direction. The aspect ratio of the micropillar is 3 in all cases and the initial dislocation microstructure consists of FR sources uniformly distributed on the twelve FCC slip systems in the $\gamma$ phase with a total dislocation density of $10^{13}$ m$^{-2}$. Dislocation cross-slip is allowed in the matrix only. In these simulations, the effects of three microstructural features, namely, the precipitate volume fraction, the APB energy, the

precipitate size, as well as one geometric feature, the crystal size, on the micropillar strength and dislocation microstructure evolution were investigated. In each study, only one parameter was varied at a time. For the APB energy study, the same initial dislocation microstructure was used for all the tested energies. Three different random configurations were simulated to ensure that the results are statistically significant. The nominal values for the volume fraction, APB energy, average precipitate size and crystal size are 0.7, 0.2 J/m$^2$, 0.3 μm and 1 μm, respectively. For the precipitate volume fraction effects study, the volume fraction was varied as 0.25, 0.5, and 0.7. For the APB energy effects study, the APB energy was varied as, 0.1 J/m$^2$, 0.3 J/m$^2$, and 0.5 J/m$^2$. For the precipitate size effect study, the precipitate size was varied as 0.2 μm, 0.3 μm, and 0.5 μm. For the crystal size study, two crystal sizes of 0.75 μm and 1 μm crystal size were simulated. A baseline simulation of a pure Ni micropillar having the same dimensions as the simulated Ni based superalloy crystals as well as a similar initial dislocation density was used as the case having a zero precipitate volume fraction, APB energy and precipitate size for comparison purposes. In all cases, the precipitates are cuboidal or near cuboidal with sides facing the matrix {100} planes, similar to that reported experimentally [213]. The shear modulus and Poisson's ratio are taken to be 80 GPa and 0.31, respectively, for both the $\gamma$ and $\gamma'$ phases.

## 5.7 Results and Discussion

### 5.7.1 The Effect of Precipitate Volume Fraction

The evolution of the dislocation density with strain for different volume fractions is shown in Figure 5.9. The dislocation density multiplication rate decreases with increasing precipitate volume fraction. The dislocation density evolution follows a pattern of sudden jumps followed low multiplication rate intervals. The jumps cor-

respond to the times when dislocations move across inter-precipitate channels where they can expand at no resistance while the low rate dislocation density multiplication corresponds to the situations when the active dislocations are stuck at a matrix-precipitate interface or are slowly working their way into a precipitate. The dislocation microstructure before loading the crystal and after yielding for different volume fractions is shown in Figure 5.10. In all cases, and due to the lack of initial superdislocations, dislocations avoid shearing the precipitates whenever possible. For low volume fraction cases, no shearing takes place at all because dislocations can avoid precipitate shearing by forming dislocation loops in the wider channels surrounding them, or cross-slipping on planes to avoid the interaction with the precipitate. As the volume fraction increases, dislocations either squeeze into the now narrow channels or they penetrate the high resistance precipitates depending on the channel width and the APB energy. Precipitate shearing in the high volume fraction cases is usually bowing assisted such that a dislocation stuck at the matrix-precipitate interface would start bowing around the precipitate creating a high attractive stress region between the nearby segments of the dislocation. The attractive stress brings the two segments together by shearing through the precipitate until they annihilate. The dislocation then advances through the precipitate and a similar bowed out configuration is recreated resulting in further advancements until the dislocation exits the precipitate from the other end. The bowing assisted shearing process is shown schematically in Figure 5.11.

The engineering stress vs engineering strain curves for single crystal superalloys of varying volume fractions are shown in Figure 5.12. As the volume fraction increases, the flow stress increases. The variation of the yield stress with the volume fraction is linear, which is in agreement with [245], with a slope of about 1800 MPa. The zero volume fraction however does not yield at zero stress because there is an activation stress associated with a FR source that depends on its length. The FR sources used

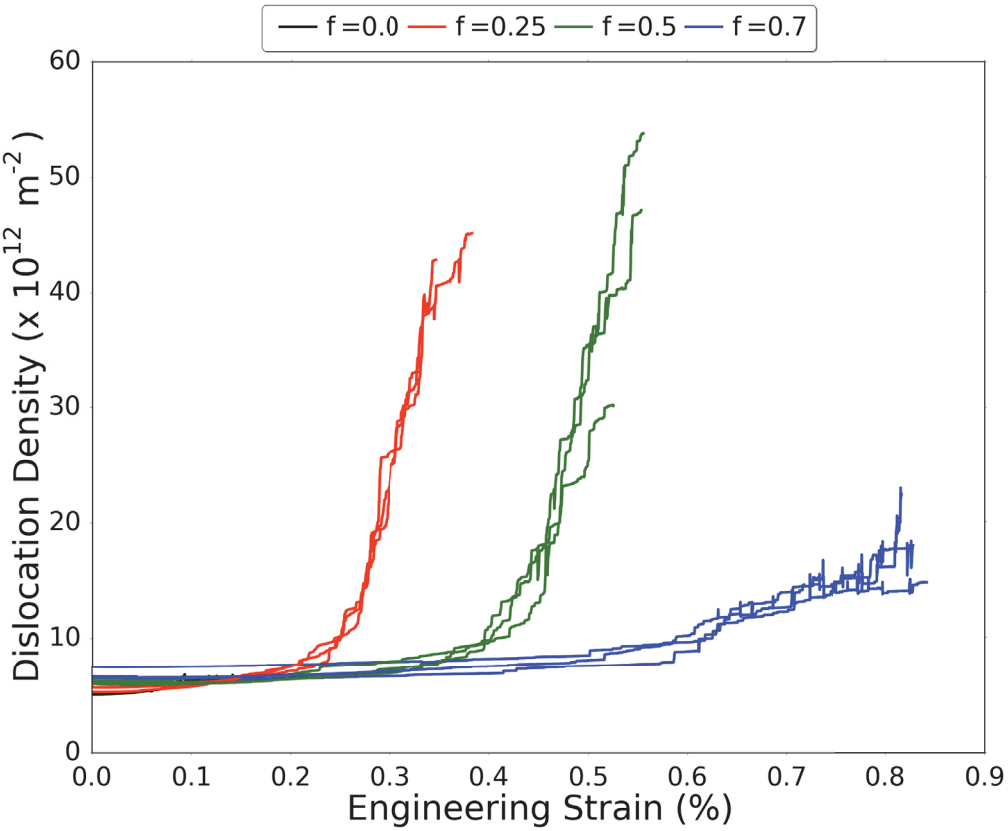


Figure 5.9: The dislocation density-strain curves for crystals of different precipitate volume fractions.

in these simulations have the same length distribution for all volume fractions, hence, the effect of the source length is a constant shift in the flow strength for all cases. The stress-strain curve for the baseline case is also shown in Figure 5.12 for comparison and it shows a baseline strength of 152 MPa, which highlights the strong strengthening effect of precipitates even for low precipitate volume fractions. No strain hardening has been observed in all volume fractions up to the simulated strain level which is in agreement with [23, 245, 252]. It should be noted that the predicted flow stresses are slightly lower than the experimentally reported ones for the same volume fractions [252]. This could be a result of differences in the initial dislocation densities in the simulation and experiments.

Flow occurs when the plastic strain rate reaches the imposed strain rate. For low

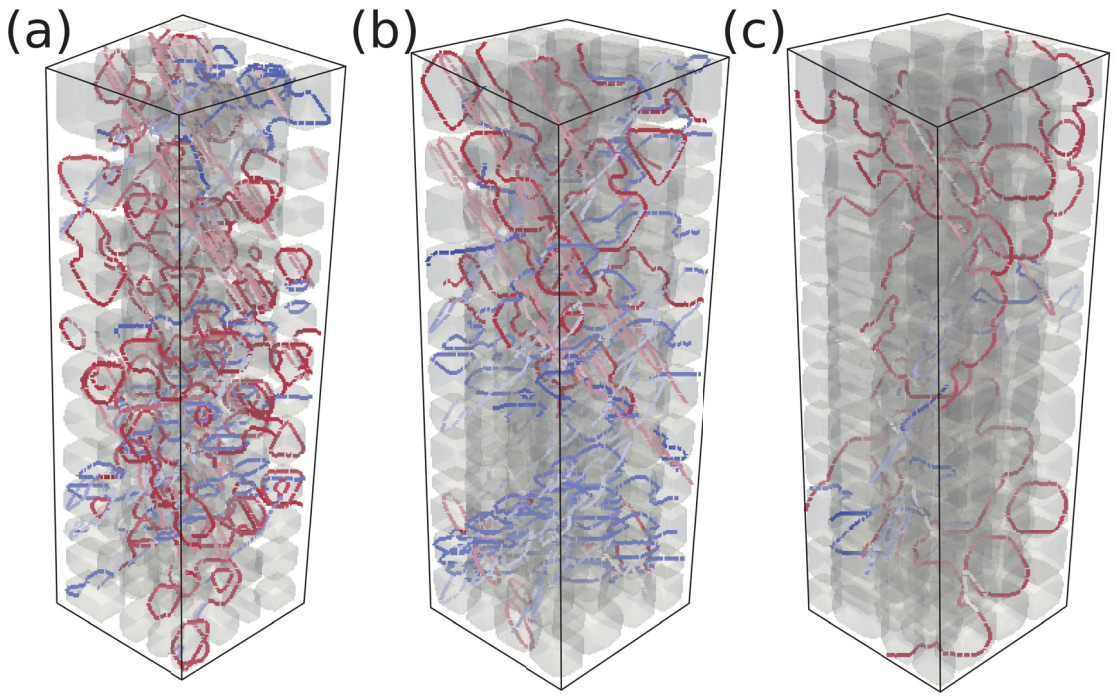


Figure 5.10: The precipitate (grey) and dislocation microstructure after yielding for three different precipitate volume fractions: (a) $f = 0.25$, (b) $f = 0.5$ and (c) $f = 0.7$. The dislocations are color coded according to their slip systems.

volume fraction, the imposed strain rate can be sustained by the dislocation activity in the channels alone because there is a larger area for dislocation expansion, thus, the crystal yields without any precipitate shearing and the strength is determined in this case by the stress required to move the dislocations in the channels, which is in turn dependent on the channel width. As the volume fraction increases, the dislocation activity in the channels drops, increasing the yield strength, for two reasons. First, the stress required to activate the dislocations in the channels increases due to the decrease in the channel width, which is also associated with the increase in the precipitate volume fraction. Second, even when the stress is high enough for channel flow, sustaining the imposed strain rate by channel flow only is more difficult because there is no room for dislocations to expand as required. These observations can be quantified using the dislocation source activation strength expression [41]

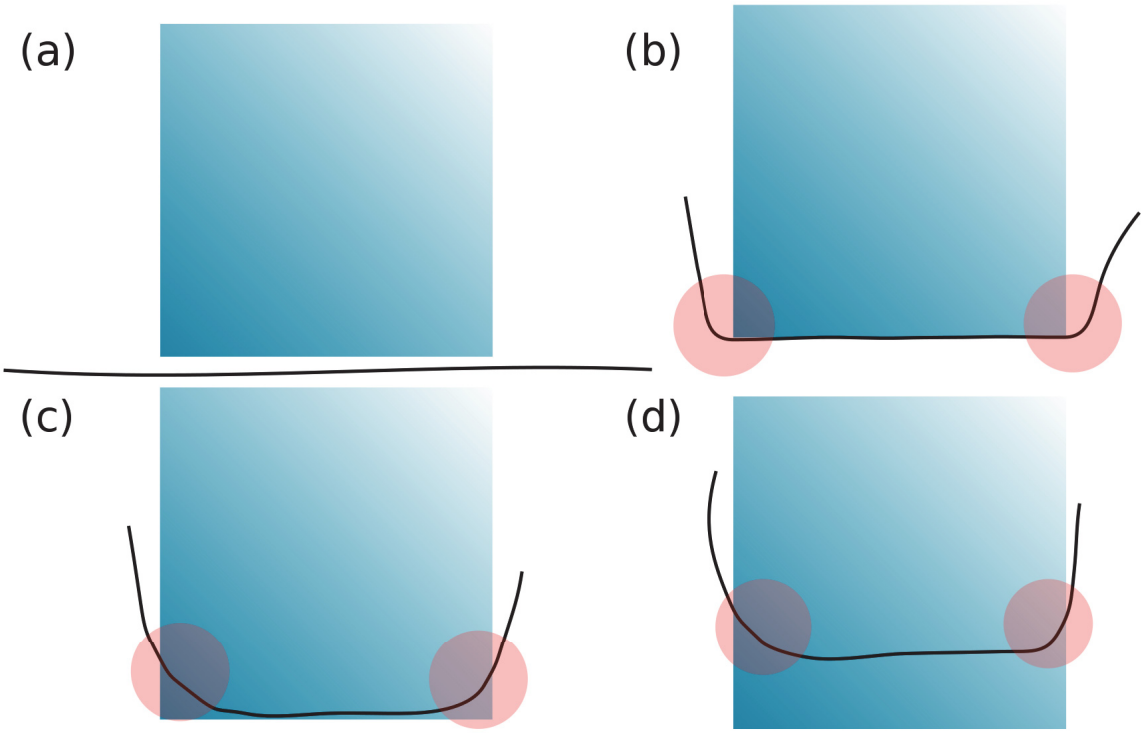


Figure 5.11: A schematic of the bowing assisted cutting process: (a) a straight dislocation segment approaches a precipitate and gets stuck at the $\gamma$-$\gamma'$ interface; (b) the dislocation bows into the channels surrounding the precipitate creating high local self stresses in the regions indicated by the red circles due to the high curvature of the dislocation in that region; (c) the high attractive self stress pulls the blocked dislocation segment into the precipitate; and (d) the dislocation progresses into the precipitate using the same mechanism.

$$\tau = \frac{\mu b}{l} \tag{5.8}$$

where $\tau$ is the activation shear stress, $\mu = 80$ GPa is the material's shear modulus, $b = 0.25 \times 10^{-9}$ m is the magnitude of the dislocation's Burgers vector, and $l$ is the source length. In the case of channel flow, the active glide length is the channel width $l = w$, where $w$ is the channel width. The reported stresses are the applied (axial) stresses, hence, dividing by the Schmidt factor $m = 0.408$ gives a flow stress

$$\sigma_f = \frac{\mu b}{mw} \approx \frac{49}{w} \tag{5.9}$$

The channel width in the current simulations is not constant but the average width can be estimated. For cubic precipitates, which is the case in the current simulations, the average crystal volume, $d^3$, that contains only one precipitate, can be approximated as the unit precipitate cube. From the definition of the volume fraction

$$f = \frac{r^3}{d^3} \tag{5.10}$$

where $r$ is the precipitate's side length. The average channel width $\bar{w}$ is equal to the difference between the unit precipitate cube side length and that of the precipitate.

$$\bar{w} = d - r = d - d\sqrt[3]{f} = d(1 - \sqrt[3]{f}) \tag{5.11}$$

In the current simulations, there are about 192 cubic precipitates in a $1 \times 1 \times 3$ $\mu$m$^3$ crystal, thus $d = 0.25$. Substituting back in equations 5.11 and 5.9

$$\sigma_f \approx \frac{196}{1 - \sqrt[3]{f}} \tag{5.12}$$

Equation 5.12 gives a flow strength of 530 MPa, 950 MPa and 1748 MPa for 0.25, 0.5 and 0.7 volume fractions, respectively. The first two estimates match the ones obtained from the simulations while the third is 34.5% higher. Because dislocations shear through the precipitates in the high volume fraction cases, the strength determining factor becomes the precipitate resistance, which depends on the APB energy, rather than the channel width, and thus, Equation 5.12 cannot be used.

The average number of cross-slip events before plastic flow was 112, 61 and 12 for the cases of 0.25, 0.5 and 0.7 volume fractions, respectively. The decrease in the cross-slip frequency with volume fraction, even though the applied stress reaches higher levels, is because the probability of a dislocation orienting itself near the screw-orientation in a channel decreases with decreasing channel width. Unlike what was

discussed in Section 3.6, the cross-slip activity did not result in strain hardening in all cases because of the qualitative difference between the dislocation microstructures developed in the superalloys and the single phase crystals. In the former, no dislocation patterns or entanglements were observed in contrast with thick localized and highly interconnected dislocation networks observed in the latter, especially for bigger crystals.

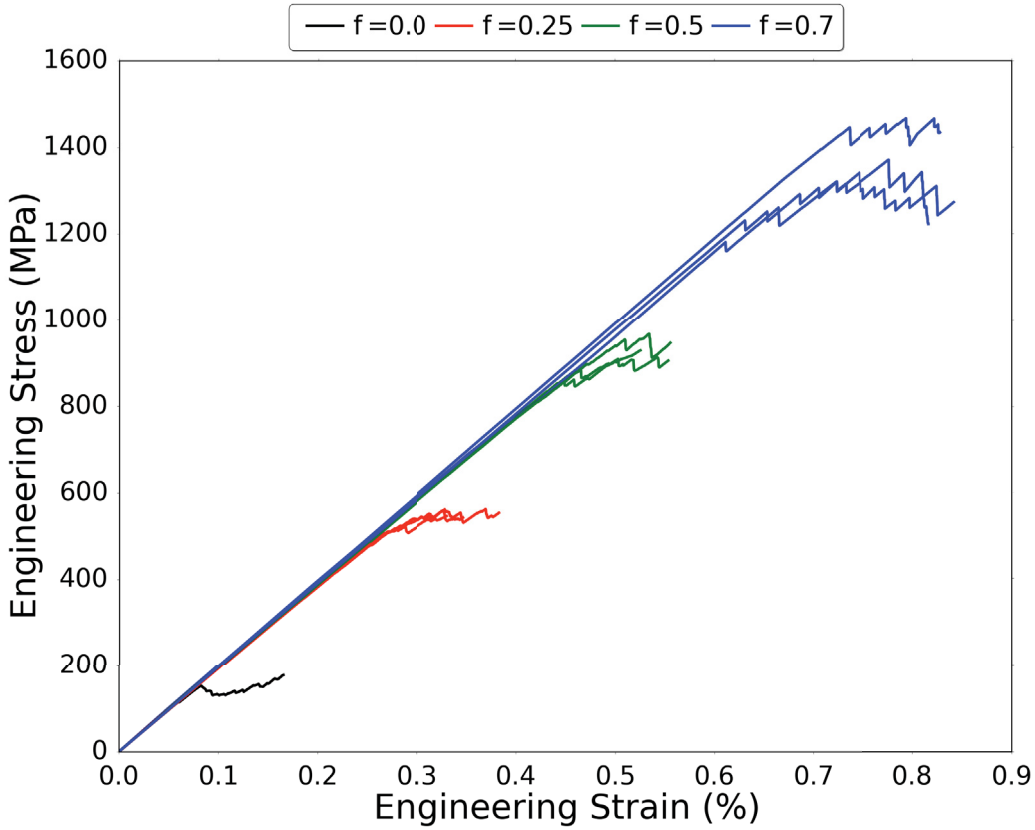


Figure 5.12: The engineering stress-strain curves for crystals of different precipitate volume fractions.

### 5.7.2 The Effect of the APB Energy

The engineering stress versus engineering strain curves for crystals of the same size, dislocation density and precipitate microstructure but having different APB energies

are shown in Figure 5.13. The strength-APB energy relation approximately follows a power-law of the form

$$\sigma_f \approx 2000(\Gamma_{APB})^{0.4014} + 150 \tag{5.13}$$

where $\sigma_f$ is in MPa and $\Gamma_{APB}$ is in J/m$^2$. It should be noted that previous simplified DDD simulations predicted a square-root dependence on the APB energy for planar [221] and 3D single precipitate [245] simulations, respectively, while in the current simulations the dependence is slightly weaker than a square-root dependence (power-law exponent is 0.4). As the APB energy increases, the precipitate resistance increases and it becomes more difficult for the dislocations to penetrate and glide through the precipitates. For the case of an infinitely long dislocation penetrating an infinitely large precipitate, the shear stress required is $\tau = \frac{\Gamma_{APB}}{b}$ which gives an ideal flow strength of

$$\sigma_f^{id} = \frac{\Gamma_{APB}}{mb} \approx 9.8\Gamma_{APB} \tag{5.14}$$

This gives an ideal flow strength of 0.98 GPa, 1.96 GPa and 4.9 GPa for the simulated 0.1 J/m$^2$, 0.2 J/m$^2$ and 0.5 J/m$^2$ APB energies, respectively. For the lowest APB energy, the predicted flow strength from the current DDD simulations is close to the ideal strength, while for the two higher energies, the strength deviates significantly. This is because in the ideal case, the dislocation has to directly penetrate the precipitate for yielding, in the current simulations, however, dislocation glide through the channels provides some plastic strain rate carrying capacity. According to Equation 5.12, the maximum flow strength for this volume fraction (if no precipitate penetration takes place) is about 1.75 GPa. In addition, dislocation penetration is bowing assisted so an overall lower applied stress is required for penetration. However, bowing assisted cutting is still sensitive to the APB energy as the bowing angle should

increase before cutting takes place to provide enough attractive interaction stress for the shearing dislocation segments. As the APB energy increases, the yield strength is expected to plateau at 1.75 GPa when the APB energy becomes too high for any shearing to take place.

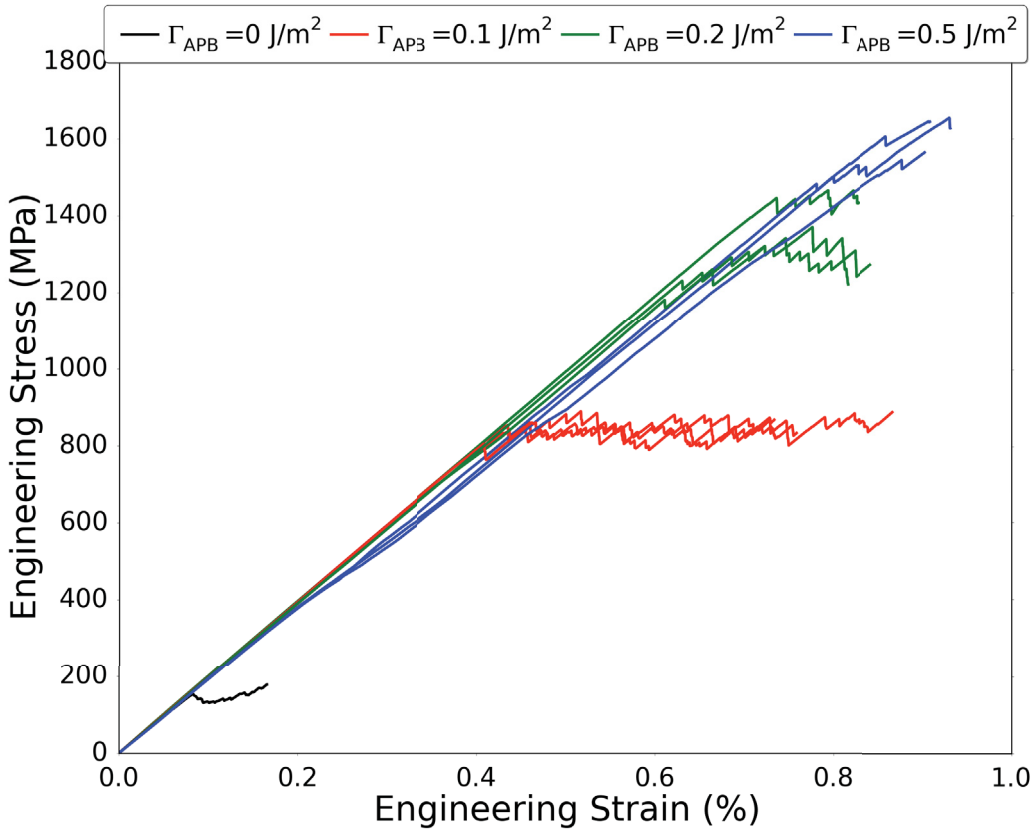


Figure 5.13: The engineering stress-strain curves for crystals of different precipitate APB energies.

The dislocation density evolution with strain for the different APB energies is shown in Figure 5.14. The density multiplication rate increases with increasing the APB energy because more dislocations favor channel glide, which results in an increase in their lengths. The final microstructure after yielding at different APB energies is shown in Figure 5.15 (the three cases have the same initial dislocation microstructure). The final microstructure consists primarily of dislocation loops surrounding

the precipitates in the high energy case, with fewer loops in the intermediate energy case and none for the lowest energy case. These loops form when dislocations bow around a precipitate, fail to shear through it, and end up looping around the precipitate. These loops become immobile, which also partially explains the high strength observed. With fewer mobile dislocations, higher stresses are required to move the dislocation at a rate at which they can sustain the imposed plastic strain. Precipitate shearing takes place, even for the higher energies, when the area of intersection between the precipitate and the dislocation's slip plane is small. The flow in the low energy case was found to be rather smooth in contrast to a more intermittent flow in the high energy case. For low APB energies, the precipitate penetration stress is lower than the channel flow stress, so channel flow never occurs. The dislocations glide through both the precipitate and the channel without any bowing or squeezing into the channels and the flow is smooth. As the APB energy increases, dislocations get stuck at channel entrances until the stress builds up to a high enough value for their bowing into the channels. After which they bow, squeeze, and glide at a high speed, due to the high stress, until they get stuck on the surface of another precipitate and another channel flow gets activated, which explains the flow intermittency. The accumulation of dislocation loops on the precipitate surfaces in the high energy case indicates the possibility of strain hardening at higher strain levels because the channels in which the loops accumulate would resist further dislocation flow in them through mutual repulsion.

No significant cross-slip activity was observed for all APB energies. In particular, the average number of cross-slip events before yielding is 12 for the lowest two APB energies and 19 for the highest energy. The weak dependence of the cross-slip frequency on the APB energy can be indirect where the flow stress increases with APB energy and, because cross-slip is stress assisted, it increases the cross-slip potential in turn. The majority of the cross-slip events in the high energy case were of the surface

cross-slip type. No dislocation patterns developed for all APB energies for the strain levels simulated here.

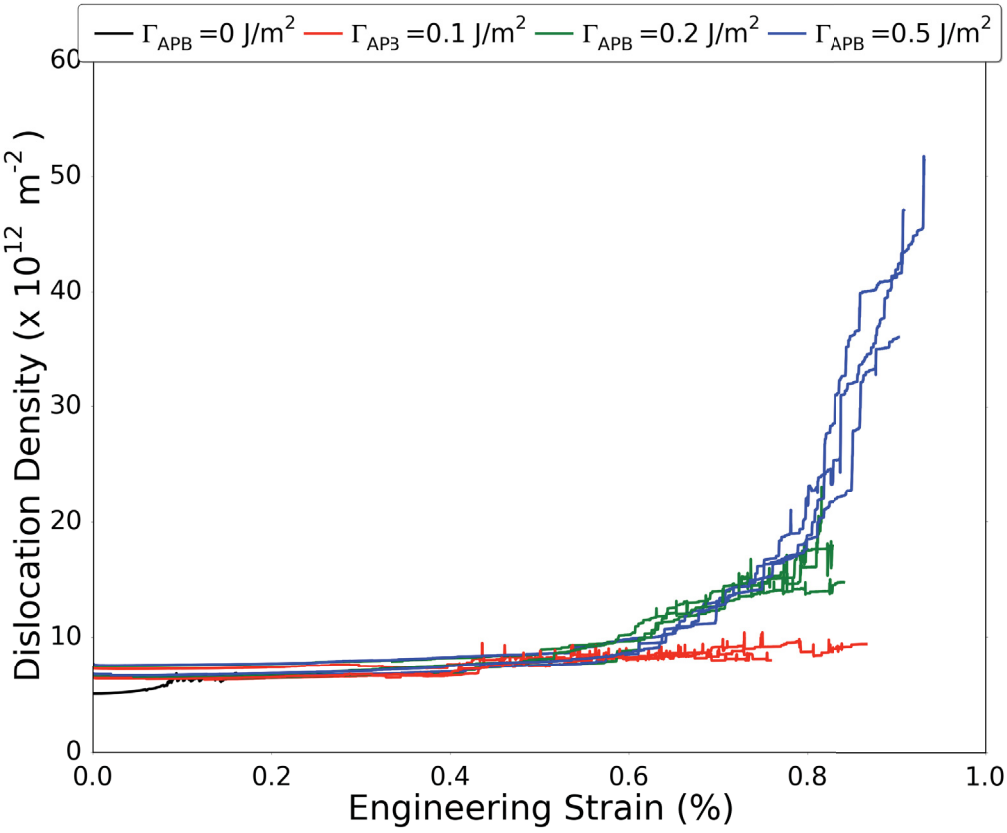


Figure 5.14: The dislocation density-strain curves for crystals of different precipitate APB energies.

### 5.7.3 The Effect of the Precipitate Size

A dislocation forming a loop around a smaller precipitate would require less applied stress to shear through it compared to another looping around a bigger precipitate. This is because the attractive stress between the dislocation segments on either side of the precipitate is the main driver for the shearing, and for smaller precipitates, the segments are closer to each other. The whole, however, is not the sum of its parts when it comes to the effect of the precipitate size on the overall micropillar strength. Figure

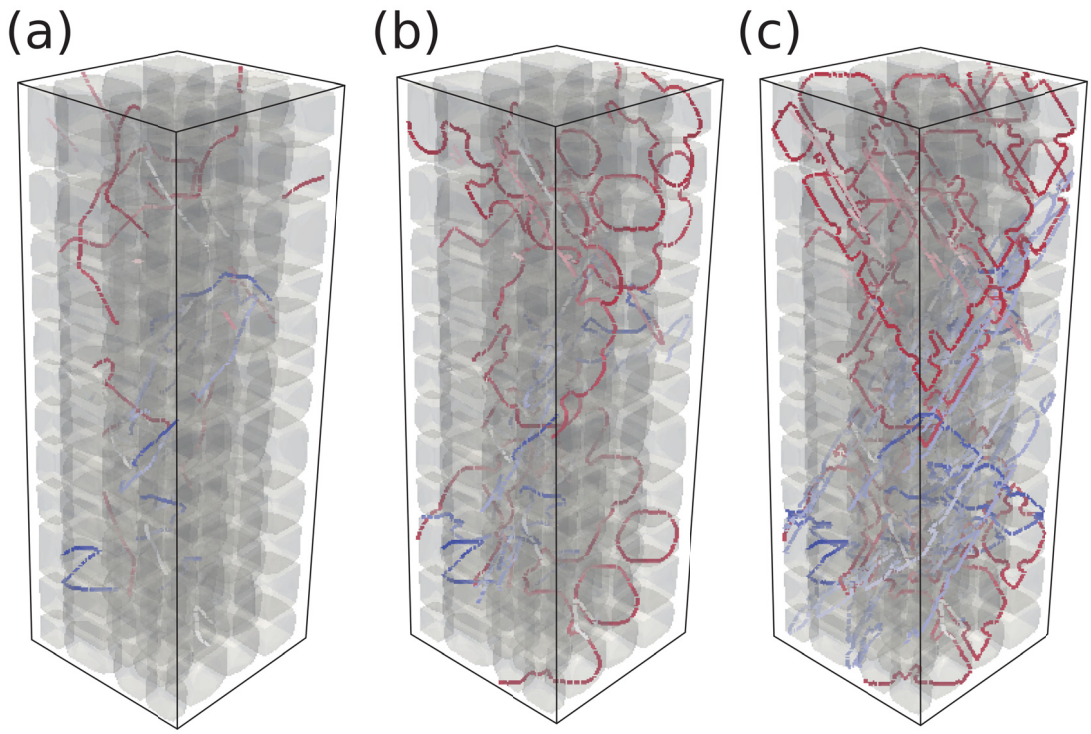


Figure 5.15: The precipitate (grey) and dislocation microstructure at yield for precipitates with different APB energies: (a) $\Gamma_{APB} = 0.1$ J/m$^2$, (b) $\Gamma_{APB} = 0.2$ J/m$^2$ and (c) $\Gamma_{APB} = 0.5$ J/m$^2$. The dislocations are color coded according to their slip systems.

5.16 shows the engineering stress-strain curves for same sized micropillars, having the same precipitate volume fraction, and APB energy, but different precipitate sizes. The flow strength decreases with increasing precipitate size and the relationship can be described by a power-law

$$\sigma_f \approx \frac{568}{r^{0.5832}} + 150 \tag{5.15}$$

where $\sigma_f$ is in MPa and $r$ is the precipitate side length in microns. A similar trend was reported in [221] from planar simulations of superdislocations. The analytical expression by Reppich [253] for the shear strength required for defeating a regular array of precipitates has an inverse square-root relationship between the strength

and the precipitate size, although the expression is more complicated than Equation 5.15. The large precipitate size cases show mild strain hardening but it cannot be confirmed whether it is consistent hardening or just a temporary stress build-up for the low strain levels modeled here.

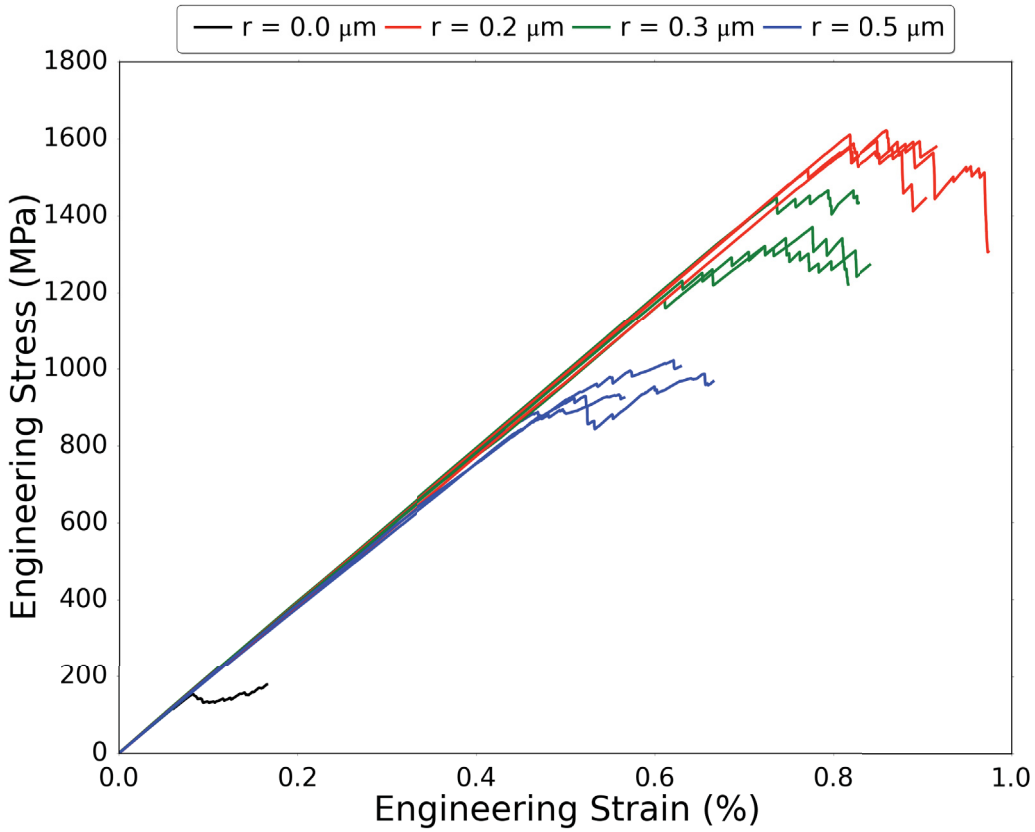


Figure 5.16: The engineering stress-strain curves for crystals of different precipitate sizes.

Bowing assisted cutting is easier for smaller precipitates, as explained above, which lowers the applied stress required for yielding, however, as the precipitate size decreases, the channel size decreases for the same volume fraction. From Equation 5.10, one can rewrite Equation 5.11 for $\bar{w}$ as

$$\bar{w} = d - r = \frac{r}{\sqrt[3]{f}} - r = r(\frac{1}{\sqrt[3]{f}} - 1) \tag{5.16}$$

substituting in Equation 5.9 and setting $f = 0.7$

$$\sigma_f \approx \frac{49}{r(\frac{1}{\sqrt[3]{f}} - 1)} = \frac{388.12}{r} MPa \tag{5.17}$$

which is different than Equation 5.15 in that it has a different precipitate size exponent. The values are off by 21%, 0.4% and −22% from the ones reported from the current DDD simulations because Equation 5.17 does not take into account the effects of the dislocation interaction stresses. From these results, it is clear that the effect of the channel width on the flow strength is stronger than that of the interaction stress that causes the bowing assisted cutting. Huang et. al. [246] studied the effect of different precipitate sizes but the same channel width (through changing the crystal size) and they concluded that larger precipitate crystals are stronger. This prediction is similar to the current one although the result is seemingly contradictory. This can be explained by that in [246] both the effects of the crystal size and precipitate size were considered while in the current simulations, it is the effects of the precipitate size and channel width that are considered. In all cases, one can only isolate the effects of one geometric parameter out of the three (precipitate size, channel width and crystal size).

The dislocation density multiplication increases with increasing the precipitate size as shown in Figure 5.17. An intermittent dislocation activity, similar to the one observed for high APB energy precipitate microstructures, is observed for the cases with larger precipitates. From the final dislocation microstructures shown in Figure 5.18, one can observe a large number of dislocation loops in the 0.5 μm precipitate size cases compared to more straight dislocations for smaller precipitates. This means that although the large precipitate microstructure crystal is weaker, the main flow mechanism is channel flow not precipitate shearing, while the opposite is true for smaller precipitate crystals that experience precipitate shearing but in a more difficult manner due to the narrower channels. The dislocations in small precipitate

crystals, $r = 0.2$ μm, form complete or near complete loops surrounding a group of precipitates, rather than individual precipitates, as shown in Figure 5.19 before they shear and collapse within the crystal, which explains the low density multiplication rate observed in smaller precipitate crystals. This occurs because the channels are not wide enough for the dislocations to squeeze into them under the applied stress and the interaction stress between the different segments of the dislocation is weaker because the dislocation loop is larger in radius as it surrounds a number of precipitates. A weakest-link like mechanism takes place in this case when two dislocation segments on the same loop approach each other by gliding in the widest channel until they collide and pinch off, spawning a number of smaller loops that can collapse independently. This corresponds to a spike in the dislocation density where the total length increases instantaneously and then drops immediately after the loop collapse. The average number of cross-slip events for the 0.2, 0.3, and 0.5 μm cases after yielding are 8, 12 and 55, respectively. Similar to the different volume fraction cases, the change in the channel width allows for more cross-slip to take place.

### 5.7.4 The Effect of the Crystal Size

From the previous three discussions regarding the effects of volume fraction, APB energy, and precipitate size, it is apparent that the most important factor determining the superalloy strength at room temperature is the inter-precipitate channel width. Similar conclusions were presented in [245, 246]. On the other hand, the effects of crystal size on its strength in pure metals have been well established [131, 254]. In [131], the size effect was explained in terms of the probability of finding a dislocation (FR source, single arm source or a dislocation segment in a dislocation network) in a crystal of a particular size and how this probability decreases with crystal size. For superalloys however, the intrinsic length scale that controls the strength is the channel width. The engineering stress-strain curves for crystals of different sizes but the same

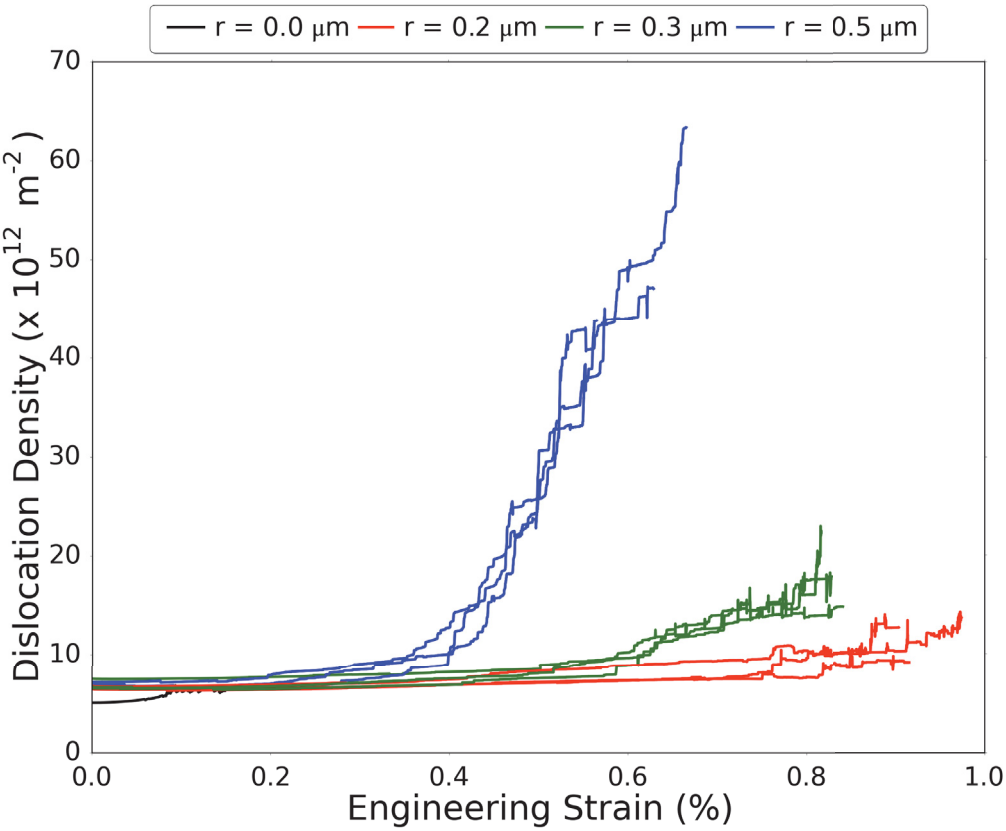


Figure 5.17: The dislocation density-strain curves for crystals of different precipitate sizes.

precipitate volume fraction, APB energy, and size (hence, same channel width) are shown in Figure 5.20. It is apparent that the crystal size weakly affects the crystal strength for the two crystal sizes modeled here. More, and longer, dislocation sources are expected in larger crystals and their plastic strain carrying capacity makes larger crystals weaker. However, in the case of superalloys, the strength slightly decreases because there is a higher probability of finding a dislocation that is highly stressed to squeeze into a channel or bow and induce precipitate cutting. The experiments conducted by Shade et. al. [255] on Rene N5 microcrystals showed that the strength is independent of the crystal size where the exponent in the strength size relationship was estimated to be as low as 0.05. The dislocation density multiplication rate is more or less the same for both crystal sizes as shown in Figure 5.21. The average

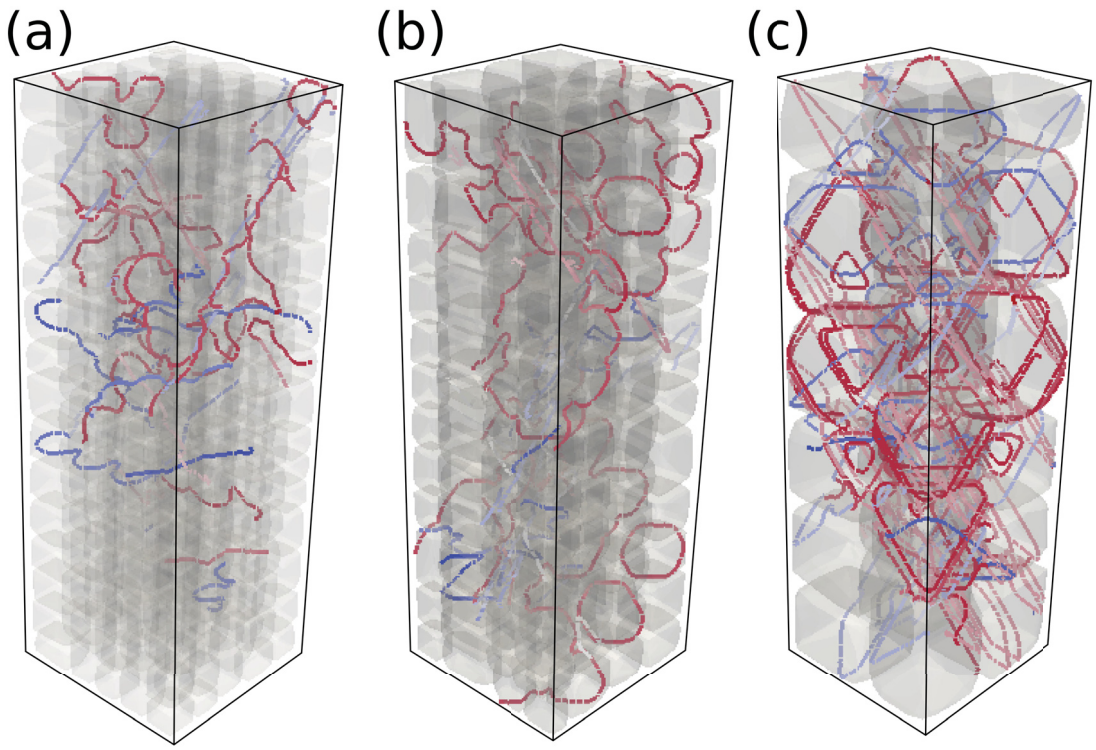


Figure 5.18: The precipitate (grey) and dislocation microstructure at yield for precipitates of different sizes: (a) $r = 0.2$ μm; (b) $r = 0.3$ μm; and (c) $r = 0.5$ μm. The dislocations are color coded according to their slip systems.

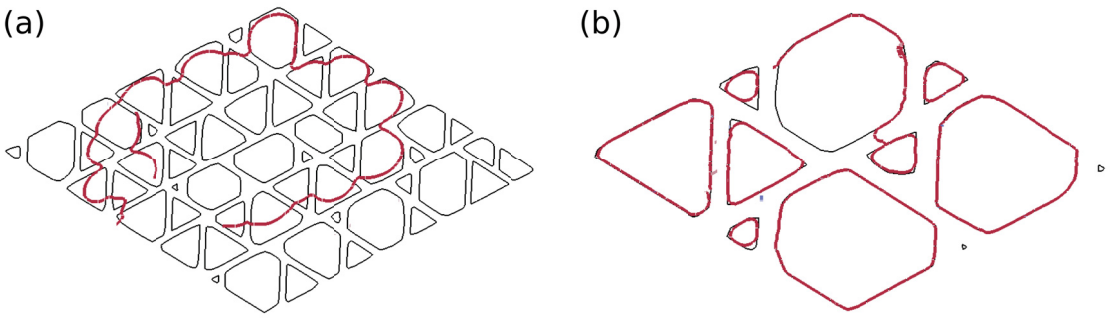


Figure 5.19: A cross-section in two crystals with different precipitate sizes: (a) $r = 0.2$ μm and (b) $r = 0.5$ μm. The dislocation line is in red and the precipitates are in black.

cross-slip events counts before yield were 5 and 12 for the 0.75 μm and 1 μm crystal sizes, respectively, which is in agreement with the trends of the cross-slip event counts with size discussed in Section 3.7.3.

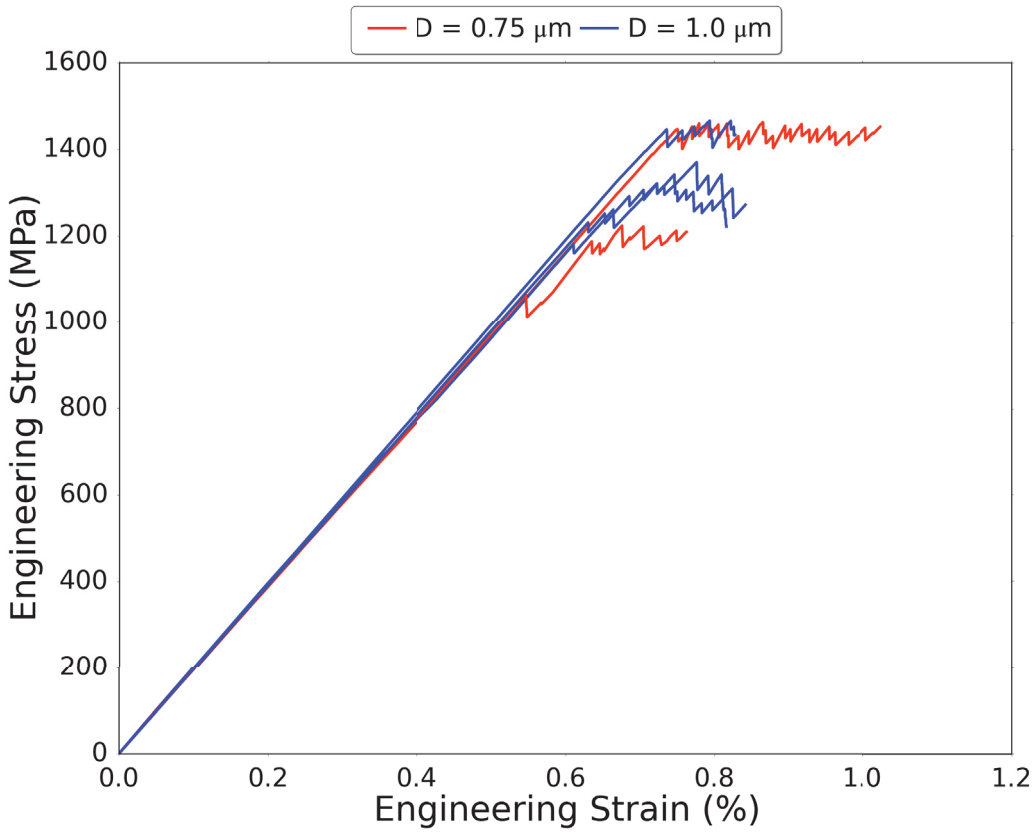


Figure 5.20: The engineering stress-strain curves for crystals of different sizes.

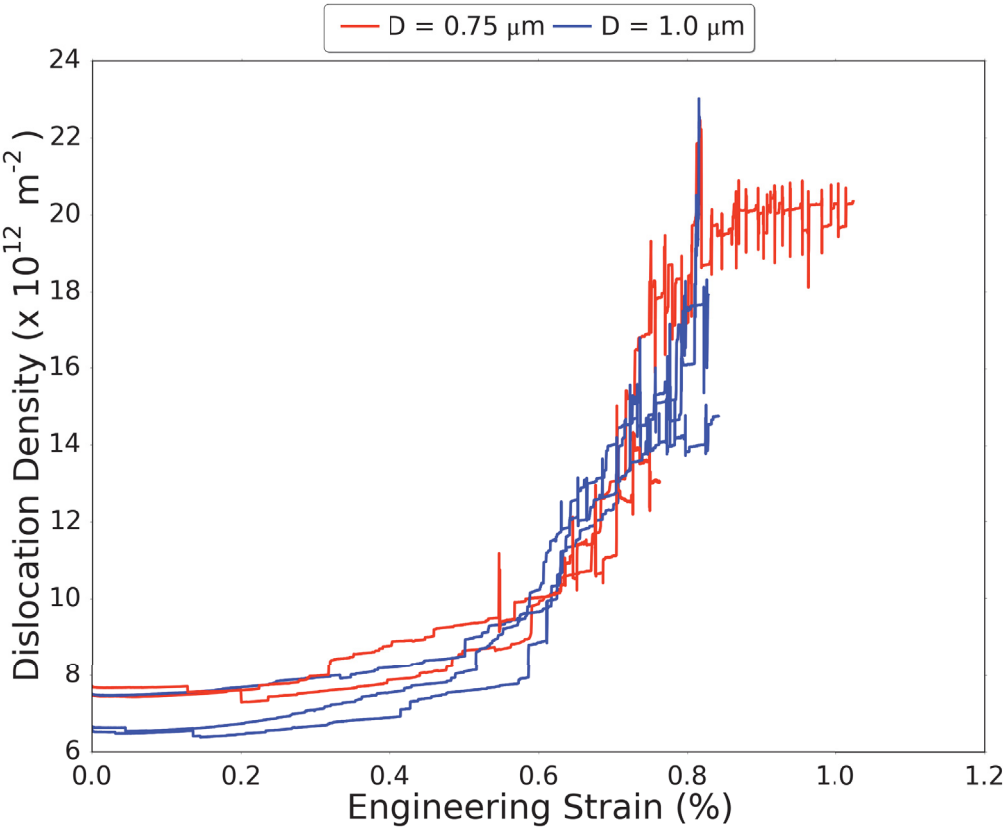


Figure 5.21: The dislocation density-strain curves for crystals of different sizes.

## 5.8 Summary and Conclusions

In this chapter, the DDD framework described in Chapter 2 has been extended to model the interaction of general dislocation microstructures residing initially in the $\gamma$ phase with an arbitrary distribution of $\gamma'$ precipitates with focus on experimentally observed precipitate microstructures. The implementation was validated through calculating the flow strength of an ideal configuration where an infinitely long superdislocation interacts with a cubic precipitate. Excellent agreement between the predicted flow strength from the current simulations and the analytical predictions was found. A number of Ni based superalloy micropillars with different precipitate microstructure were loaded monotonically in order to study the effects of the precipitate volume fraction, APB energy, precipitate size, and crystal size on the strength and the dislocation microstructure evolution. The following summarizes key observations.

- The crystal's strength varies linearly with the precipitate volume fraction.
- At low volume fractions, the dislocation density multiplication is faster and cross-slip in the $\gamma$ phase is more frequent.
- The strength-APB energy relationship follows a power law with an exponent of 0.4014, close to the square-root dependence previously predicted in other planar DDD simulations.
- The strength-precipitate size relationship follows an inverse square-root law in agreement with the analytical model by Reppich [253].
- The crystal size does not influence the micropillar strength.
- The most influential factor on the crystal's strength is the channel width.
- As the volume fraction increases or the APB energy decreases, the dislocation glide shifts from channel flow to precipitate shearing.

- No strain hardening has been observed in all cases up to the simulated strain level.

# Chapter 6

# Conclusions and Suggested Future Directions

## 6.1 Summary and Conclusions

In this work, the DDD method was utilized to study a number of phenomena related to the deformation and failure of metallic material systems. The details of the DDD framework, the necessary extensions and a number of post-processing methods were fully described. The problems presented in this dissertation focused on materials, loading, and environmental conditions usually found in aerospace applications. The target was to provide more details and a better physical understanding of the active dislocation mechanisms during plastic flow and failure. The results of the current simulations can be hierarchically incorporated into higher length scale simulations for a more physics-based predictions of a component/structure life.

Three cross-slip mechanisms, bulk, surface and intersection cross-slip, which have been recently identified from atomistic simulations, have been implemented for the first time into the DDD framework and a number of simulations were performed to study the effects of cross-slip types on the mechanical response and dislocation

microstructure evolution on nickel single crystals under monotonic loading. Strain hardening has been observed in larger crystals ($D \geq 5$ μm) at low strains ($\epsilon \leq 0.5\%$) when cross-slip was enabled. No similar hardening takes place in smaller crystals or when cross-slip is inactive. Cross-slip was also found to greatly facilitate the dislocation density multiplication irrespective of the crystal size. A precursor to the formation of dislocation cell like structure is the increase in the number of dislocation fixed points, which result from excessive local dislocation collisions, a behavior which was found to increase when the cross-slip is active. Consequently, dislocation patterning has been observed in larger crystals ($D \geq 5$ μm) when all cross-slip mechanisms were active. These simulations were in excellent agreement with experimental observations. When only one mechanism is active, dislocation patterning did not emerge up to the simulated strain level. The formation and thickening of surface slip bands has also been observed when surface cross-slip was active as opposed to the no cross-slip case where surface slip was more localized on certain slip planes. This explains the observed slip band thickening observed during micropillar compression experiments. Bulk cross-slip was found to be the least frequent cross-slip type, followed by intersection cross-slip and then surface cross-slip. In most DDD simulations to date, only bulk cross-slip has been taken into account, which led to erroneously not predicting dislocation patterning. The current frequency results emphasize the importance of considering all the different cross-slip types.

With the cross-slip mechanisms implemented, the behavior of nickel single crystals under cyclic loading was studied through two types of DDD simulations. First, free standing single crystals of different sizes and initial dislocation densities with an initial dislocation microstructure consisting of randomly distributed FR sources were loaded in fully reversed constant strain rate cyclic loading. Larger crystals showed early cyclic hardening, rapid dislocation density multiplication and the evolution of dislocation cell like structures after a few number of loading cycles. Similar to the

case of monotonic loading, the formation of dislocation cell structures was found to rely on the generation of fixed dislocation points which in turn depends on the cross-slip frequency. Larger crystals show dislocation cell structure formation at a lower number of cycles compared to smaller crystals even when the initial dislocation density is lower. It is possible that there is a size dependent initial dislocation density beyond which dislocation cell structures form. However, this has not been confirmed in the current simulations due to the limitations on the number of loading cycles imposed by the computational requirements. The dislocation cell structures have sizes and wall thicknesses that depend on the crystal size but not on the number of cycles. As the loading continues, more cells develop external to the already developed cells and cell refinement does not take place. The surface roughness of the simulated crystals has been quantified as well and it was found that in smaller crystals, the surface roughness is localized to thick bands where most of the plastic activity takes place, while in larger crystals they are spread out over the entire surface of the crystal. The surface step growth rate was quantified and it was found that the step growth is rarely reversed even though the loading is fully reversed. Second, crystals initially containing a well developed PSB structure with periodic boundary conditions in all three directions were loaded cyclically in the same fashion as the free standing crystals. The PSB walls did not move at all during the simulations and the edge dipolar loop forming them showed minimal to no motion. The screw dislocations in the PSB channels on the other hand were very active and they carried almost all of the plastic strain. The flow strength of the PSB was shown to depend on two factors; the stress required to activate a screw dislocation in the channels, which depends on the channel width, and the passing stress required for two oppositely signed screw dislocations to pass each other without forming a lock, which depends on the density of screw dislocations in the channel. The generation of interstitial-type and vacancy-type point defects was also quantified and the evolution of their atomic concentrations with time was given.

The DDD framework was extended to model the interaction of dislocations with precipitates that have an $L1_2$ crystal structure. The system can handle an arbitrary distributions of precipitates and an initially general dislocation microstructure. The creation and destruction of APB regions inside the precipitates is fully tracked in time and the correct APB forces can now be applied on the dislocations gliding inside precipitates. A number of single superalloy single crystals ($Ni_3Al$ precipitates embedded in a Ni matrix), having different sizes, precipitate sizes, volume fractions and APB energies, were monotonically loaded to study the effects of the various microstructural features on the crystal's strength. The strength was found to vary linearly with the volume fraction with rapid dislocation density multiplication and frequent matrix cross-slip taking place in low volume fraction cases. A power law relationship was found between the strength and the APB energy with an exponent of 0.4014, which is close to the square-root dependence predicted by analytical models and simple planar DDD simulations. On the other hand, an inverse square root relationship was found between the crystal's strength and the precipitate size. The crystal size was found to have no effects on its strength in the case of superalloys because the strength controlling length scale is associated with the precipitate microstructure not the crystal size which agrees with the experimental findings. The width of the inter-precipitate channels was found to have the biggest effects on the crystal strength. A change in the dislocation glide pattern takes place as the APB energy decreases or the volume fraction increases where the dislocations stop gliding in the channels and start shearing through the precipitates. In all of the simulated superalloy cases, no strain hardening was observed.

## 6.2 Suggested Future Directions

The research described in this dissertation is only a humble step in the direction towards developing a complete, physically accurate, meaningful description of the dynamics of defects in pure metals and alloys. There is a huge number of idealizations, simplifications, approximations and neglected mechanisms that need to be addressed. An equal emphasis should also be placed on improving the computational tools used in these simulations. In this section, a number of these problems will be briefly described. This is by no means an extensive list of the issues that need to be addressed in the future.

First and foremost, the DDD method suffers from an intrinsic performance bottleneck that seriously limits its applicability. Because dislocations in particular and material defects in general do not follow conservation laws like masses or electric charges found in most physics problems, explicitly tracking them requires an ever increasing computational power because as dislocations multiply, the number of degrees of freedom handled by the DDD system increases. Hence, large scale DDD simulations reach a saturation-like state where clock time required for pushing the simulations further grows exponentially. In contrast, MD and FEM simulations, while in some cases they could be more demanding than DDD simulations, they have a constant clock time requirement per simulation time step. Since this problem arises from the nature of defect dynamics and has nothing to do with the design of DDD frameworks, any solution effort should be based on the fact that the number of degrees of freedom is constantly growing. Most of the clock time in a DDD simulation is spent on calculating the interaction forces between dislocations, which is an $O(N^2)$ operation that can be sped up in different ways as described in Section 2.3. One way to reduce the computational cost of this operation is by selective integration. The time step in DDD simulations is adaptively chosen so as to accurately capture the finest dislocation interactions as described in Section 2.2.7. For a system consisting of thou-

sands of dislocation segments, these finest interactions usually take place between a few number of dislocation at any one time but the drop in the time step is global. Selective integration is a time-step splitting technique where more than one time step can be simultaneously used in the simulation such that a larger time step is used to integrate the slowly moving dislocation segments that experience weak interactions while a finer time step can be used for the segments that strongly interact with each other. This way, the force calculation is reduced from calculating the forces on all the segments every fine time step to calculating it for a few number of segments. The full force calculation then takes place every large time step only. The criteria for strong versus weak dislocation interactions and the robust automatic detection of the strongly interacting systems are not well defined and it is expected that a number of heuristic measures need to be implemented, tested and compared. A second way that can help with the time cost associated with the force calculation is the increased parallelism. Since the force calculation is a static operation where the calculation of the forces between a pair of segments is independent of the force calculation between any other pair, implementing the force calculation part on faster computer architectures, such as Graphics Processing Units (GPUs), can potentially cut the calculation clock time. A combination of these two methods is worth experimenting with as well in order to achieve the best possible performance.

A fundamental approximation that is used in most DDD systems is elastic isotropy. At the crystal level, most metals are anisotropic. Cubic crystals show a mild degree of anisotropy where three, instead of two, elastic constants are required to fully describe their elastic behavior. The extra elastic constant however greatly complicates the calculation of Green's function. For anisotropic solids, there is no closed form expression for Green's function [88] which subsequently complicates the expressions for the dislocation's displacement, strain and stress fields. Anisotropic DDD frameworks have been developed for 2D simulations [256] but they are yet to be addressed in 3D set-

tings where the main problem is still the computational cost of the force calculations using the expressions for a dislocation stress field in an anisotropic medium.

As described in Section 4.8, the surface roughness grows almost monotonically during fatigue loading. The change in the surface geometry alters the stress field distribution in the crystal and the subsequent dislocation-surface interactions. The current DDD system assumes that the surface deformation is negligible and that the stress field can be calculated based on the reference crystal configuration. While this approximation is valid when only a few number of dislocations escape from the surface, it breaks down as significant surface extrusions and intrusions start forming. To handle this problem, the surface deformation has to be calculated in real time during the simulation and the new volume has to be remeshed automatically. Each of these problems is computationally expensive in itself but with the proper parallelization the overall cost can be brought down. For instance, by allocating few processing units to the surface displacement calculations and connecting them and the DDD simulation processors to a common data store, the surface development can be tracked as the DDD simulation is running at a relatively small extra computational cost.

The Ni based superalloy simulations described in Chapter 5 are based on an approximation similar to the one described above; the precipitate geometries are static. The successive shearing of precipitates with dislocations and superdislocations results in a gradual change in their geometries which has to be accounted for because eventually, the precipitate microstructure changes shape entirely and the precipitates start losing their strength. At the simulated strain levels (about 1% strain), the approximation is justifiable because the shearing is only a few Burgers vectors wide but this is not the case when the strain levels increase. An approach similar to the one suggested above for surface roughness tracking can be used to track the current precipitate geometries.

The future development of physics-based large-scale material mechanics simula-

tion frameworks rests on experimental and theoretical advances as well. Experimental findings provide modelers with the accurate defect microstructures needed to initialize their simulations as well as the data required for validating the computational tools especially in their development phase. As finer length and time scales become experimentally accessible, the predictions from computational simulations will converge with the experimental results which will increase the confidence in the explanations provided by simulations, which are experimentally difficult to construct. On the other hand, the progress in theoretical models, mathematical technology and algorithms will extend the application area of computational simulations to length scales, time scales and simulation conditions that are traditionally challenging.

# Appendix A

# Green's Function for Isotropic Media

Green's function for a linear differential operator $L$ is defined to be the response of an infinite domain due to a loading concentrated at one point of that domain. This can be a concentrated force in solid mechanics, a concentrated heat source in heat transfer problems or a point charge in electromagnetics. In general, consider the linear differential equation

$$Lu = b \tag{A.1}$$

where $L$ is a linear differential operator, $u$ is, in general, a tensor for which the solution is sought and $b$ is the forcing in the medium. Green's function $U$ for the operator $L$ is then the solution to the differential equation when the forcing $b$ becomes

$$LU = \delta \tag{A.2}$$

where $\delta$ is Dirac delta function. The importance of Green's function stems from the fact that for linear differential operators, the solution under a certain forcing

distribution can be broken down to the sum of the solutions under subsets of that forcing. Hence, the full solution can be given through a convolution operator with the forcing distribution such that

$$u(x) = \int_{\Omega} U(x,y)b(y)d\Omega(y) \tag{A.3}$$

where $\Omega$ is the solution domain.

In solid mechanics, the differential equation describing the displacement field distribution under a given domain forcing $b$ and static conditions is given by [83, 85]

$$C_{ijkl}u_{j,kl} + b_i = 0 \tag{A.4}$$

where $C_{ijkl}$ is the tensor of stiffness moduli. For isotropic materials, $C_{ijkl}$ can be written as [41]

$$C_{ijkl} = \lambda\delta_{ij}\delta_{kl} + \mu(\delta_{ik}\delta_{jl} + \delta_{il}\delta_{jk}) \tag{A.5}$$

by plugging this back into equation A.4

$$(\lambda+\mu)u_{j,ji} + \mu u_{i,jj} + b_i = [(\lambda+\mu)D_iD_j + \mu\nabla^2\delta_{ij}]u_j + b_i = 0 \tag{A.6}$$

The differential operator $L_{ij}$ in this case becomes

$$L_{ij} = (\lambda+\mu)D_iD_j + \mu\nabla^2\delta_{ij} \tag{A.7}$$

and the equation for Green's function then becomes

$$L_{ij}U_{jp}(x,y) = (\lambda+\mu)D_iD_j + \mu\nabla^2\delta_{ij}U_{jp}(x,y) = -\delta\delta_{ip} \tag{A.8}$$

where $U_{jp}$ is Green's function, defined to be the displacement in the $j^{th}$ direction at

point $x$ due to a unit concentrated force in the $p^{th}$ direction at point $y$.

In order to solve this differential equation, the following transformation can be used. Write $U_{jp}$ as

$$U_{jp} = M_{jp}\Phi \tag{A.9}$$

where $\Phi$ is an unknown scalar function to be solved for and $M_{jp}$ is the transpose of the adjoint operator of $L$

$$M_{jp} = \tilde{L}^T_{jp} \tag{A.10}$$

with tilde denoting the adoint operator. By definition, the inverse operator is equal to the transpose of the adoint operator multiplied by the inverse of the determinant of the operator, similar to matrices

$$L^{-1}_{jp} = \tilde{L}^T_{jp} D^{-1} = M_{jp} D^{-1} \tag{A.11}$$

where $D = det(L)$. Hence, the operator $M$ is known and can be directly derived from $L$, the differential equation A.8 can now be rewritten

$$L_{ij} U_{jp}(x, y) = L_{ij} M_{jp} \Phi = L_{ij} L^{-1}_{jp} D\Phi = \delta_{ip} D\Phi = -\delta\delta_{ip} \tag{A.12}$$

which gives

$$D\Phi = -\delta \tag{A.13}$$

This transformation allows us to solve for a scalar function $\Phi$ instead of the matrix function $U_{jp}$ and then obtain $U_{jp}$ directly from $\Phi$. This comes at the cost of complicating the differential operator which is now

$$D = \epsilon_{ijk} L_{1i} L_{2j} L_{3k} = \mu^2(\lambda + 2\mu)\nabla^6 \tag{A.14}$$

Plugging this back into equation A.13 gives

$$\mu^2(\lambda + 2\mu)\left(\nabla^2\right)^3 \Phi = -\delta \tag{A.15}$$

Noting that the Laplacian operator acting on the function $\frac{1}{4\pi r}$ gives

$$\nabla^2\left(\frac{1}{4\pi r}\right) = \frac{1}{4\pi}\frac{3r_i r_i - r^2\delta_{ii}}{r^5} \tag{A.16}$$

which is zero if $r \neq 0$. At the origin however, its value is unspecified but can be solved for using the following integral defined over a sphere centered at the space origin with radius $R$

$$\int_\Omega \nabla^2\left(\frac{1}{4\pi r}\right) d\Omega = \frac{1}{4\pi}\int_\Gamma \frac{-r_{,i}}{r^2} n_i d\Gamma = \frac{-1}{4\pi R^2}\int_\Gamma d\Gamma = 1 = \int_\Omega \delta(x) d\Omega \tag{A.17}$$

where $\Omega$ is the spherical volume and $\Gamma$ is the spherical surface. Gauss theorem was used to obtain the second expression from the first and the fact that $r_{,i} n_i = 1$ for all spheres was used to obtain the third integral. By taking the limit as the sphere radius approaches zero, the equality still holds, which means that

$$\nabla^2\left(\frac{1}{4\pi r}\right) = -\delta \tag{A.18}$$

then equation A.15 can be recast in the form

$$\mu^2(\lambda + 2\mu)\left(\nabla^2\right)^3 \Phi = \nabla^2\left(\frac{1}{4\pi r}\right) \tag{A.19}$$

which can be simplified to be

$$\left(\nabla^2\right)^2 \Phi = \frac{1}{4\pi\mu^2(\lambda+2\mu)r} \tag{A.20}$$

but we know that

$$\nabla^2 r = \frac{2}{r} \tag{A.21}$$

thus, the equation can be further simplified to give

$$\nabla^2\Phi = \frac{r}{8\pi\mu^2(\lambda+2\mu)} \tag{A.22}$$

A closer look at the $M_{jp}$ operator reveals that it can be written as

$$M_{jp} = \left(\mu(\lambda+2\mu)\nabla^2\delta_{ij} - \mu(\lambda+\mu)D_iD_j\right)\nabla^2 \tag{A.23}$$

which means that Green's function are

$$U_{jp} = M_{jp}\Phi = \left(\mu(\lambda+2\mu)\nabla^2\delta_{ij} - \mu(\lambda+\mu)D_iD_j\right)\nabla^2\Phi \tag{A.24}$$

Hence, there is no need to actually solve for $\Phi$ since $\nabla^2\Phi$ is the required factor in the previous equation. Substituting with equation A.22 in the previous equation gives $U_{jp}$

$$U_{jp} = \frac{1}{4\pi\mu}\left(\frac{\delta_{jp}}{r} - \frac{r_{,jp}}{4(1-\nu)}\right) \tag{A.25}$$

# Appendix B

# Graph Search Algorithms for Cross-Slip Event Predictions

The graph search algorithms required for the isolation of dislocation chains in the cross-slip event prediction calculations are presented here. The generation of the dislocation graph chains takes place at two levels. First, on the level of the graph, the procedure *GenerateGraphChains* described in algorithm 1 loops over all the graph nodes and tries to generate only one chain containing each node as long as no chains containing that node have been generated already. In doing so, it uses the lower level procedure *GenerateNodeChain* described in algorithm 2. When done, the generation of the stub chains, defined to be chains consisting of exactly two nodes and one segment, begins. The stub chains are necessary, although they are less likely to cross-slip, because they provide all the information required to predict interection cross-slip events.

**Algorithm 1** The algorithm to generate all the chains in a given graph

```
1: procedure GenerateGraphChains(graph)
2:     for node in graph.nodes do
3:         node.visited ← false
4:     for node in graph.nodes do
5:         if node.visited = false then
6:             chain ← GenerateNodeChain(node)
7:             if chain.length < 2 then
8:                 continue
9:             for node in chain.nodes do
10:                node.visited ← true
11:            AllChains ← chain
12:    for node in graph.nodes do
13:        node.visited ← false
14:    for node in graph.nodes do
15:        if node.visited = false then
16:            if node.neighbours > 2 then
17:                for neighbourinnode.neighbours do
18:                    if neighbour.neighbours > 2 then
19:                        if neighbour.visited = false then
20:                            StubChain ← node
21:                            StubChain ← neighbour
22:                            AllChains ← StubChain
23:            node.visited ← true
       return AllChains
```

**Algorithm 2** The algorithm to generate the chain containing a given node

```
1: procedure GenerateNodeChain(node)
2:     NewChain ← node
3:     if node.neighbours > 2 or node.neighbours < 1 then return NewChain
4:     NodeBeforeLast ← node
5:     LastNode ← node.RightNeighbour
6:     NewChain ← LastNode
7:     Proceed ← true
8:     IsLoop ← false
9:     while Proceed do
10:        TempNode ← LastNode.GetOtherNeighbour(NodeBeforeLast)
11:        if TempNode = NULL then
12:            Proceed ← false
13:        else
14:            NewChain ← TempNode
15:            NodeBeforeLast ← LastNode
16:            LastNode ← TempNode
17:            if TempNode = node then
18:                Proceed ← false
19:                IsLoop ← true
20:    if node.neighbours = 2 and not IsLoop then
21:        NodeBeforeLast ← node
22:        LastNode ← node.LeftNeighbour
23:        NewChain ← LastNode
24:        Proceed ← true
25:        while Proceed do
26:            TempNode ← LastNode.GetOtherNeighbour(NodeBeforeLast)
27:            if TempNode = NULL or TempNode = node then
28:                Proceed ← false
29:            else
30:                NewChain ← TempNode
31:                NodeBeforeLast ← LastNode
32:                LastNode ← TempNode
33:                if TempNode = node then
34:                    Proceed ← false
35:                    IsLoop ← true
       return NewChain
```

# Bibliography


[1] R.F. Heizer. The background of thomsen's three-age system. *Technology and Culture*, 3(3):259–266, 1962.

[2] C. Soares. *Gas Turbines : A Handbook of Air, Land and Sea Applications, 2nd Ed.* Butterworth-Heinemann, 2014.

[3] K.J. Bathe. *Finite Element Procedures*. Prentice Hall, 1996.

[4] O.C. Zienkiewicz, R.I. Taylor, and J.Z. Zhu. *The Finite Element Method: Its Basis and Fundamentals, 7th Ed.* Butterworth-Heinemann, 2013.

[5] D. Krajcinovic. Damage mechanics. *Mechanics of Materials*, 8:117–197, 1989.

[6] J. Lemaitre. *A Course on Damage Mechanics*. Springer-Verlag, 1996.

[7] J.C. Simo. *Computational Inelasticity*. Springer, 2000.

[8] E.A. de Souza Neto, D. Peric, and D.R.J. Owen. *Computational Methods for Plasticity: Theory and Applications*. Wiley, 2008.

[9] R.J. Asaro. Crystal plasticity. *J. App. Mech.*, 50:921–934, 1983.

[10] T. Hochrainer, S. Sanfeld, M. Zaiser, and P. Gumbsch. Continuum dislocation dynamics: Towards a physical theory of crystal plasticity. *J. Mech. Phys. Solid.*, 63:167–178, 2014.

[11] L.P. Kubin, G. Canova, M. Condat, B. Devincre, V. Pontikis, and Y. Bréechet. Dislocation microstructures and plastic flow: a 3-D simulation. *Solid State Phenomena*, 23–24:455–472, 1992.

[12] E. van der Giessen and A. Needleman. Discrete dislocation plasticity: a simple planar model. *Modelling Simul. Mater. Sci. Eng.*, 3:689–735, 1995.

[13] M. Rhee H.M. Zbib and J.P. Hirth. On plastic deformation and the dynamics of 3d dislocations. *Int. J. Mater. Sci.*, 40:113–127, 1998.

[14] N.M. Ghoniem, S.-H. Tong, and L.Z. Sun. Parametric dislocation dynamics: A thermodynamics-based approach to investigations of mesoscopic plastic deformation. *Phys. Rev. B*, 61(2):913–927, 2000.

[15] A.A. Benzerga, Y. Brechet, A. Needleman, and E. Van der Giessen. Incorporating three-dimensional mechanisms into two-dimensional dislocation dynamics. *Model. Sim. Mater. Sci. Eng.*, 12:159–196, 2004.

[16] M. Tang M. Rhee T. Oppelstrup G. Hommes T. G. Pierce A. Arsenlis, W. Cai and V. V. Bulatov. Enabling strain hardening simulations with dislocation dynamics. *Modelling Simul. Mater. Sci. Eng.*, 15(6):553–595, 2007.

[17] Y.S. Chen, W. Choi, S. Papanikolaou, M. Bierbaum, and Sethna J.P. Scaling theory of continuum dislocation dynamics in three dimensions: Self-organized fractal pattern formation. *Int. J. Plasticity*, 46:94–129, 2013. doi: 10.1016/j.ijplas.2013.02.011.

[18] S. Xia and A. El-Azab. Computational modelling of mesoscale dislocation patterning and plastic deformation of single crystals. *Model. Simul. Mater. Sci. Eng.*, 23:005009, 2015. doi: 10.1088/0965-0393/23/5/055009.

[19] B. Liu, D. Raabe, P. Eisenlohr, F. Roters, A. Arsenlis, and G. Hommes. Dislocation interactions and low-angle grain boundary strengthening. *Acta Mater.*, 59(7125–7134), 2011.

[20] B. Liu, P. Eisenlohr P., F. Roters, and D. Raabe. Simulation of dislocation penetration through a general low-angle grain boundary. *Acta Mater.*, 60(5380–5390), 2012.

[21] H. Fan, S. Aubry, A. Arsenlis, and J. El-Awady. The role of twinning deformation on the hardening response of polycrystalline magnesium from discrete dislocation dynamics simulations. *Acta Mat.*, 92:126–139, 2015. doi: 10.1016/j.actamat.2015.03.039.

[22] A. Vattré, B. Devincre, and A. Roos. Orientation dependence of plastic deformation in nickel-based single crystal superalloys: Discrete-continuous model. *Acta Mater.*, 58:1938–1951, 2010. doi: 10.1016/j.actamat.2009.11.037.

[23] H. Yang, Z. Li, and M. Huang. Modeling of abnormal mechanical properties of nickel-based single crystal superalloy by three-dimensional discrete dislocation dynamics. *Model. Simul. Mater. Sci. Eng.*, 22:085009, 2014. doi: 10.1088/0965-0393/22/8/085009.

[24] D.C. Rapaport. *The Art of Molecular Dynamics Simulation*. Cambridge University Press, 2004.

[25] E. Bitzek, D. Weygand, and P. Gumbsch. Atomistic study of edge dislocations in fcc metals: Drag and inertial effects. *IUTAM Symposium on Mesoscopic Dynamics of Fracture Process and Materials Strength*, 115:45–57, 2004.

[26] S.I. Rao, D.M. Dimiduk, J.A. El-Awady, T.A. Parthasarathy, M.D. Uchic, and C. Woodward. Atomistic simulations of athermal cross-slip nucleation at screw

dislocation intersections in face-centered cubic nickel. *Phil. Mag.*, 89(34–36): 3351–3369, 2009.

[27] S.I. Rao, D.M. Dimiduk, J.A. El-Awady, T.A. Parthasarathy, M.D. Uchic, and C. Woodward. Activated states for cross-slip at screw dislocation intersections in face-centered cubic nickel and copper via atomistic simulation. *Acta Mater.*, 58:5547–5557, 2010. doi: 10.1016/j.actamat.2010.06.005.

[28] S.I. Rao, D.M. Dimiduk, T.A. Parthasarathy, J. El-Awady, Woodward C., and M.D. Uchic. Calculations of intersection cross-slip activation energies in fcc metals using nudged elastic band method. *Acta Mater.*, 59(19):7135 – 7144, 2011. doi: 10.1016/j.actamat.2011.08.029.

[29] S.I. Rao, D.M. Dimiduk, J.A. El-Awady, T.A. Parthasarathy, M.D. Uchic, and C. Woodward. Spontaneous athermal cross-slip nucleation at screw dislocation intersections in fcc metals and L12 intermetallics investigated via atomistic simulations. *Phil. Mag.*, 93(22):3012–3028, 2013.

[30] S.I. Rao, D.M. Dimiduk, T.A. Parthasarathy, M.D. Uchic, and C. Woodward. Atomistic simulations of surface cross-slip nucleation in face-centered cubic nickel and copper. *Acta Mater.*, 61(7):2500–2508, 2013.

[31] A. Dutta, M. Bhattacharya, N. Gayathri, G.C. Das, and P. Barat. The mechanism of climb in dislocationnanovoid interaction. *Acta Mater.*, 60:3789–3798, 2012.

[32] M.I. Mendelev, C. Deng, C.A. Schuh, and D.J. Srolovitz. Comparison of molecular dynamics simulation methods for the study of grain boundary migration. *Model. Sim. Mater. Sci. Eng.*, 21:045017, 2013. doi: 10.1088/0965-0393/21/4/045017.

[33] I.N. Kar'kin, Y.N. Gronostyrev, and L.E. Kar'kina. Molecular dynamics simulation of the formation of twin boundaries during agglomeration of nanoparticles. *Phys. Solid State*, 52(2):431–435, 2010.

[34] D. Sholl and J.A. Steckel. *Density Functional Theory: A Practical Introduction*. Wiley, 2009.

[35] P. Hohenberg and W. Kohn. Inhomogeneous electron gas. *Phys. Rev.*, 136(3B): B864–B871, 1964.

[36] F. Ercolessi and J. B. Adams. Interatomic potentials from first-principles calculations: The force-matching method. *Europhys. Lett.*, 26:583–588, 1994.

[37] X. Zeng and S. Li. *Advances in Engineering Mechanics Vol. 1*, chapter Recent Developments on Concurrent Multiscale Simulations, pages 1–56. Nova Science, 2010.

[38] H. Talebi, M. Silani, and T. Rabczuk. Concurrent multiscale modeling of three dimensional crack and dislocation propagation. *Adv. Eng. Software*, 80:82 – 92, 2015. doi: doi:10.1016/j.advengsoft.2014.09.016.

[39] D. Caillard and J.L. Martin. *Thermally Activated Mechanisms in Crystal Plasticity*. Pergamon, 2003.

[40] D. Hull and D.J. Bacon. *Introduction to Dislocations*. Butterworth-Heinemann, 2001.

[41] J.P. Hirth and J. Lothe. *Theory of dislocations.* John Wiley & Sons, New York, 2nd ed. edition, 1982.

[42] R. Madec, B. Devincre, and L.P. Kubin. Simulation of dislocation patterns in multislip. *Scripta Mater.*, 47(10):689 – 695, 2002. doi: 10.1016/S1359-6462(02)00185-9.

[43] Jackson P. J. The role of cross-slip in the plastic deformation of crystals. *Mater. Sci. Eng.*, 57:39–47, 1983.

[44] P.J. Jackson. Dislocation modelling of shear in FCC crystals. *Prog. Mater. Sci.*, 29(1-2):139–175, 1985.

[45] G. Saada. Cross-slip and work hardening of fcc crystals. *Mater. Sci. Eng. A.*, 137:177–183, 1991.

[46] M.S. Duesbery, N.P. Louat, and K. Sadananda. The mechanics and energetics of cross-slip. *Acta Metall. Mater.*, 40(1):149–158, 1992. doi: 10.1016/0956-7151(92)90208-V.

[47] K. Jumonji, S. Ueta, A. Miyahara, M. Kato, and A. Sato. Rapid work hardening caused by cube cross slip in Ni3Al single crystals. *Phil. Mag. A*, 73:345–364, 1996.

[48] J. Bonneville and B. Escaig. Cross-slipping process and the stress-orientation dependence in pure copper. *Acta Metall.*, 27(9):1477–1486, 1979.

[49] J. Bonneville, B. Escaig, and J.L. Martin. A study of cross-slipping activation parameters in pure copper. *Acta Metall.*, 36:1989–2002, 1988.

[50] O. Couteau, T. Kruml, and J.-L. Martin. About the activation volume for cross-slip in Cu at high stresses. *Acta Mater.*, 59(10):4207 – 4215, 2011. doi: 10.1016/j.actamat.2011.03.045.

[51] T. Rasmussen, K.W. Jacobsen, T. Leffers, O.B. Pedersen, S.G. Srinivasan, and H. Jónsson. Atomistic determination of cross-slip pathway and energetics. *Phys. Rev. Lett.*, 79(19):3676–3679, 1997. doi: 10.1103/PhysRevLett.79.3676.

[52] T. Rasmussen, K.W. Jacobsen, T. Leffers, and O.B. Pedersen. Simulations of

the atomic structure, energetics, and cross slip of screw dislocations in copper. *Phys. Rev. B*, 56:2977–2990, 1997. doi: 10.1103/PhysRevB.56.2977.

[53] M. Verdier, M. Fivel, and I. Groma. Mesoscopic scale simulation of dislocation dynamics in FCC metals: Principles and applications. *Mod. Sim. Mater. Sci. Eng.*, 6(6):755–770, 1998.

[54] D. Weygand, L. H. Friedman, E. Van der Giessen, and A. Needleman. Aspects of boundary-value problem solutions with three-dimensional dislocation dynamics. *Modelling Simul. Mater. Sci. Eng.*, 10:437–468, 2002.

[55] J.A. El-Awady, S.B. Biner, and N.M. Ghoniem. A self-consistent boundary element, parametric dislocation dynamics formulation of plastic flow in finite volumes. *J. Mech. Phys. Solids*, 56(5):2019–2035, 2008. doi: 10.1016/j.jmps.2007.11.002.

[56] Stephens R.R. Stephens R.I., Fatemi A. and H.O. Fuchs. *Metal Fatigue in Engineering, 2nd Ed.* Wiley, 2000.

[57] J. Schijve. Fatigue damage in aircraft structures not wanted but tolerated. *Int. J. Fatigue*, 31:998–1011, 2009.

[58] S. Suresh. *Fatigue of Materials, 2nd Ed.* Cambridge University Press, 1998.

[59] Q. Yu, R.K. Mishra, J.W. Morris, and A.M. Minor. The effect of size on dislocation cell formation and strain hardening in aluminum. *Phil. Mag.*, 94: 2062–2071, 2014. doi: 10.1080/14786435.2014.906755.

[60] B. Jakobsen, U. Lienert, J. Almer, W. Pantleon, and H.F Poulsen. Properties and dynamics of bulk subgrains probed in-situ using a novel x-ray diffraction method. *Materials Science Forum*, 550:613–618, 2007.

[61] D.M. Norfleet, D.M. Dimiduk, S.J. Polasik, M.D. Uchic, and M.J. Mills. Dislocation structures and their relationship to strength in deformed nickel microcrystals. *Acta Mater.*, 56(13):2008, 2008.

[62] G Makov P Landau, R Z Shneck and A Venkert. Evolution of dislocation patterns in fcc metals. *IOP Conf. Ser.: Mater. Sci. Eng*, 3, 2009.

[63] Z.S. Basinski and S.J. Basinski. Fundamental aspects of low amplitude cyclic deformation in face-centred cubic crystals. *Prog. Mater. Sci.*, 36(9):89–148, 1992.

[64] Reed R.C. *The superalloys fundamentals and applications*. Cambridge University Press, 2006.

[65] A.M. Hussein, S.I. Rao, M.D. Uchic, D.M. Dimiduk, and J.A. El-Awady. Microstructurally based cross-slip mechanisms and their effects on dislocation microstructure evolution in fcc crystals. *Acta Mater.*, 85:180–190, 2015. doi: 10.1016/j.actamat.2014.10.067.

[66] A.M. Hussein and J.A. El-Awady. Quantifying dislocation microstructure evolution and cyclic hardening in fatigued nickel single-crystals. *Submitted*, 2015.

[67] A.M. Hussein and J.A. El-Awady. The early cycle development of surface roughness of cyclically loaded fcc single crystals. *In Preparation*, 2015.

[68] A.M. Hussein and J.A. El-Awady. Deformation evolution in persistent slip bands. *In Preparation*, 2015.

[69] A.M. Hussein, S.I. Rao, M.D. Uchic, and J.A. El-Awady. The deformation response of nickel based superalloy microcrystals under monotonic loading. *In Preparation*, 2015.

[70] H. Fan, A.M. Hussein, and J.A. El-Awady. *Multiscale Modeling for Nanomechanics*, chapter Multiscale Modeling of the Size Effect on Plasticity in Metals. Springer, in preparation.

[71] V. Volterra. Sur l'quilibre des corps lastiques multiplement connexes. *Ann. Sci. c. Norm. Sup.*, 24:401–517, 1907.

[72] E. Orowan. Zur kristallplastizitat. i. tieftemperaturplastizitat und beckersche formel. *Z. Physik*, 89(9-10):605–613, 1934.

[73] E. Orowan. Zur kristallplastizitat. ii. die dynamische auffassung der kristallplastizifat. *Z. Physik*, 89(9-10):614–633, 1934.

[74] E. Orowan. Zur kristallplastizitat. iii. uber den biechanismus des gleitvorganges. *Z. Physik*, 89(9-10):634–659, 1934.

[75] G.I. Taylor. The mechanism of plastic deformation of crystals. part i. theoretical. *Proc. Roy. Soc. London*, 145(855):362–387, 1934.

[76] G.I. Taylor. The mechanism of plastic deformation of crystals. part ii. comparison with observations. *Proc. Roy. Soc. London*, 145(855):388–404, 1934.

[77] M. Polanyi. Uber eine art gitterstorung, die einen kristall plastisch machen konnte. *Z. Physik*, 89(9-10):660–664, 1934.

[78] J.P. Hirth. A brief history of dislocation theory. *Metal. Trans. A*, 16A:2085–2090, 1985.

[79] C. Somigliana. *R.C. Acca. Lincei.*, 23:463, 1914.

[80] C. Somigliana. *Ibid.*, 24:655, 1915.

[81] R. Bonnet, G. Marcon, and A. Ati. On the use of somigliana dislocations to describe some interfacial defects. *Phil. Mag. A.*, 51(3):429–448, 1985.

[82] J.D. Eshelby. Dislocation theory for geophysical applications. *Phil. Trans. R. Soc. Lond. A*, 274:331–338, 1973.

[83] S. Timoshenko and J.N. Goodier. *Theory of Elasticity.* McGraw-Hill, 1951.

[84] P. Mullner. In-plane edge somigliana dislocation dipoles and quadrupoles. *Script. Metal. et Mater.*, 33(7):1181–1186, 1995.

[85] T. Mura. *Micromechanics of Defects in Solids, 2nd Ed.* Martinius Nijhoff Publishers, 1986.

[86] R. DeWit. The continuum theory of stationary dislocations. *Solid St. Phys.*, 10:249–292, 1960.

[87] E. Kroener. *Continuum theory of dislocations and self stresses.* Springer-Verlag, 1958.

[88] T. Mura and N. Kinoshita. Green's function for anisotropic elasticity. *Phys. Stat. Sol. b*, 47:607–618, 1971.

[89] W. Cai, A. Arsenlis, C.R. Weinberger, and V.V. Bulatov. A non-singular continuum theory of dislocations. *J. Mech. Phys. Solid*, 54:561–587, 2006.

[90] R. Madec, B. Devincre, and L.P. Kubin. New line model for optimized dislocation dynamics simulations. *Proc. MRS Fall Meeting*, 653, 2000. doi: 10.1557/PROC-653-Z1.8.

[91] A. Bondy and U.S.R. Murty. *Graph Theory.* Springer-Verlag London, 2001.

[92] E. Nadgornyi. Dislocation dynamics and mechanical properties of crystals. *Progress in Materials Science*, 31:1–536, 1988.

[93] C. Déprés, C.F. Robertson, and M.C. Fivel. Low strain fatigue in 316L steel surface grains: a three-dimension discrete dislocation dynamics modeling of the

early cycles. part 2: Persistent slip markings and micro-crack nucleation. *Phil. Mag.*, 86(1):79–97, 2006. doi: 10.1080/14786430500341250.

[94] A.S. Argon U.F. Kocks and M.F. Ashby. Thermodynamics and kinetics of slip. *Progress in Materials Science*, 19:1–291, 1975.

[95] D. S. Wood J.A. Gorman and T. Vreeland Jr. Mobility of dislocations in aluminum. *Journal of Applied Physics*, 40:833–841, 1969.

[96] D.L. Olmsted, L.G. Hector Jr., W.A. Curtin, and R.J. Clifton. Atomistic simulations of dislocation mobility in al, ni and al/mg alloys. *Model. Sim. Mater. Sci. Eng.*, 13:371–388, 2005. doi: 10.1088/0965-0393/13/3/007.

[97] W. Cai and V.V. Bulatov. Mobility laws in dislocation dynamics simulations. *Mat. Sci. Eng. A*, 387-389:227–281, 2004.

[98] W. Cai. Atomistic and mesoscale modeling of dislocation mobility. *PhD Thesis, MIT*, 2001.

[99] E. Isaacson and H.B. Keller. *Analysis of Numerical Methods*. Dover Publications, 1994.

[100] L. Greengard and V. Rokhlin. A fast algorithm for particle simulations. *J. Comput. Phys.*, 73:325–348, 1987.

[101] N.M. Wang, Z. Ghoniem and R. LeSar. Multipole representation of the elastic field of dislocation ensembles. *Phys. Rev. B*, 69(174102), 2004.

[102] E.Y. Gutmanas and Nadgornyi E.M. Dislocation multiplication by multiple cross slip. *Sov Phys - Solid State*, 12:733–734, 1970.

[103] Y. Tang and J.A. El-Awady. Formation and slip of pyramidal dislocations in hexagonal close-packed magnesium single crystals. *Acta Mater.*, 71:319–332, 2014. doi: 10.1016/j.actamat.2014.03.022.

[104] A. Seeger, J. Diehl, S. Mader, and H. Rebstock. Work-hardening and work-softening of face-centred cubic metal crystals. *Phil. Mag.*, 2(15):323–350, 1957.

[105] J.P. Poirier. On the symmetrical role of cross-slip of screw dislocations and climb of edge dislocations as recovery process controlling high-temperature creep. *Rev. Phys. Appl.*, 11:731, 1976.

[106] L.P. Kubin, B. Devincre, and T. Hoc. Inhibited dynamic recovery and screw dislocation annihilation in multiple slip of fcc single crystals. *Phil. Mag.*, 86: 4023–4036, 2006.

[107] B. Escaig. Cross-slipping process in the FCC structure. In *Proc. Battelle Coll. Disl. Dyn.*, pages 655–677, New York, 1968. McGraw- Hill.

[108] F.J. Humphreys and P.B. Hirsch. The deformation of single crystals of copper and copper-zinc alloys containing alumina particles. ii. microstructure and dislocation-particle interactions. *Proc. Royal Society A*, 318:73–92, 1970.

[109] W. Puschl. Models for dislocation cross-slip in close-packed crystal structures: A critical review. *Prog. Mat. Sci.*, 47:415–461, 2002.

[110] R. Watanabe. Possible slip systems in body centered cubic iron. *Materials Transactions*, 47:1886–1889, 2006.

[111] C.R. Weinberger, B.L. Boyce, and C.C. Battaile. Slip planes in bcc transition metals. *Int. Mater. Rev.*, 58(5):296–314, 2013.

[112] A. J. Opinsky and R. Smoluchowski. The crystallographic aspect of slip in bodycentered cubic single crystals. ii. interpretation of experiments. *J. Appl. Phys.*, 22:1488–1492, 1951.

[113] D. Caillard and J.L. Martin. Some aspects of cross-slip mechanisms in metals and alloys. *J. de Physique*, 50(18):2455–3473, 1989.

[114] K. Kang, J. Yin, and W. Cai. Stress dependence of cross slip energy barrier for face-centered cubic nickel. *J. Mech. Phys. Sol.*, 62:181–193, 2014.

[115] S. Glasstone, K.J. Laidler, and H. Eyring. *The theory of rate processes: the kinetics of chemical reactions, viscosity, diffusion and electrochemical phenomena.* McGraw-Hill, 1941.

[116] R. Smallman, I. Dillamore, and P. Dobson. The measurement of stacking fault energy. *J. de Physique*, 27:C3–86 – C3–93, 1966.

[117] G. Schoeck and A. Seeger. Activation energy problems associated with extended dislocations. In *Report of the Bristol Conference on Defects in Crystalline Solids*, pages 340–346. Physical Society, London, 1955.

[118] H. Wolf. Die aktivierungsenergie fr die quergleitung aufgespaltener schraubenversetzungen. *Z. Naturforsch A*, 15:180–193, 1960.

[119] J. Friedel. Regarding seeger's paper on work hardening. In J.C. Fisher, W.G. Johnston, R. Thromson, and T. Vreeland, editors, *Dislocations and mechanical properties of crystals.*, pages 330–332, New York, 1957. John Wiley And Sons Inc.

[120] R.L. Fleischer. Cross slip of extended dislocations. *Acta Metal*, 7:134–135, 1959.

[121] M.S. Duesbery. Dislocation motion, constriction and cross-slip in fcc metals. *Model. Simul. Mater. Sci. Eng*, 6, 1998.

[122] W. Cai, V.V. Butalov, J. Chang, J. Li, and S. Yip. *Dislocations in Solids*, volume 12, chapter Dislocation core effects on mobility. North-Holland Publishing Company, 2004.

[123] J. Washburn. Intersection cross slip. *App. Phys. Lett.*, 7:183, 1965.

[124] A.N. Stroh. Constrictions and jogs in extended dislocations. *Proc. Phys. Soc. B*, 67:427–436, 1954.

[125] T. Vegge, T. Rasmussen, T. Leffers, Pedersen O.B., and K.W. Jacobsen. Atomistic simulations of cross-slip of jogged screw dislocations in copper. *Phil. Mag. Lett.*, 81:137–144, 2001.

[126] C. Motz, D. Weygand, J. Senger, and P. Gumbsch. Initial dislocation structures in 3-D discrete dislocation dynamics and their influence on microscale plasticity. *Acta Mater.*, 57(6):1744–1754, 2009. doi: 10.1016/j.actamat2008.12.020.

[127] J.A. El-Awady, M.D. Uchic, P. Shade, S.-L Kim, S.I. Rao, D.M. Dimiduk, and C. Woodward. Pre-straining effects on the power-law scaling of size-dependent strengthening in ni single crystals. *Scrtipta Mater.*, 68:207–210, 2013. doi: 10.1016/j.scriptamat.2012.10.035.

[128] D.M. Dimiduk, M.D. Uchic, and T.A. Parthasarathy. Size-affected single-slip behavior of pure nickel microcrystals. *Acta Mater.*, 53(15):4065–4077, 2005.

[129] E. Göttler. Dislocation structure and work-hardening of copper single crystals with [100] axis orientation : I. dislocation arrangement and cell structure of crystals deformed in tension. *Phil. Mag.*, 28:1057–1976, 1973.

[130] P. Landau, R.Z. Shneck, G. Makov, and A. Venkert. In-situ tem study of dislocation patterning during deformation in single crystal aluminum. *J. Phys*, 241(1):012060, 2010.

[131] J.A. El-Awady. Unravelling the physics of size-dependent dislocation-mediated plasticity. *Nature Communications*, 2015. doi: 10.1038/ncomms6926.

[132] S.I. Rao, D.M. Dimiduk, T.A. Parthasarathy, M.D. Uchic, M. Tang, and C. Woodward. Athermal mechanisms of size-dependent crystal flow gleaned

from three-dimensional discrete dislocation simulations. *Acta Mater.*, 56(13): 3245–3259, 2008. doi: 10.1016/j.actamat.2008.03.011.

[133] B. Devincre and L.P. Kubin. Mesoscopic simulations of dislocations and plasticity. *Mater. Sci. Eng. A*, 234-236:8–14, 1997. doi: 10.1016/S0921-5093(97)00146-9.

[134] H. Neuhauser. Slip propagation and fine structure. *Solid Stae Phen.*, 3–4: 407–415, 1991.

[135] Y.W. Zhang, T.C. Wang, and N.G. Liang. The inhomogeneity of plastic deformation in ductile single crystals. *Mod. Sim. Mater. Sci. Eng.*, 2(6):1171, 1994.

[136] M.D. Uchic, P.A. Shade, and D.M. Dimiduk. Plasticity of micrometer-scale single crystals in compression: a critical review. *Annu. Rev. Mater. Res.*, 39 (1):361–386, 2009. doi: 10.1146/annurev-matsci-082908-145422.

[137] J.R. Greer and J.Th.M. De Hosson. Plasticity in small-sized metallic systems: Intrinsic versus extrinsic size effect. *Prog. Mater. Sci.*, 56(6):654–724, 2011. doi: 10.1016/j.pmatsci.2011.01.005.

[138] A. El-Azab. Statistical mechanics of dislocation systems. *Scripta Mater.*, 54 (5):723–727, 2006. doi: 10.1016/j.scriptamat.2005.11.031.

[139] H. Mughrabi. Fatigue, an everlasting materials problem - still en vogue. *Procedia Engineering*, 2:3–26, 2010.

[140] J. Schijve. *Fatigue of Structures and Materials, 2nd Ed.* Springer, 2009.

[141] M.D. Sangid. The physics of fatigue crack initiation. *Int. J. Fatigue*, 57:58–72, 2013.

[142] K.S. Chan. Roles of microstructure in fatigue crack initiation. *Int. J. Fatigue*, 32(9):1428 – 1447, 2010. doi: doi:10.1016/j.ijfatigue.2009.10.005.

[143] D.L. McDowell, K. Gall, M.F. Horstemeyer, and J.Fan. Microstructure-based fatigue modeling of cast a356-t6 alloy. *Engineering Fracture Mechanics*, 70:49 – 80, 2003.

[144] D.L. McDowell and F.P.E. Dunne. Microstructure-sensitive computational modeling of fatigue crack formation. *Int. J. Fatigue*, 32(9):1521 – 1542, 2010. doi: doi:10.1016/j.ijfatigue.2010.01.003.

[145] C. Zhou and R. Lesar. Dislocation dynamics simulations of plasticity in polycrystalline thin films. *Int. J. Plasticity*, 30-31:185–201, 2012.

[146] T. Zhai, A.J. Wilkinson, and J.W. Martin. A crystallographic mechanism for fatigue crack propagation through grain boundaries. *Acta Mat.*, 48(20):4917–4927, 2000.

[147] B.A. Cowles. High cycle fatigue in aircraft gas turbinesan industry perspective. *Int. J. Fracture*, 80(2-3):147 – 163, 1989.

[148] Maier H.J. Sangid M.D. and Sehitoglu H. The role of grain boundaries on fatigue crack initiation an energy approach. *Int. J. Plasticity*, 27(5):801–821, 2011.

[149] N. Kawagoishi Q.Y. Wang, C. Bathias and Q. Chen. Effect of inclusion on subsurface crack initiation and gigacycle fatigue strength. *Int. J. Fatigue*, 24 (12):1269–1274, 2002.

[150] R. Gu and A.H.W. Ngan. The mechanisms of metal fatigue (ii). *Phys. Stat. Sol. B.*, 47:359 – 396, 1971.

[151] J.A. Ewing and J.C.W. Humfrey. The fracture of metals under repeated alternations of stress. *Philos Trans Roy Soc Lond, Ser A.*, pages 241–250, 1903.

[152] J. Polak. Resistivity of fatigued copper single crystals. *Mat. Sci. Eng.*, 89: 35–43, 1987.

[153] H. Mughrabi. The cyclic hardening and saturation behaviour of copper single crystals. *Mater. Sci. Eng.*, 33:207–223, 1978.

[154] Z.S. Basinski, S.J. Basinski, and A. Howie. Early stages of fatigue in copper single crystals. *Phil. Mag.*, 19:899–924, 1969.

[155] H. Mughrabi. Dislocation wall and cell structures and long-range internal stresses in deformed metal crystals. *Acta Metall.*, 31(9):1367–1379, 1983.

[156] T.H. Alden and W.A. Backofen. The formation of fatigue cracks in aluminum single crystals. *Acta Metall.*, 9(4):352–366, 1961.

[157] H. Mughrabi, F. Ackermann, and K. Herz. *Fatigue Mechanisms*, chapter Persistent slip bands in fatigued face-centered and body-centered cubic metals. ASTM, 1979.

[158] U. Gosele U. Essmann and H. Mughrabi. A model of extrusions and intrusions in fatigued metals. I. point-defect production and growth of extrusions. *Phil. Mag. A*, 44:405–426, 1981.

[159] P. Neumann. Low energy dislocation configurations : A possible key to the understanding of fatigue. *Mat. Sci. Eng.*, 81:465–475, 1986.

[160] D. Walgraef and E.C. Aifantis. On the formation and stability of dislocation patterns : one-dimensional considerations. *Int. J. Engng. Sci*, 23(12):1351–1358, 1985.

[161] D. Walgraef and E.C. Aifantis. On the formation and stability of dislocation patterns : two-dimensional considerations. *Int. J. Engng. Sci*, 23(12):1359–1364, 1985.

[162] D. Walgraef and E.C. Aifantis. On the formation and stability of dislocation patterns : three-dimensional considerations. *Int. J. Engng. Sci*, 23(12):1365–1372, 1985.

[163] E.C. Aifantis. On the dynamical origin of dislocation patterns. *Mat. Sci. Eng.*, 81:563–574, 1986.

[164] C. Schiller and D. Walgraef. Numerical simulation of persistent slip band formation. *Acta Metall.*, 36(3):563–574, 1988.

[165] E.A. Repetto and M. Ortiz. A micromechanical model of cyclic deformation and fatigue-crack nucleation in FCC single crystals. *Acta mater.*, 45(6):2577–2595, 1997.

[166] J. Polak and J. Man. Mechanisms of extrusion and intrusion formation in fatigued crystalline materials. *Mat. Sci. Eng. A*, 596:15–24, 2014.

[167] V.S. Deshpande, A. Needleman, and E. Van der Giessen. A discrete dislocation analysis of near-threshold fatigue crack growth. *Acta Mater.*, 49(16):3189–3203, 2001.

[168] V.S. Deshpande, A. Needleman, and E. Van der Giessen. Discrete dislocation modeling of fatigue crack propagation. *Acta Mater.*, 50(4):831–846, 2002.

[169] V.S. Deshpande, A. Needleman, and E. Van der Giessen. Discrete dislocation plasticity modeling of short cracks in single crystals. *Acta Mater.*, 51:1–15, 2003.

[170] V.S. Deshpande, A. Needleman, and E. Van der Giessen. Scaling of discrete dislocation predictions for near-threshold fatigue crack growth. *Acta Mater.*, 51:4637–4651, 2003.

[171] S. Brinckmann and E. Van der Giessen. A discrete dislocation dynamics study aiming at understanding fatigue crack initiation. *Mat. Sci. Eng. A*, 387-389: 461–464, 2004.

[172] C. Déprés, C.F. Robertson, and M.C. Fivel. Low strain fatigue in 316L steel surface grains: a three-dimension discrete dislocation dynamics modeling of the early cycles. part 1: Dislocation microstructures and mechanical behavior. *Phil. Mag.*, 84(22):2257–2275, 2004. doi: 10.1080/14786430410001690051.

[173] C. Déprés, Prasad Reddy G.V., C.F. Robertson, and M.C. Fivel. An extensive 3d dislocation dynamics investigation of stage-i fatigue crack propagation. *Phil. Mag.*, 94(36):4115–4137, 2014. doi: 10.1080/14786435.2014.978830.

[174] J.A. El-Awady, N.M. Ghoniem, and H. Mughrabi. Dislocation modelling of localized plasticity in persistant slip bands. In B.L. Adams and A. Garmestani, editors, *Proceedings of the 136th TMS Annual Meeting and Exhibition*, pages 23–35, 2007.

[175] D. Kiener, C. Motz, W. Grosinger, D. Weygand, and R. Pippan. Cyclic response of copper single crystal micro-beams. *Scripta Mater.*, 63:500–503, 2010.

[176] J. Senger, D. Weygand, O. Kraft, and P. Gumbsch. Dislocation microstructure evolution in cyclically twisted microsamples: a discrete dislocation dynamics simulation. *Modelling Simul. Mater. Sci. Eng.*, 19:1–16, 2011. doi: 10.1088/0965-0393/19/7/074004.

[177] C.S. Shin, C.F. Robertson, and M.C. Fivel. Fatigue in precipitation hardened materials: a three-dimensional discrete dislocation dynamics mod-

elling of the early cycles. *Phil. Mag.*, 87(24):3657–3669, 2007. doi: 10.1080/14786430701393159.

[178] Huang M., Tong J., and Li Z. A study of fatigue crack tip characteristics using discrete dislocation dynamics. *Int. J. Plasticity*, 54:229–246, 2014.

[179] J.H. Wilkinson. *Rounding Errors in Algebraic Processes*. Dover Publications, 1994.

[180] N.J. Higham. The accuracy of floating point summation. *SIAM J. Sci. Comput.*, 14(4):783–799, 1993.

[181] J. M. McNamee. A comparison of methods for accurate summation. *ACM SIGSAM Bulletin,*, 38(1):1 – 7, 2004.

[182] C. Zhou, S.B. Biner, and R. LeSar. Discrete dislocation dynamics simulations of plasticity at small scales. *Acta. Mater.*, 58(5):1565–1577, 2010. doi: 10.1016/j.actamat.2009.11.001.

[183] Ma A. Gao S., Fivel M. and Hartmaier A. Influence of misfit stresses on dislocation glide in single crystal superalloys: A three-dimensional discrete dislocation dynamics study. *Journal of the Mechanics and Physics of Solids*, 76:276–290, 2015.

[184] Déprés C., Fivel M., Robertson Ch., Fissolo A., and Verdier M. etude des stades precurseurs de l'endommagement en fatigue : experiences et simulations a l'echelle des dislocations. *J. Phys. IV France*, 106:81–90, 2003. doi: 10.1051/jp4:20030218.

[185] Peach M. and Koehler J.S. The forces exerted on dislocations and the stress fields produced by them. *Physical Review*, 80(3):436, 1950.

[186] Shannon C.E. A mathematical theory of communication. *Bell system technical journal*, 27(3):379–423, 1948.

[187] M. Zaiser, K. Bay, and P. Hähner. Fractal analysis of deformation-induced dislocation patterns. *Acta Mater.*, 47(8):2463 – 2476, 1999. doi: 10.1016/S1359-6454(99)00096-8.

[188] R. Deltombe, K.J. Kubiak, and M. Bigerelle. How to select the most relevant 3d roughness parameters of a surface. *Scanning*, 36:150–160, 2014.

[189] B. Mandelbrot. *The Fractal Geometry of Nature*. Freeman: San Francisco, 1982.

[190] C.D. Zachmann and J. Brickmann. Hausdorff dimension as a quantification of local roughness of protein surfaces. *J. Chem. Inf. Comut. Sci.*, 32:120–122, 1992.

[191] J. M. Elson and J.M. Bennett. Calculation of the power spectral density from surface profile data. *Appl. Optics*, 34(1):201–208, 1995.

[192] A. Duparre, J.F. Borrull, S. Gliech, G. Notni, J. Steinert, and J.M. Bennett. Surface characterization techniques for determining the root-mean-square roughness and power spectral densities of optical components. *Appl. Optics*, 41 (1):154–171, 2002.

[193] U. Essmann and M. Rapp. Slip in copper crystals following weak neutron bombardment. *Acta Metall.*, 21:1305–1317, 1979.

[194] S. Brinckmann, R. Sivanesapillai, and A. Hartmaier. On the formation of vacancies by edge dislocation dipole annihilation in fatigued copper. *Int. J. Fatigue*, 33:1369–1375, 2011.

[195] W. Kienle H. Mughrabi, T. Ungar and M. Wilkens. Long-range internal stresses and asymmetric x-ray line-broadening in tensile-deformed [001]-orientated copper single crystals. *Phil. Mag.*, 53(6):793–813, 1986.

[196] J. Cuddy and N. Bassim. Study of dislocation cell structures from uniaxial deformation of aisi 4340 steel. *Mat. Sci. Eng. A*, 113:421–429, 1989.

[197] C.D. Liu, D.X. You, and M.N. Bassim. Cyclic strain hardening in polycrystalline copper. *Acta Metall. Mater.*, 42(5):1631–1638, 1993.

[198] D.J. Morrison and Chopra V. Cyclic stress-strain response of polycrystalline nickel. *Mater. Sci. Eng. A*, 177:29–42, 1994.

[199] N.Y Jin and A.T. Winter. *Basic Questions in Fatigue, Vol I*, chapter Role of cross-slip of screw dislocations in fatigue behavior of copper single crystals, pages 17–25. ASTM, 1988.

[200] J. Schrank, W. Prantl, and Stuwe H.P. The influence of crystal orientation on the fatigue softening behaviour of severely predeformed copper. *Mat. Sci. Eng. A*, 110:61–68, 1989.

[201] J. Man, K. Obrtlik, and J. Polak. Study of surface relief evolution in fatigued 316l austenitic stainless steel by afm. *Mat. Sci. Eng. A*, 351(1–2):123 – 132, 2003. doi: 10.1016/S0921-5093(02)00846-8.

[202] H. Mughrabi. Long-range internal stress field in the dislocation wall structure of persistent slip bands. *Phys. Stat. Sol.*, 104:107–120, 1987.

[203] J. Kristan and J. Kratochvil. Interactions of glide dislocations in a channel of a persistent slip band. *Phil. Mag.*, 87(29):4593–4613, 2007.

[204] H. Mughrabi and F. Pschenitzka. Constrained glide and interaction of bowed-out screw dislocations in confined channels. *Phil. Mag.*, 85(26–27):3029–3045, 2005.

[205] K.W. Schwarz and H. Mughrabi. Interaction and passing stress of two threading dislocations of opposite sign in a confined channel. *Phil. Mag.*, 86(12):773–785, 2006.

[206] B. Tippelt, J. Breitschneider, and P. Hahner. The dislocation microstructure of cyclically deformed nickel single crystals at different temperatures. *Phys. Stat. Sol. A*, 163:11–26, 1997.

[207] U. Essmann and H. Mughrabi. Annihilation of dislocations during tensile and cyclic deformation and limits of dislocation densities. *Phil. Mag. A*, 40:731–736, 1979.

[208] J.W Westbrook. Temperature dependence of the hardness of secondary phases common in turbine bucket alloys. *Trans. AIME*, 209:898, 1957.

[209] R.G. Davies and P.H. Thornton. The temperature dependence of the flow stress of gamma prime phases having the ll2 structure. *Metall. Mater. Trans. B*, 1(2): 549–550, 1977.

[210] P. Veyssiere and G. Saada. *Dislocations in Solids*, volume 10, chapter Microscopy and plasticity of the $L1_2$ $\gamma'$ phase. Elsevier Science Ltd, 1996.

[211] B.H. Kear and H.F. Wilsdorf. Dislocation configurations in plastically deformed cu3au alloys. *Trans. Metall. Soc.*, 224:382–386, 1962.

[212] V. Paidar, D.P. Pope, and V. Vitek. A theory of the anomalous yield behavior in $l1_2$ ordered alloys. *Acta Metall.*, 32:435–448, 1984.

[213] T.M. Pollock and S. Argon. Creep resistance of cmsx-3 nickel base superalloy single crystals. *Acta Metall. Mater.*, 40:1–30, 1992.

[214] L. Kovarik, R.R. Unocic, J. Li, P. Sarosi, C. Chen, Y. Wang, and M.J. Mills. Microtwinning and other shearing mechanisms at intermediate temperatures in ni-based superalloys. *Prog. Mater. Sci.*, 54:839–873, 2009.

[215] W. Betteridge and S.W.K. Shaw. Development of superalloys. *Mater. Sci. Tech.*, 3:682–694, 1987.

[216] E.E. Brown and D.R. Muzyka. *Superalloys II: High Temperature Materials for Aerospace and Industrial Power*, chapter Nickel-iron alloys. John Wiley and Sons, 1987.

[217] R.A. Ricks, A.J. Porter, and R.C. Ecob. The growth of $\gamma'$ precipitates in nickel-base superalloys. *Acta metall.*, 31(1):43–53, 1983.

[218] R.W. Cahn, P.A. Siemers, J.E. Geiger, and P. Bardhan. The order-disorder transformation in ni3al and ni3al fe alloysi. determination of the transition temperatures and their relation to ductility. *Acta metall.*, 35(11):2737–2751, 1987.

[219] Y.Q. Sun and P.M. Hazzledine. *Dislocations in Solids*, volume 10, chapter Geometry of dislocation glide in Ll2-phase: TEM observations. Elsevier Science Ltd, 1996.

[220] J. Sun, C.S. Lee, J.K.L. Lai, and J.S. Wu. Dislocation dissociations and fault energies in ni3al alloys doped with palladium. *Intermetallics*, 7:1329–1335, 1999.

[221] S.I. Rao, T.A. Parthasarathy, D.M. Dimiduk, and P.M. Hazzledine. Discrete dislocation simulations of precipitation hardening in superalloys. *Phil. Mag.*, 84(30):3195–3215, 2004.

[222] A.C. Picasso, A.J. Marzocca, and I. Alvarez. Cross-slip and dislocation climb in nickel based superalloys. *Mat. Sci. Eng. A*, 234-236:1099–1102, 1997.

[223] S.S. Ezz, D.P. Pope, and V. Paidar. The tension/compression flow stress assymetry in ni3(al,nb) single crystals. *Acta Metall.*, 30:921–926, 1982.

[224] D.C. Chrzan and M.J. Mills. *Dislocations in Solids*, volume 10, chapter Dynamics of dislocation motion in L12 compounds. Elsevier Science Ltd, 1996.

[225] M.J. Mills and D.C. Chrzan. Dynamical simulation of dislocation motion in ll2 alloys. *Acta Matall. Mater.*, 40(11):3051–3064, 1992.

[226] A.E. Staton-Bevan and R.D. Rawlings. Deformation behavior of single crystal $ni_3$(al,ti). *Phys. Stat. Solidi A*, 29(2):613–622, 1975.

[227] F. Takeuchi and E. Kuramoto. Temperature and orientation dependence of the yield stress in $ni_3$ga single crystals. *Acta Metall.*, 21:415–425, 1973.

[228] Y. Umakoshi, D.P. Pope, and V. Vitek. The asymmetry of the flow stress in $ni_3$(al,ta) single crystals. *Acta. Metall.*, 32(3):449–456, 1984.

[229] C. Lall, S. Chin, and P.Pope. The orientation and temperature dependence of the yield stress of ni3(al,nb) single crystals. *Metall. Trans. A*, 10(9):1323–1332, 1979.

[230] M.H. Yoo. On the theory of anomalous yield behavior of $ni_3$al - effect of elastic anisotropy. *Script. Mater.*, 20:915–920, 1986.

[231] A.J.E. Foreman and M.J. Makin. Dislocation movement through random arrays of obstacles. *Phil. Mag.*, 14(131):911–924, 1966.

[232] B. Devincre, P. Veyssiere, L.P. Kubin, and G. Saada. A simulation of dislocation dynamics and of the flow stress anomaly in l12 alloys. *Phil. Mag. A*, 75(5):1263–1286, 1997.

[233] B. Devincre, P. Veyssiere, and G. Saada. Simulation of the plastic flow in ni$_3$al.

[234] V. Mohles, D. Ronnpagel, and E. Nembach. Simulation of dislocation glide in precipitation hardened materials. *Comp. Mat. Sci.*, 16:144–150, 1999.

[235] V. Mohles. Simulation of dislocation glide in overaged precipitation hardened materials. *Phil. Mag. A*, 81(4):971–990, 2001.

[236] V. Mohles. Orowan process controlled dislocation glide in materials containing incoherent particles. *Mat. Sci. Eng. A*, 309–310:256–269, 2001.

[237] V. Mohles and E. Nembach. The peak- and overaged states of particle strengthened materials: Computer simulations. *Acta Mater.*, 49:2405–2417, 2001.

[238] V. Mohles. The critical resolved shear stress of single crystals with long-range ordered precipitates calculated by dislocation dynamics simulations. *Mat. Sci. Eng. A*, 365(1–2):144–150, 2004.

[239] S.I. Rao, T.A. Parthasarathy, D.M. Dimiduk, and P.M. Hazzledine. Discrete dislocation simulations of precipitation hardening in inverse superalloys. *Phil. Mag. Lett.*, 86(4):215–225, 2006.

[240] S.I. Rao, M.D. Uchic, P.A. Shade, C. Woodward, T.A. Parthasarathy, and D.M. Dimiduk. Critical percolation stresses of random frankread sources in micrometer-sized crystals of superalloys. *Model. Sim. Mat. Sci. Eng.*, 20:065001, 2012.

[241] C. S. Shin, M.C. Fivel, and K.H. Oh. Nucleation and propagation of dislocations near a precipitate using 3d discrete dislocation dynamics simulations. *J. Phys. IV*, 11(5):27–34, 2001.

[242] C. S. Shin, M.C. Fivel, M. Verdier, and K.H. Oh. Dislocationimpenetrable precipitate interaction: a three-dimensional discrete dislocation dynamics analysis. *Phil. Mag.*, 83:3691–3704, 2003.

[243] K. Yashiro, F. Kurose, Y. Nakashima, K. Kubo, Y. Tomita, and H.M. Zbib. Discrete dislocation dynamics simulation of cutting of precipitate and interfacial dislocation network in ni-based superalloys. *Int. J. Plast.*, 22(4):713–723, 2006. doi: 10.1016/j.ijplas.2005.05.004.

[244] C.S. Shin, M.C. Fivel, and M. Verdier C.F. Robertson. Dislocation dynamics simulations of fatigue of precipitation-hardened materials. *Mat. Sci. Eng. A*, 25:166–169, 2005.

[245] A. Vattré, B. Devincre, and A. Roos. Dislocation dynamics simulations of precipitation hardening in ni-based superalloys with high $\gamma'$ volume fraction. *Intermetallics*, 17(12):988–994, 2009. doi: 10.1016/j.intermet.2009.04.007.

[246] M. Huang, L. Zhao, and J. Tong. Discrete dislocation dynamics modelling of mechanical deformation of nickel-based single crystal superalloys. *Int. J. Plasticity*, 28(1):141–158, 2012.

[247] H. Yang, Z. Li, and M. Huang. Modeling dislocation cutting the precipitate in nickel-based single crystal superalloy via the discrete dislocation dynamics with sisf dissociation scheme. *Comp. Mater. Sci.*, 75:52–59, 2013.

[248] S.M. Haghighat, G. Eggeler, and D. Raabe. Effect of climb on dislocation mechanisms and creep rates in $\gamma'$ strengthened ni base superalloy single crystals: A discrete dislocation dynamics study. *Acta Mater.*, 61:3709–3723, 2013.

[249] B. Liu, D. Raabe, F. Roters, , and A. Arsenlis. Interfacial dislocation motion and interactions in single-crystal superalloys. *Acta Mater.*, 79(216–233), 2014.

[250] J. O'Rourke. *Computational Geometry in C*. Cambridge University Press, 1998.

[251] T.H. Cormen, C.E. Leiserson, R.L. Rivest, and C. Stein. *Introduction to Algorithms, 3rd Ed.* MIT Press, 2009.

[252] M.D. Uchic and D.M. Dimiduk. A methodology to investigate size scale effects in crystalline plasticity using uniaxial compression testing. *Mat. Sci. Eng. A*, 400–401(1):268–278, 2005.

[253] B. Reppich. *Materials Science and Technology A Comprehensive Treatment*, volume 6, chapter Particle Strengthening. Weinheim VCH, 1993.

[254] M.D. Uchic, D.M. Dimiduk, J.N. Florando, and W.D. Nix. Sample dimensions influence strength and crystal plasticity. *Science*, 305:986–989, 2004.

[255] P.A. Shade, M.D. Uchic, D.M. Dimiduk, G.B. Viswanathan, R. Wheeler, and H.L. Fraser. Size-affected single-slip behavior of ren n5 microcrystals. *Mat. Sci. Eng. A*, 535:53–61, 2012. doi: 10.1016/j.msea.2011.12.041.

[256] S.S. Shishvan, S. Mohammadi, M. Rahimian, and E. Van der Giessen. Plane-strain discrete dislocation plasticity incorporating anisotropic elasticity. *Int. J. Sol. Struc.*, 48(2):374–387, 2011.

# Vita

Ahmed Hussein was born in Cairo, Egypt in 1986. In 2003, he graduated high school from Orouba School in Maadi, Cairo. He started his undergraduate studies in the School of Engineering in Cairo University. He graduated in 2008 with first class honors from the department of Aerospace Engineering. He started his Master degree studies immediately after graduation and obtained his M.Sc. in Aerospace Engineering in 2010. Between September 2008 and February 2011, he held the position of a full time software developer in Applied Science International where he developed geometry processing libraries and mathematical models for structural materials behavior to be used in engineerign analysis software. He also had a secondary appointment as a teaching assistant in the department of Aerospace Engineering in Cairo University. In February 2011, he joined the Computational and Experimental Materials Engineerign Laboratory at Johns Hopkins University as a research assistant working on the computational modeling of plasticity and crack initiation in metals.

**List of Publications**

- Hussein et. al. "Microstructurally based cross-slip mechanisms and their effects on dislocation microstructure evolution in fcc crystals", Acta Mater. 85(2015), 180-190

- A.M. Hussein and J.A. El-Awady "Quantifying Dislocation Microstructure Evolution and Cyclic Hardening in Fatigued Nickel Single-Crystals", Submitted

- A.M. Hussein and J.A. El-Awady "The early cycle development of surface roughness of cyclically loaded FCC single crystals", In preparation
- A.M. Hussein and J.A. El-Awady "Deformation Evolution in Persistent Slip Bands", In preparation
- Hussein et. al. "The Deformation Response of Nickel Based Superalloy Microcrystals under Monotonic Loading", In preparation